Short-time Hanbury-Brown and Twiss correlation of a single-electron beam in ballistic conductors

François Parmentier

Département de Physique
École Normale Supérieure

Laboratoire Pierre Aigrain

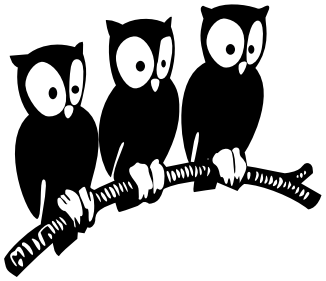

THÈSE de DOCTORAT de l'UNIVERSITÉ PARIS 6

Spécialité : Physique Quantique

présentée par

François PARMENTIER

pour obtenir le grade de DOCTEUR de l'UNIVERSITÉ PARIS 6

Short-time Hanbury-Brown and Twiss correlation of a single-electron beam in ballistic conductors

---

Soutenue le 26 Novembre 2010
devant le jury composé de :

M.	**Jean-Marc BERROIR**	Directeur de thèse
M.	**Alberto BRAMATI**	Président du jury
M.	**Pertti J. HAKONEN**	Rapporteur
M.	**Frank HEKKING**	Rapporteur
M.	**Laurent SAMINADAYAR**	Examinateur
M.	**Gwendal FÈVE**	Invité

Remerciements

Je tiens en premier lieu à remercier Jean-Marc Berroir, sans qui (pour plusieurs raisons) ce manuscrit n'aurait très probablement pas existé : Jean-Marc m'a d'abord accueilli, en tant que directeur de la Formation Interuniversitaire de Physique (qui à l'époque s'est très brièvement appelée Parcours Interuniversitaire de Physique), au sein du cursus de physique de l'Ecole Normale Supérieure. Il m'a ensuite, coiffé de sa double casquette de directeur du Laboratoire Pierre Aigrain et de directeur de thèse, accueilli en thèse au LPA. J'ai eu l'occasion, au cours de ces six années, d'apprécier sa vision de la science, où recherche et enseignement sont indissociables.

Je voudrais également remercier chaleureusement les membres du groupe de physique mésoscopique, en particulier Gwendal Fève, qui m'a encadré au cours de ma thèse avec sagacité, bonne humeur et chansons. Merci également à Christian Glattli et à Bernard Plaçais pour leurs idées, conseils et soutiens, qui auront été décisifs dans l'accomplissement de cette thèse. Merci enfin à Takis Kontos, pour sa bonne humeur méditerranéenne, ses discussions stimulantes, et sa participation compulsive à nos concours d'imitations (pas toujours réussies).

Je souhaite remercier les membres du jury : Pertti Hakonen et Frank Hekking, qui ont accepté d'être rapporteurs de ce manuscrit, ainsi qu'Alberto Bramati et Laurent Saminadayar, pour l'intérêt qu'ils ont porté à ces travaux. Je les remercies également pour leur présence lors de la soutenance.

J'ai travaillé durant ma thèse avec Adrien Mahé et Erwann Bocquillon, qui m'ont respectivement précédé et succédé. Les travaux présentés dans ce manuscrit n'auraient pu aboutir sans leur participation. Avec Gwendal, ils ont formé une équipe où la bonne humeur est permanente (obligatoire ?), y compris dans les moments où rien ne marche (si, ça arrive). J'ai énormément apprécié notre collaboration, et souhaite bon courage à Erwann, à qui reviennent les lourdes responsabilités de manoeuvrer la manip, de former un futur successeur, et de... d'apprécier les chants de Gwendal, voila.

L'excellente ambiance en P13 (pardon, L175) et affiliés a fait de ces trois années de thèse un moment extrêmement agréable. Je remercie pour cela Chéryl, Thomas, Julien, Adrien, Gwendal, Lorenz, Emiliano, Andreas, Erwann, Matthieu, Dora, Jérémie et Manu, et espère pouvoir continuer les traditionnelles "bières-labo".

J'ai bénéficié du soutien et de l'amitié des membres du personnel administratif et technique du LPA et du Département de Physique. Je remercie chaleureusement Anne Matignon, Fabienne Renia, Anne Denis, David Darson, Philippe Pace, Pascal Morfin, Jean-Charles Dumont, Sylvain Plenel, ainsi que le gardien de nos addictions aux liquides cryogéniques et non moins fameux cascadeur sur chaise Olivier Andrieu. J'en profite pour remercier ici tous les membres du LPA avec qui j'ai pu interagir autour d'un café/d'un ballon de foot/d'une bière/d'une galette des rois/d'un fish and chips. Merci en particulier à Benjamin et Sukhy, pour m'avoir laissé imprimer des exemplaires de mon manuscrit chez eux, page par page.

Je remercie également tous les membres de la communauté de physique mésoscopique avec qui j'ai pu collaborer au cours de ces trois années de thèse, en particulier Pascal Degiovanni, Charles Grenier, Frédéric Pierre, Hélène Lesueur, Carles Altimiras, Ulf Gennser, Yong Jin, Fabien Portier, Patrice Roche, Preden Roulleau, Markus Büttiker, Christian Flindt et Mathias Albert.

Maintes heures du déjeuner ont été rythmées par le martèlement (léger quand même) des foulées du membres du club-des-gens-qui-courent-au-Luxembourg-le-midi-mais-qui-n'en-est-pas-un ; courir avec eux a toujours été très agréable, même dans les pires conditions météorologiques. Un grand merci à Olivier, Mickaël, Marie-Béatrice, Matthieu, Erwann, Nir, Sukhy, Nicolas, Andreas, Adrien, Bernard,

Jean-Marc, Jean-François, et aux autres coureurs occasionnels.

La pratique de la musique m'a permis de bien me changer les idées, particulièrement aux rares moments pénibles de cette thèse. Merci pour cela aux membres de (feu) Do You Schoolbus?, Henri-Alex, Matthieu, Jean-No et Eloi ; aux fulgurants Pamplemousses Ethyliques, Nicko "Lowest Landau Level" Rougerie, Jean-Pierre Baguette et Camille "Guitar Magique" Bouvard ; merci enfin à tous ceux avec qui j'ai pu occasionnellement beuffer : Billitch, Simon Colvinter, Nicolas Brantut, et bien d'autres.

Je remercie enfin tous mes amis, dont je ne vais pas énumérer les noms ici, parce que ceci est un manuscrit de thèse, et pas un annuaire ; un grand merci à mes parents, mes frères, ma grand-mère, mes cousins, ainsi qu'à Elizabeth et Pierre ; enfin, un très grand merci à Judy, pour son amour, sa patience, et son coq au vin.

"Si le ciel est un parapluie, où sont les baleines ?"
F'Murrr.

"The dominant tradition in late 20th century scientific prose has been to produce something suitable for direct transmission from one computer to another..."
N. David Mermin, Writing Physics.

"C'est de la contemplation des cieux que naissent les grandes idées !"
F'murrr.

Table of contents

Introduction **1**

1 Electron quantum optics in 2-D electron gases . . . 2
2 Single-charge electron quantum optics . . . 6
3 Results obtained during the thesis . . . 11
4 Perspectives . . . 13

Chapter 1 - Realization of a Single Electron Source **15**

1.1 Response of a mesoscopic capacitor to a periodic excitation: theory . . . 17
1.2 Measurement of the average AC current emitted by the source . . . 24
1.3 Average AC current in the linear regime . . . 26
1.4 Average AC current in the non-linear regime . . . 32
1.5 Validity of the model . . . 46

Chapter 2 - Current fluctuations emitted by the source **51**

2.1 Current correlations under periodic driving . . . 54
2.2 Scattering model . . . 55
2.3 Heuristic model . . . 64
2.4 Experimental setup . . . 70
2.5 Experimental results . . . 73

Chapter 3 - Current fluctuations in the Hanbury-Brown and Twiss geometry **81**

3.1 Current auto and cross-correlations in the HBT geometry . . . 83
3.2 Partition of a single-charge beam: scattering model . . . 87
3.3 Experimental setup . . . 101
3.4 Preliminary results . . . 104

Chapter 4 - High-frequency and low-frequency noise measurement setups **119**

4.1 High sensitivity ultra-low temperature RF current and noise measurement setup . . . 121
4.2 Low frequency noise measurement setup . . . 132

Conclusion **142**

Appendix A - Scattering Formalism **145**

Appendix B - Summary of the samples parameters **153**

List of figures **155**

Bibliography **159**

Introduction

The purpose of this thesis, pertaining to the field of mesoscopic physics, is the study of the current fluctuations emitted by a single electron source both in a direct measurement of the single-electron beam, and after partition of the beam by a beam-splitter. The recent developments in micro and nano-fabrication techniques, as well as in cryogenic instrumentation, have allowed the study of structures and materials in which electronic transport is ruled by quantum mechanics. In particular, the ability to engineer ballistic conductors presenting large phase coherence lengths and elastic mean free paths has opened the way to the practical realization of electronic interferometry devices mimicking cornerstone wave optics experiments, such as the double slit experiment [1], and the electronic Mach-Zehnder interferometer [2]. Both these experiments were implemented in high-mobility two-dimensional electron gases (2DEGs) obtained at the heterojunction between two semiconductors (here, $GaAs$-$AlGaAs$), and put into light the role of the magnetic field (applied perpendicularly to the 2DEG) in the interferences through the Aharonov-Bohm phase [3] acquired by electrons in the interferometer. Along with the striking demonstration of particle/wave duality of electrons in a mesoscopic conductor, these experiments have led to studies of fundamental quantum mechanics processes occurring in a mesoscopic conductor, such as the controlled loss of interferences caused by a which-path detector [4], or the precise determination of the electronic phase coherence length in a Mach-Zehnder interferometer [5]. Herein lies the great interest of the field of electron quantum optics, where one uses electrons in a ballistic quantum conductor to reproduce wave and quantum optics experiments: the tools of wave and quantum optics can be transposed to mesoscopic devices, in order to probe the fundamental properties of quantum electronic transport. In a further analogy with quantum optics, even more quantitative informations can be extracted from the measurement of current fluctuations, as they unveil two-particle correlation within the current, particularly two-particle interferences [6, 7]; moreover, a great richness is brought in comparison with quantum optics by the presence of interactions. As of yet, all of these electron quantum optics experiments were performed with sources continuously emitting a large number of charges, without precise control over the energy and emission time; as in quantum optics, it is thus crucial to implement experiments where ultimate control over a single electron is achieved in order to study fundamental quantum mechanics processes occurring at the single particle scale. Similarly to single-photon quantum optics, these so-called single-charge electron quantum optics experiments would for instance allow to perform the entanglement of two independent single particles [8, 9], leading to quantum information processing based on the coherent control of single charges.

While the basic building blocks of electron quantum optics were masterfully implemented in previous experiments, the development of a fully controlled single electron emitter, obviously essential to the realization of single-charge electron quantum optics experiments, was only reported recently [10]. In this thesis, we present the first experimental realizations of single-charge electron quantum optics experiments using the single electron emitter developed at the Laboratoire Pierre Aigrain [10, 11]. We also give a theoretical description of our source within a Floquet scattering matrix formalism in order to interpret our experimental results.

In this introduction, we first present the framework of electron quantum optics in two-dimensional electron gases in the integer Quantum Hall Effect (QHE) regime, where electrons propagate along edge channels defined by the edges of the sample; we present the electronic Mach-Zehnder interferometer experiment, allowing us to describe the basic building blocks used in electron quantum optics in the QHE regime. We then present the concepts motivating the development of single-charge electron quantum optics, and describe several types of single electron emitter, including the one studied in this

thesis; we also discuss the importance of noise measurements in single-charge electron quantum optics experiments. Lastly, we briefly describe the two single-charge electron quantum optics experiments performed during my thesis, that is the measurement of the current fluctuations emitted by the source and the current fluctuations after partition by a beam splitter, in a Hanbury-Brown and Twiss (HBT) configuration. We also present the principle of the next experiment, where two synchronized sources are used to collide single charges in a Hong-Ou-Mandel geometry [12].

1 Electron quantum optics in 2-D electron gases

Two-dimensional electron gases are formed at the heterojunction between two semiconductors. The progress in epitaxial growth has allowed to engineer samples with exceptional degrees of purity, with two-dimensional electron gases presenting mobilities larger than 10×10^6 cm^2/Vs [13, 14]. In such structures, the large phase coherence length and mean free path (~ 10 μm) have allowed the observation of electronic interferences.

1.1 Electronic coherence in 2DEGs: the electronic Mach-Zehnder interferometer

One of the most striking examples of quantum interference devices in a 2DEG is the Mach-Zehnder interferometer, first realized at the Weizmann Institute in 2003 [2]. The principle of the interferometer is described in Fig.1, along with its optics equivalent and the measured interference signal. A high perpendicular magnetic field is applied to the sample, so as to enter the quantum Hall effect regime; a source contact (S) is used to send electrons towards a first beam splitter (QPC1). The reflected and transmitted paths are then recombined on a second beam splitter (QPC2); the phase difference between the two paths is given by the Aharonov-Bohm phase $\phi = 2\pi\mathcal{A} \times B/\Phi_0$, where $\mathcal{A}$ is the area of the loop defined by the two paths, B the perpendicular magnetic field, and $\Phi_0 = h/e$ the flux quantum. This phase can be modulated by either changing the magnetic field, or by changing the length of the lower path with the side gates MG1 and MG2, thus modifying the area of the loop. After recombination, the two output currents are collected on the detectors D1 and D2; Fig.1 shows the variation of the current collected on D1 as a function of the magnetic field (blue) and side gate voltage V_{MG} (red). Both currents present clear periodic oscillations, demonstrating electronic interferences in the device. The visibility of these interferences is very high ($\sim 60\%$); visibilities up to 90% have been recently demonstrated [7].

The electronic Mach-Zehnder interferometer has been since then realized in several other groups [15, 16, 17], and has allowed to study the decoherence of electrons in QHE edge channels [5, 18, 19] as well as to observe two-particle interferences in a double electronic Mach-Zehnder interferometer [7].

1.2 Building blocks of electron quantum optics in 2DEGs

We now describe the basic building blocks of electron quantum optics, in analogy with quantum optics: QHE edge channels are used as one-dimensional phase coherent quantum rails, quantum point contacts as tunable electronic beam splitters, and ohmic contacts as sources and detectors.

1.2.1 QHE edge channels

When a strong perpendicular magnetic field is applied to a two-dimensional electron gas, electron transport only occurs along the edges of the sample defining the 2DEG. Furthermore, the conductance of the sample becomes quantized in units of e^2/h, equal to the inverse of the resistance quantum $R_k \approx 25.8$ kΩ. This so-called quantum Hall effect (QHE) can be described in a semi-classical view

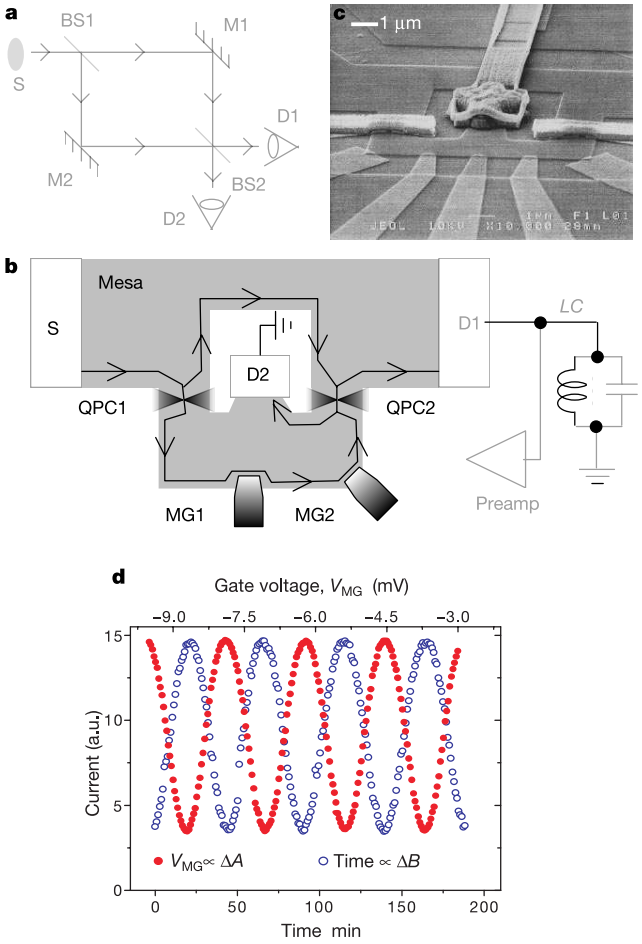

Figure 1: Electronic Mach-Zehnder interferometer. **a)** principle of the optical Mach-Zehnder interferometer. **b)** schematic of the electronic Mach-Zehnder interferometer, as implemented in [2] in a 2DEG. **c)** SEM view of the device. **d)** Measured interference patterns in the current detected on contact $D1$. Red dots: the side gate MG is swept, changing the area of the Aharonov-Bohm loop. Blue circles: current as a function of time: the slow decay of the persistent current in the superconducting magnet effectively changes the magnetic field. These figures were taken from [2].

by considering the cyclotron motion of electrons in the 2DEG in presence of a perpendicular magnetic field. The semi-classical motion of electrons is depicted in Fig.2a: electrons in the bulk move in closed cyclotron orbits with a fixed center of motion, and therefore cannot travel from one end of the sample to the other. The cyclotron orbits of electrons near the edges, on the other hand, are interrupted by the edges, so that electrons "bounce" forward along skipping orbits. Because of the fixed direction of rotation, all electrons on one edge propagate in the same direction (in Fig.2a, electrons in the upper edge propagate from left to right), whereas electrons near the other edge propagate in the opposite direction: electronic transport in the QHE regime is therefore chiral.

The quantized value of the conductance can be explained by considering the energy spectrum of electrons in the 2DEG: electrons in the bulk are distributed on Landau levels with an energy $E_n = \hbar\omega_c(n+1/2)$, where $\omega_c = |eB/m^*|$ is the cyclotron pulsation (the effective mass m^* of electrons in 2DEGs is equal to $0.067m_e$) [20]. These Landau levels are bent near the potential barriers constituting the edges of the sample, see Fig.2b; at high magnetic field, spin-degeneracy in the Landau levels is

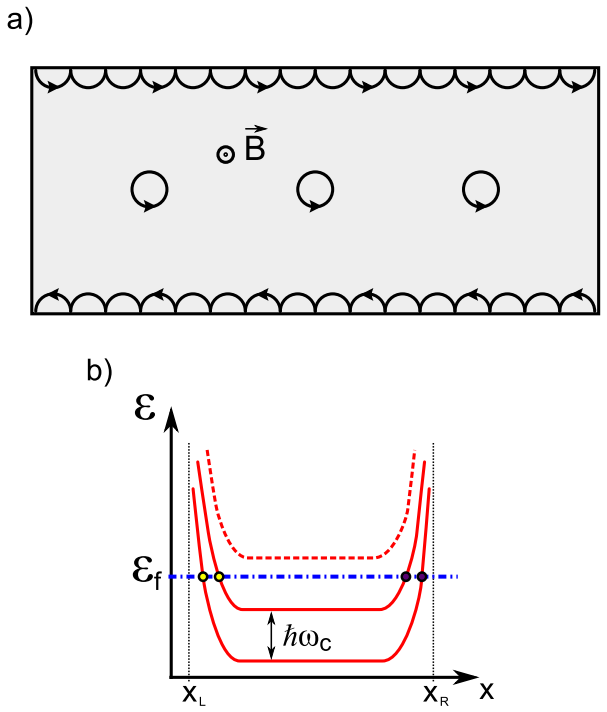

Figure 2: a) semi-classical interpretation of the quantum Hall effect: The 2DEG is represented in light gray, and electrons propagate chirally along the upper and lower edges of the gas. The electrons in the bulk do not take part in the transport. **b)** energy diagram of the Landau levels (red lines) in the presence of edges at the positions x_L and x_R. Edge states (green and purple dots) follow the equipotential lines formed at the intersection with the Fermi level (blue dashed line). Here, the filling factor ν is equal to 4 (2 Landau levels $\times$ 2 spins; Zeeman splitting is not shown on this diagram).

removed by Zeeman splitting, and enhanced by interactions. The finite number of electrons in the 2DEG defines the Fermi energy, which, for given values of the magnetic field, only crosses the Zeeman-split Landau levels near the edges, thus defining a finite number of chiral edge channels. This number depends on the magnetic field: as B increases, the Landau levels are shifted upward with respect to the Fermi energy, so that the number of Zeeman-split Landau levels crossing the Fermi level (that is, the number of filled Landau levels, called filling factor ν) decreases. In particular, at filling factor $\nu = 2$, electronic transport occurs on two edge channels, which are spin-polarized [20] (the first Landau level is completely filled, spin up and spin down).

Finally, the absence of backscattering in the edge channels [21] dramatically increases the mean free path ($\sim 100\mu m$) of electrons; large phase coherence lengths have also been measured (~ 20 μm at 20 mK [5]).

In the quantum Hall effect regime, electrons thus propagate along one-dimensional, phase coherent, chiral edge channels without backscattering, that can be used as quantum rails in the realization of electron quantum optics experiments. In this respect, many studies (experimental as well as theoretical) have been performed in order to fully characterize the properties of electronic transport in edge channels: among others, the noiseless character of transport in edge channels has been demonstrated [22, 23]; an electronic Mach-Zehnder interferometer was used to measure the value of the phase coherence length given above, and the study of energy relaxation between adjacent edge channels was recently realized [24, 25, 26]. More generally, theoretical predictions were made regarding the relaxation

and decoherence of electronic excitations in an edge channel in the presence of a Fermi sea [27].

1.2.2 Quantum point contact

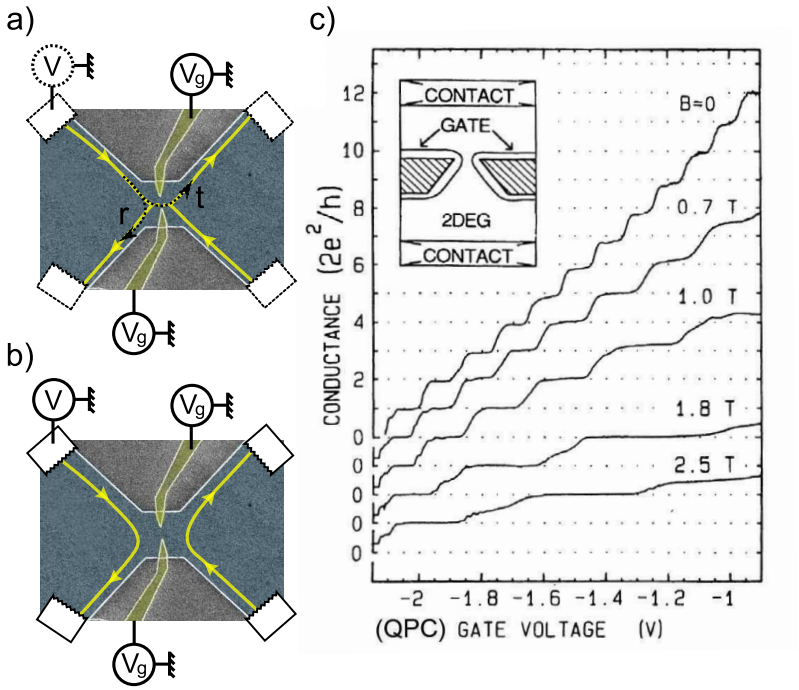

Figure 3: a) and **b)** false-colors SEM view of a quantum point contact. The 2DEG is colored in blue, and the metallic QPC gates are colored in yellow. The yellow arrows represent the typical trajectories of the edge channels (corresponding to equipotential lines): in **a)**, the transmission of the QPC is finite, so that electrons can be partially transmitted. In **b)**, the transmission is zero: the electrons are systematically reflected. **c)** experimental realization of a QPC: the conductance, plotted as a function of the QPC gate voltage, presents quantized plateaus. The number of plateaus decreases as the magnetic field increases, corresponding to a decrease in the number of conduction channels. The data are taken from [28].

The electronic analog of a beam splitter can be implemented in a two-dimensional electron gas in the form of a quantum point contact (QPC) which consists of a pair of electrostatic gates deposited on the surface of the sample. The typical geometry of QPC gates is shown in Fig.3a: when a negative gate voltage is applied on the gates, a constriction is created in the 2DEG between the gates because of electrostatic repulsion. This constriction gives rise to a potential barrier, the shape of which can be determined from the geometry of the gates [29]. At zero field, because of the finite width of the constriction w, the number n of transmitted electronic modes becomes quantized in units of $\lambda_f/2w$ [30], where $\lambda_f \approx 60$ nm is the Fermi wavelength of electrons in the 2DEG. The relatively large value of λ_f allows to design QPCs with typical widths comparable to λ_f, which can be tuned by changing the gate voltage. In particular, when large negative gate voltages are applied, the potential barrier becomes very large, and no electron can be transmitted (Fig.3b).

At high magnetic field, the description of the transmission through the QPC in terms of spin-degenerate electronic modes is replaced by the description in terms of edge channels following equipotential lines, which are reflected one by one as the QPC gate voltage is swept towards large negative

values. This effect was first experimentally demonstrated in [28], see Fig.3c: the conductance at magnetic fields below $B = 1T$ presents steps in units of $2e^2/h$. At high magnetic field, the height of the conductance steps is equal to e^2/h, reflecting the removal of spin-degeneracy, while the number of conductance steps n decreases with the magnetic field, and corresponds to the number of edge channels (given by the filling factor ν). Between two conductance plateaus, the conductance G of the QPC is proportional to the transmission probability D: $G = D\frac{e^2}{h}$, and can be generalized for finite number of edge channels ν: $G = \sum_{i=1}^{\nu} D_i \frac{e^2}{h}$, where D_i is the transmission of the i-th edge channel. Fig.3c therefore demonstrates that one can tune the transmission of a QPC by changing its gate voltage; in particular, when set at the exact half of the opening of the first conductance plateau, the outer edge channel is partially transmitted with a probability amplitude $|t|^2 = D = 0.5$, while all other edge channels are fully reflected. The quantum point contact therefore acts as a tunable, channel-selective beam splitter.

Quantum point contacts are crucial elements in electron quantum optics experiments, such as the electronic Mach-Zehnder interferometer; QPCs also allow to put into evidence striking phenomena through noise measurements.

- **Partition noise**

The study of the fluctuations of a current partitioned by a QPC at low temperature allows to probe the quantum statistics underlying electron transport in edge channels: indeed, in the case of a classical current $I = GV = D\frac{e^2}{h}V$, where V is the bias voltage applied to the upper left contact in Fig.3a, one expects Poissonian fluctuations $S_{II} = 2eI = 2e\frac{e^2}{h}V \times D$. However, it was experimentally demonstrated that the fluctuations of a partitioned current in an ideal quantum conductor [31], and in an edge channel [32] are sub-Poissonian: $S_{II} = 2eI(1-D) = 2e\frac{e^2}{h}V \times D(1-D)$. The shot noise $2eI$ is thus reduced by a factor $(1-D)$; in particular, at unity transmission, the fluctuations vanish. This suppression of shot noise demonstrates that Pauli exclusion principle correlates the flow of electrons participating in mesoscopic currents.

Furthermore, noise measurements in Hanbury-Brown and Twiss geometries [32, 33], where a QPC is used to partition the current, allow to put into light transport through multiple energy levels of a localized state [34], as well as to observe fractional charges in the fractional quantum Hall effect regime [23, 35].

In all previously discussed experiments, currents were generated in the edge channels by applying a bias voltage V to an ohmic contact upstream of the edge channel, at low temperature. Electrons are therefore emitted in an energy window defined between ϵ_f and $\epsilon_f + eV$ (where ϵ_f is the Fermi energy), and Pauli exclusion principle ensures that their flow is noiseless. However, the number of electrons emitted within this energy range is not controlled, nor is the emission time of the charges. Symmetrically, currents are detected on output ohmic contacts, connected to the measurement circuit. Although they are very efficient electron sources and detectors, ohmic contacts are very far from presenting a single charge resolution. It is therefore interesting to develop single electron detectors [36, 37, 38, 39, 40, 41], as well as single electron sources. In particular, the realization of single electron sources is crucial in order to perform single-charge electron quantum optics experiments.

2 Single-charge electron quantum optics

Aside from the analogy with single photon quantum optics, single-charge electron quantum optics allow to probe fundamental processes taking place in Fermionic systems at the single charge scale. Indeed, a great richness is brought by the presence of both a Fermi sea and electronic interactions, which induce

decoherence and relaxation. As mentioned above, decoherence and relaxation processes have been studied at a large scale with thermal populations; however, they can only be fully characterized through the study of the relaxation and decoherence of coherently-emitted single charges with a controlled emission time and energy. Furthermore, one can study the fundamental differences between quantum statistics of photons and electrons at the single-particle scale; in particular, the direct observation of Pauli exclusion principle at the single charge scale can be considered using a two-particle Hong-Ou-Mandel [42] collider geometry [12], and a two-particle entanglement scheme was recently proposed [9]. The obvious requirement in such experiments is the development of a single electron emitter; in the next paragraph, we briefly describe the various types of 2DEG devices used to emit single charges, and discuss their respective advantages and limitations.

2.1 Single electron emitters

We now present several types of recently realized single electron sources; in particular, we describe the single electron emitter developed at the Laboratoire Pierre Aigrain, which we have used during my thesis to perform single-charge electron quantum optics experiments. We finally present a recent theoretical proposal for a noiseless single electron source, which is currently in development at the Nanoelectronics Group (SPEC-CEA).

2.1.1 Surface acoustic waves

The piezoelectric properties of $GaAs$ can be used to generate single-charge excitations in a 2DEG with a large repetition rate [43, 44, 45, 46]. Applying a surface acoustic wave (SAW) to the $GaAs$ substrate generates a propagating wave of electrostatic potential in the 2DEG. The minima of this potential then act as propagating localized states, each one carrying a single charge for a sufficiently large amplitude of the SAW. The good piezoelectric properties of $GaAs$ allow to generate single-electron pulses at GHz frequencies and thus create quantized DC currents (in units of ef_{SAW}) useful for metrology. However, these devices do not offer a full control over the electron escape time, since it cannot be decoupled from the repetition frequency f_{SAW}.

2.1.2 Quantum turnstiles and charge pumps

One of the main challenges in the realization of a single electron source lies in the ability to isolate a single charge from the Fermi sea, in order to release it within a controlled emission time. High-frequency charge pumps [47, 48] and quantum turnstiles [49] allow to sequentially trap and release a single charge to perform single charge emission. In [47], a set of parallel fast gates is used to isolate an electron from a continuous stream generated by a biased contact, then release it towards a measurement contact. The fast gates allow to briefly create potential barriers in the 2DEG: one can electrostatically confine a single electron by raising the potential barriers in a time smaller than h/eV, where V is the bias voltage. The electron trapped in the localized state can then be released by lowering the potential barrier upstream of the measurement contact. This type of source has demonstrated a quantization of the emitted DC current in units of ef, where f is the repetition rate of the source, with an uncertainty of 15 parts per million [50]. The downside of this technique is the poor energy resolution of the emitted charges.

2.1.3 Quantum dots: Coulomb blockade

As described in the previous paragraph, localized states can be used to temporarily trap electrons in order to isolate them from the Fermi sea. One can also define a quantum dot by isolating a small

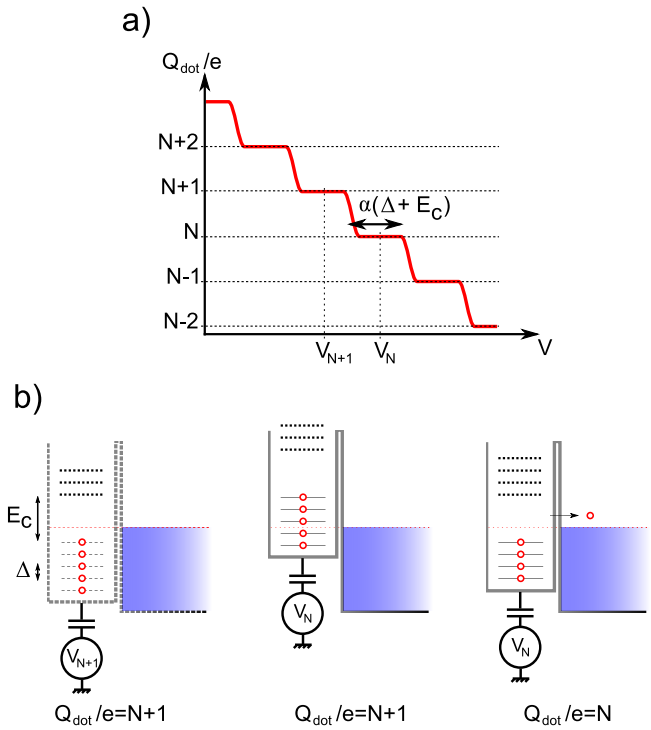

Figure 4: a) Coulomb blockade: the charge of a quantum dot presents quantized steps as a function of the gate voltage controlling the potential in the dot. **b)** single-charge emission with a quasi-metallic quantum dot: the dot is rapidly brought out of equilibrium by changing the gate voltage from V_{N+1} to V_N. An electron from one of the levels promoted above the Fermi energy can tunnel out of the dot: a single charge is emitted.

portion of the 2DEG (either electrostatically, or by etching the edges of the gas) weakly coupled to a reservoir, and directly emit the charges sitting on the dot. Indeed, the number of charges on an isolated island is quantized, and Pauli exclusion principle prevents two electrons in the dot from having the same energy. The energy spectrum of a quantum dot presents two typical scales, one given by the orbital motion of the charges in the dot (orbital level spacing Δ), and the other reflecting the Coulomb repulsion between electrons in the dot. The latter, called charging energy E_C, is equal to the energy one must pay in order to add an electron to the dot, and is given by $E_C = e^2/C_\Sigma$, where C_Σ is the total capacitance of the dot.

Charges can be exchanged between the dot and a reservoir through a tunnel barrier, and one usually controls the potential in the dot with an electrostatic gate. The total charge of the dot then varies with the gate voltage as a series of quantized steps (see Fig.4a), corresponding to successive additions of electrons in the dot. When spin degeneracy is removed, the voltage distance between each charge step is proportional to the addition energy $\Delta + E_C$. On the plateaus of the charge steps, the total charge of the dot is independent of the gate voltage: indeed, in these conditions the lowest unoccupied energy level is far above the chemical potential of the reservoir, and no charge can tunnel in or out of the dot.

This so-called Coulomb blockade phenomenon allows to perform single charge emission: by rapidly changing the value of the gate voltage, one can change the total charge in the dot from $N + 1$ to N (see Fig.4b), thus emitting a single charge. This type of single-electron pump based on a metallic quantum dot presenting a charging energy substantially larger thant the orbital level spacing has been

thoroughly studied, theoretically as well as experimentally [51, 52, 53, 54]; however, since the electron sitting on any one of the levels promoted above the Fermi energy can be emitted (Coulomb blockade then prevents the emission of a second charge), the energy of the emitted charge is not well-controlled. Moreover, the typical tunneling rates in these systems restrict the repetition frequency to a few MHz.

2.1.4 The mesoscopic capacitor as a single electron source

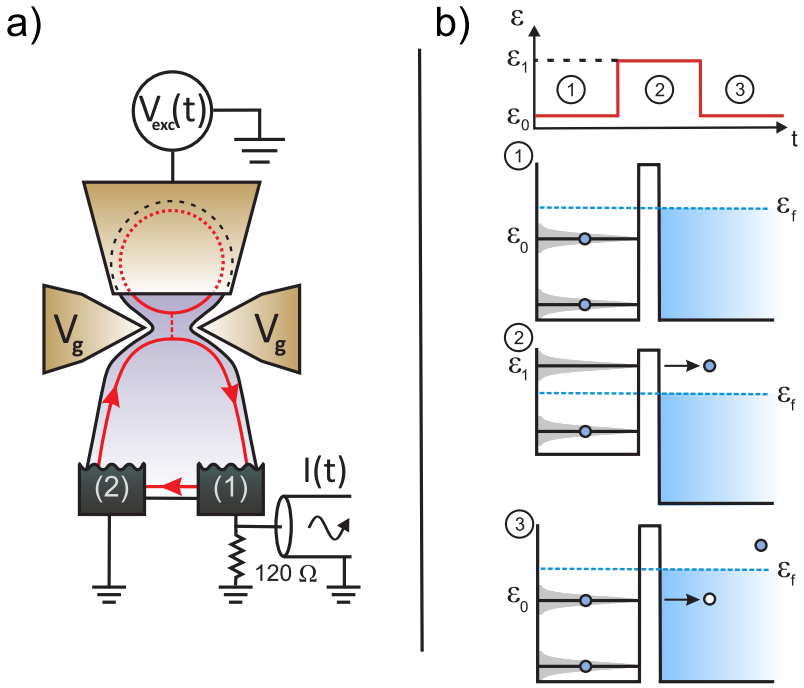

Figure 5: a) schematic of the mesoscopic capacitor. A quantum dot with a large level spacing is coupled to the reservoir through a QPC (gate voltage V_g). The potential in the dot is tuned using the top gate, and the emitted current is collected on contact (1). **b)** principle of single charge emission with the mesoscopic capacitor. The upper graph represents the evolution of the potential of the dot during the emission cycle. ① the dot is at equilibrium. ② the application of a large voltage step to the dot top-gate shifts the energy levels upwards with respect to the Fermi energy, promoting a single occupied level above the Fermi energy. A single electron is emitted. ③ the excitation voltage is switched back to its original value: the emptied level is shifted back below the Fermi energy, and can absorb an electron from the reservoir. A single hole is emitted. During this cycle, only one level takes part in the emission. Since only one state is promoted above the Fermi energy, the escape time only depends on the transmission of the QPC, whereas in the case of a quasi-metallic quantum dot depicted in Fig.4b, where the orbital level spacing is much smaller than the charging energy, the escape time is highly dependent on the number of levels promoted above the Fermi energy.

In the quasi-metallic case described in the previous paragraph, a large number of electronic levels are promoted above the Fermi energy in order to emit a single charge, thus decreasing the control over the energy of the emitted charge. A single electron source based on a quantum dot presenting an orbital level spacing comparable or larger than the charging energy allows, however, to emit single charges with a control over the energy and emission time close to the quantum limit. Indeed, in the

case of a large orbital level spacing Δ, one can promote a single electronic level at an arbitrary energy $eV \leq \Delta$ above the Fermi level; the uncertainty on the energy of the emitted single charge is then only given by the energy width of the promoted level.

The single electron emitter developed at the Laboratoire Pierre Aigrain is based on a mesoscopic capacitor [55], which consists of a submicronic quantum dot presenting a large orbital level spacing, coupled to the reservoir through a quantum point contact (see Fig.5a). The potential in the dot is tuned using an electrostatic top-gate deposited at the surface of the sample. The principle of operation of such a source is depicted in Fig.5b: a large voltage step is applied to the top gate in order to shift the energy levels upwards with respect to the Fermi energy. If the energy shift is comparable to the level spacing, only one level is promoted above the Fermi energy. The single electron sitting on that level (provided spin degeneracy is lifted) can then be emitted at an energy above ϵ_f in the reservoir through the tunnel barrier formed by the QPC, with an escape time depending on the transmission of the tunnel barrier. After emission of the electron, the voltage on the top gate is set to its original value, so that the level previously promoted above the Fermi energy is shifted back to its position below the Fermi energy. The dot can then absorb an electron from the reservoir, thus emitting a hole at an energy below ϵ_f with the same escape time as the electron (provided the transmission of the tunnel barrier is independent of energy). On a single cycle, the source therefore emits one single electron, followed by a single hole, both with a controlled energy. This cycle is repeated at GHz rates (typically, $f_0 = 1.5$ GHz), thus generating an AC current composed of alternatively emitted single electrons and single holes. The top gate and the QPC gates allow to independently tune the energy of the emitted charges and their escape time. The energy and temporal widths of the emitted single-charge wavepackets are respectively given by the width of the levels in the dot and the escape time, both of which only depend on the level spacing Δ and the transmission D. In this respect, the source allows a control over the energy and emission instant of the charges close to the quantum limit; a controlled variation of the escape time over several orders of magnitude (< 0.1 ns $\leftrightarrow$ 10 ns) was experimentally demonstrated [10]. The mesoscopic capacitor is thus a promising candidate to perform single charge emission in single-charge electron quantum optics experiments.

2.1.5 Modulated contacts

Recent theoretical studies [56, 57] have shown that the emission of a single charge can be achieved by applying a voltage pulse $V(t)$ to an ohmic contact that verifies the relation $\int dt V(t) = h/e$. Indeed, as demonstrated in [58], an ohmic contact biased with a constant voltage V generates a continuous stream of electrons, each electron occupying a wavepacket with a temporal width h/eV. One therefore expects to emit a single electron when the bias voltage is applied during a well-controlled time equal to the temporal width of the wavepacket. The shape of the voltage pulse is expected to determine the number of additional electron/hole pairs emitted along with the single electron: this property is crucial, since the emission of additional electron/hole pairs renders the description of the experiments in terms of electron quantum optics irrelevant. In particular, it was predicted that applying a Lorentzian voltage pulse allows the emission of a single charge with no spurious emission of additional electron/hole pairs. Furthermore, the ability to tune the amplitude and the duration of the pulse allows to accurately control the emission time of the charge. However, the energy of the emitted charge is not well controlled, which does not allow the energy separation of the emitted charge and the Fermi sea.

2.2 Noise in single-charge electron quantum optics experiments

In quantum optics, the coherence of the emitted particles is probed by the successive correlators $g^{(n)}$ (also called n-th order coherence), introduced by Roy Glauber in [59]. In particular, the first-

order correlator $g^{(1)}$, probing the amplitude correlation of the electric field, is measured in classical interferometers, such as the Mach-Zehnder and Michelson interferometers; the second-order correlator $g^{(2)}$ probes the intensity correlation, and allows to discriminate between quantum and classical states of light. The latter is commonly measured to probe the outcome of quantum optics experiments such as Hanbury-Brown and Twiss, or Hong-Ou-Mandel experiments. In general, $g^{(1)}$ is only sensitive to the wave nature of light, whereas higher order correlators are sensitive to its particle nature.

The measurements performed in the experiments mentioned in the beginning of this introduction show an analogy with those correlators. Indeed, in the electronic Mach-Zehnder and double-slit experiments, interference patterns are observed in the emitted currents, which are then the analog of the first-order correlator $g^{(1)}$ of quantum optics. In [31] the quantum statistics correlating the flow of electrons is probed by measuring the partition noise. The correlation of the current fluctuations is thus the analog of the quantum optics second-order correlator $g^{(2)}$. As such, the noise is the relevant signal one should measure in a realization of single-charge electron quantum optics experiments.

3 Results obtained during the thesis

During my thesis, we have used a mesoscopic capacitor built in a $GaAs/AlGaAs$ 2DEG as a single electron emitter to perform two basic single-charge electron quantum optics experiments: the measurement of the noise of a single-charge beam, in a direct configuration as well as in a HBT configuration.

Measuring the intrinsic high-frequency noise of the source is of crucial importance, for it establishes the short-time current autocorrelation as an unambiguous criterion of single-particle emission, and confirms that the mesoscopic capacitor can indeed be used as an on-demand single electron source. Furthermore, the measurement of high-frequency noise allows to probe the occurrence of spurious charges transfer events which do not appear in the average current, and thus define optimal operating conditions for the source.

The measurement of the current fluctuations in the HBT geometry is the direct electronic analog of HBT measurements in quantum optics, used to characterize single photon sources [60, 61]; in addition to completing the validation of the mesoscopic capacitor as a single electron source, partitioning allows to quantify the presence of additional electron/hole pairs specific to Fermionic systems, by physically separating them. Moreover, the use of time and energy-resolved single charges in this HBT experiment yields a much larger richness in comparison to the previous Fermionic HBT experiments [32, 33] performed on a continuous flow of electrons generated by an ohmic contact.

The realization of these two experiments required the development of a consistent theoretical description of the source and the implementation of noise measurement setups able to detect the fluctuations of single-electron currents.

In the first chapter of this manuscript, we describe the mesoscopic capacitor within a Floquet scattering matrix theory, and show that the study (both theoretical and experimental) of the emitted average AC current indicates that the mesoscopic capacitor can indeed be used as a single electron source. In the linear regime (where the amplitude of the voltage step V_{exc} is much smaller than the frequency f_0 and the level spacing Δ, with $hf_0 \ll \Delta$), the average AC current reflects the dynamics of charge relaxation through the QPC [62] as well as the density of states in the dot; it therefore allows to extract the parameters of the source. In the non-linear regime (V_{exc} comparable to the level spacing), we demonstrate the quantization of the average AC current in units of $2ef_0$, corresponding to the emission, in average, of one electron followed by one hole at each cycle [10]. We furthermore show that the average AC current gives access to the escape time, as well as the average transfered charge per half-period.

In the second chapter, we describe the measurement of the autocorrelation of the current fluctuations emitted by the source, constituting the first of the two single-charge electron quantum optics experiments realized during my thesis. We first calculate the noise of the source using the Floquet scattering model introduced in the first chapter. We then compare this model with a semi-classical heuristic model describing the mesoscopic capacitor as an ideal single electron emitter. This comparison allows us to define the optimal operating conditions of the source. In particular, we show that in these optimal operating conditions, the noise reduces to a fundamental noise limit called *quantum jitter*, which is the signature of single particle emission.

We finally present experimental measurements of the high-frequency noise of the source realized during my thesis. In the optimal operating conditions, the noise is indeed given by the quantum jitter, demonstrating on-demand single particle emission [63]. Furthermore, we observe an increase in the noise when the source is driven out of the optimal operating conditions, that is when charges are emitted in resonance with the Fermi energy. This excess noise, corresponding to the generation of spurious additional charges, is well reproduced by the scattering model, indicating that the model correctly describes our device.

In the two first chapters, the signals are measured in the direct configuration depicted in Fig.5 shown above, where the emitted current is directly collected on an ohmic contact.

In the third chapter, we describe the second single-charge electron quantum optics experiment performed during my thesis: the measurement of the current fluctuations of a single-charge beam partitioned by a QPC. The geometry of this experiment, shown on Fig.6, is the single-charge electron quantum optics analog of the HBT geometry frequently used to characterize photon sources in quantum optics. As in the previous chapters, we first derive an expression for the noise after partition by the QPC using the Floquet scattering model. This theoretical study shows that the HBT geometry allows to probe a large variety of properties of electronic transport in QHE edge channels; in particular, we show that the measurement of the zero-frequency part of the noise after partition directly counts the number of emitted electron/hole pairs per period. This property, first predicted in [64], allows quantitative studies of the generation of spurious electron/hole pairs caused by the charge emission mechanism. It also opens the way to the study of energy relaxation between adjacent edge channels at the single charge scale: indeed, as the source only emits charges in a single edge channel (more precisely, the outer edge channel, see first chapter), one can measure the number of electron/hole pairs in the other edge channels, caused by energy relaxation. Furthermore, this property can be used to measure the number of excess electron/hole pairs generated when a charge is emitted in resonance with the Fermi energy. We also show that applying a bias voltage to the ohmic contact located at the second input of the QPC (contact (B) in Fig.6) allows to measure the energy distribution of the emitted charges.

We then present an experimental study of sample *S434-8*, designed to perform noise measurements in the HBT geometry. We show the first experimental observation of the partition noise of a single-electron beam, which is well reproduced by the Floquet scattering matrix theory. These noise measurements show that in the ideal operating conditions, the number of emitted electron/hole pairs is close to the ideal value (that is, one electron/hole pair per period); they however put into light crucial issues regarding the electronic environment that must be solved before proceeding to further measurements.

In the fourth chapter, we finally describe the noise measurement setups used two perform the two single-charge electron quantum optics experiments. As we show in the second and third chapters, the typical scale of the current fluctuations is given by $e^2 f_0$, where f_0 is the repetition frequency of

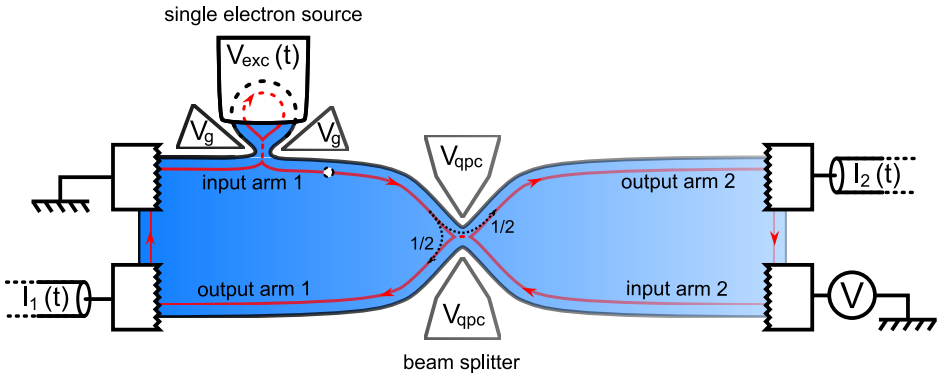

Figure 6: Schematic of the single-charge HBT experiment: a single electron emitter is placed at the first input arm of a QPC, acting as a beam splitter. The correlation of the current fluctuations in the two output arms are measured. The ohmic contact on the second input arm can be biased to measure the energy distribution of the emitted charges.

the electron/hole emission cycle; with $f_0 = 1.5$ GHz, this corresponds to a current noise equal to $\sim 4 \times 10^{-29}$ A$^2/Hz$. The required resolution thus corresponds to typical resolutions demonstrated by state-of-the-art low-frequency noise measurement setups.

We first describe the high-frequency measurement setup developed to measure the noise emitted by the source in the direct configuration. At high frequency (here, the noise is measured around the drive frequency $f_0 = 1.5$ GHz), noise measurements are much more challenging because of the characteristic impedance of microwave circuits, equal to 50 Ω. We therefore use the combination of an impedance transformer, which increases the measurement impedance to 120 Ω (thus increasing the noise power by a factor 2.4), and an interferometric amplification technique, called modulated double-balanced amplifier. This setup allows us to measure high-frequency noise with a state of the art resolution of 1.3×10^{-29} A$^2/Hz$ in 5 minutes.

In the second part of the chapter, we describe the low-frequency noise measurement setup used in the single-charge HBT measurements. The setup is a fairly basic one, where one measures the cross-correlation of the noise detected by two distinct amplification lines. The sensitivity of this setup is lower than the one of the high-frequency noise measurement setup; we nonetheless propose several easy-to-implement practical solutions to increase the sensitivity.

These two independent noise measurement setups allow to simultaneously measure the high and low-frequency noise at the outputs of our sample.

4 Perspectives

In the third chapter, we show that the HBT geometry allows to measure the energy distribution of the emitted charges, using a biased ohmic contact located at the second input of the QPC. This property can be generalized to the case of a periodic excitation voltage applied to the contact, to measure the off-diagonal terms of the density matrix of the emitted charges. It is thus possible to perform single-electron tomography [65]. One can then consider a wide range of derivations of the HBT geometry where a tunable source of relaxation and/or decoherence is inserted between the single electron source and the partitioning QPC: for instance, a voltage probe such as the one used in [19]. This collection of experiments would allow to accurately characterize electronic transport in QHE edge channels.

Finally, one can use a second synchronized single electron source placed at the second input of

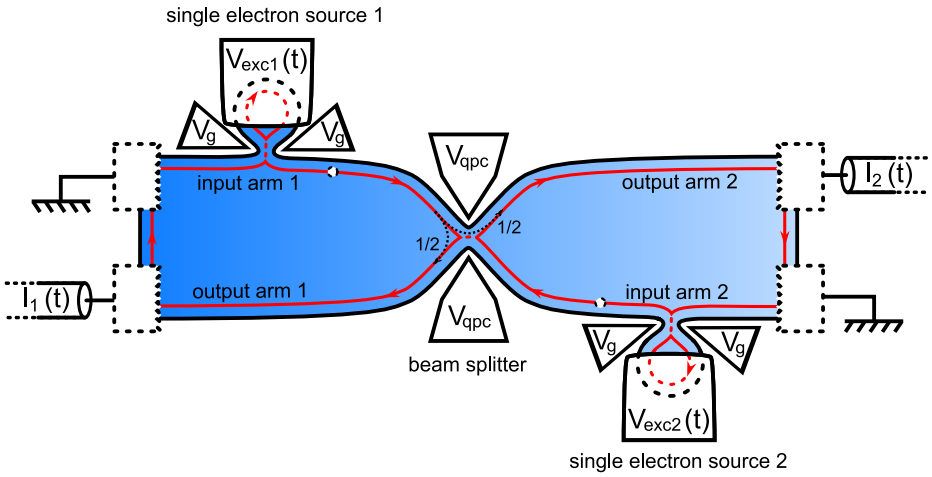

Figure 7: Schematic of the single-charge Hong-Ou-Mandel experiment: two synchronized single electron sources are placed at each input of a QPC. The emitted charges collide on the central QPC, which acts as a beam splitter. The correlation of the current fluctuations in the two output arms are measured: if the charges arrive simultaneously and in the same state on the QPC, the noise vanishes.

the QPC to perform single-electron HOM collisions [12]; the principle of the experiment is shown on Fig.7. If the two electrons sent towards the central QPC are in the same state, Pauli exclusion principle causes each one to be transmitted/reflected in a different output of the QPC; one therefore expects positive correlation at short time between the two outputs. This experiment furthermore allows to probe Coulomb interactions between two single charges, as the interactions should become predominant in the partition when the energies of the two colliding charges differ. As for the HBT geometry, this experiment presents a great richness in the number of tunable parameters, such as the respective energy of the emitted charges, the desynchronization of the sources, or the temporal widths of the emitted wave packets.

Chapter 1

Realization of a Single Electron Source

1.1 Response of a mesoscopic capacitor to a periodic excitation: theory 17
1.1.1 Modeling the device 17
1.1.2 Floquet scattering matrix 18
1.1.3 Stationary scattering matrix 21
1.1.4 Calculation of the average AC current 22
1.2 Measurement of the average AC current emitted by the source 24
1.2.1 Excitation line 24
1.2.2 Measurement line 26
1.2.3 Parasitic signal 26
1.3 Average AC current in the linear regime 26
1.3.1 Theory 26
1.3.2 Experimental results: determination of the sample parameters 28
1.3.3 Conclusion on the linear regime 32
1.4 Average AC current in the non-linear regime 32
1.4.1 Scattering theory 32
1.4.2 Heuristic model 37
1.4.3 Experimental results 40
1.5 Validity of the model 46

Introduction of chapter 1

In this chapter, we describe the basic properties of a mesoscopic capacitor, and show that it can be used as a single electron source when driven in the non-linear regime. We first propose a theoretical description of the source using a time-dependent scattering formalism with which we calculate the average AC current. This description will be used to predict the properties of the current fluctuations in the next chapters. We then present measurements of the average AC current emitted by the device. Our calculations show that when the excitation voltage compensates the level spacing, the first harmonic of the emitted AC current becomes quantized in units of $2ef_0$, corresponding to the periodic emission of a single electron followed by a single hole. The homodyne measurement of the first harmonic confirms this prediction and provides a characterization protocol for the source: we first study the low-amplitude excitation regime of the device in order to extract the fundamental parameters of each device such as level spacing, coupling between the metallic gates and the dot potential, and electronic temperature. We then verify the predicted quantization of the first harmonic and determine the correct operating conditions of the source.

1.1 Response of a mesoscopic capacitor to a periodic excitation: theory

In this section, we present a theoretical description of the mesoscopic capacitor depicted in Fig.1.1. The mesoscopic capacitor is made of a submicronic quantum dot etched in a two-dimensional electron gas, connected to the leads via a Quantum Point Contact (QPC), which acts as a tunable tunnel barrier. The potential in the dot can be tuned by applying voltages to an electrostatic gate placed near the dot. When the potential is modulated periodically, a periodic charge transfer between the dot and the leads occurs. This charge relaxation process can be described in terms of RC-circuit elements, which will allow us to give a simple definition of charge relaxation time (or escape time).

We describe the scattering of electrons in the leads on the dot with a time-dependent scattering matrix, or Floquet matrix, which was introduced for the mesoscopic capacitor in [66].

1.1.1 Modeling the device

A schematic view of the device is represented in Fig.1.1. When a strong magnetic field is applied perpendicularly to the sample, electronic transport occurs along the edge states of the Quantum Hall Effect, represented by the red and blue lines in Fig.1.1, here corresponding to a filling factor $\nu = 2$. We restrict the transmission of the quantum point contact coupling the dot to the leads to values for which only the outer edge channel (red line) is partially transmitted. As a consequence, we can neglect the influence of the inner edge channel (blue line), which does not take part in the emitted current since the inner edge channel in the dot is completely decoupled from the one in the leads. We therefore describe the system in a one-dimensional scattering formalism in which an electron from the outer edge channel can tunnel into the dot with an amplitude d and perform several turns in the dot before tunneling back to the lead. The description of electronic trajectories inside the dot in terms of QHE edge channels is valid as long as the dot is larger than the width of an edge channel (a few hundreds of nanometers [67]). The dots used in our experiments typically reach this limit in order to make them as small as possible while still presenting well defined trajectories.

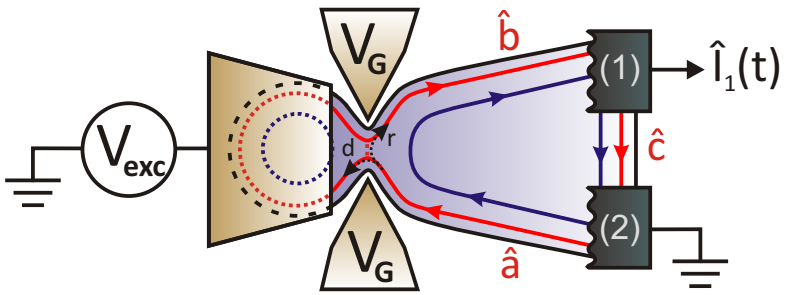

Figure 1.1: Modeling of a mesoscopic capacitor. Two edge channels are considered: the inner edge channel (blue line) does not take part in the current emitted by the capacitor. We measure the current collected on contact (1), while contact (2) is grounded.

We express the electronic states in the outer edge channel in each region of the sample with creation/annihilation operators depicted in Fig.1.1: $\hat{a}^\dagger, \hat{a}$ from contact (2) to the dot, $\hat{b}^\dagger, \hat{b}$ from the dot to contact (1), $\hat{c}^\dagger, \hat{c}$ from contact (1) to contact (2). We neglect propagation effects in the edge channel; the creation/annihilation operator are therefore only time dependent, and we express the outgoing states $\hat{b}^\dagger(t), \hat{b}(t)$ as a function of the incoming states $\hat{a}^\dagger(t), \hat{a}(t)$ using a time-dependent scattering matrix (or Floquet matrix) formalism described in the next paragraph. Since the edge states of the

QHE are spin-polarized, we do not take spin into account; we also consider non-interacting edge channels.

1.1.2 Floquet scattering matrix

1.1.2.1 Time-dependent scattering matrix and gauge transformation

In this model, we suppose that the incoming states $\hat{a}^\dagger(t), \hat{a}(t)$ are sent towards a scatterer which is related to the time-dependent potential $V(\tau')$ applied to the dot. This is somewhat different to the description used in previous works [10, 11, 68], where a gauge transformation was performed to maintain the electrostatic potential in the dot equal to zero, while the potential of the contacts was modulated by the periodic signal $-V(\tau')$. Although very efficient for the resolution of problems where only one time-dependent potential is considered, this gauge transformation becomes useless whenever we have to take several non-synchronized potentials into account. This is particularly bothersome for two-electrons interference experiments where two distinct sources are used. These two formalisms yield however the same results for a single source, as we demonstrate in appendix A.3.1.

1.1.2.2 Expression of the Floquet scattering matrix

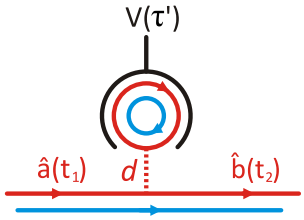

Figure 1.2: Time-dependent scattering matrix description of the quantum dot: electrons in the outer edge channel can tunnel into the dot with an amplitude d, or be reflected with an amplitude $r = \sqrt{1-d^2}$. Electrons in the dot are subject to the time-dependent potential $V(\tau')$.

Fig.1.2 depicts the relation between an outgoing state at a time t_2 and incoming states at times t_1: an incoming electron can either be reflected on the dot with an amplitude r, or enter the dot with an amplitude $d = \sqrt{1-r^2}$, where it can perform several turns, each in a finite time $\tau_0 = l/v_d$ (where l is the perimeter of the dot, and v_d the electron drift velocity), before escaping back to the lead. Between times t_1 and t_2, an electron in the dot is subject to the time-dependent potential $V(\tau') = V_0 + V^{'}(\tau')$, where $V^{'}(\tau')$ is periodic with an angular frequency $\Omega = 2\pi f_0 = 2\pi/T$ and has no DC part, and V_0 controls the equilibrium potential of the dot. It therefore acquires a phase $e^{-i\frac{e}{\hbar}\int_{t_1}^{t_2} V(\tau')d\tau'}$, where e is the charge of the electron. The relation between the outgoing state at time t_2 and the incoming states at time t_1 is therefore:

$$\hat{b}(t_2) = \int dt_1 U(t_2, t_1)\hat{a}(t_1) \tag{1.1}$$

where the time-dependent scattering matrix $U(t_2, t_1)$ is given by:

$$U(t_2, t_1) = \left(r\delta(t_2 - t_1) - d^2 \sum_q r^{q-1}\delta(t_2 - t_1 - q\tau_0) \right) e^{-i\frac{e}{\hbar}\int_{t_1}^{t_2} V(\tau')d\tau'} \tag{1.2}$$

We will now express this scattering matrix in the energy domain $U(\epsilon, \epsilon')$, defined by:

$$\hat{b}(\epsilon) = \int d\epsilon' U(\epsilon,\epsilon')\hat{a}(\epsilon') \tag{1.3}$$

with:

$$\begin{aligned} \hat{b}(t_2) &= \frac{1}{\sqrt{h}}\int d\epsilon e^{-i\epsilon t_2/\hbar}\hat{b}(\epsilon) \\ \hat{b}(\epsilon) &= \frac{1}{\sqrt{h}}\int dt_2 e^{i\epsilon t_2/\hbar}\hat{b}(t_2) \end{aligned} \tag{1.4}$$

When using Eq.1.1, this last relation leads to:

$$\begin{aligned} \hat{b}(\epsilon) &= \frac{1}{\sqrt{h}}\int dt_1 dt_2 e^{i\epsilon t_2/\hbar}U(t_2,t_1)\hat{a}(t_1) \\ &= \frac{1}{h}\int d\epsilon' dt_1 dt_2 e^{i\epsilon t_2/\hbar}e^{-i\epsilon' t_1/\hbar}U(t_2,t_1)\hat{a}(\epsilon') \end{aligned} \tag{1.5}$$

$U(\epsilon,\epsilon')$ can then be calculated from the following expression:

$$U(\epsilon,\epsilon') = \frac{1}{h}\int dt_1 dt_2 e^{i\epsilon t_2/\hbar}e^{-i\epsilon' t_1/\hbar}U(t_2,t_1) \tag{1.6}$$

When using the definition of $U(t_2,t_1)$ given in Eq.1.2, with the variable substitution $\tau = t_2 - t_1$, we have:

$$\begin{aligned} U(\epsilon,\epsilon') &= \frac{1}{h}\int dt_2 d\tau e^{i(\epsilon-\epsilon')t_2/\hbar}e^{i\epsilon'\tau/\hbar}\left[r\delta(\tau) - d^2\sum_q r^{q-1}\delta(\tau - q\tau_0)\right]e^{-i\frac{e}{\hbar}\int_{t_2-\tau}^{t_2}V(\tau')d\tau'} \\ &= \frac{1}{h}\int dt_2 e^{i(\epsilon-\epsilon')t_2/\hbar}\left[r - d^2\sum_q r^{q-1}e^{i((\epsilon'-eV_0)/\hbar)q\tau_0}e^{-i\frac{e}{\hbar}\int_{t_2-q\tau_0}^{t_2}V'(\tau')d\tau'}\right] \end{aligned} \tag{1.7}$$

Since the potential $V'(\tau')$ is T-periodic and has no DC part, the phase term $e^{-i\frac{e}{\hbar}\int_0^{t_2}V'(\tau')d\tau'}$ is T-periodic as well, and can then be expressed in terms of its Fourier components c_n defined in [11, 68]:

$$c_n = \frac{1}{T}\int_0^T dt e^{in\Omega t}e^{-i\frac{e}{\hbar}\int_0^t V'(\tau')d\tau'} \tag{1.8}$$

$$e^{-i\frac{e}{\hbar}\int_0^t V'(\tau')d\tau'} = \sum_n c_n e^{-in\Omega t} \tag{1.9}$$

$$\sum_n c_n c_{n+k}^* = \delta_{k,0} \tag{1.10}$$

The phase term in Eq.1.7 is then equal to:

$$\begin{aligned} e^{-i\frac{e}{\hbar}\int_{t_2-q\tau_0}^{t_2}V'(\tau')d\tau'} &= e^{-i\frac{e}{\hbar}\int_0^{t_2}V'(\tau')d\tau'}e^{+i\frac{e}{\hbar}\int_0^{t_2-q\tau_0}V'(\tau')d\tau'} \\ &= \sum_n c_n e^{-in\Omega t_2}\sum_{n'} c_{n'}^* e^{in'\Omega(t_2-q\tau_0)} \end{aligned} \tag{1.11}$$

This gives us:

$$U(\epsilon,\epsilon') = \frac{1}{h}\int dt_2 e^{i(\epsilon-\epsilon')t_2/\hbar}\left[r - d^2\sum_{q,n,n'} c_n c_{n'}^* r^{q-1} e^{iq\tau_0(\epsilon'-eV_0-n'\hbar\Omega)/\hbar} e^{i(n'-n)\Omega t_2}\right] \tag{1.12}$$

Eq.1.10 implies $\sum_{n,n'} c_n c_{n'}^* e^{i(n'-n)\Omega t_2} = 1$. We then have, with $d^2 = 1-r^2$:

$$\begin{aligned} U(\epsilon,\epsilon') &= \sum_{n,n'} c_n c_{n'}^* \int \frac{dt_2}{h} e^{i((\epsilon-\epsilon')/\hbar+(n'-n)\Omega)t_2}\left[r - \frac{1-r^2}{r}\frac{re^{i\tau_0(\epsilon'-eV_0-n'\hbar\Omega)/\hbar}}{1-re^{i\tau_0(\epsilon'-eV_0-n'\hbar\Omega)/\hbar}}\right] \\ &= \sum_{n,n'} c_n c_{n'}^*\left[r - \frac{1-r^2}{r}\frac{re^{i\tau_0(\epsilon-eV_0-n\hbar\Omega)/\hbar}}{1-re^{i\tau_0(\epsilon-eV_0-n\hbar\Omega)/\hbar}}\right]\delta(\epsilon-\epsilon'+(n'-n)\hbar\Omega) \\ &= \sum_{n,n'} c_n c_{n'}^* \frac{r-e^{i\tau_0(\epsilon-eV_0-n\hbar\Omega)/\hbar}}{1-re^{i\tau_0(\epsilon-eV_0-n\hbar\Omega)/\hbar}}\delta(\epsilon-\epsilon'+(n'-n)\hbar\Omega) \end{aligned} \tag{1.13}$$

The substitution $m = n'-n$ finally gives us:

$$U(\epsilon,\epsilon') = \sum_{n,m'} c_n c_{n+m}^* \frac{r-e^{i\tau_0(\epsilon-eV_0-n\hbar\Omega)/\hbar}}{1-re^{i\tau_0(\epsilon-eV_0-n\hbar\Omega)/\hbar}}\delta(\epsilon-\epsilon'+m\hbar\Omega) = \sum_m U_m(\epsilon)\delta(\epsilon-\epsilon'+m\hbar\Omega) \tag{1.14}$$

Using this expression, Eq.1.3 then becomes:

$$\hat{b}(\epsilon) = \sum_m U_m(\epsilon)\hat{a}(\epsilon+m\hbar\Omega) \tag{1.15}$$

Because of the periodic driving, the energy ϵ' of outgoing electrons only takes values defined by $\epsilon+m\hbar\Omega$, where ϵ is the energy of electrons incoming on the dot. Eq.1.15 therefore shows that energy transfers on the scatterer are quantized in units of the driving frequency $\hbar\Omega$. The quantized Floquet scattering matrix $U_m(\epsilon)$ is given by:

$$U_m(\epsilon) = \sum_n c_{n+m}^* c_n U^0(\epsilon-n\hbar\Omega) \tag{1.16}$$

where

$$U^0(\epsilon) = \frac{r-e^{i\tau_0(\epsilon-eV_0)/\hbar}}{1-re^{i\tau_0(\epsilon-eV_0)/\hbar}} = \frac{r-e^{2i\pi(\epsilon-eV_0)/\Delta}}{1-re^{2i\pi(\epsilon-eV_0)/\Delta}} \tag{1.17}$$

is the stationary scattering matrix, noted $S(\epsilon)$ in [11, 68] and defined by the relation $\hat{b}(\epsilon) = U^0(\epsilon)\hat{a}(\epsilon)$ when no periodic drive is applied to the top gate.

In all other scattering theory sections of this manuscript, we shall express the properties of the emitted currents (AC average as well as fluctuations) as functions of the quantized Floquet scattering matrix, which contains all the information on the periodic excitation drive $V(\tau')$ and the parameters of the dot: level spacing $\Delta = h/\tau_0$, transmission $D = 1-r^2$, and the dot equilibrium potential eV_0, corresponding to the energy shift of the levels in the dot.

1.1.3 Stationary scattering matrix

The scattering model describes the dot as a single-contact electronic Fabry-Perot interferometer with a tunable transmission (see Eq.1.17), which presents discrete energy levels with a constant spacing Δ and a tunable width proportional to the transmission D (see Fig.1.3). The position of the levels relative to the Fermi energy can be shifted by the potential V_0.

1.1.3.1 Density of states

The density of states in the dot $\mathcal{N}(\epsilon)$ can be defined from the stationary scattering matrix $U^0(\epsilon)$ [69]:

$$\begin{aligned} \mathcal{N}(\epsilon) &= \frac{1}{2i\pi} U^{0*}(\epsilon) \frac{dU^0}{d\epsilon} \\ &= \frac{1}{\Delta} \frac{1-r^2}{1-2r\cos(2\pi(\epsilon - eV_0)/\Delta) + r^2} \end{aligned} \tag{1.18}$$

For unity transmission ($r = 0$), the density of states is constant and equal to $1/\Delta$; for low transmissions, $\mathcal{N}(\epsilon)$ becomes a succession of Lorentzian peaks with a regular spacing Δ and a finite width $\hbar\gamma = 2\pi D\Delta$:

$$\begin{aligned} \mathcal{N}(\epsilon) &\approx \sum_n \frac{2}{\Delta(1-r)} \frac{1}{1+\left(\frac{2\pi(\epsilon - eV_0 - n\Delta)}{\Delta(1-r)}\right)^2} \\ &\approx \sum_n \frac{2}{\pi\hbar\gamma} \frac{1}{1+\left(\frac{\epsilon - eV_0 - n\Delta}{\hbar\gamma/2}\right)^2} \end{aligned} \tag{1.19}$$

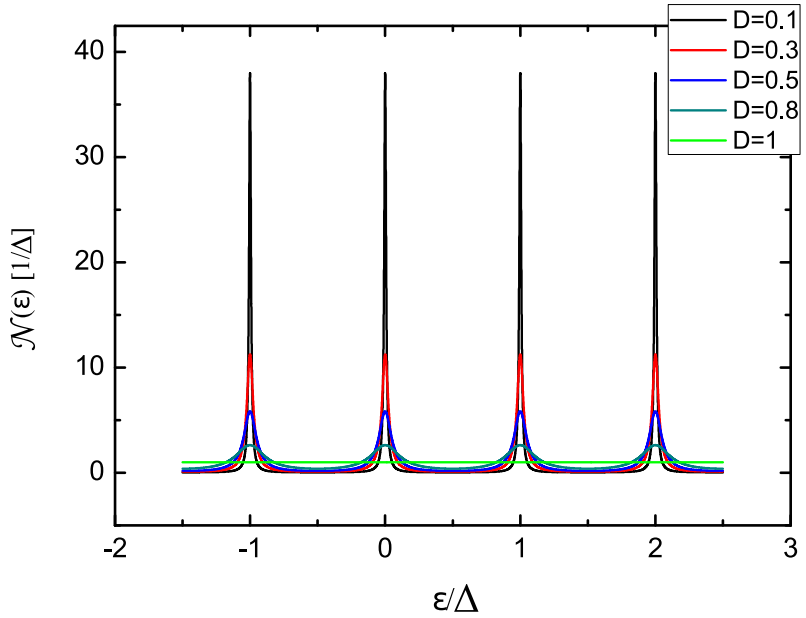

Figure 1.3: Calculated density of states in the dot for several values of the QPC transmission. The peaks in the density of states are broadened as the transmission increases. For unity transmission , the density of states is constant and equal to $1/\Delta$.

1.1.3.2 Effects of the static gate voltages

We can modulate the extrinsic parameters of the dot (QPC transmission D and position of the levels with respect to the Fermi energy eV_0) encoded in the density of states by applying voltages to the QPC gates and the top gate. The main effect of a voltage V_g applied to the QPC gates is to change the QPC transmission D by varying the electrostatic potential in the constriction. For an ideal saddle-point constriction [29], the relation between the transmission D and the gate voltage V_g is rather simple and only depends on two parameters:

$$D(V_g) = \frac{1}{1 + e^{-\frac{V_g - V_{g0}}{\Delta V}}} \tag{1.20}$$

V_{g0} determines the position of transmission 1/2, while ΔV determines the width of the opening of the QPC. We will show in 1.3 that these two parameters can be extracted from the dependence of the measured current with V_g. Because there is also a non-negligible capacitive coupling between the QPC gates and the dot potential, changing V_g also shifts the position of the energy levels in the dot with a lever arm α given by $\alpha\delta V_g = \delta\epsilon$. A large portion of the measurements presented in this chapter are measurements of the first harmonic of the average AC current as a function of the gate voltage V_g; as such, they demonstrate the two effects of V_g on the dot.

The potential of the dot can also, as described in the introduction, be modulated by applying voltages to the top gate. The lever arm β between a DC voltage applied to the top gate and the energy shift $\epsilon_0 = eV_0$ in the dot is given by $\beta\delta V_{DC} = \delta\epsilon_0$. We neglect however the influence of the top gate on the QPC transmission.

1.1.4 Calculation of the average AC current

1.1.4.1 General expression of the current

In the two-contacts geometry depicted in Fig.1.1, the measured current $\hat{I}_1(t)$ is not directly equal to the current emitted from the dot, but rather to the difference between the current incoming on contact (1), noted $\hat{I}_b(t)$, and the current emitted from contact (1) towards contact (2), noted $\hat{I}_c(t)$. Since contact (1) is connected to a measurement impedance equal to $Z_0 = 50\ \Omega \ll R_K \approx 25\ \mathrm{k}\Omega$, it is effectively grounded and therefore only emits, similarly to contact (2), electrons with populations given by an equilibrium Fermi function $f(\epsilon)$, where we have taken the Fermi energy ϵ_F equal to zero:

$$\left\langle \hat{a}^\dagger(\epsilon)\hat{a}(\epsilon') \right\rangle = \left\langle \hat{c}^\dagger(\epsilon)\hat{c}(\epsilon') \right\rangle = f(\epsilon)\delta(\epsilon - \epsilon') \tag{1.21}$$

It appears clearly that the inner edge channel does not take part in the measured current, since the contribution of the current in the inner channel incoming on contact (1) and emitted from contact (1) are equal if the two contacts are at the same temperature. We can then express the measured current $\hat{I}_1(t)$ as a function of the creation/annihilation operators in the outer edge channel:

$$\hat{I}_1(t) = \frac{e}{h}\int d\epsilon d\epsilon' \left(\hat{b}^\dagger(\epsilon)\hat{b}(\epsilon') - \hat{c}^\dagger(\epsilon)\hat{c}(\epsilon')\right) e^{i\frac{\epsilon-\epsilon'}{\hbar}t} = \hat{I}_b(t) - \hat{I}_c(t) \tag{1.22}$$

With:

$$\hat{I}_b(t) = \frac{e}{h}\int d\epsilon d\epsilon' \hat{b}^\dagger(\epsilon)\hat{b}(\epsilon') e^{i\frac{\epsilon-\epsilon'}{\hbar}t} \tag{1.23}$$

$$\hat{I}_c(t) = \frac{e}{h}\int d\epsilon d\epsilon' \hat{c}^\dagger(\epsilon)\hat{c}(\epsilon') e^{i\frac{\epsilon-\epsilon'}{\hbar}t} \tag{1.24}$$

When using Eq.1.3 to substitute $\hat{b}^\dagger(\epsilon)$ and $\hat{b}(\epsilon')$ in the expression of $\hat{I}_b(t)$, we have:

$$\hat{I}_b(t) = \frac{e}{h}\sum_{m,m'}\int d\epsilon d\epsilon' U_m^*(\epsilon)U_{m'}(\epsilon')\hat{a}^\dagger(\epsilon+m\hbar\Omega)\hat{a}(\epsilon'+m'\hbar\Omega)e^{i\frac{\epsilon-\epsilon'}{\hbar}t} \tag{1.25}$$

From here on, we take $\hbar\Omega = 1$, so that $\hat{a}^\dagger(\epsilon+m\hbar\Omega) = \hat{a}^\dagger(\epsilon+m)$. Eq.1.25 then becomes:

$$\hat{I}_b(t) = \frac{e}{h}\sum_{m,m'}\int d\epsilon d\epsilon' U_m^*(\epsilon)U_{m'}(\epsilon')\hat{a}^\dagger(\epsilon+m)\hat{a}(\epsilon'+m')e^{i\frac{\epsilon-\epsilon'}{\hbar}t} \tag{1.26}$$

This general expression of $\hat{I}_b(t)$ will be useful when calculating the current correlation in the next chapters.

1.1.4.2 Average AC current

To calculate the measured average AC current, we simply take the quantum average of the current operators:

$$\left\langle \hat{I}_1(t)\right\rangle = \left\langle \hat{I}_b(t)\right\rangle - \left\langle \hat{I}_c(t)\right\rangle \tag{1.27}$$

Eq.1.21 then gives:

$$\begin{aligned}\left\langle \hat{I}_b(t)\right\rangle &= \frac{e}{h}\sum_{m,m'}\int d\epsilon d\epsilon' U_m^*(\epsilon)U_{m'}(\epsilon')f(\epsilon+m)\delta(\epsilon+m-(\epsilon'+m'))e^{i\frac{\epsilon-\epsilon'}{\hbar}t}\\ &= \frac{e}{h}\sum_{m,m'}\int d\epsilon U_m^*(\epsilon)U_{m'}(\epsilon+m-m')f(\epsilon+m)e^{i(m'-m)t}\end{aligned} \tag{1.28}$$

and:

$$\begin{aligned}\left\langle \hat{I}_c(t)\right\rangle &= \frac{e}{h}\int d\epsilon d\epsilon' f(\epsilon)\delta(\epsilon+\epsilon')e^{i\frac{\epsilon-\epsilon'}{\hbar}t}\\ &= \frac{e}{h}\int d\epsilon f(\epsilon)\end{aligned} \tag{1.29}$$

We can then use sum rules on $U_m(\epsilon)$, demonstrated in appendix A.1, to express $\left\langle \hat{I}_c(t)\right\rangle$ as a function of $U_m(\epsilon)$:

$$\sum_{m,m'} U_m^*(\epsilon)U_{m'}(\epsilon+m-m')e^{i(m'-m)t} = 1 \tag{1.30}$$

This gives us:

$$\left\langle \hat{I}_c(t)\right\rangle = \frac{e}{h}\int d\epsilon \sum_{m,m'} U_m^*(\epsilon)U_{m'}(\epsilon+m-m')e^{i(m'-m)t}f(\epsilon) \tag{1.31}$$

When combining the expressions of $\left\langle \hat{I}_b(t)\right\rangle$ and $\left\langle \hat{I}_c(t)\right\rangle$, and performing the substitution $m'-m=k$, we finally obtain a compact expression of the average AC current as a sum of Fourier components:

$$I_1(t) = \left\langle \hat{I}_1(t)\right\rangle = \frac{e}{h}\sum_{k,m}\int d\epsilon U_m^*(\epsilon)U_{m+k}(\epsilon-k)\left[f(\epsilon+m)-f(\epsilon)\right]e^{ik\omega t} \tag{1.32}$$

In particular, the first harmonic I_Ω is given by:

$$I_\Omega = \frac{e}{h}\sum_m \int d\epsilon U_m^*(\epsilon)U_{m+1}(\epsilon - \hbar\Omega)\left[f(\epsilon+m) - f(\epsilon)\right] \tag{1.33}$$

These two compact expressions will be used to numerically compute the average AC current (in time-domain and first harmonic) to fit the experimental results presented in the next sections. It is however interesting to expand Eq.1.32 and Eq.1.33 as a function of the coefficients c_n and the stationary scattering matrix $U^0(\epsilon)$ in order to calculate analytical limits of the current. This calculation yields (see appendix A.2.1):

$$I_1(t) = \left\langle \hat{I}_1(t) \right\rangle = \frac{e}{h}\sum_{k,m} c_m c_{m+k}^* \int d\epsilon \left[U^{0*}(\epsilon)U^0(\epsilon - k) - 1\right] f(\epsilon + m)e^{ik\Omega t} \tag{1.34}$$

The expanded expression for the first harmonic is then:

$$I_\Omega = \frac{e}{h}\sum_m c_m c_{m-1}^* \int d\epsilon \left[U^{0*}(\epsilon)U^0(\epsilon + \hbar\Omega) - 1\right] f(\epsilon + m\hbar\Omega) \tag{1.35}$$

These two expressions are strictly equivalent to the ones calculated by my predecessors using the gauge transformation [11, 68], see demonstration in appendix A.3.1.

1.2 Measurement of the average AC current emitted by the source

In order to measure the AC current emitted by our sample, we install the sample in a dilution fridge with a base temperature of ~ 30 mK $\ll \Delta$. The fridge is equipped with a high-frequency conductance measurement setup detailed in [70, 11]. We briefly recall the setup in this section; however, it has been subject of profound modifications in order to perform ultra-high precision noise measurements presented in the next chapters. The details of these modifications will be given in chapter 4.

The measurement setup of the first harmonic of the current is represented in Fig.1.4. We describe both the excitation and measurement parts of the setup in the next paragraphs.

1.2.1 Excitation line

To drive the sample out of equilibrium, we use an *Agilent 81134A* microwave pulse/pattern generator and a broadband transmission line that transmits the excitation signal from room temperature to the base temperature of the dilution refrigerator. We use square signals with a rise time shorter than $60ps$. We can add a DC component to the square signal by using a bias tee at room temperature with its low-frequency input connected to a DC voltage generator.

The microwave excitation line is composed of *Huber+Suhner EZ-118* broadband (40 GHz) semi rigid cables separated by attenuators regularly placed in the fridge, see Fig.1.4. The purpose of these attenuators is to thermalize the thermal radiation generated at 300 K; each cable section between two attenuators is carefully thermalized to the corresponding stage of the refrigerator, as described in [70].

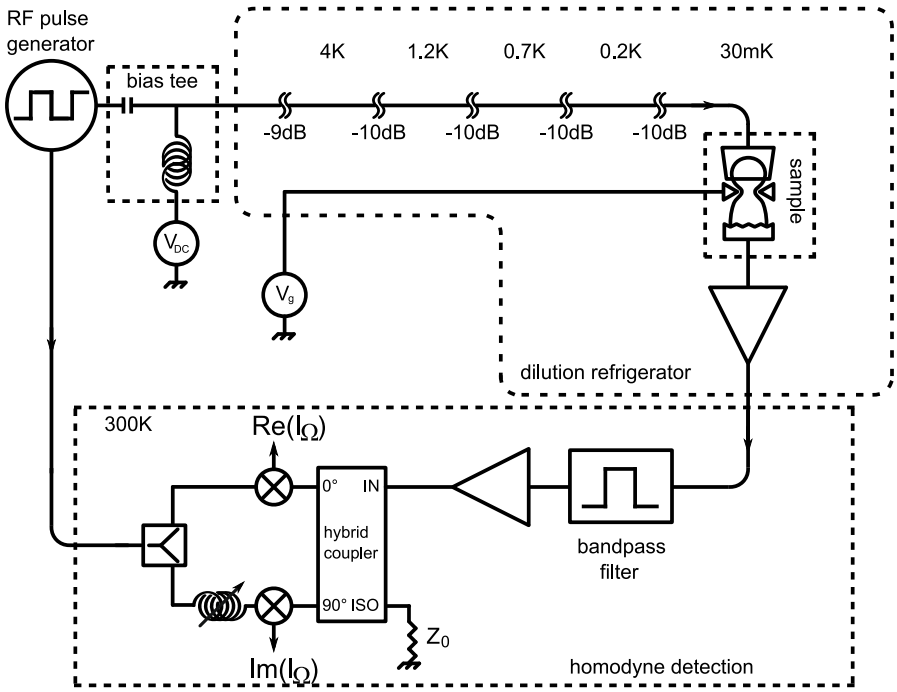

Figure 1.4: Measurement setup for the first harmonic of the average AC current. A microwave homodyne detection is used to measre the in-phase and out-of-phase parts of the average AC current.

It is crucial to use attenuators with characteristics presenting variations as small as possible when used at very low temperatures. We use *XMA* attenuators with a *NiCr* inner conductor, which are well suited for cryogenic applications. The total attenuation in the insert is -50 dB; we also use an additional -10 dB attenuator at room temperature (not pictured in Fig.1.4). Because of skin effect, the total attenuation on the line is slightly larger at room temperature than the one given by the attenuators (about 3 dB at 4 GHz). We expect this additional attenuation to decrease when the insert is cooled-down.

The excitation line is connected to a sample holder thermally anchored to the mixing chamber of the dilution refrigerator. The sample is directly wired to the signal line without any resistor in parallel, contrary to [70, 11]. Because of the large mismatch between the impedances of the line and of the sample (the impedance of the sample is typically given by the resistance quantum $R_K \approx 25.8\ \mathrm{k}\Omega \gg 50\ \Omega$), a stationary wave appears in the last section of the excitation line, with the sample placed at an anti-node of the wave. The sample therefore appears as a quasi-open line, so that all spectral components of the excitation voltage are maximal where the sample is located. The sample holder is described in detail in chapter 4.

DC gate voltages, such as V_g, are applied via high-resistivity DC lines mounted in the insert. These lines are filtered at room temperature, mainly to protect the sample against large voltage variations. The wiring is made with *Lakeshore ultra miniature* coaxial cables from the insert's inputs to the 1K pot stage of the refrigerator, and with manganin microcoax from the 1K pot stage to the mixing chamber. The high total resistance (about 120 Ω) of the cables ensures proper thermalization.

1.2.2 Measurement line

The average AC current measurement line was first implemented in the refrigerator by Julien Gabelli, and is described in details in [70, 11]. The signal is first amplified using cryogenic amplifiers thermalized in the helium bath vapors. We have changed the amplifiers used in [70, 11] for cryogenic amplifiers presenting better characteristics (noise temperature $T_N \approx 7$ K, bandwidth $1 - 4$ GHz) in order to perform the noise measurements presented in chapter 2.

Depending on the frequency, we can perform two kinds of measurements. For frequencies below 500 MHz, we record the current in the time domain and average it in real-time using a fast acquisition card [71]. We will briefly present some measurements in the time domain made by my predecessors [71, 68] in the next sections. For higher frequencies, we measure the in-phase and out-of-phase parts of the first harmonic of the signal with a microwave homodyne detection depicted in Fig.1.4. Most of the measurements presented in this manuscript are performed at the frequency $f_0 = 1.5$ GHz. The principle of the microwave homodyne detection is the same as lock-in detection techniques: the measured signal is split in an in-phase part and out-of-phase part using a 90° hybrid coupler; each quadrature is then multiplied with a reference (with the same frequency f_0) provided by the pulse generator and split between the two quadratures. The zero-frequency part of the result of each multiplication is then proportional to the amplitude of each quadrature of the first harmonic of the signal. The lengths of the cables between the splitter and the two multipliers have to be matched in order to obtain two signals with a 90° phase difference. This is experimentally done by using a phase shifter in one of the two cables. The quadrature is achieved within less than 2°, see [11].

Because of the propagation in the measurement lines, the signal acquires a global phase relative to the reference. We will show in the next sections how the properties of the sample can be used to determine this global phase.

1.2.3 Parasitic signal

At high frequency, finite parasitic couplings exist between the top gate and the leads and between the excitation and measurement lines on the sample holder. These couplings, which can be viewed as essentially capacitive, give rise to a finite parasitic signal. In order to remove this parasitic signal, we measure the difference between the measured signal at a given V_g and the signal when the QPC is completely closed, while keeping constant all other parameters (DC voltage applied to the top gate V_{DC}, temperature, or any other external parameter). This subtraction of the reference allows us to isolate the signal emitted by the mesoscopic capacitor; we will show in the next chapters that it has crucial implications in the measurement of current fluctuations emitted by the single electron source.

1.3 Average AC current in the linear regime

In this section, we focus on the properties of the linear conductance of a mesoscopic capacitor. As well as providing information on the intrinsic parameters of the sample, the linear conductance reveals striking phenomena such as the violation of Kirchoff's laws, and the quantization of charge relaxation resistance, demonstrated by Julien Gabelli [70].

1.3.1 Theory

Let us first consider the expression of the average AC current in Eq.1.34. We will expand it for a low-amplitude sinusoidal driving potential in order to derive an analytical expression of the linear conductance of the device. These calculations where first presented in [55].

1.3.1.1 Conductance of the sample

For a sinusoidal excitation $V^{'}(\tau') = V_{exc}cos(\Omega\tau')$, the Fourier coefficients c_n in Eq.1.34 are given by the nth-order Bessel function J_n:

$$c_n = J_n\left(\frac{eV_{exc}}{\hbar\Omega}\right) \tag{1.36}$$

The linear regime occurs when $eV_{exc} \ll \hbar\Omega$. Since $J_n\left(\frac{eV_{exc}}{\hbar\Omega}\right) \approx \left(\frac{eV_{exc}}{\hbar\Omega}\right)^{|n|}$ in this regime, we only consider the terms $\{m,k\} = \{\pm 1, \mp 1\}$ and $\{m,k\} = \{0, \pm 1\}$ in Eq.1.34. The average current only presents components at $\pm\Omega$, and is given by:

$$\begin{aligned} I_1(t) &= \frac{e^2}{h}\frac{V_{exc}}{2}\int d\epsilon \left[U^{0*}(\epsilon)U^0(\epsilon-\hbar\Omega) - 1\right]\frac{f(\epsilon-\hbar\Omega) - f(\epsilon)}{\hbar\Omega}e^{i\Omega t} \\ &\quad + \frac{e^2}{h}\frac{V_{exc}}{2}\int d\epsilon \left[U^{0*}(\epsilon)U^0(\epsilon+\hbar\Omega) - 1\right]\frac{f(\epsilon) - f(\epsilon+\hbar\Omega)}{\hbar\Omega}e^{-i\Omega t} \\ &= \frac{V_{exc}}{2}g(-\Omega)e^{i\Omega t} + \frac{V_{exc}}{2}g(\Omega)e^{-i\Omega t} \end{aligned} \tag{1.37}$$

The conductance of the sample at frequency Ω is then given by:

$$g(\Omega) = \frac{e^2}{h}\int d\epsilon \left[U^{0*}(\epsilon)U^0(\epsilon+\hbar\Omega) - 1\right]\frac{f(\epsilon) - f(\epsilon+\hbar\Omega)}{\hbar\Omega} \tag{1.38}$$

1.3.1.2 Low-frequency equivalent circuit

In order to express the linear conductance of the device in terms of usual linear electronic components such as resistor and capacitor, we perform a second-order expansion of Eq.1.38 in frequency Ω:

$$g(\Omega) = \frac{e^2}{h}\int d\epsilon \left(U^{0*}\frac{dU^0}{d\epsilon}\hbar\Omega + \left(U^{0*}\frac{dU^0}{d\epsilon}\right)^2\frac{(\hbar\Omega)^2}{2}\right)\frac{df}{d\epsilon} + \mathcal{O}(\Omega^3) \tag{1.39}$$

We can introduce the definition of the density of states (Eq.1.18) in this expression:

$$g(\Omega) = \int d\epsilon \left(-i\Omega e^2\mathcal{N}(\epsilon)\frac{-df}{d\epsilon}\right) + \int d\epsilon \left(\Omega^2\frac{h}{2e^2}(e^2\mathcal{N}(\epsilon))^2\frac{-df}{d\epsilon}\right) \tag{1.40}$$

Within the low-frequency approximation, this conductance is identical to the conductance of a series RC circuit, with:

$$\begin{aligned} C_q &= e^2\int d\epsilon \mathcal{N}(\epsilon)\frac{-df}{d\epsilon} \\ R_q &= \frac{h}{2e^2}\frac{\int d\epsilon \mathcal{N}(\epsilon)^2\frac{-df}{d\epsilon}}{\left(\int d\epsilon \mathcal{N}(\epsilon)\frac{-df}{d\epsilon}\right)^2} \end{aligned} \tag{1.41}$$

The low-frequency conductance of the mesoscopic capacitor is therefore given by the association in series of a quantum capacitance C_q and a quantum resistance R_q, each one depending on the density of states of the dot and the temperature. In this respect, the measurement of the conductance of the sample brings quantitative information on the properties of the dot: at low temperature, the quantum capacitance probes the density of states in the dot, and the relaxation time of the dot is given by the product R_qC_q.

1.3.1.3 Validity of the expansion

In the previous paragraph, we have expressed the linear conductance of the mesoscopic capacitor under the assumption that the driving frequency Ω is small compared to the scale of the variations of the scattering matrix $U^0(\epsilon)$. This scale is typically given by the width of the peaks in the density of states, proportional to the product $D\Delta$, and therefore related to the relaxation time in the dot R_qC_q. While the previous results are only valid in the regime where $R_qC_q\Omega \ll 1$, it appears that the numerical computation of the exact formula 1.32 using experimental parameters bears results that are quite comparable with the conductance of an RC circuit given by Eq.1.41, even in regimes where the $R_qC_q\Omega \ll 1$ criterion is clearly not satisfied. This allows us to understand our results in an RC-circuit framework, with a conductance given by Eq.1.41.

1.3.1.4 Zero-temperature limit

At zero temperature, the quantum capacitance is simply proportional to the density of states evaluated at the Fermi energy: $C_q = e^2\mathcal{N}(\epsilon_f)$. It therefore presents very narrow peaks at low transmission, with a height however limited by the geometrical capacitance. The relaxation resistance becomes independent of all parameters, and equal to half the resistance quantum: $R_q = \frac{h}{2e^2}$ [72]. The fact that it becomes independent of the QPC transmission D is a striking property, and has been experimentally demonstrated by my predecessors [70, 11]. It can be understood by again considering the quantum dot as a one-contact fully-coherent electronic Fabry-Perot interferometer; as such, its resistance is given by the resistance of the single contact $\frac{h}{2e^2}$. The zero-temperature limit is also valid as long as the temperature is small compared to the variation scale of the density of states, *i.e.* $k_BT \ll D\Delta$, which is the case for large enough transmissions: experimentally, $T \approx 100$ mK and $\Delta \approx 2-4$ K (the zero-temperature limit is thus obtained for $D > 0.2$).

1.3.1.5 Finite temperature

When the temperature becomes comparable to the variation scale of the density of states, R_q and C_q are given by the convolution of the density of states with the derivative of the Fermi function. In particular, in the so-called sequential regime where $D\Delta \ll k_BT \ll \Delta$, the density of states presents distinct Lorentzian peaks; in the calculation of R_q and C_q, we therefore consider $\mathcal{N}(\epsilon)$ as a single Dirac peak at energy ϵ_n. We thus have:

$$\begin{aligned} C_q &\approx \frac{e^2}{4k_BT\cosh^2\left(\frac{\epsilon_n-\epsilon_f}{2k_BT}\right)} \\ R_q &\approx \frac{D\Delta}{h}\frac{e^2}{4k_BT\cosh^2\left(\frac{\epsilon_n-\epsilon_f}{2k_BT}\right)} \end{aligned} \tag{1.42}$$

In this regime, the capacitance is therefore bounded by $\frac{e^2}{4k_BT}$, and only depends on the temperature, whereas the resistance depends on the transmission as well as the temperature. The characteristic shape of the conductance as a function of the energy in this regime will be helpful in the calibration of the level spacing Δ and the coupling between the top gate and the levels in the dot.

1.3.2 Experimental results: determination of the sample parameters

The comparison between the theoretical predictions presented in the previous paragraph and the experimental measurements allows us to determine the parameters of the sample, such as the level

spacing and the variation of the transmission as a function of the QPC gate voltage V_g. In order to extract these parameters, we first need to tune the global phase acquired by the signal relative to the reference mentioned in 1.2.2.

1.3.2.1 Global phase tuning

The resolution of the measurement of the relaxation time R_qC_q is directly related to the resolution of the global phase tuning. Indeed, the ratio between the real and imaginary parts of the current is equal to $R_qC_q\Omega$ (see Eq.1.40), that is the relaxation time multiplied by the driving angular frequency.

At unity transmission, $R_qC_q\Omega \approx 0.05$ for samples with a typical capacitance of 0.5 fF, driven at 1.5 GHz. For an accurate measurement of both quadratures of the current, we need to tune the global phase with a precision smaller than a few degrees.

Two tuning procedures have been implemented by my predecessors. The first one, presented in [70], is based on the properties of the linear regime, where the resistance R_q becomes constant, and therefore independent of the dot equilibrium potential. In this regime, when the phase is correctly tuned, the oscillations in the measured resistance should vanish as a function of the gate voltage V_g. The main drawback of this method comes from the fact that the tuning criterion is based on the precise measurement of the real part of the current at unity transmission, thus making the method extremely sensitive to noise added by the measurement setup. For this reason, we rather use the method expanded by Gwendal Fève [11], which involves properties of the capacitance in the non-linear regime: when the excitation voltage exactly compensates the level spacing, the capacitance becomes independent of the transmission while the resistance varies between infinity and $h/2e^2$. The Nyquist diagram of the current when D varies is therefore a semicircle with a radius ef_0, centered on $(0, ef_0)$. The application of this procedure for the sample studied here is detailed in the next section.

1.3.2.2 Conductance as a function of the QPC gate voltage

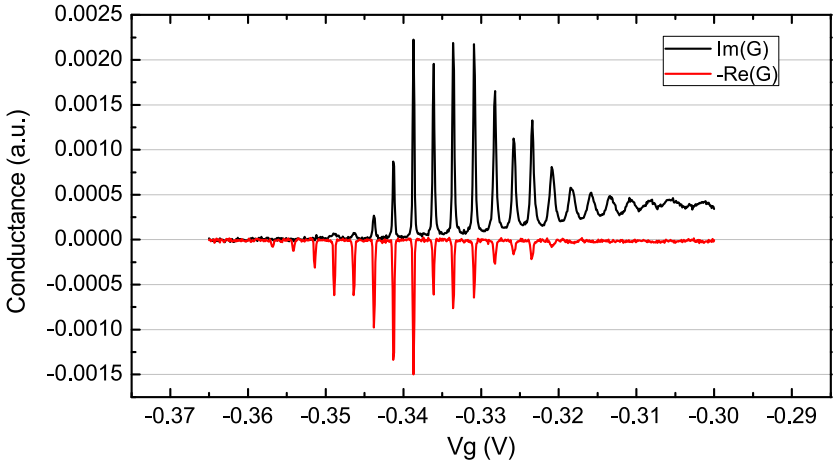

Figure 1.5: Conductance trace at 1.5 GHz as a function of the QPC gate voltage V_g, measured on sample *S528-11*. The applied magnetic field ($B \approx 1.8T$) corresponds to a filling factor $\nu = 4$.

The linear conductance of sample *S528-11* measured at 1.5 GHz as a function of the QPC gate voltage V_g is presented on Fig.1.5. As predicted in 1.3.1, the conductance at high transmission (small

negative gate voltages) probes the density of states at the Fermi energy, convoluted with the temperature. The oscillations of the conductance with the gate voltage reflect the fact that the QPC gate is coupled to the levels in the dot; V_g therefore shifts the levels with respect to the Fermi energy. When V_g is swept towards smaller transmissions, the energy levels pass in front of the Fermi energy while becoming narrower. In the $R_q C_q \Omega \sim 1$ regime, the real part of the conductance becomes preponderant, then decreases again as the transmission is lowered. When the transmission reaches zero, the current flowing through the mesoscopic capacitor vanishes; we will refer to this regime as the pinch-off.

1.3.2.3 Calibration of the quantum capacitance

In the sequential regime ($D\Delta \ll k_B T$), the observed conductance peaks when the energy levels in the dot are shifted in resonance with the Fermi energy have a width given by the temperature, while the distance between two peaks is proportional to the level spacing Δ. If the temperature is known, it is thus possible to calibrate the level spacing.

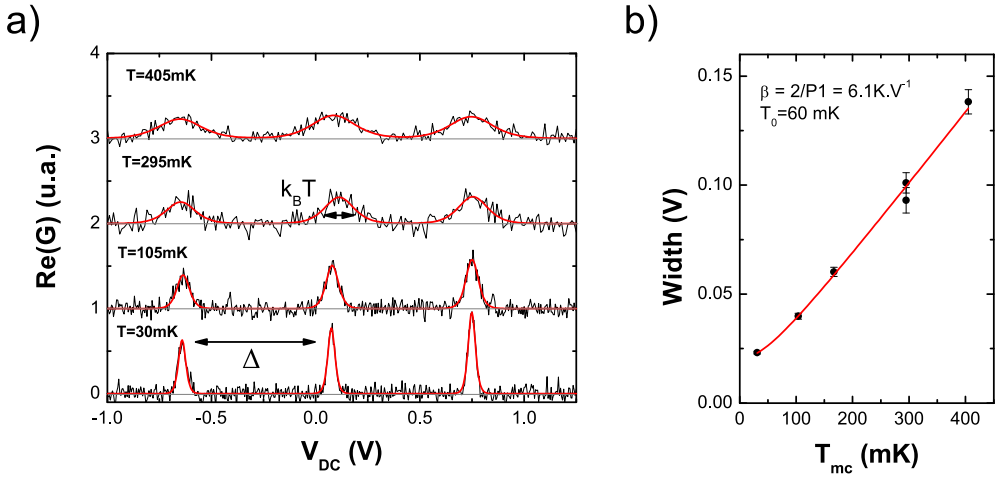

Figure 1.6: Calibration of the quantum capacitance of sample *S528-11*: **a)** real part of the conductance in the sequential regime as a function of the top gate voltage V_{DC}, for different temperatures of the mixing chamber. The conductance peaks corresponding to the levels in the dot are broadened when the temperature increases. The experimental data (black lines) are adjusted with functions given by Eq.1.42 (red lines). **b)** width of the conductance peaks as a function of the mixing chamber temperature. The red curve corresponds to the fit $\frac{2}{\beta}\sqrt{T_{mc}^2 + T_0^2}$, where β is the coupling between the top gate and the energy levels.

We have calibrated the level spacing at filling factor $\nu = 4$ for sample *S528-11* by varying the DC gate voltage applied to the top gate V_{DC} for different values of the mixing chamber temperature of the dilution refrigerator, see Fig.1.6. The observed conductance peaks have a shape given by $1/\cosh^2(\beta(V_{DC} - V_0)/2T)$, derived from Eq.1.42, where β is the coupling between the voltage applied to the top gate and the position of the levels in the dot (expressed in Kelvin) introduced in 1.1.3.2, and V_0 is the position of the peak of the density of states. We have fitted the experimental data, spanning on three peaks, with the sum of three functions $1/\cosh^2((V_{DC} - V_0)/2L(T))$, where $L(T)$ is the width of the peaks, expressed in Volts, as a function of the temperature of the mixing chamber (see Fig.1.6a). We have plotted on Fig.1.6b the measured width as a function of the temperature; as expected, the relation is linear at high temperatures, but saturates at low temperature. This saturation is caused by a residual temperature T_0 that reflects an insufficient thermalization of the electrons, or instabilities

in the sample leading to gate noise. A fit of the data by the function $P_1\sqrt{T^2+T_0^2}$ allows us to extract the coupling $\beta = 6.1$ KV^{-1} and the residual temperature $T_0 = 60$ mK. The level spacing is then simply given by the product of the distance in gate voltage between two peaks times the coupling constant. For sample *S528-11*, we find $\Delta = 4.2 \pm 0.2$ K; the value of the quantum capacitance is therefore $C_q = e^2/\Delta = 0.44 \pm 0.03$ fF.

1.3.2.4 QPC transmission law

Once the level spacing and the values of the capacitances of the system are known, we can adjust the measured conductance as a function of the QPC gate voltage using the simple QPC transmission given in Eq.1.20. The coupling α between the QPC gates and the levels in the dot is first extracted by simply measuring the distance in QPC gate voltage between two conductance peaks in Fig.1.5. We have fitted the linear conductance of sample S528-11 at three different temperatures (see Fig.1.7) using the following parameters: coupling constant $\alpha = 1.65$ KmV^{-1}, QPC opening width $\Delta V = 4.4$ mV, half-transmission voltage $V_{g0} = -329.8$ mV. The electronic temperature $T = \sqrt{T_{mc}^2 + T_0^2}$ was set to 70 mK, according to the results of the calibration. This temperature is quite low, so that the linear regime $eV_{exc} \ll k_B T$ is not fully achieved. We have therefore taken into account the finite value of the excitation voltage. The agreement between experimental data and the scattering theory

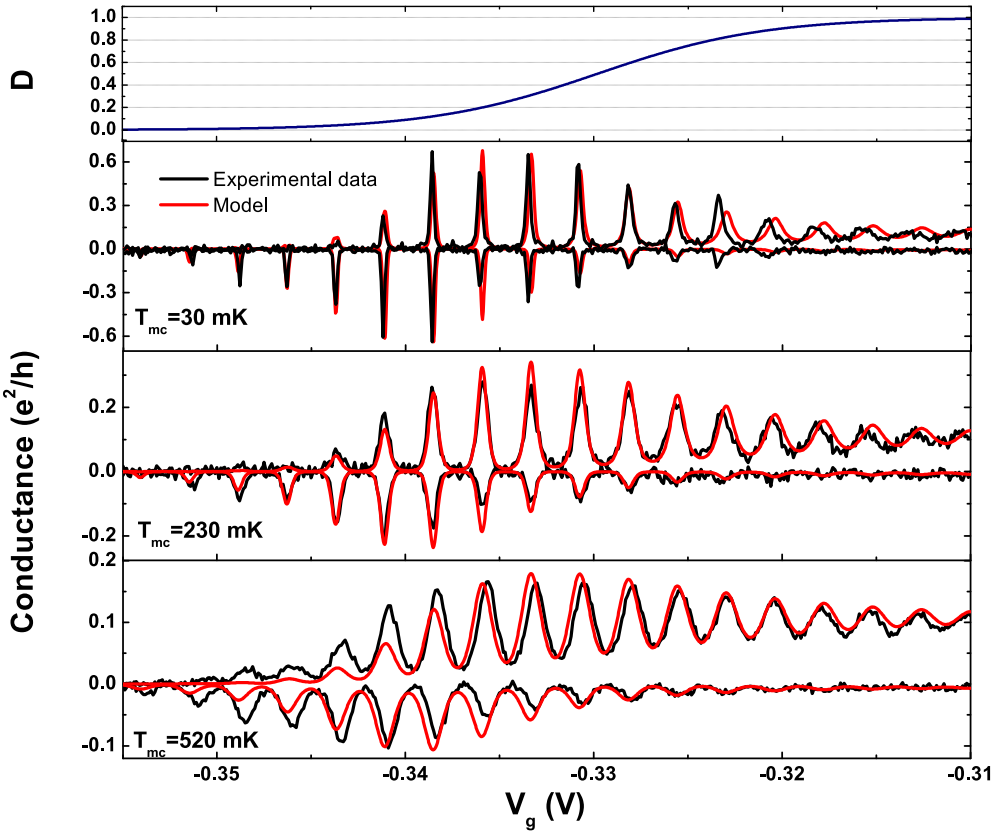

Figure 1.7: Linear conductance at 1.5 GHz of sample *S528-11*, for different temperatures. The first figure corresponds to the QPC transmission law used for the theoretical adjustment (red lines). At large transmissions, the conductance is equal for all three temperatures.

is quite good, except for small transmissions. In particular, the experimental data at 520 mK show

conductance oscillations persisting at lower negative voltages than the theoretical fit. This can be explained by a variation of the transmission with energy, which will have an non negligible effect in the non-linear regime presented in the next section. Nonetheless, the excellent agreement between experimental data and the model at large transmission and low temperature confirms the quantization of the charge relaxation resistance $R_q = h/2e^2$, which was first demonstrated on sample *E3* by Julien Gabelli [62, 70].

1.3.3 Conclusion on the linear regime

Beyond its fundamental properties emphasizing the effects of quantum coherence in mesoscopic conductors, the linear regime of the mesoscopic capacitor allows us to determine every parameter of the sample. We will use these parameters to compare the experimental results in the non linear regime with our scattering theory with no adjustable parameter.

1.4 Average AC current in the non-linear regime

In order to inject single charges into the two-dimensional electron gas, we drive the mesoscopic capacitor with a square signal the amplitude of which is equal to the level spacing. At zero temperature, and for narrow enough levels in the dot, this places the last occupied energy level of the dot above the Fermi energy. The electron sitting on this level can then escape form the dot within a characteristic emission time $\tau \approx h/D\Delta$ depending on the QPC transmission.

In this section we will describe the properties of the mesoscopic capacitor in the non-linear regime, and show that the quantization of the first harmonic of the average AC current in units of $2ef_0$ is a first proof that the device can be used as a single electron source. We first present theoretical considerations on the non-linear regime by introducing an extension of the scattering model for strong driving amplitudes, as well as a heuristic model describing the device as a perfect single electron source. We then present experimental results obtained for two samples, and compare them with the predictions.

1.4.1 Scattering theory

In order to derive analytical expressions of the current in the non-linear regime, we expand Eq.1.35 for a perfect square excitation. This calculation was first presented in [11].

1.4.1.1 AC response to a square excitation

The Fourier coefficients c_n (defined in Eq.1.8) for a perfect square excitation with an amplitude V_{exc} have been defined in [11]. These coefficients have a very simple expression when the ratio of the drive amplitude divided by the frequency $eV_{exc}/\hbar\Omega$ is an even integer substantially larger than one. This is the case for sample *S528-11*, where $2p = eV_{exc}/\hbar\Omega \approx 30$ for $eV_{exc} = \Delta/2$ ($\Delta \approx 4$ K, $\Omega = 1.5$ GHz). The coefficients c_n are then given by:

$$\begin{array}{lcll} c_{2p} & \approx & 1/2 & \\ c_k & \approx & 0 & (k \neq p) \\ c_{2p+2k+1} & \approx & \dfrac{1}{i\pi(2k+1)} & \\ c_{-n} & \approx & -c_n & \end{array} \tag{1.43}$$

Combined with Eq.1.35, these coefficients yield:

$$I_\Omega = \frac{e}{2i\pi h}\int d\epsilon \left(U^{0*}(\epsilon)U^0(\epsilon+\hbar\Omega)-1\right)\left[f(\epsilon+eV_{exc})-f(\epsilon-eV_{exc})\right. \\ \left.+f(\epsilon+\hbar\Omega+eV_{exc})-f(\epsilon+\hbar\Omega-eV_{exc})\right] \tag{1.44}$$

We now proceed to a second-order expansion in the frequency (for $D\Delta \gg \hbar\Omega$), as it was done in the linear regime:

$$I_\Omega = \frac{i2V_{exc}}{\pi}\int d\epsilon \left[-i\Omega e^2\mathcal{N}(\epsilon)+\Omega^2\frac{h}{2e^2}(e^2\mathcal{N}(\epsilon))^2\right]\frac{f(\epsilon-eV_{exc})-f(\epsilon+eV_{exc})}{2eV_{exc}} \tag{1.45}$$

For the first harmonic of the AC current, in the low-frequency regime, we once again find that the equivalent circuit is the series association of a capacitance C_q^{nl} and a resistance R_q^{nl} given by:

$$\begin{aligned} C_q^{nl} &= e^2\int d\epsilon\mathcal{N}(\epsilon)\frac{f(\epsilon-eV_{exc})-f(\epsilon+eV_{exc})}{2eV_{exc}} \\ R_q^{nl} &= \frac{h}{2e^2}\frac{\int d\epsilon\mathcal{N}(\epsilon)^2\frac{f(\epsilon-eV_{exc})-f(\epsilon+eV_{exc})}{2eV_{exc}}}{\left(\int d\epsilon\mathcal{N}(\epsilon)\frac{f(\epsilon-eV_{exc})-f(\epsilon+eV_{exc})}{2eV_{exc}}\right)^2} \end{aligned} \tag{1.46}$$

These two components are highly similar to their linear counterparts, except for the derivative of the Fermi function in Eq.1.41, now replaced by the term $\frac{f(\epsilon-eV_{exc})-f(\epsilon+eV_{exc})}{2eV_{exc}}$, which emphasizes the non-linearity of the circuit.

This equivalent circuit allows for a simple interpretation of the properties of the current in the non-linear regime. Indeed, for a classical RC circuit driven by a square voltage, the capacitance defines the average electric charge transfered per half-period in the circuit at low frequency, and the product RC defines the characteristic charge transfer time. The quantum capacitance defined in Eq.1.46 is equal to the integral of the density of states on a window defined by the two potentials the dot is brought on during one period of the drive. This integral is equal to the difference of the mean occupation numbers for each of the two potentials: when the voltage step $2V_{exc}$ exactly compensates the level spacing, it is independent of the dot equilibrium potential and equal to 1, provided that the density of states is Δ-periodic. A single peak in the density of states is fully integrated, and the quantum capacitance becomes then independent of temperature, QPC transmission and equilibrium potential: $C_q^{nl} = e^2/\Delta$.

As for the linear regime, this expansion is only valid when the escape time is small compared to the drive period, that is $R_q^{nl}C_q^{nl}\Omega \ll 1$. However, it is once again possible to extend these definitions to regimes where the escape time becomes comparable or larger than the period; we then define a non-linear conductance G^{nl} for the first harmonic of the average AC current:

$$G^{nl}(\Omega) = \frac{-iC_q^{nl}\Omega}{1-iR_q^{nl}C_q^{nl}\Omega} \tag{1.47}$$

When $2eV_{exc} = \Delta$ for large transmissions, the current is essentially capacitive and the quadratic term in Ω in Eq.1.45 can be neglected. The current is therefore equal to $e\Omega/\pi = 2ef_0$, corresponding to the emission of a single electron followed by a single hole at each period.

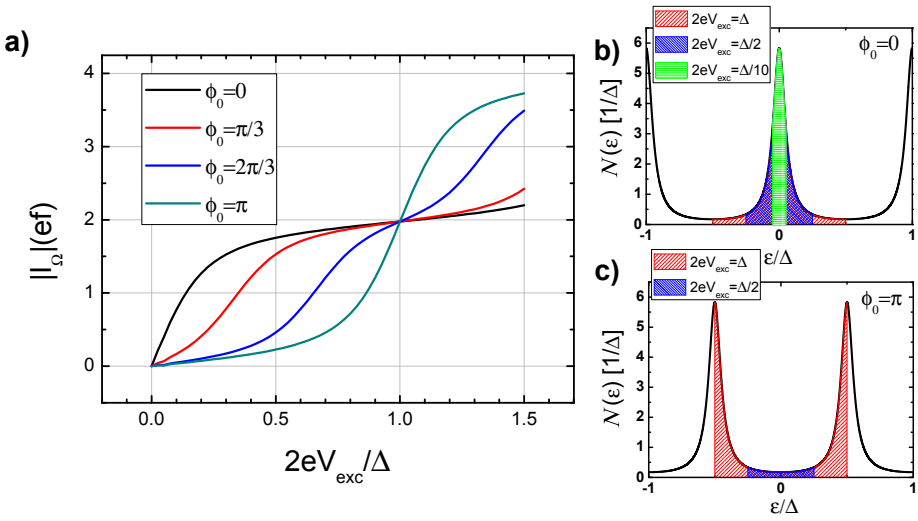

Figure 1.8: Calculated first harmonic as a function of the excitation amplitude V_{exc}, for a transmission $D = 0.5$. **a)** modulus of the first harmonic, for different values of the dot equilibrium potential expressed as a phase in the scattering amplitude $\phi_0 = 2\pi eV_0/\Delta$. When $\phi_0 \approx 0$, the current presents a plateau at a value $2ef_0$. **b)** density of states at equilibrium, for an equilibrium potential $\phi_0 = 0$. The checked areas correspond to the integrated portion of the density of states in Eq.1.46, for three values of the excitation amplitude ($2eV_{exc} = \Delta, \Delta/2, \Delta/10$). **c)** same as **b)**, for $\phi_0 = \pi$.

1.4.1.2 Modulus of the current: quantization of the first harmonic

As seen in the previous paragraph, the average current becomes constant and equal to $2ef_0$ when the excitation voltage compensates the level spacing in the dot. Numerical computations of Eq.1.33 and 1.35, using the parameters extracted from the linear regime ($\Delta \approx 4$ K, $f_0 = 1.5$ GHz, $T = 100$ mK), show that the modulus of the current is in fact quantized in units of $2ef_0$ whenever the system is driven in the injection regime, that is whenever the highest occupied level in the dot is shifted significantly high above the Fermi level. The quantization of the modulus of the average current is illustrated in Fig.1.8: depending on the dot equilibrium potential, the first harmonic of the average AC current presents a plateau at $I_\Omega = 2ef_0$ when the amplitude of the excitation voltage V_{exc} is changed. When $2eV_{exc} = \Delta$, all curves join at $I_\Omega = 2ef_0$, where an entire peak of the density of states is integrated.

We express the initial value of the dot equilibrium potential eV_0 as a function of the level spacing Δ using the phase term $\phi_0 = 2\pi eV_0/\Delta$. The situation where $\phi_0 = 0$ is called anti-resonant because the active energy level is alternatively brought to $-eV_{exc}$ and $+eV_{exc}$ (with $\epsilon_F = 0$). For small excitation voltages, the level is slightly shifted around the Fermi energy, so that the integrated portion of the density of states varies quickly with V_{exc}, see Fig.1.8b. When V_{exc} increases, the level is brought far off-resonance with the Fermi energy. In this case, the current has a small dependence with the excitation voltage since the active level is much farther above (or below) the Fermi energy than its width. In other terms, the boundaries of the integrals in Eq.1.46 are changed in regions where the density of states is close to zero, which only slightly changes R_q^{nl} and C_q^{nl}. On the other hand, the resonant case $\phi_0 = \pi$ does not present a plateau in the current when V_{exc} is changed. Indeed, when the active energy level is brought in resonance with the Fermi energy, the current is maximally sensitive to small shifts in the position of the level in respect to the Fermi energy: when V_{exc} is changed around $2eV_{exc} = \Delta$, the boundaries of the integrals in Eq.1.46 are changed on peaks of the density of states (see Fig.1.8c).

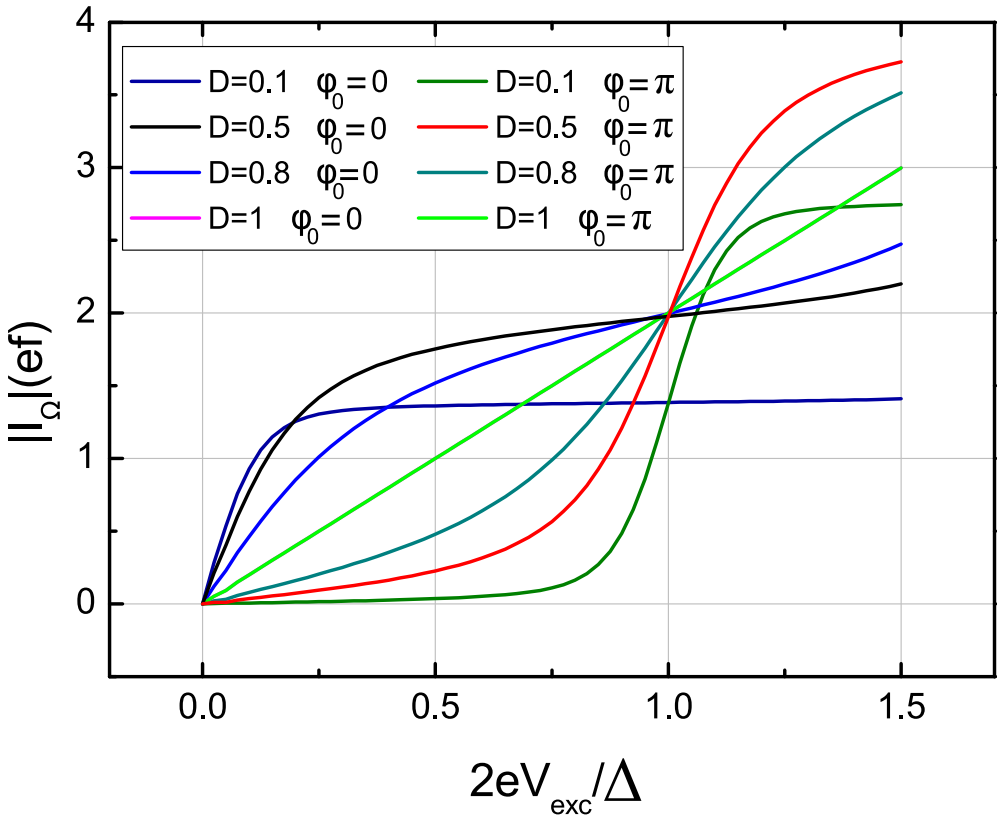

Figure 1.9: Calculated first harmonic as a function of the excitation amplitude, for several values of the transmission. At low transmission, the current plateau does not reach the value $2ef_0$ for $\phi_0 = 0$. Likewise, the current plateau for $\phi_0 = \pi$ is lower than $4ef_0$. At transmission unity, the current becomes linear with the excitation amplitude.

The curves corresponding to every other value of the dot equilibrium potential (here, $\phi_0 = \pi/3$ and $\phi_0 = 2\pi/3$) are comprised within the area defined by the difference of the curves where $\phi_0 = 0$ and $\phi_0 = \pi$. The size of this area gives an insight on the accuracy of the quantization of the first harmonic, and is affected by the QPC transmission. In Fig.1.9, we have plotted the value of the first harmonic of the current as a function of the excitation amplitude, for different values of the transmission, in the anti-resonant ($\phi_0 = 0$) and resonant ($\phi_0 = \pi$) cases. For large transmissions (here, $D = 0.8$), the first harmonic is still equal to $2ef_0$ when $2eV_{exc} = \Delta$; however, the plateau is less pronounced, leading to a smaller area between the curves $\phi_0 = 0$ and $\phi_0 = \pi$. This is due to the fact that the levels in the dot are well-coupled to the continuum of the leads, thus degrading the quantization of the charge sitting on each level. For unity transmission, the density of states is uniform and quantization is lost: the current becomes linear with the driving amplitude V_{exc}.

Finally, for small transmission (here, $D = 0.1$), the current presents a plateau at a value lower than $2ef_0$: although the peaks in the density of states are well-defined, the escape time becomes larger than the half-period of the excitation and charges are not always emitted before the excitation signal changes sign: the average AC current therefore has a value lower than $2ef_0$, determined by the escape time. The phase of the first harmonic of the current allows us to gain access to the escape time. Indeed, the ratio between real and imaginary part of the first harmonic is equal to $R_q^{nl}C_q^{nl}\Omega$, that is the escape time $\tau = R_q^{nl}C_q^{nl}$ multiplied by the frequency of the drive. A simple expression of τ can be derived from Eq.1.46 for $2eV_{exc} = \Delta$, provided $R_q^{nl}C_q^{nl}\Omega \ll 1$, and $D \ll 1$ so that the density of states

can be approximated by a series of Lorentzian peaks. At zero temperature, the Fermi functions in the integrals in Eq.1.46 set the boundaries of the integrals over a single peak of the density of states. We then have:

$$\begin{aligned} C_q^{nl} &= \frac{e^2}{2eV_{exc}} \int\limits_{1peak} d\epsilon \mathcal{N}(\epsilon) = \frac{e^2}{\Delta} \\ R_q^{nl} &= \frac{h}{2e^2} \frac{\int_{1peak} d\epsilon \mathcal{N}^2(\epsilon)}{\left[\int_{1peak} d\epsilon \mathcal{N}(\epsilon)\right]^2} \approx \frac{h}{De^2} \end{aligned} \tag{1.48}$$

In this regime, the equivalent circuit is therefore given by the incoherent addition of the quantum capacitor and the resistance of the quantum point contact, and the escape time is given by $\tau = \frac{h}{D\Delta}$.

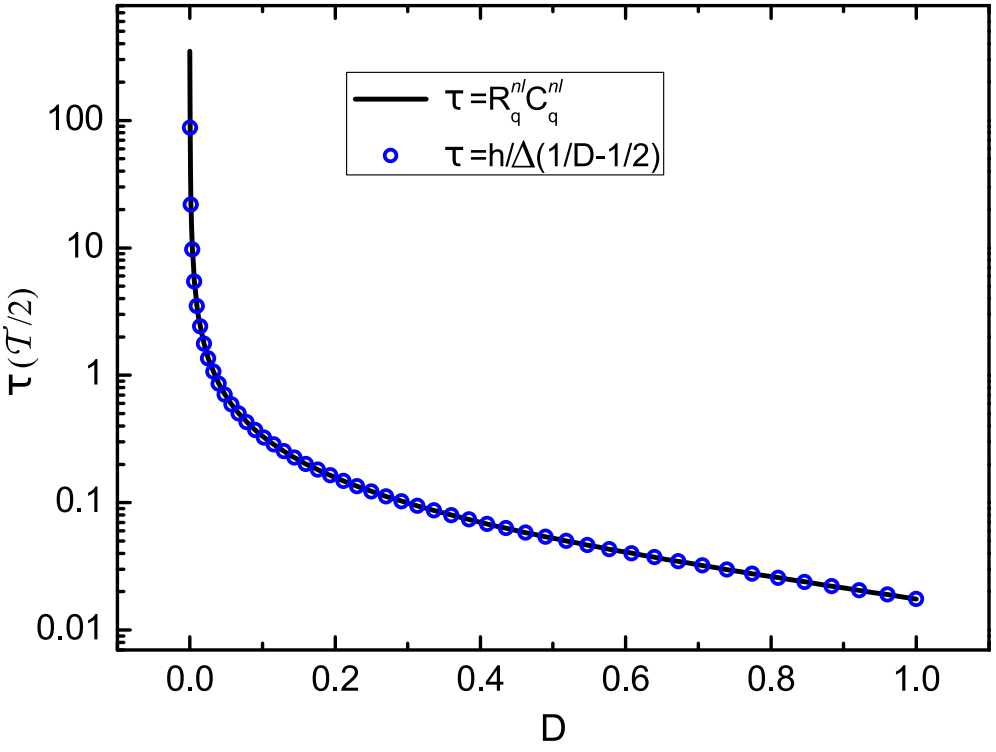

Figure 1.10: Calculated escape time as a function of the QPC transmission. The black line corresponds to the escape time given by the formula $\tau = R_q^{nl} C_q^{nl}$. The blue circles correspond to Eq.1.49. For low transmissions, the escape time becomes larger than the half-period $\mathcal{T}/2$.

The expression of the quantum resistance in Eq.1.48 is in fact the low-transmission limit of the charge relaxation resistance calculated in [73] in the linear regime, including a loss of electronic coherence in the dot. The charge relaxation resistance is given by the series association of the Landauer resistance [74] of the quantum point contact and the interface resistance of a single contact: $R_q = \frac{h}{e^2}\frac{1-D}{D} + \frac{h}{2e^2}$. Since the capacitance is constant when $2eV_{exc} = \Delta$, the escape time in the charge emission regime is given by:

$$\tau = \frac{h}{\Delta}\left(\frac{1}{D} - \frac{1}{2}\right) \tag{1.49}$$

This simple formula is consistent with the numerical computations of the scattering model (see Fig.1.10), and allows us to precisely reproduce the experimental data by extracting the exact QPC transmission law as a function of the QPC gate voltage.

1.4.2 Heuristic model

In order to gain a better comprehension of the physics of the single electron source in the anti-resonant case ($\phi_0 = 0$), we present a heuristic numerical model describing the device as a perfect single electron source. This simple semiclassical model was introduced by Adrien Mahé [68] in order to interpret the noise measurements presented in [63]. Although its main interest is to provide a complete understanding of the physical processes giving rise to the different noise regimes (see chapter 2), we present it in this chapter since it supports the description of the device in terms of RC-circuit elements. The principle of

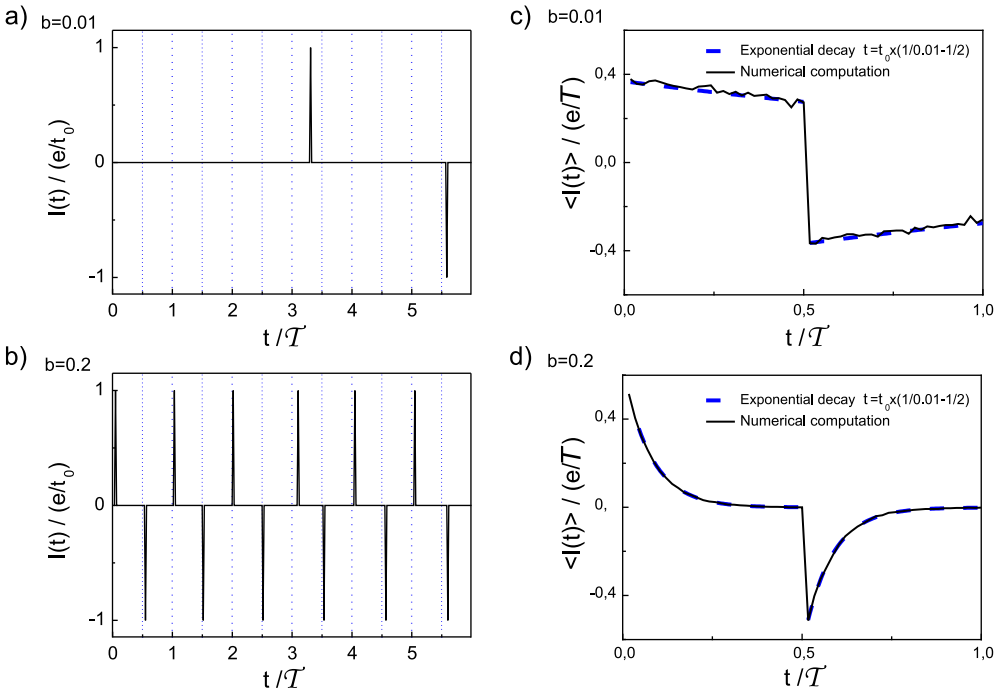

Figure 1.11: AC current emitted by the source, calculated with the heuristic model. **a)** and **b)** emitted current as a function of time for escape probability $b = 0.01$ (**a**), and $b = 0.2$ (**b**). A peak (dip) appears whenever an electron (hole) is emitted. **c)** and **d)** statistical average of the current displayed on one period of the drive, for $b = 0.01$ (**c**), and $b = 0.2$ (**d**). The calculations (black lines) display the expected exponential decay with a characteristic time given by $\tau = \tau_0(1/b - 1/2)$.

this model is as follows: we restrict the number of electrons in the dot to either 1 or 0 (thus effectively considering a single-level dot). When an electron is inside the dot, it performs circles along the edges of the dot, each one in a time τ_0. At each turn, the electron can escape the dot with a probability b. The half-period of the excitation drive is divided in a large number of turns N (typically, $N \approx 60$ to mimic our experiments). Single charge emission is enforced by prohibiting any additional charge

transfer process within the half-period after an electron is emitted. After N time units τ_0, the other half-period of the excitation drive sets in, and an electron can be absorbed in the dot with a probability b per unit time τ_0 only if the electron was emitted in the previous half-period. Only a single absorption process can take place during this half-period, and all other processes are prohibited. This defines a sequence in which during a period of the excitation drive, a single electron can be emitted if the dot was previously occupied, and a single hole can be emitted only if the electron has escaped. The repetition of this sequence generates an AC current comprised of peaks/dips whenever an electron/hole is emitted, see Fig.1.11; for low probabilities b, charges may not have enough time to escape within one half-period, and the peaks/dip appear semi-randomly (Fig.1.11a), each peak being followed some time after by a dip, thus enforcing net charge conservation on the dot. When b is increased, charges are systematically emitted with an uncertainty on the emission time illustrated by the distribution of the peaks/dips within a period, see Fig.1.11b. This randomness on charge emission is put into light when taking the statistical average of the current, that is the average AC current emitted by the system (see Fig.1.11c and d): the average AC current presents series of exponential decays described in the introduction at each half-period, which are expected for a RC-circuit.

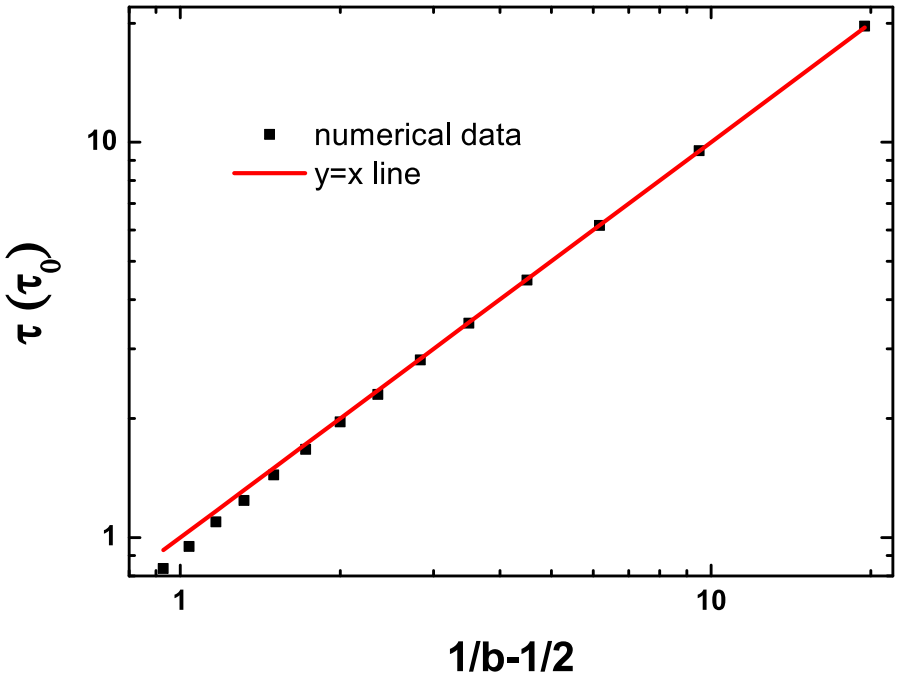

Figure 1.12: Escape time, given by the characteristic time of the exponential decay in the average current, versus $1/b-1/2$ (corresponding to the expression of the escape time given in Eq.1.49), in the heuristic model. The red line has a unit slope.

The escape time is given by the characteristic decay time of the current, and we find a good agreement with the formula similar to Eq.1.49: $\tau = \tau_0(1/b - 1/2)$, see Fig.1.12. The agreement with the previous formula is not quite as good for large probabilities b, where the escape time becomes comparable and smaller than the time unit τ_0. This is not surprising, since we expect singularities for escape times smaller than the time unit: the current then cannot be treated as a continuous variable anymore.

The average transfered charge per half-period is fairly easy to compute: $\mathcal{Q}^t = e \times \tanh(1/4f_0\tau)$. As expected, it becomes quantized for short escape times. This expression can be compared with the

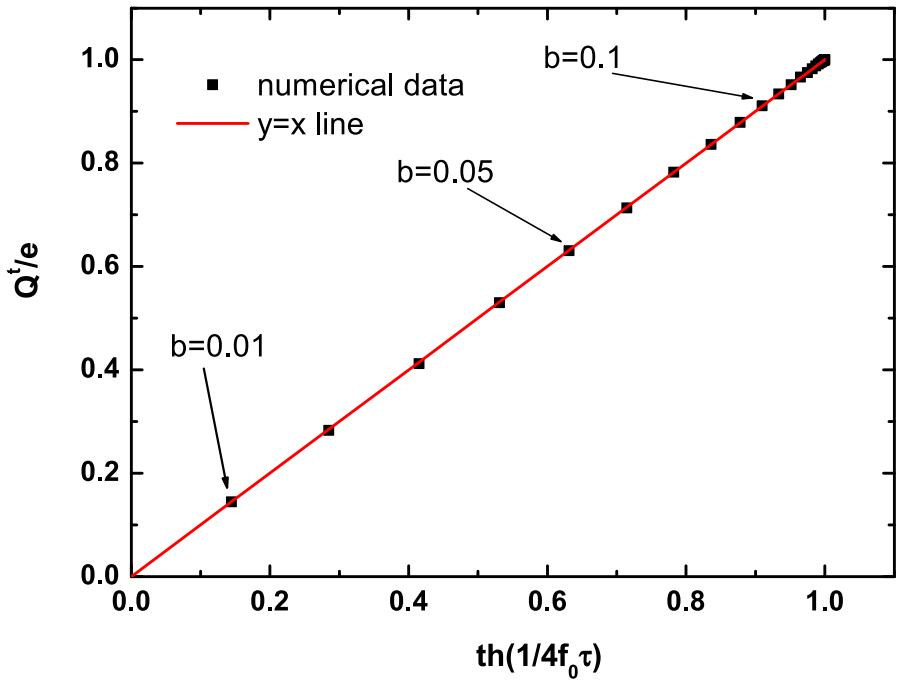

Figure 1.13: Average transfered charge per half-period versus $\tanh(1/4f_0\tau)$, in the heuristic model. The red line has a unit slope, thus verifying Eq.1.50.

average transfered charge $\mathcal{Q}^t$ in a RC circuit driven by a square voltage with an amplitude V_{exc}:

$$\mathcal{Q}^t = 2V_{exc}C\tanh(\frac{1}{4f_0\tau}) \tag{1.50}$$

In Fig.1.13, we have plotted the average transfered charge per half-period in the model, given by the integral of the average AC current on one half-period, as a function of $\tanh(\frac{1}{4f_0\tau})$, where the drive frequency is equal to $(2N\tau_0)^{-1}$, and the escape time τ is extracted from the exponential decay. All the calculated points fall on the line given by Eq.1.50. This allows us to define the capacitance of the circuit, given by the slope of the line: $C = e/2V_{exc} = e^2/\Delta$. This capacitance is constant, which confirms the result presented for the scattering model.

In conclusion, the heuristic model supports the description of the sample in terms of RC-circuit elements, since it reproduces the exponential decays in the average current, as well as the variation of the average transfered charge with the escape time. Furthermore, it exactly reproduces the results of the scattering model for $2eV_{exc} = \Delta$, particularly the escape time, provided one makes the following links between the two models:

$$\begin{aligned} \tau_0 &= \frac{h}{\Delta} \\ b &= D \end{aligned} \tag{1.51}$$

These relations are rather intuitive: the time unit τ_0 has the exact same definition in the two models (see 1.1.2), and the escape probability b is the semi-classical equivalent of the square of the tunneling amplitude, that is the QPC transmission D.

This model will be extremely useful in the next chapter, where we study the fluctuations of the emitted current.

1.4.3 Experimental results

We now describe the experimental results obtained in the non-linear regime. We first briefly present time-domain measurements performed on a different sample by Gwendal Fève and Adrien Mahé [11, 68], and described in [71]. We then present measurements of the first harmonic of the average current emitted for sample *S528-11*, which confirms the theoretical results described in the previous section, particularly the quantization of AC current in the injection regime.

1.4.3.1 Time domain

In this paragraph, we briefly describe the time-domain measurements performed by Gwendal Fève and Adrien Mahé on sample $E3$ (see samples parameters in appendix B). In order to measure the average AC current as a function of time, the excitation frequency is set to $32MHz$. The current is recorded and averaged in real time using a *Acqiris AP240* fast acquisition card with a $500ps$ time resolution. Although this resolution is too small to probe the coherent wave packets emitted by the source, this measurement corroborates the description of the sample in terms of RC-circuit elements.

Details on the measurement protocol are given in [71]. The excitation drive is used to trigger the acquisition of the signal, which is averaged over a large number (typically 10^8) of periods. We use the parasitic signal, modeled as a pure capacitive coupling, to deconvolute the effects of the finite bandwidth on the measurements.

Results are presented in Fig.1.14, and demonstrate the expected exponential decay of the current as a function of time. The decay time gives access to the escape time which is modulated by changes in the QPC transmission over an order of magnitude. These results also demonstrate that the RC-circuit description of the sample is still valid in regimes where $\Omega\tau \approx 1$. Furthermore, while the amplitude of the traces depicted in Fig.1.14b and c differ because the QPC transmission varies from almost zero (b) to almost one (c), we have shown in [71] that the integral of the current over one half-period, that is the average transfered charge, remains constant as long as the escape time τ is significantly smaller than the period $2\pi/\Omega \approx 30ns$, which is compatible with the periodic emission of single charges.

Although we did not reproduce these measurements for sample *S528-11*, the measurements performed on sample $E3$ both validate the RC-circuit description of the system even in regimes where the escape time is comparable with the drive period, and demonstrate the quantization of the emitted charge when all harmonics of the average current are considered. A more quantitative indication of single charge emission is given by the measurements of the first harmonic presented below.

1.4.3.2 First harmonic

We now present measurements of the first harmonic of the average AC current in the non-linear regime obtained on sample *S528-11*. We used the homodyne measurement technique presented in 1.2.

- **Global phase tuning**

As mentioned in 1.2 and 1.3.2.1, the homodyne detection measures the two quadratures of the first harmonic of the average current, rotated by a phase due to the propagation of the signal in the measurement lines.

A first method for tuning the global phase in the linear regime is presented in 1.3.2.1; we have mentioned that the properties of the non-linear regime offer a more efficient protocol that was used for sample *S528-11*. Indeed, in the injection regime, the sample can be described as the series association

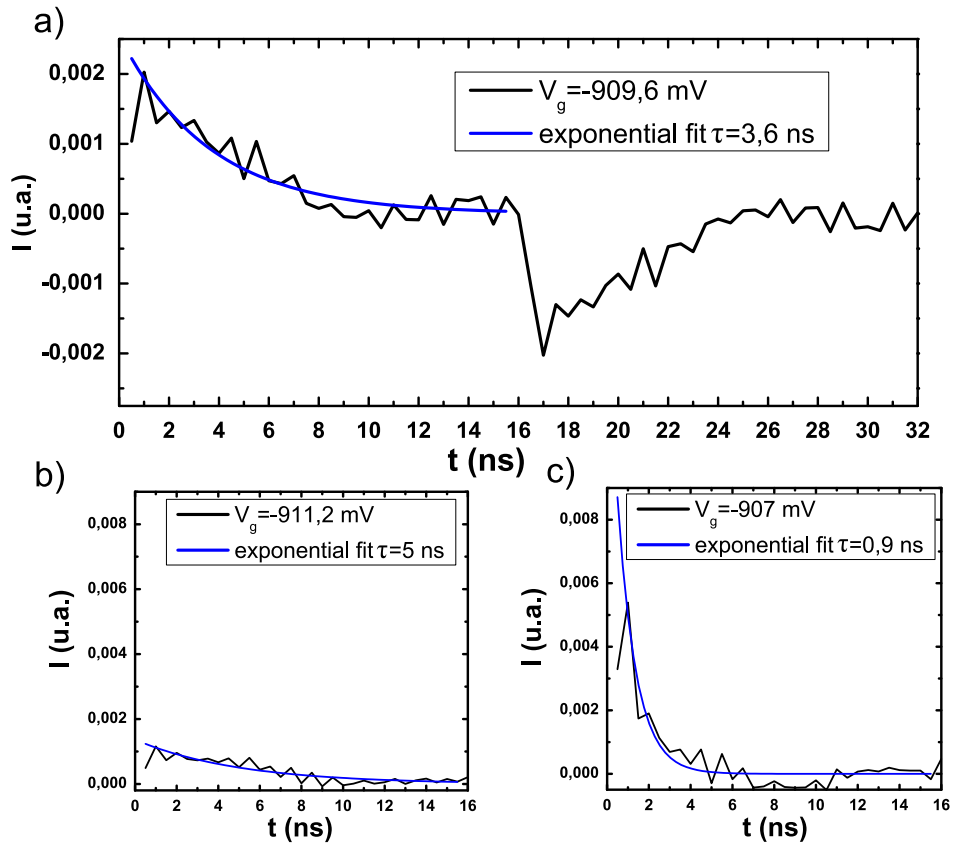

Figure 1.14: Measured average AC current as a function of time, for sample *E3*. Black lines correspond to experimental data measured at several values of the QPC gate voltage. Blue lines correspond to exponential fits.

of a constant capacitance $C = e^2/\Delta$ and a resistance which varies between $h/2e^2$ and infinity. The Nyquist diagram of the current as the transmission varies is therefore given by a circle with a radius ef_0 centered on $(0, ef_0)$. In order to tune the global phase, we first determine the injection voltage $V_{exc} = \Delta/2e$, for which the capacitance oscillations presented in 1.3.2.2 vanish: when the driving amplitude exactly compensates the level spacing, the current becomes independent of the transmission and the dot equilibrium potential, *i.e.* independent of the QPC gate voltage V_g. We then plot the Nyquist diagram of the current and try to align it with the circle defined above.

The results of the phase tuning at 1.5 GHz are shown in Fig.1.15. Since the level spacing varies slightly as V_g changes, the excitation amplitude V_{exc} does not exactly compensate the level spacing for all values of the QPC gate voltage. It is therefore difficult to perfectly align the measured signal on the circle: the blue curve in Fig.1.15 seems better for high transmissions (upper part of the circle), whereas the black curve suits the low transmissions better. It however presents a negative real part, which is not compatible with the RC-circuit model. We therefore use the phase tuning of the black curve (upper panel). The error on the phase tuning is estimated to $\pm 2°$, which corresponds to an error on the escape time of about $5ps$ for large transmissions.

- **AC current quantization**

We have plotted the modulus of the first harmonic of the current as a function of the QPC gate voltage for several values of the excitation amplitude in Fig.1.16. When $2eV_{exc} \approx \Delta$, the current is zero for large negative V_g be cause the escape time is much larger than the half-period (pinch-off). As V_g increases,

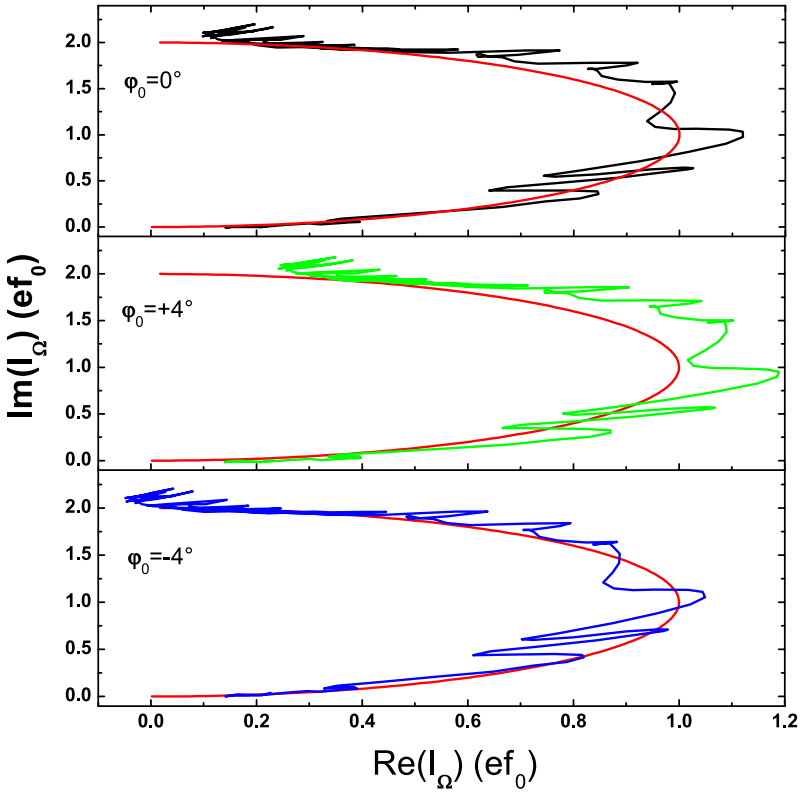

Figure 1.15: Nyquist diagram of the measured current at 1.5 GHz, for $2eV_{exc} = \Delta$. Since the capacitance of the sample is constant and equal to e^2/Δ while the resistance varies, the Nyquist diagram of the current is given by a circle centered on $(0, ef_0)$ (black line). We present three different phase tunings, separated by 4°.

the current rises, the becomes independent of V_g for large enough transmissions. It slightly increases and presents small oscillations for small negative gate voltages because the level spacing diminishes at high transmissions. This can be qualitatively understood by the fact that the shape of the dot changes with the QPC gate voltage: when the electrostatic repulsion due to the QPC gates diminishes, the dot widens and the level spacing due to orbital confinement becomes smaller. This effect, which was not observed in former samples, may be due to the fact that the dot in sample *S528-11* is rather small, its width ($600nm$) being comparable to the distance between the two QPC gates (approx. $350nm$).

The oscillations observed at lower excitation voltages appear again for excitation voltages larger than the injection voltage, with a π-phase shift. The peaks of the oscillations at lower excitation, which become dips at larger excitation, correspond to the anti-resonant case, noted $\phi_0 = 0$, where the active energy level is shifted far away ($\pm\Delta/2$) from the Fermi energy. In this injection regime, we expect the current to be quantized, which is illustrated in the measurements by the fact that the value of the current in the peaks for $V_{exc} < \Delta/2e$ and in the dips for $V_{exc} > \Delta/2e$ is quite close to the one obtained when $V_{exc} = \Delta/2e$. This qualitative agreement with the theory allows us to calibrate the measured current, and set the value of the current for $V_{exc} = \Delta/2e$ to $2ef_0$. These measurements have however put into light another discrepancy of sample *S528-11* with the model: indeed, we were not able to adjust the current in the non-linear regime with the QPC transmission law extracted from the linear regime. This variation of the transmission with the excitation amplitude may also be related to the size of the dot: this effect was not observed in sample E3, which had a level spacing of about 2.5 K (dot width: $1\mu m$). The energy shifts considered in sample *S528-11* are therefore almost two times

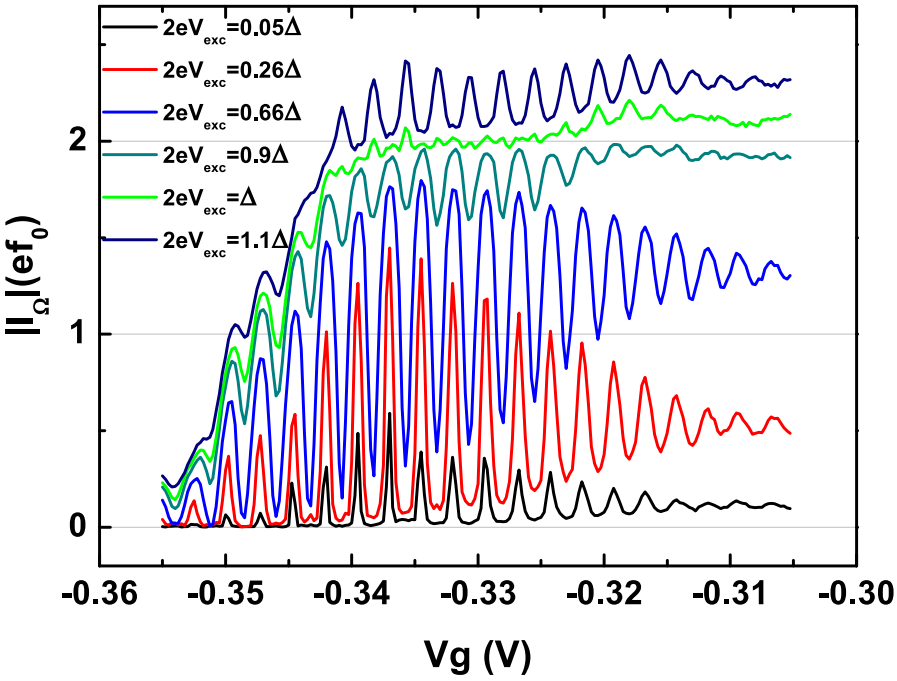

Figure 1.16: Modulus of the first harmonic of the average AC current as a function of V_g, for several values of V_{exc}. The conductance oscillations vanish when $2eV_{exc} = \Delta$.

larger, and thus become significantly larger than the usual energy scales considered for quantum point contacts.

A more quantitative comparison between experimental data and theory can be made when considering the variation of the first harmonic as a function of V_{exc} for a fixed QPC gate voltage. The results, presented in Fig.1.17, display the characteristic quantization plateaus described in 1.4.1.2. The plateaus are, as expected, less pronounced when the transmission increases, while all the curves corresponding to different values of the dot equilibrium potential join at the quantized value $2ef_0$ when the excitation amplitude compensates the level spacing. The value of the current, given by the theory, is in reasonable agreement (within $\sim 10\%$, see dotted line Fig.1.17) with an independent calibration of the gain of the homodyne detection (described in [68]). Due to the variation of the transmission with the excitation voltage, we cannot adjust the experimental data using a simple transmission law: the transmission varies from 0.27 in the linear regime to 0.47 in the injection regime for the first set of data, and from 0.75 to 0.9 in the second set. The agreement between the experimental data and a theory using a fixed transmission (0.47 for the first set, 0.8 for the second) is still reasonable, thus demonstrating that beyond its discrepancies with an ideal quantum point contact model, sample *S528-11* verifies the theoretical predictions for both the linear and non-linear regimes, particularly the quantization of AC current in units of $2ef_0$, corresponding to the periodic emission of a single electron followed by a single hole.

The properties of the modulus of the first harmonic can be summarized in a two-dimensional plot of the current versus the excitation amplitude V_{exc} and the QPC gate voltage V_g, presented in Fig.1.18: both experimental and theoretical data present white diamond-like structures, which correspond to the plateaus where the current is quantized and equal to $2ef_0$. The sharpness of diamonds is related to the accuracy of the quantization; this representation therefore allows to immediately locate the optimal operating conditions of the single electron source, which are given by the center of the sharpest diamonds. In these conditions, the source emits single charges at a well defined energy far above the

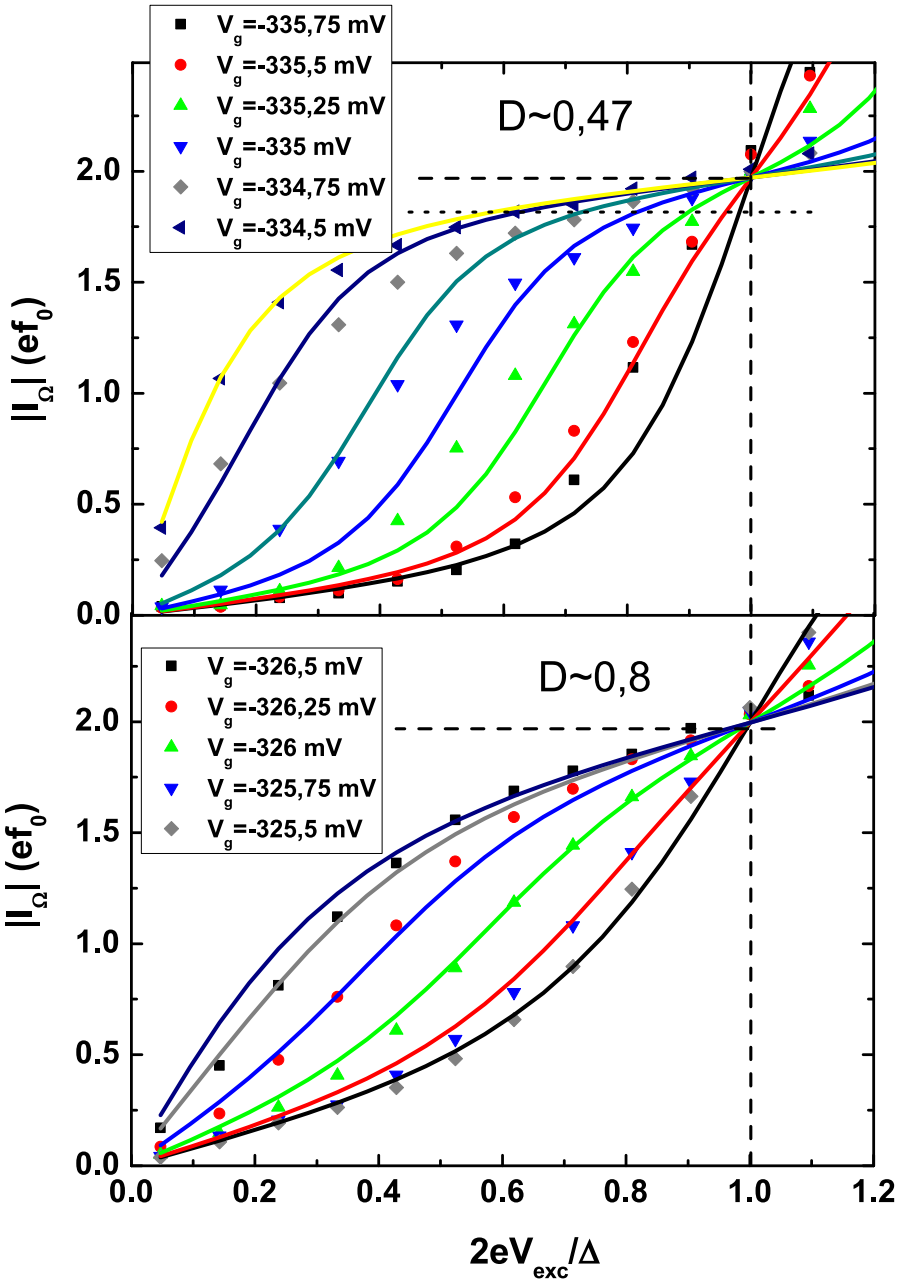

Figure 1.17: Observation of AC current quantization for sample *S528-11*. The dots correspond to the experimental data, for different values of V_g; the lines correspond to the calculations using the scattering model, for a fixed transmission 0.47 in the upper panel, and 0.8 in the lower panel. The curves join at the value $2ef_0$ when $2eV_{exc} = \Delta$. The dotted line in the upper panel corresponds to the value of the current given by an independent calibration of the homodyne detection.

Fermi level. As the transmission increases, the quantization is gradually lost and the diamonds fade into a linear dependence of the current with the driving amplitude. The qualitative agreement between theory and experiment once again demonstrates that the scattering model is well-suited to describe the sample, and seems to be mainly limited by the behavior of the quantum point contact as a function

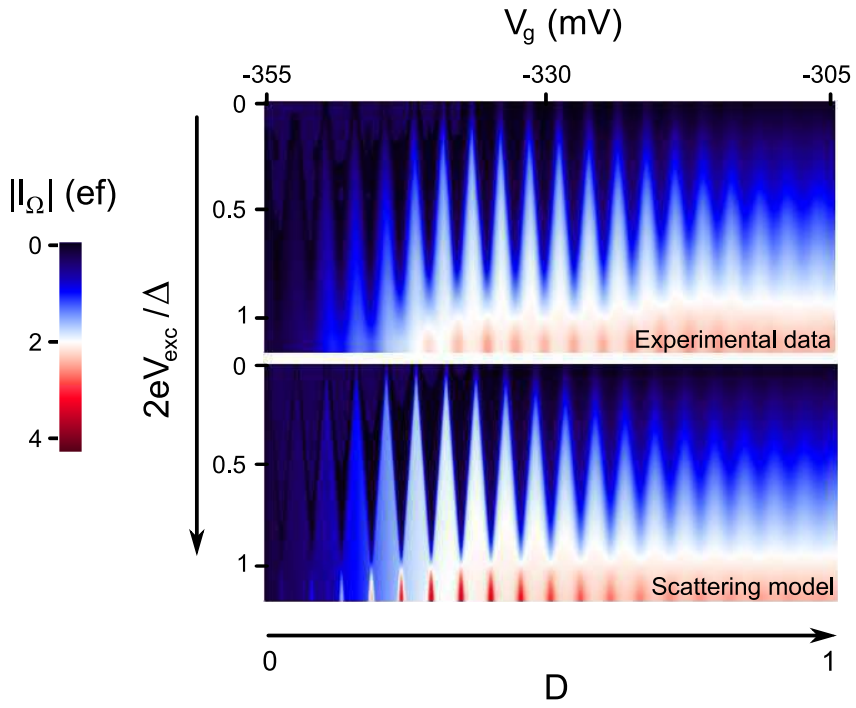

Figure 1.18: Two-dimensional plot of the first harmonic, as a function of V_g and V_{exc}. The upper panel corresponds to experimental data, the lower panel corresponds to calculations using a QPC transmission law extracted from the non-linear regime: $\Delta V = 4.5$ mV, $V_{g0} = -334.5$ mV. Both panels present white diamonds on which the current is quantized in units of $2ef_0$.

of the extrinsic parameters of the system. We will show in the following paragraph that the exact transmission variation law can be rather simply extracted from the measurements, at least in the non-linear regime.

- **Escape time and average transfered charge**

The escape time, given by $R_q^{nl}C_q^{nl}$, can be extracted from the measurements by calculating the ratio between the real and imaginary part of the first harmonic. This ratio is equal to $\Omega\tau$, and therefore yields the escape time in units of the half-period when divided by π. Besides the obvious interest of studying its variation with the QPC transmission, the escape time is useful to extract the average transfered charge over one half-period which we define with the RC-circuit model. When combining Eq.1.50 with the expression of the conductance in the non-linear regime given in Eq.1.47, it yields:

$$\begin{aligned} \mathcal{Q}^t &= 2V_{exc}C\tanh\left(\frac{1}{4f_0\tau}\right) \\ &= \frac{\pi}{\Omega}|I_\Omega|\sqrt{1+\Omega^2\tau^2}\tanh\left(\frac{2\pi}{4\Omega\tau}\right) \end{aligned} \tag{1.52}$$

The knowledge of the two quadratures of the first harmonic of the current therefore allows us to determine both the escape time and the average transfered charge.

We have plotted the escape time and the average transfered charge extracted from the measurements on sample *S528-11* at 1.5 GHz in Fig.1.19 ($2eV_{exc} = \Delta$). The theoretical adjustment of the escape time was done using the definition of τ given in Eq.1.49, combined with the ideal QPC transmission law used

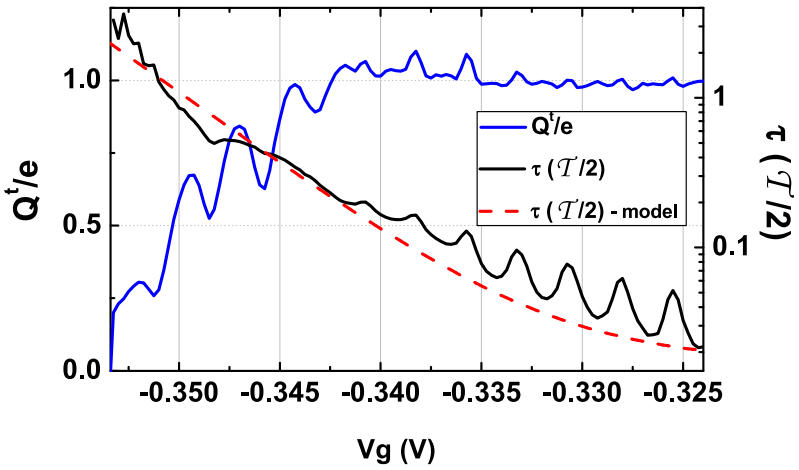

Figure 1.19: Escape time and average transfered charge as a function of V_g, for $2eV_{exc} = \Delta$. The red dashed line corresponds to simulations using the ideal non-linear QPC transmission law. Discrepancies appear at smaller negative voltages, where the ideal transmission law does not exactly reproduce the experimental data.

to calculate the current measurement in the non-linear regime (QPC opening width $\Delta V = 4.5$ mV, half-transmission voltage $V_{g0} = -334.5$ mV). The agreement is once again reasonable; in order to completely reproduce the measurements as a function of V_g, one needs to precisely know the QPC transmission law, which significantly differs from the ideal Fermi function-like law for strong driving amplitudes. It is possible to extract the exact QPC transmission law from the escape time by reverting Eq.1.49. We will use this transmission law to adjust the noise measurements presented in the next chapter.

The optimal operating conditions of the source, defined by the sharpest diamonds in Fig.1.18, correspond to the zone in Fig.1.19 where the average transfered charge becomes equal to e while the escape time varies between $\sim 0.5\ \mathcal{T}/3$ and $\sim 0.5\ \mathcal{T}/10$, where $\mathcal{T}$ is the period of the excitation.

1.5 Validity of the model

In this last section of chapter 1, we discuss the validity of the scattering model in the light of our experimental results. The main issue discussed here is the description of the density of states in the dot, related to the trajectories of electrons visiting the dot. In our model, we have supposed that electrons visiting the dot propagate on a closed trajectory given by the edges of the dot. This gives rise to an orbital level spacing defined in Eq.1.17: $\Delta = \frac{h}{\tau_0}$, where τ_0 is the time needed by an electron to perform a full turn in the dot. We neglect the effect of the interactions; however, in the model previously expanded by Gwendal Fève [11], the effects of interactions in the dot are taken into account by adding to the level spacing a charging energy contribution E_c, which was found to be small compared to the orbital level spacing. Indeed, the samples are engineered in order to maximize the geometrical capacitance: the dot is almost entirely covered by the top gate, as described in the introduction. Several theoretical models have been proposed [75, 76, 72] in order to include the effects of interactions in the linear regime, but a model fully including interactions in the non-linear regime has yet to be developed.

The hypothesis of a quantum dot presenting a large orbital level spacing and a charging energy smaller or comparable is validated in a rather naive way by calculating an approximation of the orbital

level spacing from the sample geometry: for a circular dot with a diameter $d = 1$ μm, and a typical value of drift velocity in III-V two-dimensional electron gases $v_d \approx 2 \times 10^5$ ms^{-1}, we find an orbital level spacing $\Delta = \frac{h}{\tau_0} = \frac{hv_d}{\pi d} \approx 3$ K. This value is quite comparable with the measured level spacings: 2 K for sample *E3*, 4.2 K for sample *S528-11*. The charging energy can be estimated through the geometrical capacitance $C_g = \epsilon_0 \epsilon_r S/d$, where S is the surface of the dot, d the distance between the dot and the top gate, and $\epsilon_r \approx 12.8$ is the relative permittivity of $GaAs$. For the typical circular dot mentioned above, with $d = 100$ nm, we have $C_g \approx 0.9$ fF, that is $E_c \approx 2$ K.

A more quantitative justification of our hypothesis consists in comparing the variation of the escape time as a function of the excitation amplitude between our model and its opposite where the quantum dot has a uniform density of states and a large charging energy E_c. It was shown [77] in this type of metallic-like quantum dots that the tunneling rate from the dot to the leads is proportional to $(\Delta E/E_c)/(1 - e^{-\frac{\Delta E}{k_B T}})$, where ΔE is the difference between the electrochemical potential of the leads and the electrochemical potential of the dot. At low temperature ($T \ll \Delta E, E_c$), this relation is essentially linear, which implies that the escape time varies as the inverse of the excitation voltage. Fig.1.20 shows the variation of the escape time as a function of V_{exc}, extracted from the results presented in Fig.1.18, for both the model and the experiment. As it turns out, the variation of the escape time depends greatly on the dot equilibrium potential: in the anti-resonant case ($\phi_0 = 0$), the escape time slowly decreases with V_{exc}, whereas in the resonant case ($\phi_0 = \pi$), the escape time is small at low excitation[1], then suddenly rises above the value at $\phi_0 = 0$ when V_{exc} reaches $\Delta/2e$, and slowly decreases for larger excitations. This behavior is well reproduced by the scattering model for $\phi_0 = 0$; however, the increase of the escape time at $\phi_0 = \pi$ above its value at $\phi_0 = 0$ can only be reproduced with the scattering model by assuming a variation of the transmission with ϕ_0. This discrepancy is directly related to the oscillations in the escape time shown in Fig.1.19. Nevertheless, it is not possible to reasonably adjust any of the curves with the metallic case formula: an approximative fit of the experimental data (green dashed line) yields an electronic temperature $T_{el} = 2.6$ K comparable to the level spacing, which is not compatible with the temperature deduced from the calibration $T_{el} \approx 70$ mK. The experimental data can only be adjusted by increasing the temperature so as to make the density of states uniform, thus proving the incompatibility of the metallic-like quantum dot description for our samples.

These two considerations show that the experimental data are well reproduced by a model where interactions are neglected: since we expect the charging energy to be comparable or smaller than the orbital level spacing, it is reasonable to describe our results using the level spacing Δ, where the interactions only renormalize its value.

The other discrepancies with the proposed model are mostly sample dependent; the most cumbersome, such as extremely irregular density of states or double quantum dot structures may be ruled out by careful sample post-selection. In samples presenting smaller orbital level spacings, the charging energy cannot be neglected, as it was the case for sample *E3* studied by Gwendal Fève. The description of the dot as an effective two-level system in the presence of interactions [11] allows to take into account the observed deviations.

[1] The standard deviation of the measurements are however rather large for these values of the excitation amplitude, because both real and imaginary part of the first harmonic are almost zero.

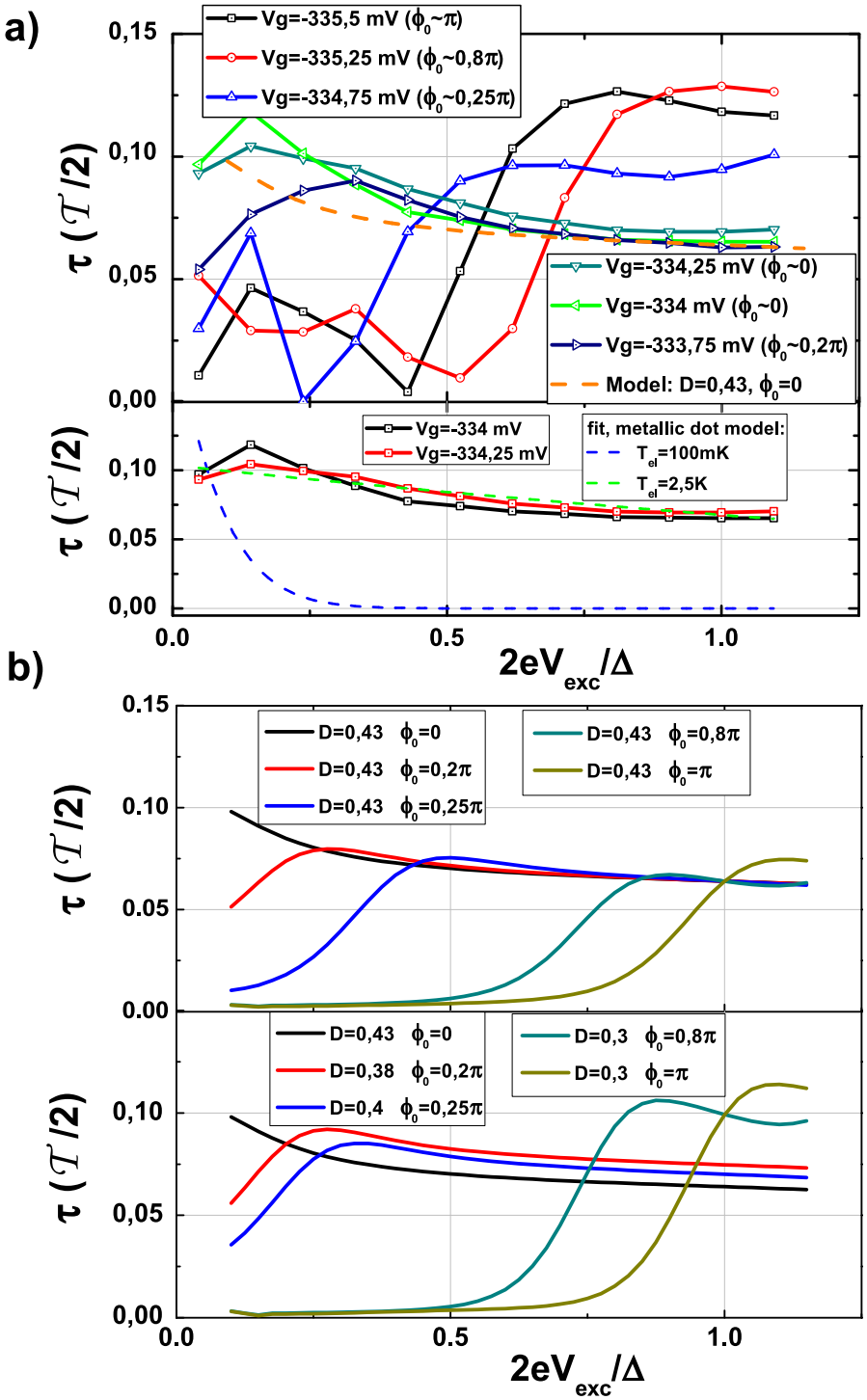

Figure 1.20: Escape time as a function of V_{exc}. **a)** Experimental data, measured for several values of V_g. The dashed line in the upper panel is the calculated value of the escape time for the estimated transmission $D = 0.43$ at $\phi_0 = 0$. Lower panel: fits (dashed lines) of the experimental data (hollow dots) at $\phi_0 = 0$ with the metallic dot formula. The green dashed line yields an electronic temperature equal to $2.6K$. For the blue dashed line, the temperature is fixed at 100 mK. **b)** Numerical calculations of the scattering model. Upper panel: the transmission is fixed at 0.43. Lower panel: the transmission is estimated using the value of the escape time at $2eV_{exc} = \Delta$.

Conclusion of chapter 1

In this chapter, we have described the basic properties of the average AC current emitted by a mesoscopic capacitor. We have first provided a theoretical description of the mesoscopic capacitor using a scattering formalism based on a Floquet scattering matrix. This approach differs from the one developed by my predecessors, and allows the consideration of systems presenting several time-dependent potentials, such as as two-electron interferometry in the Hong-Ou-Mandel geometry using two distinct single electron emitters.

The presented experimental results obtained on sample *S528-11* are in very good agreement with the model, and allow to extract all the parameters describing the energy spectrum of the dot. Furthermore, the results put into light the quantization of the first harmonic of the average AC current in units of $2ef_0$, corresponding to the periodic emission of a single electron followed by a single hole. In addition to providing a full characterization process for our samples, the study of the average AC current demonstrates that the mesoscopic capacitor in the non-linear regime can be used as a single electron source, therefore paving the way to single-charge electron quantum optics.

Chapter 2

Current fluctuations emitted by the source

2.1 Current correlations under periodic driving 54
2.2 Scattering model 55
2.2.1 Current operators 55
2.2.2 Calculation of the current autocorrelation 56
2.2.3 Numerical calculations 59
2.3 Heuristic model 64
2.3.1 Computation of the noise 64
2.3.2 Comparison with the scattering model 67
2.4 Experimental setup 70
2.4.1 Sample design 70
2.4.2 Setup 73
2.5 Experimental results 73
2.5.1 Noise versus QPC gate voltage 75
2.5.2 Universal graphs 76
2.5.3 Noise oscillations and QPC transmission law 77

Introduction of chapter 2

The study of the average AC current presented in the previous chapter demonstrates the quantization of AC current in units of $2ef_0$, corresponding to the periodic emission of a single electron followed by a single hole. The mesoscopic capacitor therefore acts on average, when driven in the non-linear regime, as a single electron emitter, thus enabling single charge electron quantum optics experiments.

Similarly to single photon sources used in quantum optics, it is then necessary to study the current fluctuations emitted by the source. This serves several purposes; the most obvious one is the characterization of the accuracy of single particle emission, in order to rule out any other charge transfer process generating an average current equal to $2ef_0$. Indeed, one might naively consider a situation where two electrons are emitted during one period, and none during the next period, which would still correspond on average to the emission of one electron at each period. The generation of additional electron-hole pairs within one half-period of the drive, would also yield the same average transfered charge per half-period, and thus cannot be detected by average current measurements. They are however natural excitations of a Fermi sea, and would as well diminish the accuracy of single particle injection, thus jeopardizing the realization of electron quantum optics experiments. In this respect, going beyond average quantities and studying the correlation of the current fluctuations introduces conceptual tools which, in analogy with intensity correlation measurements commonly performed in quantum optics, are the dedicated tools for probing the outcome of single charge electron quantum optics experiments. It is therefore natural to develop these tools on the basic building block of single-charge electron quantum optics, that is the single electron emitter. Finally, such a study has a fundamental interest in the field of quantum noise, for it unveils the crossover between shot noise (or charge noise), where the number of emitted charges per half-period is fluctuating, and a regime of phase noise, where a single charge is systematically emitted at each half-period, while a finite noise arises because of the quantum uncertainty on the emission time.

In this chapter, we focus on the direct autocorrelation of the current fluctuations generated by the source, without partition on a beam splitter. This is somewhat different from quantum optics, where intensity correlations are usually measured in a Hanbury-Brown and Twiss configuration. Indeed, while cross-correlation and autocorrelation probe the same physical processes in quantum optics (mainly, photon antibunching at zero time interval for ideal single photon sources [60, 61]), the implementation of the latter is more challenging because one has to overcome the finite temporal resolution of photon detectors [78]. In our case, the autocorrelations are on the contrary more easily implemented, because they do not require the additional Quantum Point Contact used as the beam splitter in the HBT configuration mentioned in the introduction. Furthermore, we will show in the next chapter that the understanding of the direct autocorrelations is crucial for the complete analysis of the results of the HBT experiment.

Conservation of the average charge on the dot implies that a hole is always eventually emitted after an electron is emitted. The current generated by the source has therefore no zero-frequency part: we study the noise of the single electron emitter at frequencies around the driving frequency $f_0 = 1.5$ GHz. We first discuss general considerations on high frequency noise generated by a periodic excitation. We then present two theoretical descriptions of the noise, in continuity with the scattering and heuristic models presented in the previous chapter; we finally compare the results yielded by the two models with noise measurements performed on sample *S528-11*, using the high sensitivity microwave noise measurement setup described in chapter 4. These results demonstrate that in ideal operating conditions, the noise reduces to a fundamental noise regime, called *quantum jitter*, which is the signature of periodic single charge emission. In this regime, a single charge is systematically emitted at each half-period and charge noise is suppressed. The residual noise arises from quantum fluctuations in the emission time, leading to a jittering of the emitted current. The measurement of

the reduction of the noise to the quantum jitter is the single-charge electron quantum optics analog of the absence of photon bunching at zero time interval for ideal single photon sources.

2.1 Current correlations under periodic driving

The fluctuations of a stationary current around its mean value are usually determined by its successive moments. The second moment particularly describes the power of the fluctuations: $\Delta I^2 =< (I- < I >)^2 >$. Gaussian fluctuations are entirely described by the second moment; in the case of non-Gaussian fluctuations however, the study of higher moments is relevant, experimentally as well as theoretically. We will first consider the case of classical currents, focusing on the second moment of the fluctuations, which is related to the autocorrelation of the current fluctuations $C(t,t')$:

$$C(t,t') =< \delta I(t)\delta I(t+t') > \tag{2.1}$$

In the case of a stationary current, $C(t,t')$ depends only on the time difference t', and is therefore equal to $< \delta I(0)\delta I(t') >$. We can then focus on the spectrum of these fluctuations, defined by the power spectral density which is equal to the Fourier transform of the autocorrelation:

$$S(\omega) = 2\int dt' < \delta I(0)\delta I(t') > e^{i\omega t'} \tag{2.2}$$

The factor 2 allows us to restrict on positive values of the frequency ω.

In our case, the current is generated by a single electron emitter driven at a finite frequency Ω, and is therefore non-stationary. $C(t,t')$ depends then on both times t and t'; for a fixed t', $C(t,t')$ is furthermore $\mathcal{T} = 2\pi/\Omega$-periodic, and can be decomposed as a Fourier series [79, 80]:

$$C(t,t') = \sum_l \mathcal{P}_l(t')e^{il\Omega t} \tag{2.3}$$

The second moment is therefore time-dependent and presents harmonics at multiples of the driving frequency Ω. In analogy with the fluctuations of a stationary signal, we focus on the mean value of the power of the fluctuations, that is the mean value of the second moment, given by the term $l = 0$. We therefore define the mean power spectral density for a non-stationary current:

$$S(\omega) = 2\int dt' \overline{< \delta I(t)\delta I(t+t') >}^t e^{i\omega t'} = 2\mathcal{P}_0(\omega) \tag{2.4}$$

where $\overline{\dots}^t$ defines the average over time t and $\mathcal{P}_l(\omega')$ is the Fourier transform of $\mathcal{P}_l(t')$. We can now generalize Eq.2.4 for a quantum system by replacing the statistical average $< ... >$ by the quantum average of the current operators defined in 1.1.4.

- **Emission and absorption noise**

We have defined above the power spectral density of current fluctuations for positive frequencies. Since $S(\omega)$ is symmetric for classical currents, the above definition does not imply any loss of generality. It is however not the case for quantum signals, because the current operators $\hat{I}(t)$ and $\hat{I}(t+t')$ do not usually commute. We therefore need to separately consider negative and positive values of ω. We define the emission noise power spectral density $S_+(\omega)$ for positive frequencies[2]:

$$S_+(\omega) = 2\int dt' \overline{< \delta\hat{I}(t)\delta\hat{I}(t+t') >}^t e^{i\omega t'} \tag{2.5}$$

The absorption noise power spectral density $S_-(\omega)$, for positive frequencies as well, is then given by:

[2] This convention is the opposite of the one used in [81, 82], where the emission noise is defined for negative frequencies.

$$\begin{aligned} S_-(\omega) &= 2\int dt' \overline{< \delta\hat{I}(t+t')\delta\hat{I}(t) >}^t e^{i\omega t'} \\ &= 2\int dt' \overline{< \delta\hat{I}(t)\delta\hat{I}(t+t') >}^t e^{-i\omega t'} \\ &= S_+(-\omega) \end{aligned} \tag{2.6}$$

These two power spectral densities are usually discriminated using a quantum spectrum analyzer [82], such as Josephson junctions [83, 84, 85]. We show however in appendix A.4 that because of both the geometry of the sample and the measurement process described in 1.2.3, where the current at the pinch-off is subtracted in order to isolate the signal of the source, the emission and absorption noise are equal in our experiment. In the following sections, we shall therefore use the quantum equivalent of Eq.2.4 without discriminating emission and absorption processes.

2.2 Scattering model

2.2.1 Current operators

In this section, we derive an expression for the power spectral density of the current fluctuations emitted by the source in the three-terminal geometry, using the expressions of the current operators defined in 1.1.4. For this purpose, we recall the notations for the current operators in Fig.2.1: $\hat{I}_b(t)$ flows form the dot to contact (1), and $\hat{I}_c(t)$ flows from contact (1) to contact (2). The measured current $\hat{I}_1(t)$ is therefore equal to $\hat{I}_1(t) = \hat{I}_b(t) - \hat{I}_c(t)$.

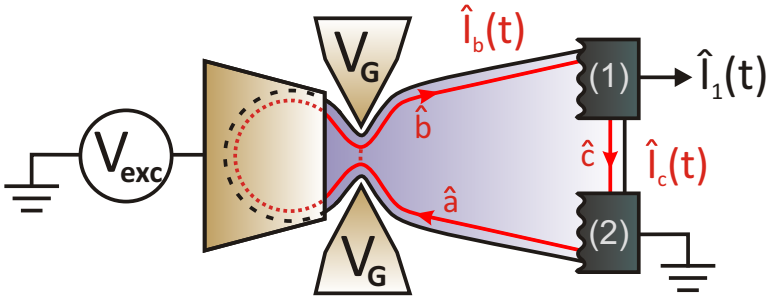

Figure 2.1: Definition of the current operators.

Let us first focus on the correlation of the measured current $< \hat{I}_1(t)\hat{I}_1(t+t') >$. For more clarity, we write $\hat{I}_{(1,b,c)}(t) = \hat{I}_{(1,b,c)}$ and $\hat{I}_{(1,b,c)}(t+t') = \hat{I}'_{(1,b,c)}$. With this notation, $< \hat{I}_1(t)\hat{I}_1(t+t') >$ becomes:

$$\begin{aligned} < \hat{I}_1\hat{I}'_1 > &= < \hat{I}_b\hat{I}'_b - \hat{I}_b\hat{I}'_c - \hat{I}_c\hat{I}'_b + \hat{I}_c\hat{I}'_c > \\ &= < \hat{I}_b\hat{I}'_b > - < \hat{I}_b\hat{I}'_c > - < \hat{I}_c\hat{I}'_b > + < \hat{I}_c\hat{I}'_c > \end{aligned} \tag{2.7}$$

Following the expressions of $\hat{I}_b$ and $\hat{I}_c$ given in Eq.1.23 and 1.24, the terms $< \hat{I}_b\hat{I}'_c >$ and $< \hat{I}_c\hat{I}'_b >$ contain combinations of the creation/annihilation operators $\hat{b}^\dagger, \hat{b}, \hat{c}^\dagger, \hat{c}$. Because $\hat{b}^\dagger, \hat{b}$ and $\hat{c}^\dagger, \hat{c}$ are independent, the cross terms $< \hat{b}^\dagger\hat{c} >$ (and any other combination of both $\hat{b}$ and $\hat{c}$) vanish, leaving only the two direct terms $< \hat{b}^\dagger\hat{b} >$ and $< \hat{c}^\dagger\hat{c} >$. The cross-correlation of currents $\hat{I}_b$ and $\hat{I}_c$ does not

take part in the noise, since:

$$\begin{aligned} < \hat{I}_b \hat{I}'_c > &= < \hat{I}_b >< \hat{I}'_c > \\ < \hat{I}_c \hat{I}'_b > &= < \hat{I}_c >< \hat{I}'_b > \end{aligned} \tag{2.8}$$

As a result, only $< \hat{I}_b \hat{I}'_b >$ and $< \hat{I}_c \hat{I}'_c >$ contribute to the correlation of the fluctuations $< \delta\hat{I}_1 \delta\hat{I}'_1 >$. Furthermore, the term $< \hat{I}_c \hat{I}'_c >$, which gives rise to the thermal noise of the edge channel flowing from contact (1) to contact (2), is independent of the QPC transmission D, and therefore vanishes when the reference is subtracted. We thus only measure the autocorrelation of the fluctuations of $\hat{I}_b$, which are given by the cross terms in $< \hat{I}_b \hat{I}'_b >$.

2.2.2 Calculation of the current autocorrelation

Keeping only the contribution of current $\hat{I}_b$, the power spectral density of the current fluctuations emitted by the source is given, following Eq.2.4, by:

$$\begin{aligned} S(\omega) &= 2\int dt' \overline{< \delta\hat{I}_b(t)\delta\hat{I}_b(t+t') >}^t e^{i\omega t'} \\ &= 2\int dt' \overline{(< \hat{I}_b(t)\hat{I}_b(t+t') > - < \hat{I}_b(t) >< \hat{I}_b(t+t') >)}^t e^{i\omega t'} \end{aligned} \tag{2.9}$$

Let us expand the first term of this equation, using Eq.1.23:

$$2\int dt' \overline{< \hat{I}_b(t)\hat{I}_b(t+t') >}^t e^{i\omega t'} = 2\frac{e^2}{h^2}\int dt' d\epsilon_1 d\epsilon_2 d\epsilon_3 d\epsilon_4 < \hat{b}^\dagger(\epsilon_1)\hat{b}(\epsilon_2)\hat{b}^\dagger(\epsilon_3)\hat{b}(\epsilon_4) > \overline{e^{i(\epsilon_1-\epsilon_2+\epsilon_3-\epsilon_4)t/\hbar}}^t e^{i((\epsilon_3-\epsilon_4)/\hbar+\omega)t'} \tag{2.10}$$

Applying Wick's theorem allows us to isolate the terms contributing to the noise in this equation:

$$< \hat{b}^\dagger(\epsilon_1)\hat{b}(\epsilon_2)\hat{b}^\dagger(\epsilon_3)\hat{b}(\epsilon_4) >=< \hat{b}^\dagger(\epsilon_1)\hat{b}(\epsilon_2) >< \hat{b}^\dagger(\epsilon_3)\hat{b}(\epsilon_4) > + < \hat{b}^\dagger(\epsilon_1)\hat{b}(\epsilon_4) >< \hat{b}(\epsilon_2)\hat{b}^\dagger(\epsilon_3) > \tag{2.11}$$

The direct term $< \hat{b}^\dagger(\epsilon_1)\hat{b}(\epsilon_2) >< \hat{b}^\dagger(\epsilon_3)\hat{b}(\epsilon_4) >$ vanishes when the correlation $< \hat{I}_b >< \hat{I}'_b >$ is subtracted in Eq.2.9. $S(\omega)$ is therefore given by:

$$S(\omega) = 2\frac{e^2}{h^2}\int dt' d\epsilon_{1,2,3,4} < \hat{b}^\dagger(\epsilon_1)\hat{b}(\epsilon_4) >< \hat{b}(\epsilon_2)\hat{b}^\dagger(\epsilon_3) > \overline{e^{i(\epsilon_1-\epsilon_2+\epsilon_3-\epsilon_4)t/\hbar}}^t e^{i((\epsilon_3-\epsilon_4)/\hbar+\omega)t'} \tag{2.12}$$

We now express the operators $\hat{b}(\epsilon)$ as a function of the incoming operators $\hat{a}(\epsilon')$ using Eq.1.15. With the notation $\epsilon + m\hbar\Omega \equiv \epsilon + m$ used in chapter 1, we have:

$$\begin{aligned} < \hat{b}^\dagger(\epsilon_1)\hat{b}(\epsilon_4) > &= \sum_{m_1,m_4} U^*_{m_1}(\epsilon_1)U_{m_4}(\epsilon_4) < \hat{a}^\dagger(\epsilon_1+m_1)\hat{a}(\epsilon_4+m_4) > \\ &= \sum_{m_1,m_4} U^*_{m_1}(\epsilon_1)U_{m_4}(\epsilon_4) f(\epsilon_1+m_1)\delta(\epsilon_1+m_1-(\epsilon_4+m_4)) \end{aligned} \tag{2.13}$$

$$\begin{aligned} < \hat{b}(\epsilon_2)\hat{b}^\dagger(\epsilon_3) > &= \sum_{m_2,m_3} U_{m_2}(\epsilon_2)U^*_{m_3}(\epsilon_3) < \hat{a}(\epsilon_2+m_2)\hat{a^\dagger}(\epsilon_3+m_3) > \\ &= \sum_{m_2,m_3} U_{m_2}(\epsilon_2)U^*_{m_3}(\epsilon_3)(1-f(\epsilon_2+m_2))\delta(\epsilon_2+m_2-(\epsilon_3+m_3)) \end{aligned} \tag{2.14}$$

This yields, after performing the average over t in Eq.2.12:

$$\begin{aligned} S(\omega) &= 2\frac{e^2}{h^2}\sum_{m_1,m_2,m_3}\int dt' d\epsilon_{1,2} U^*_{m_1}(\epsilon_1)U_{m_1+m_3-m_2}(\epsilon_1+m_2-m_3) \\ &\quad \times U_{m_2}(\epsilon_2)U^*_{m_3}(\epsilon_2+m_2-m_3)f(\epsilon_1+m_1)(1-f(\epsilon_2+m_2))e^{i((\epsilon_2-\epsilon_1)/\hbar+\omega)t'} \end{aligned} \tag{2.15}$$

The integral over t' being equal to $h\delta((\epsilon_2-\epsilon_1)/\hbar+\omega)$, we have, after the variable substitution $\epsilon = \epsilon_1 + m_1$:

$$\begin{aligned} S(\omega) &= 2\frac{e^2}{h}\sum_{m_1,m_2,m_3}\int d\epsilon U^*_{m_1}(\epsilon-m_1)U_{m_1+m_3-m_2}(\epsilon-m_1+m_2-m_3) \\ &\quad \times U_{m_2}(\epsilon-m_1-\hbar\omega)U^*_{m_3}(\epsilon-m_1+m_2-m_3-\hbar\omega) \\ &\quad \times f(\epsilon)(1-f(\epsilon-m_1+m_2-\hbar\omega)) \end{aligned} \tag{2.16}$$

The successive variable substitutions $m = m_2 - m_1$ and $\tilde{m}_1 = m_3 - m$ yield:

$$\begin{aligned} S(\omega) &= 2\frac{e^2}{h}\sum_{m_1,\tilde{m}_1,m}\int d\epsilon U^*_{m_1}(\epsilon-m_1)U_{m_1+m}(\epsilon-m_1-\hbar\omega) \\ &\quad \times U_{\tilde{m}_1}(\epsilon-\tilde{m}_1)U^*_{\tilde{m}_1+m}(\epsilon-\tilde{m}_1-\hbar\omega)f(\epsilon)(1-f(\epsilon+m-\hbar\omega)) \end{aligned} \tag{2.17}$$

The sums over m_1 and $\tilde{m}_1$ are complex conjugates; we thus can write a compact expression of the power spectral density of the current fluctuations emitted by the source:

$$S(\omega) = 2\frac{e^2}{h}\sum_m \int d\epsilon \left|\sum_n U^*_n(\epsilon-n\hbar\Omega)U_{n+m}(\epsilon-n\hbar\Omega-\hbar\omega)\right|^2 f(\epsilon)(1-f(\epsilon+m\hbar\Omega-\hbar\omega)) \tag{2.18}$$

As in the previous chapter, we can expand this expression as a function of the c_n coefficients and the stationary scattering matrix $U^0(\epsilon)$, with $\hbar\Omega = 1$, and $\hbar\omega \equiv \omega$ (the obtained expression is then strictly equivalent to the one obtained in Adrien Mahé's thesis [68] using the gauge transformation mentioned in the previous chapter, see appendix A.3.2):

$$S(\omega) = 2\frac{e^2}{h}\sum_m \int d\epsilon \left|\sum_n c^*_{n+m}c_n U^{0*}(\epsilon+n)U^0(\epsilon+n-\omega)\right|^2 f(\epsilon-m)(1-f(\epsilon-\omega)) \tag{2.19}$$

- **zero and unity transmission limits**

For $D = 0$ and $D = 1$, the stationary scattering matrix $U^0(\epsilon)$ is constant and equal to unity. Eq.2.19 therefore yields:

$$\begin{aligned} S(\omega)_{D=0,D=1} &= 2\frac{e^2}{h}\sum_m \int d\epsilon \left|\sum_n c^*_{n+m}c_n\right|^2 f(\epsilon-m)(1-f(\epsilon-\omega)) \\ &= 2\frac{e^2}{h}\sum_m \int d\epsilon \delta_{m,0} f(\epsilon-m)(1-f(\epsilon-\omega)) \\ &= 2\frac{e^2}{h}\int d\epsilon f(\epsilon)(1-f(\epsilon-\omega)) \end{aligned} \tag{2.20}$$

The noise is therefore equal to the equilibrium noise of an edge channel at frequency ω. The similarity between the limits $D = 0$ and $D = 1$ is explained by the fact that at unity transmission, the dot only acts as an additional length of edge channel, and therefore does not contribute to the noise.

- **Zero-frequency limit**

When $\omega = 0$, the product of the stationary scattering matrices $U^{0*}(\epsilon+n)U^{0}(\epsilon+n-\omega)$ becomes unity, so that Eq.2.19 yields:

$$\begin{aligned} S(\omega=0) &= 2\frac{e^2}{h}\sum_m \int d\epsilon \left|\sum_n c^*_{n+m}c_n\right|^2 f(\epsilon-m)(1-f(\epsilon)) \\ &= 2\frac{e^2}{h}\sum_m \int d\epsilon \delta_{m,0} f(\epsilon-m)(1-f(\epsilon)) \\ &= 2\frac{e^2}{h}\int d\epsilon f(\epsilon)(1-f(\epsilon)) \end{aligned} \tag{2.21}$$

We thus recover the equilibrium noise at zero frequency, which vanishes at zero temperature. More importantly, since we focus on the excess noise with respect to the reference $D = 0$, its value at zero frequency is given by the difference between the expression given in the last equation and the expression obtained for the $D = 0$ limit in Eq.2.20, with $\omega = 0$: the excess noise vanishes at zero frequency.

2.2.2.1 Symmetry of the excess noise with the measurement frequency

When numerically computing $S(\omega)$, we will always subtract its value at $D = 0$, corresponding to the subtracted reference mentioned above. One can then show (see appendix A.4) that $\Delta S(+\omega) = S(\omega) - S(\omega, D = 0) = \Delta S(-\omega)$: the combination of the three-terminal geometry and the subtraction of the reference implies that the emission and absorption noises of the single electron source are equal. The importance of the three-terminal geometry can be viewed as an out-of-equilibrium generalization of the formula proposed by Lesovik and Loosen [86] for stationary signals, and extended by Park and Ahn [81] in the case of a finite frequency excitation:

$$S_-(\omega) - S_+(\omega) = 2\hbar\omega G(\omega) \tag{2.22}$$

where $G(\omega)$ is the conductance of the sample, as seen by the measurement circuit. This relation can be demonstrated in our case using $\Delta S(+\omega) = \Delta S(-\omega)$ where $G(\omega) = e^2/h$ is the conductance of the edge channel between contact (1) and contact (2). Indeed, the difference between absorption and emission noises in our sample is equal to the difference between absorption and emission noises at zero transmission:

$$\begin{aligned} S_-(\omega) - S_+(\omega) &= S_-(\omega, D=0) - S_+(\omega, D=0) \\ &= 2\frac{e^2}{h}\int d\epsilon \left[f(\epsilon)(1-f(\epsilon+\hbar\omega)) - f(\epsilon)(1-f(\epsilon-\hbar\omega))\right] \\ &= 2\frac{e^2}{h}\left[\frac{\hbar\omega}{1-e^{-\hbar\omega/k_BT}} - \frac{-\hbar\omega}{1-e^{\hbar\omega/k_BT}}\right] \\ &= 2\hbar\omega\frac{e^2}{h} \end{aligned} \tag{2.23}$$

From here on, we only consider the noise after subtraction of its value at $D = 0$. We therefore confound the notations $S(\omega)$ and $\Delta S(\omega)$.

2.2.3 Numerical calculations

Because Eq.2.18 does not provide a simple analytical expression of the noise, we have computed it numerically using the parameters of sample *S528-11*: $\Delta = 4$ K; $f_0 = \Omega/2\pi = 1.5$ GHz. The simulation offers a wide range of parameters, such as the shape of the excitation signal, driving and measurement frequencies, or temperature.

2.2.3.1 Effect of the QPC transmission and temperature

The most obvious dependence of the noise $S(\omega)$ (at least qualitatively) is on the QPC transmission D, in the injection regime $2eV_{exc} = \Delta$. Indeed, as demonstrated above, we expect the noise to vanish both at zero and unity transmission.

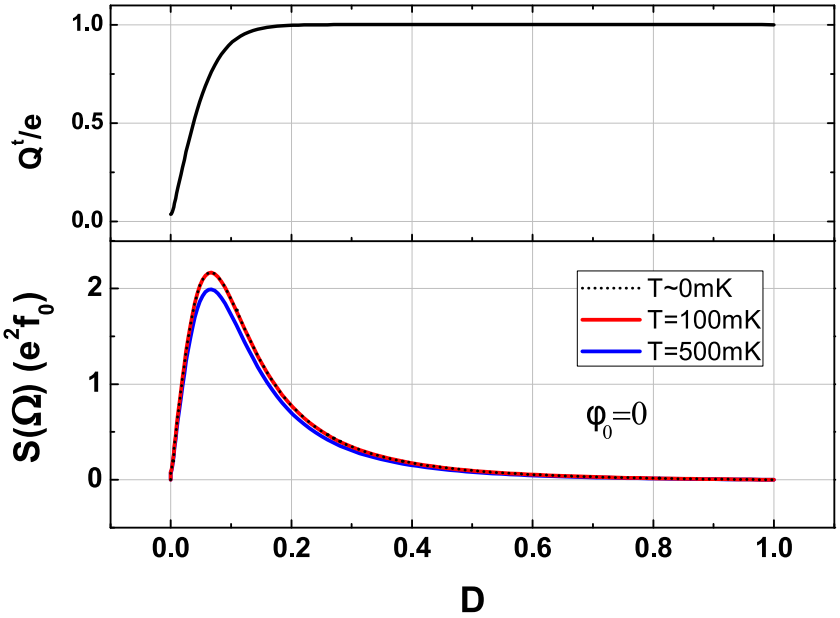

Figure 2.2: Calculated average transfered charge per half-period (upper panel) and noise (lower panel) as a function of the QPC transmission, in the scattering model. The level spacing Δ is equal to 4 K, and the measurement frequency is taken equal to the driving frequency $f_0 = 1.5$ GHz.

We first focus on the optimal operating conditions ($2eV_{exc} = \Delta$, $\phi_0 = 0$). We use a square signal containing 30 odd harmonics. We have plotted in Fig.2.2 the calculated noise as a function of the QPC transmission, for a measurement frequency $\omega/2\pi$ equal to the excitation frequency $f_0 = \Omega/2\pi$. We have also plotted the average transfered charge per half-period, calculated using Eq.1.52 (Fig.2.2a). As expected, the noise vanishes at zero and unity transmission, and describes a bell shaped curve as D changes. The maximum of the curve is obtained at a transmission $D \approx 0.07$, for which the average transfered charge is equal to $\sim 0.75e$ per half-period. This result is not consistent with a naive description of the noise as a partition noise, where the partition probability would be defined by the emission probability $P = \mathcal{Q}^t/e$: in this case the noise would be maximum for $\mathcal{Q}^t/e = 0.5$. Furthermore, $S(\Omega)$ does not vanish when the average transfered charge becomes equal to e, thus demonstrating that it cannot be described as a simple partition noise process. In the next section, we will demonstrate using the heuristic model that the finite value of the noise when the charge is quantized is due to the uncertainty on the emission time.

In the anti-resonant case depicted here, the noise is quasi-independent of the temperature: indeed, the differences between the curves for $T =\sim 0K, 100$ mK, 500 mK presented in Fig.2.2b are small. This can be explained by the fact that when the energy level of the dot is shifted at an energy $\Delta/2$ above the Fermi energy, the charge emission is insensitive to the temperature, as long as T is small compared to the level spacing.

2.2.3.2 Measurement frequency

As demonstrated above, the noise vanishes at zero frequency; this implies that the noise presents non-trivial variations with the frequency, which should depend on the transmission. We have plotted

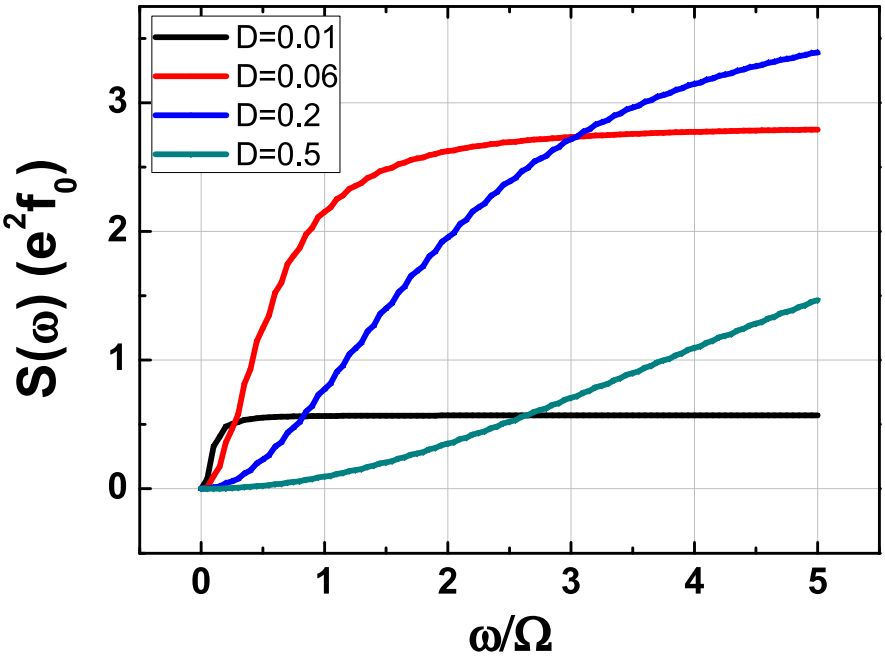

Figure 2.3: Calculated noise as a function of the measurement frequency in the injection regime: $2eV_{exc} = \Delta$, $\phi_0 = 0$. We have taken $f_0 = 1.5$ GHz (that is $\hbar\Omega/k_B = 0.07$ K), and $\Delta = 4$ K.

in Fig.2.3 the variation of the noise in the anti-resonant case with the measurement frequency up to five times the excitation frequency, for different values of the transmission. As expected, the noise vanishes at zero frequency for all transmissions. At low transmission, $S(\omega)$ rises sharply, then becomes independent of the frequency: this shot noise behavior describes the fact that the charge emission is not systematic, because the escape time is longer than the half-period of the excitation signal. When the transmission is increased, the saturation occurs at higher frequencies, while the value of the noise at the saturation increases. We will show in the next section that the maximum value of the saturation is $\sim 4e^2 f_0$. At large transmissions, the noise increases monotonously with the frequency, with an $\omega^2\tau^2$ dependence. One can however see that depending on the frequency, the noise does not reach a maximum for the same value of the transmission. The variation of the noise with the transmission presented in Fig.2.2 is therefore highly frequency dependent.

2.2.3.3 Variation with the dot equilibrium potential

All the results presented above correspond to the optimal operating condition of the single electron emitter, that is the anti-resonant case $\phi_0 = 0$, where the highest occupied level of the dot is shifted far above the Fermi energy. Since the QPC gate voltage V_g also modulates the position of the levels in the dot, it is interesting so study the variation of the noise with the equilibrium potential of the dot, that is when the phase ϕ_0 is changed.

The variation of the noise at $\omega = \Omega$ with ϕ_0 is plotted in Fig.2.4a), for a fixed transmission $D = 0.1$. In the resonant case $\phi_0 = \pi$, we observe a diminution of the noise, which broadens when the temperature is increased. This diminution of the noise is explained by the fact that the electrons responsible for thermal noise are distributed in a typical energy bandwidth $k_B T$ centered around the Fermi energy. When the highest occupied level of the dot is placed in this energy bandwidth (that is, in the vicinity of the resonant case $\phi_0 = \pi$), the emitted electrons are mixed with the thermally excited electrons, and one cannot separate the contributions of thermal noise and the noise emitted by the source. As a result, the noise after subtraction of its value at $D = 0$ (that is, after subtraction of the contribution of thermal noise) only considers electrons emitted far from the Fermi sea, and therefore diminishes. This effect is similar to the competition between temperature and bias voltage in measurements of the shot noise of a QPC [31, 87]: when the bias voltage (that is, the energy of the charges emitted by the biased contact) becomes smaller than the temperature, the partition noise vanishes, so that the measured shot noise is essentially given by thermal noise. It is also reminiscent of the measurement of the Fano factor in ballistic graphene shown in [88], where the Fano factor vanishes at zero bias because the thermal contribution of the noise is removed.

We have plotted in Fig.2.4b the variation of the noise with the measurement frequency in the resonant and anti-resonant conditions, for much larger scales of the frequency: we observe a cutoff at frequencies comparable to the level spacing, which depends on ϕ_0. The cutoff frequency is equal to $\Delta/2$ in the anti-resonant condition: indeed, the electrons (holes) are emitted at an energy $\Delta/2$ above (below) the Fermi energy, and can therefore only emit photons at frequencies lower than $\Delta/2$. In the resonant condition, a portion of the charges is emitted at an energy Δ above/below the Fermi energy; the cutoff frequency is thus equal to Δ.

2.2.3.4 Shape of the drive

We have numerically studied the noise for different shapes of the excitation signal, more specifically its dependence on the number of harmonics contained in the square excitation voltage. Indeed, when the harmonic content of a square signal is diminished, oscillations (ripples) appear in the signal (see Fig.2.5), which might affect the energy resolution of the emitted charge. The previous results where computed for a near-perfect square signal containing 30 odd harmonics; we have plotted in Fig.2.6 the noise as a function of ϕ_0, for different numbers of odd harmonics contained in the excitation square signal. It appears that the noise in the anti-resonant condition $\phi_0 = 0$ is quasi-insensitive to the number of harmonics, while it presents a strong dependence in the resonant condition: the ripples in an excitation square signal with few harmonics cause the highest occupied level in the dot to oscillate in front of the Fermi energy in the resonant case, leading to the emission and absorption of additional charges per half-period. Since these additional charges are generated close to the Fermi energy, there is a competition between this effect which tends to increase the noise because more charges are generated, and the effect described in the previous paragraph, where the generation of a charge within the thermally excited electrons in the Fermi sea causes the emission noise to diminish. This is observed for 3 harmonics in Fig.2.6: when ϕ_0 becomes close to π, the noise increases, then suddenly drops when $\phi_0 = \pi$. Furthermore, this competition can be observed even with near-perfect

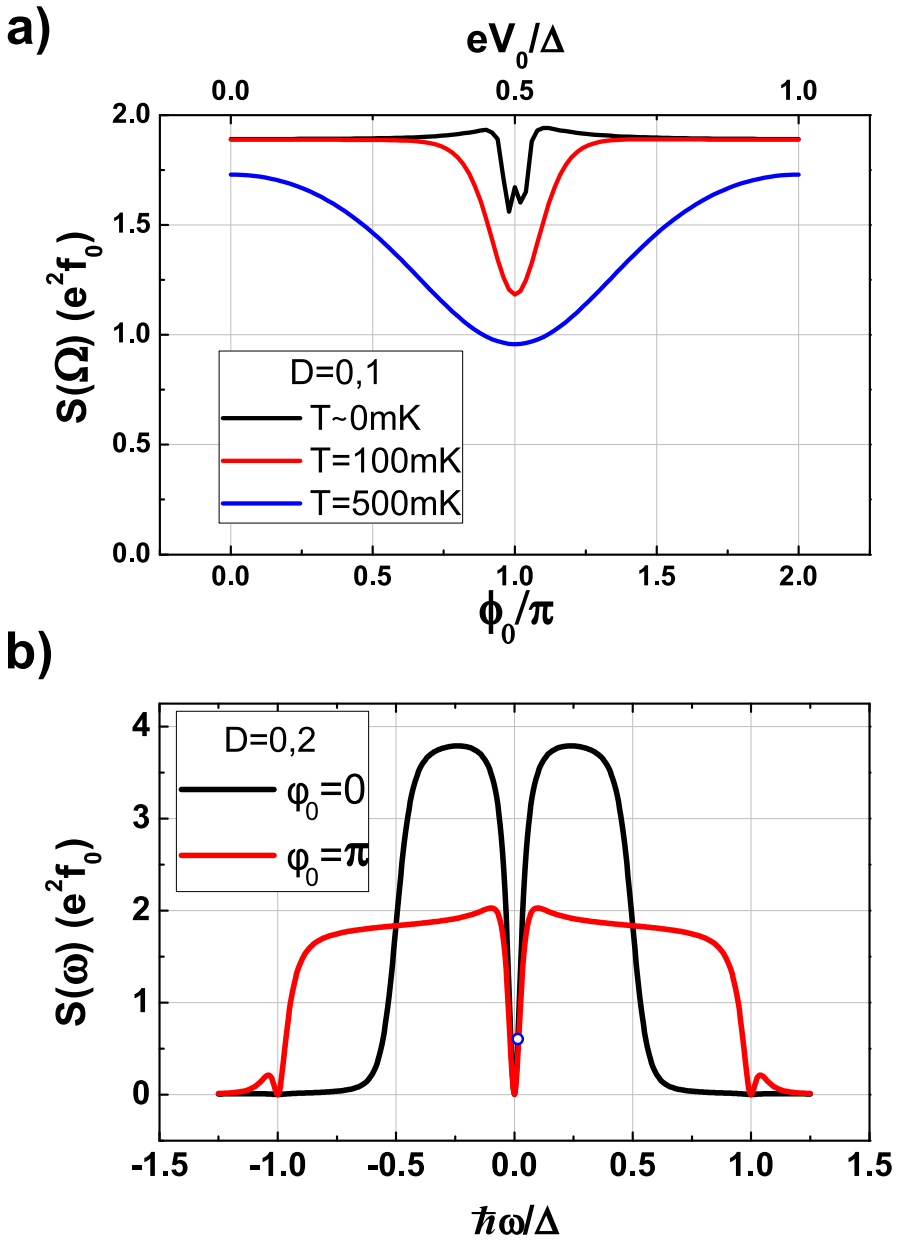

Figure 2.4: **a)** Calculated noise as a function of the dot equilibrium potential $\phi_0 = 2\pi eV_0/\Delta$, for $D = 0.1$ and $\omega = \Omega$. **b)** Calculated noise as a function of the measurement frequency (positive and negative values), for $\phi_0 = 0$ (black line) and $\phi_0 = \pi$ (red line). The blue circle corresponds to the noise at the excitation frequency Ω.

excitation square signals at $T \sim 0$, see Fig.2.4: even though the ripples in the excitation signal are small, they cause energy shifts larger than the energy bandwidth of the thermally excited electrons of the Fermi sea.

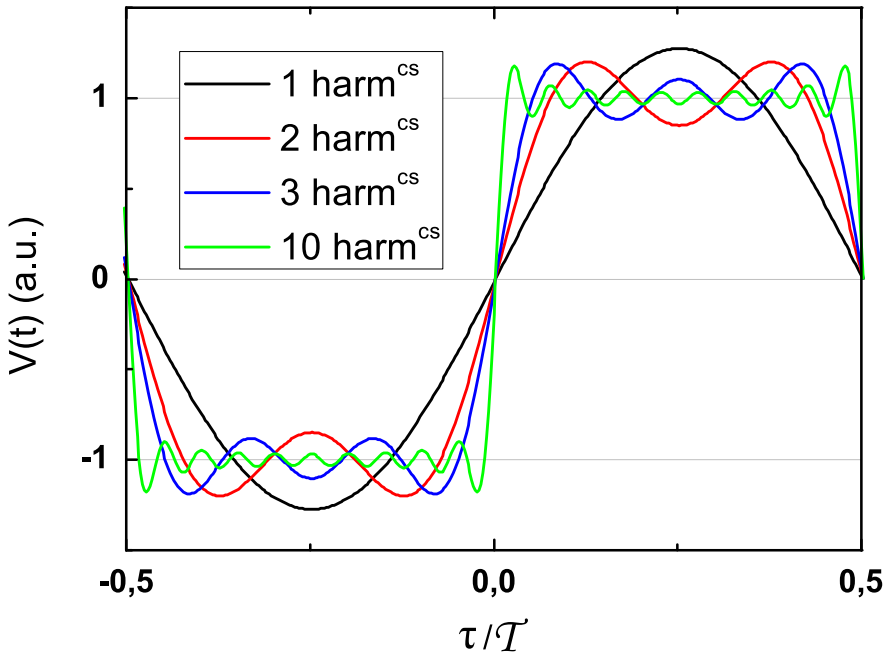

Figure 2.5: Square signals, with 1 (black), 2 (red), 3 (blue) and 10 (green) odd harmonics.

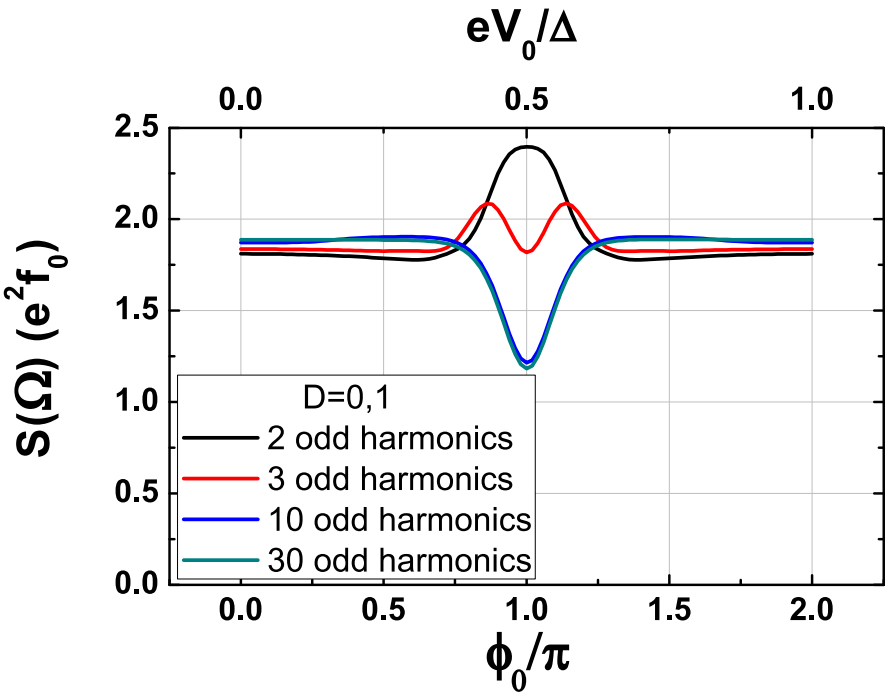

Figure 2.6: Calculated noise as a function of the dot equilibrium potential, for a square excitation signal containing 2, 3, 10 and 30 odd harmonics (resp. black, red, blue and gray line). The temperature is taken equal to 100 mK.

2.2.3.5 Conclusion on the scattering model

The scattering model allows the computation of the autocorrelation of the current fluctuations emitted by the source for a wide range of parameters, and puts into light several emission processes that cannot be discriminated by the sole study of the average AC current, particularly in the resonant condition $\phi_0 = \pi$. Because of the absence of an analytical formula, it does not however provide a simple interpretation for the presence of finite noise in the ideal operating conditions when charges are systematically emitted. We have stated that this noise is due to the uncertainty on the emission time; we will show in the next section using the heuristic model that it is indeed the case, and demonstrate that this noise is the signature of single charge emission.

2.3 Heuristic model

In this section, we use the heuristic model presented in 1.4.2 to compute the autocorrelation of the current fluctuations generated by the source. Since the model describes the mesoscopic capacitor as an ideal single electron emitter, it computes the characteristic noise associated to the periodic time-controlled single charge emission. We first present the principle of the computation of the noise, and put into light the two fundamental limits of noise in the system: shot noise (or charge noise: the probability of charge emission is small), and quantum jitter (phase noise: the noise arises from random fluctuations in the emission time). We then compare the results with the ones obtained with the scattering model, presented in the previous sections. We find an excellent agreement between the two models, thus demonstrating that the device described with the scattering model is indeed a single electron emitter.

2.3.1 Computation of the noise

The noise is calculated using the definition of the autocorrelation of the current fluctuations given in Eq.2.4: $S(\omega) = 2\int dt' \overline{< \delta I(t)\delta I(t+t') >}^t e^{i\omega t'}$. The noise is given by the Fourier transform of the current fluctuations correlator $C(t')$, which can be defined as the difference between two correlators $C_1(t')$ and $C_2(t')$:

$$\begin{aligned} C(t') &= \overline{< \delta I(t)\delta I(t+t') >}^t \\ &= \overline{< I(t)I(t+t') >}^t - \overline{< I(t) >< I(t+t') >}^t \\ &= C_1(t') - C_2(t') \end{aligned} \tag{2.24}$$

$C_1(t')$ is therefore given by the statistical average of the autocorrelation of the instantaneous current $I(t)$ (pictured in Fig.1.11a and b), averaged over time t, while $C_2(t')$ is given by the autocorrelation of the average current $< I(t) >$ (pictured in Fig.1.11c and d), averaged over time t. Depending on the escape probability per turn b, the contributions of each of those two correlators vary. The contributions are depicted in Fig.2.7: at short times t', $C_1(t')$ is a Dirac peak centered on $t' = 0$: indeed, since at most one charge is emitted per half-period, the short-time correlations vanish. In this respect, the Dirac peak is the hallmark of single particle emission. Correlations are recovered when t' becomes close to a multiple of the half-period. The height of the Dirac peak is proportional to the average transfered charge per half-period $\mathcal{Q}^t$: $C_1(t' = 0)$ counts the average number of peaks and dips in the signal, corresponding to emitted electron and holes.

$C_2(t')$ is given by the autocorrelation of the exponentially decaying average current depicted in Fig.1.11c and d. It therefore presents a peak at short times, centered on $t' = 0$, with a finite width given by the escape time τ. At times comparable with multiples of the half-period, we once again recover correlations, which compensate the long-times correlations in $C_1(t')$ (see Fig.2.7, lower panels).

Indeed, for long times t', $C(t')$ vanishes because the charges emitted by the source are not correlated. As discussed below, the timescale on which $C(t')$ becomes equal to zero (*i.e.* on which the correlations between the emitted charges are lost) depends on the transmission D. The relevant timescale for the study of $C(t')$ is thus naturally given by the escape time τ.

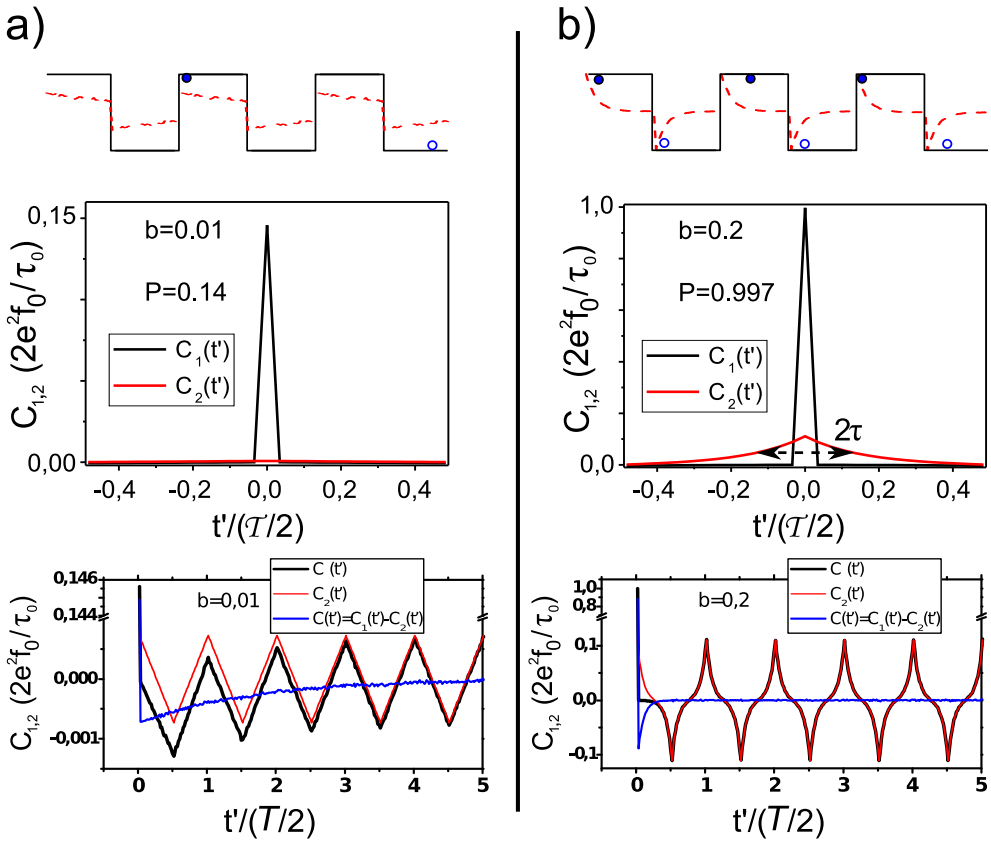

Figure 2.7: Current correlators $C_1(t')$ and $C_2(t')$, calculated with the heuristic model. **a)** shot noise limit: for small escape probability b, charges are not systematically emitted within a half-period: the emission probability per half-period $P = \mathcal{Q}^t/e$ is small, and the current fluctuations correlator is essentially given by the Dirac peak in $C_1(t')$. $C_1(t')$, $C_2(t')$ and $C(t')$ for long times t' are plotted on the lower panel (respectively in black, red and blue lines): $C(t')$ presents negative values for $t' \leq 2\mathcal{T}$, reflecting the antibunching of emitted charges. **b)** large emission probability limit: for sufficiently large escape probabilities (here, $b = 0.2$), charges are systematically emitted ($P \approx 1$), and $C_2(t')$ presents a peak with a finite width given by the escape time τ. $C(t')$ takes negative values on a smaller range of times t'.

2.3.1.1 Shot noise limit

For small escape probabilities $b \ll 1$, the escape time $\tau = \tau_0(1/b - 1/2)$ becomes larger than the half-period. The peak at $t' = 0$ in $C_2(t')$ then becomes small with respect to the Dirac peak in $C_1(t')$, see Fig.2.7a. The current fluctuations correlator $C(t')$ is given by a Dirac peak on $t' = 0$, and takes small negative values at finite times up to the escape time τ. The noise power spectral density is therefore constant (except at zero frequency, where it vanishes because the areas of $C_1(t')$ and $C_2(t')$ compensate): the source emits shot noise due to the random emission of charges. The negative values of

$C(t')$ at finite times reflect the antibunching of emitted charges: at low probabilities, this antibunching extends over a large timescale τ (see Fig.2.7a, lower panel), which illustrates the dot charge-memory: a hole must be emitted after the emission of an electron, for the source to emit a second electron.

An analytical expression of the noise can be defined in the shot noise limit, using the variation of $C_1(t')$ and $C_2(t')$ depicted in Fig.2.7a. When neglecting $C_2(t')$ and writing $C_1(t') = 2e^2 f_0 \mathcal{Q}^t / e\delta(t')$, one finds, using the expression of the average transfered charge defined in Eq.1.50 when $f\tau \gg 1$:

$$S_{shot}(\omega) = 4e^2 f_0 \times P = \frac{e^2}{\tau} \tag{2.25}$$

where $P = \mathcal{Q}^t/e$ the emission probability per half-period. This expression is identical to the usual shot noise formula $S_{II} = 2eI$, where the current I is given by the nominal emission current $I_0 = 2ef_0$, multiplied by P.

2.3.1.2 Quantum jitter limit

In the other limit, the escape probability b is high enough for the charges to be systematically emitted: the emission probability P is equal to unity, and the charge noise vanishes. The average current then presents well-defined exponential decays with a decay time given by the escape time $\tau \ll \mathcal{T}/2$: $< I(t) >= \pm e/\tau e^{-t/\tau}$. We then find a simple expression for C_2:

$$C_2(t') = \frac{e^2 f_0}{\tau} e^{-|t'|/\tau} \tag{2.26}$$

In the limit $\tau \ll \mathcal{T}/2$, the noise is thus given by:

$$S_{jitter}(\omega) = 4e^2 f_0 \frac{\omega^2\tau^2}{1+\omega^2\tau^2} \tag{2.27}$$

Even when charges are systematically emitted, we find a finite noise which only depends on the escape time τ: the uncertainty on the charge emission time, given by the escape τ, gives rise to a fundamental noise, called *quantum jitter*. The quantum jitter is an intrinsically high frequency noise, and is the signature of single charge emission: when the source systematically emits single charges, the noise reduces to the value of the quantum jitter determined only by the temporal extension τ of the emitted wave packets.

2.3.1.3 Analytic formula

Mathias Albert and collaborators have recently [89] proposed an analytic formula of the noise for the heuristic model, which interpolates between the shot noise and the quantum jitter limits. The noise is calculated by studying the charge dynamics in the dot using a master equation coupling the average number of charges in the dot at a time $t+\tau_0$, written $< Q(t+\tau_0) >$, to the average number of charges at a time t. During the time τ_0, the charge can be emitted with a probability b. Since only one charge transfer process can occur at half of the period (electron emission or electron absorption), the average number of charges at a time $t+\tau_0$ will be equal to $< Q(t+\tau_0) >= (1-b) < Q(t) >$ for the emission half-period, and to $< Q(t+\tau_0) >= b(1- < Q(t) >)+ < Q(t) >$ for the absorption half-period.

After solving this master equation, the charge correlation function $\overline{< \delta Q(t)\delta Q(t+t') >}^t$ is evaluated, and one obtains an analytic formula for the noise power spectral density:

$$S(\omega) = 4e^2 f_0 \tanh\left(\frac{1}{4f_0\tau}\right)\frac{\omega^2\tau^2}{1+\omega^2\tau^2} = \frac{\mathcal{Q}^t}{e} \times S_{jitter}(\omega) \tag{2.28}$$

This formula emphasizes the specific role of the quantum jitter in the noise generated by the single electron emitter, since it can be generally be written as the product of the quantum jitter with the charge emission probability $P = \mathcal{Q}^t/e$.

2.3.2 Comparison with the scattering model

We now present the numerical results obtained with the heuristic model, and their comparison with the results of the scattering model in the optimal emission conditions ($\phi_0 = 0$) at $T = 100$ mK. Except stated otherwise, all the results of the scattering model correspond to $\Delta = 4$ K.

2.3.2.1 Transmission and frequency dependence

We have calculated the noise power spectral density generated by the source at the driving frequency $\Omega/2\pi$ for the heuristic model as a function of the semi-classical escape probability b. The results are shown in Fig.2.8. We have plotted as well the variation of the noise power spectral density calculated with the scattering model as a function of the QPC transmission. We find a perfect agreement between the two sets in the entire range of D and b. The coincidence between the two curves verifies the validity of Eq.1.51, which links the escape probability b to its quantum counterpart D. More importantly, this demonstrates that the scattering model effectively describes the device as a single electron emitter, and proves the existence of the quantum jitter within a quantum-coherent formalism.

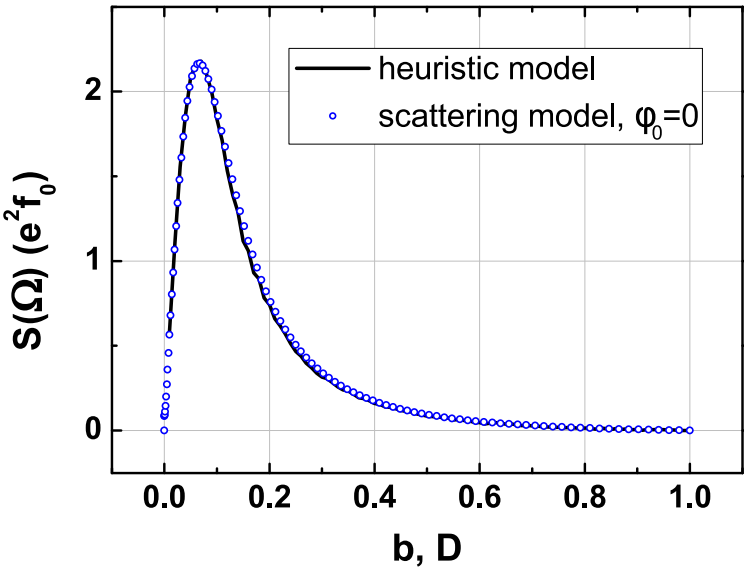

Figure 2.8: Dependence of the noise on the escape probability b in the heuristic model (black line). We also plot (blue circles) the dependence of the noise on the QPC transmission D in the scattering model ($\phi_0 = 0$, $T = 100$ mK).

We have plotted in Fig.2.9 the variation of the noise spectra in both models as a function of the measurement frequency ω. The agreement between the two models is once again outstanding, and the two analytical noise limits (dashed lines) are well reproduced.

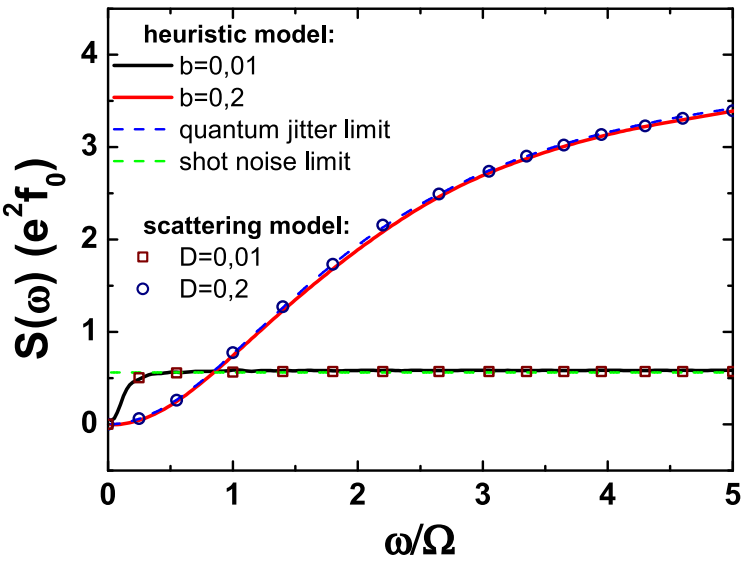

Figure 2.9: Dependence of the noise in the heuristic model (full lines) and in the scattering model for $\phi_0 = 0$ (hollow symbols) on the measurement frequency ω. The dashed lines correspond to analytical calculations of the shot noise and quantum jitter limit, using Eqs.2.25 and 2.27.

2.3.2.2 Noise versus modulus of the current

One can combine the analytical expression of the noise as a function of the escape time given in Eq.2.28, for $\omega = \Omega$, with the expression of the modulus of the first harmonic of the current derived from Eq.1.52: $|I_\Omega| = 2ef_0/\sqrt{1+\Omega^2\tau^2}$, in order to express the noise at the excitation frequency as a function of the modulus of the current:

$$S(\Omega) = 4e^2 f_0 \tanh\left(\frac{2\pi\frac{|I_\Omega|}{2ef_0}}{4\sqrt{1-(\frac{|I_\Omega|}{2ef_0})^2}}\right)(1-(\frac{|I_\Omega|}{2ef_0})^2) \tag{2.29}$$

When $|I_\Omega|$ becomes small, one finds the usual shot noise formula: $S(\Omega) \approx \pi e|I_\Omega| = 2eI$, where I is the modulus of the current emitted by the source. The expression of the quantum jitter as a function of $|I_\Omega|$ is easily deduced:

$$S_{jitter}(\Omega) = 4e^2 f_0(1-(\frac{|I_\Omega|}{2ef_0})^2) \tag{2.30}$$

We have plotted in Fig.2.10 the noise as a function of $|I_\Omega|$, as defined in Eq.2.29, and the noise as a function of the modulus of the first harmonic, calculated with the scattering model. The agreement between the two models is excellent; a small discrepancy can be observed for low values of the current, where the simulations of the scattering model suffer from the necessary discretization of the energy: indeed, at very low transmissions, the width of the peaks in the density of states becomes smaller than the energy increment used in the numerical computation. We have also plotted the variations of shot noise and quantum jitter as a function of $|I_\Omega|$ (dashed lines): it appears that $S(\Omega)$ is well described

by pure quantum jitter for values of the first harmonic larger than $\sim 1.5ef_0$, which corresponds to a quantized average transfered charge per half-period $\mathcal{Q}^t = e$.

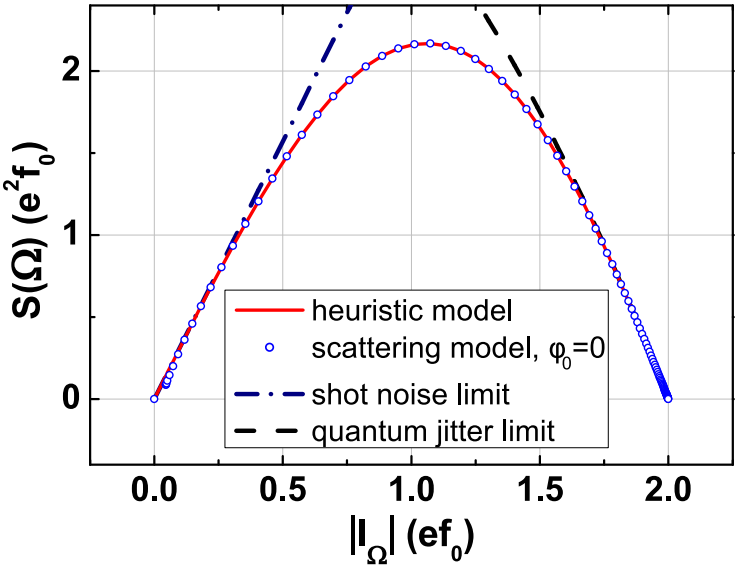

Figure 2.10: Calculated noise in the heuristic model (red line) and in the scattering model (blue circles) as a function of the modulus of the first harmonic of the average AC current. The shot noise and quantum jitter limits (dashed lines) are given by the usual shot noise formula and Eq.2.30.

The main interest of this representation is that it allows to compare the experimental results with the model quite easily, since it does not require the knowledge of the variation of the QPC transmission with the gate voltage V_g, nor the accurate measurement of the escape time τ. However, it unveils the contribution of the quantum jitter only for a reduced portion of the data. In this respect, the representation of the variation of the noise with the escape time, presented in the next paragraph, is better suited.

2.3.2.3 Universality of the noise as a function of the escape time

When $\omega = \Omega = 2\pi f_0$, Eq.2.28 shows that the power spectral density of the current fluctuations generated by the source depends only on the escape time τ. We therefore plot in Fig.2.11 the noise as a function of the escape time in the heuristic model, as well as the noise calculated in the scattering model for three values of the level spacing: $\Delta = 2, 4, 8$ K. The agreement between the heuristic model and the scattering model is excellent, regardless of the value of the level spacing: in the ideal emission conditions ($2eV_{exc} = \Delta$, $\phi \approx 0$), the value of the noise power spectral density at the excitation frequency only depends on the escape time τ. The independence of the noise with the level spacing and the temperature illustrates the universality of the noise generated by the single electron emitter: as long as the charges are emitted significantly above/below the Fermi energy, the contribution of the Fermi sea can be ignored, and the noise probes the temporal distribution of charges within the emitted electron/hole stream, without discriminating at which energy they are emitted.

The scattering model shows however that the universality is lost whenever charges are emitted close to the Fermi energy, that is in the resonant condition $\phi_0 = \pi$.

The two models, developed independently, predict that the mesoscopic capacitor can indeed be used, when driven in the appropriate regime, as a single electron emitter. Furthermore, they show

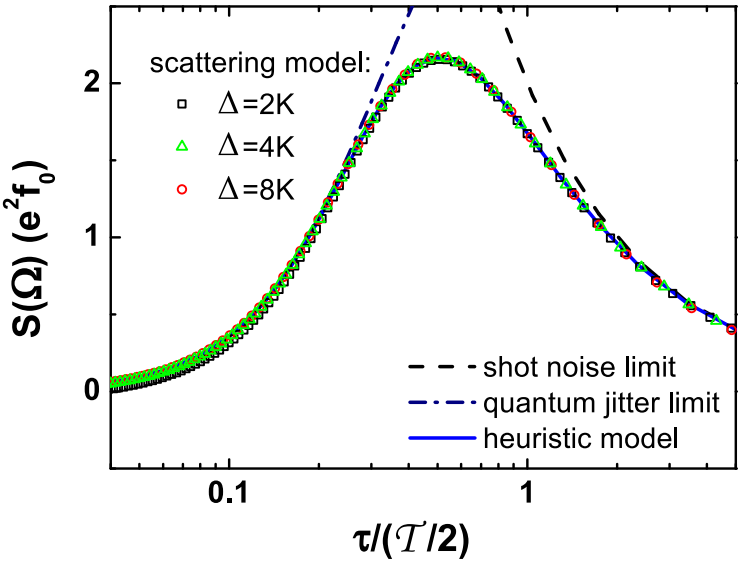

Figure 2.11: Calculated noise in the heuristic model (blue line) and in the scattering model for different values of the level spacing (hollow symbols) as a function of the escape time τ. The shot noise and quantum jitter limits (dashed lines) are given by Eqs.2.25 and 2.27.

that it can achieve a controlled emission of single charges that is robust to changes of the samples parameters.

2.4 Experimental setup

In the previous theoretical sections, we have shown that the autocorrelation of the emitted current fluctuations presents a wide spectrum, and takes values typically given by $e^2 f_0$, where f_0 is the driving frequency. For a driving frequency $f_0 = 1.5$ GHz, $e^2 f_0 \approx 3.8 \times 10^{-29}$ A^2/Hz. These values, although very small, are commonly measured at low frequency [90, 23, 48, 91], where one can transform small current fluctuations into larger voltage fluctuations by shunting the output of the samples with a large resistor (typically, a few kΩ). Since the noise power spectral density emitted by our sample vanishes at zero frequency, we need to measure it at frequencies comparable with the driving frequency. This is much more challenging, for broad-band microwave circuits must be 50 Ω-adapted; we therefore cannot rely on the use of a large resistor to increase our signal. Furthermore, the presence of high-frequency parasitic couplings brings an additional difficulty, as they yield much larger powers than the signal itself.

2.4.1 Sample design

We have designed our samples in order to optimize the noise measurement. The two-dimensional electron gas (for batch *S528*, see appendix B) has a nominal density equal to 1.9×10^{11} cm^{-2} and a nominal mobility equal to 1.3×10^6 cm^2/Vs. The depth of the gas is 105 nm. The fabrication of the samples was made by Yong Jin at *Laboratoire de Photonique et Nanostructures* in Marcoussis.

An optical view of sample *S528-11* is shown in Fig.2.12b. In order to minimize the high-frequency parasitic couplings, most of the surface of the sample is covered by an *Au* ground plane; furthermore, the metalizations corresponding to the microwave excitation and measurement lines are placed orthogonally

to reduce the crosstalk. Fig.2.12b shows that the sample actually contains two mesoscopic capacitors, which are not connected with each other. This design is a precursor of the samples used for Hanbury-Brown and Twiss (described in the next chapter) and Hong-Ou-Mandel experiments, where the two sources are connected by the electron gas, and a QPC (which acts as a beam-splitter) is placed between the sources. This design allows to optimize the number of samples per electron gas wafer, as well as to simplify the fabrication, since the designs of the two types of samples (single source and collider) are highly similar.

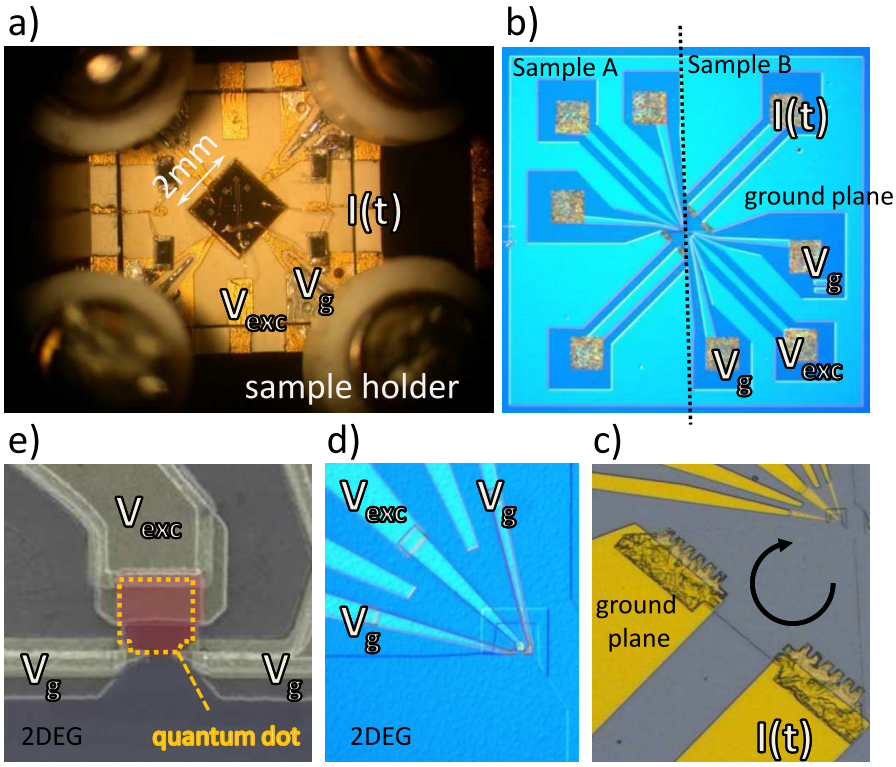

Figure 2.12: Pictures of sample *S528-11*: **a)** optical view of the sample installed in the sample holder. **b)**, **c)**, **d)** optical views with increasing zoom of the chip. As seen on **b)**, each chip contains two samples. The black arrow in **c)** depicts to the chirality of electronic transport when an strong perpendicular magnetic field is applied. **e)** SEM view of the mesoscopic capacitor (with false colors). The quantum dot is highlighted in red.

- **Three-terminal geometry**

A close-up view of the active zone of the sample where the electron gas is not removed (see Fig.2.12c) shows the two ohmic contacts mentioned in 1.1.1. Contact (1) is connected to the microwave measurement line, while contact (2) is connected to the ground plane. The purpose of this geometry is to use the chirality of the edge channels as a circulator, in order to protect the sample from the back-action noise of the amplification line. Indeed, the cryogenic amplifiers used in the measurement line send back noise towards the sample; this back-action noise is typically five orders of magnitude larger than the noise of the sample. Because of the mismatch between the impedance of the sample and the impedance of the measurement circuit, the back-action noise is partially reflected on the sample, and adds a parasitic noise to the measurement. This parasitic noise can then be removed by subtracting the reference, as long as its value is independent of the state of the sample.

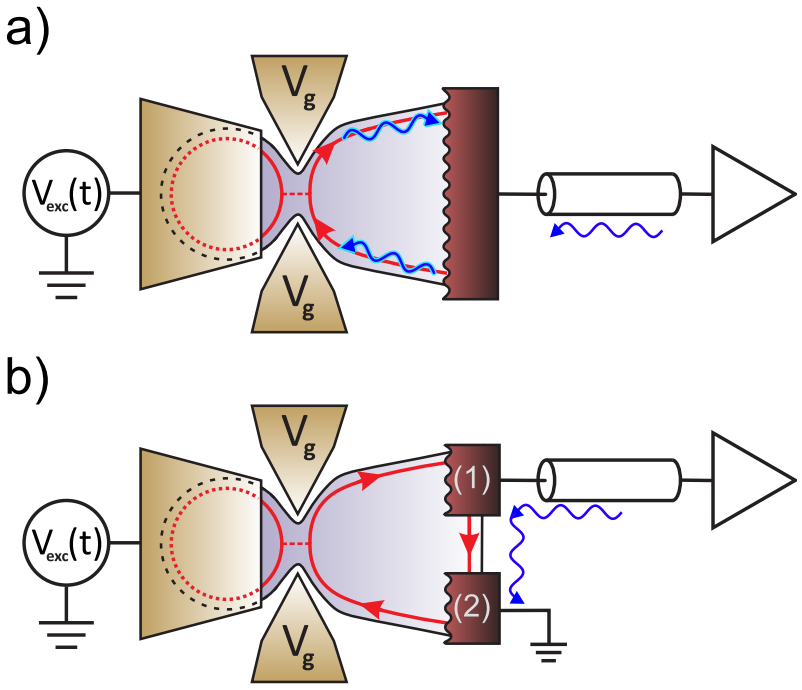

Figure 2.13: a) schematic view of a sample in the two-terminal (single contact) geometry. The back-action noise of the measurement line (blue oscillating lines) is reflected on the sample, with a coefficient depending on the dot parameters. **b)** schematic view of a sample in the three-terminal (dual contacts) geometry. The reflected part of the back-action noise only depends on the impedance of the edge channels flowing from contact (1) to contact (2).

The back-action noise is reflected on the sample with a reflection coefficient that depends on the conductance of the sample viewed from the measurement lines, noted G_m. Because the sample is shunted by a resistor equal to the characteristic impedance of the measurement line Z_0 (see Fig.2.13), the power reflection coefficient is given by:

$$|S_{11}|^2 = \frac{|Z_0 G_m|^2}{|2 + Z_0 G_m|^2} \tag{2.31}$$

In the case of a single contact (two-terminal geometry) shown n Fig.2.13a, G_m is equal to the sum of the conductance of the sample $G^{nl}(\Omega)$, defined in 1.47, and the parasitic conductance G_{para}: the reflection coefficient $|S_{11}|$ therefore depends on the state of the sample, particularly on the QPC transmission D. The value of the parasitic noise due to the reflection of the back-action noise thus changes when the reference is subtracted by a factor $\sim 10^{-4}$. Although quite small, this measured variation is still about ten times larger than the noise emitted by the single electron emitter, and the noise measurements probe as a matter of fact the conductance of the sample by noise reflectometry.

In the case of two contacts (three-terminal geometry), when a strong perpendicular magnetic field is applied, G_m is given by the sum of the parasitic conductance and the conductance of the edge channels connecting contact (1) to contact (2), see Fig.2.13b. This conductance is equal to $\nu e^2/h$, where ν is the filling factor of the quantum Hall effect corresponding to the applied magnetic field. As a result, the reflection coefficient is independent of the parameters applied to the sample, and the parasitic noise is fully removed when the reference is subtracted. This effect can be qualitatively understood by considering that the back-action noise incoming on the sample is transmitted (at least partially) from

contact (1) to the edge channels of the sample, in the form of current fluctuations. In the two terminal geometry, these current fluctuations are sent towards the quantum dot, where they are reflected with a phase depending on the density of states of the dot, as described in 1.1.2. In the three-terminal geometry however, the fluctuations are sent towards contact (2), where they are absorbed.

The use of an additional grounded contact to isolate the active part of the sample from the noise of the environment is a fundamental technique for noise measurements in quantum Hall effect systems [91].

2.4.2 Setup

We have measured the noise in a bandwidth centered around the excitation frequency $f_0 = 1.5$ GHz: $\Delta f = 1.2 - 1.8$ GHz $= \Delta\omega/2\pi$. On this bandwidth, the noise can be approximated as a linear function of the frequency, so that the noise power spectral density integrated on this bandwidth is equal to the noise at the excitation frequency:

$$\frac{1}{\Delta\omega}\int_{\Omega-\Delta\omega/2}^{\Omega+\Delta\omega/2} d\omega S(\omega) \approx S(\Omega) \tag{2.32}$$

The measurement setup is presented on Fig.2.14: while the excitation line is the same as the one presented in the first chapter, we have built a high-sensitivity noise measurement line [92] that allows us to simultaneously measure the noise and the conductance. The noise measurement line, described in details in chapter 4 (principle, implementation and calibration), is composed of a 120 Ω to 50 Ω quarter-wave impedance transformer and an interferometric amplification technique. The quarter-wave impedance transformer allows the measurement of the current fluctuations on a 120 Ω resistor instead of the usual 50 Ω resistor over a large bandwidth ($0.5 - 4.5$ GHz). The measured noise temperature, defined by:

$$T_S = Z_0 S(\Omega)/4k_B \tag{2.33}$$

is therefore increased by a factor 2.4; for a typical value of the noise power spectral density $S(\Omega) = e^2 f_0$, the measured noise temperature increases from $T_S(50\Omega) \approx 35$ μK to $T_S(120\Omega) \approx 83$ μK. This last value is still extremely small compared to the noise temperature of the cryogenic amplifiers $T_N \approx 7$ K; we therefore use an interferometric amplification technique, which is the cryogenic equivalent of the double balanced amplifier technique [93]. This technique can be seen as the microwave analog of a Mach-Zehnder interferometer, where the cryogenic amplifiers are placed in the inner arms. We show in chapter 4 that it greatly enhances the stability of the measurement.

The noise emitted by the single electron emitter is measured by subtracting the reference value when the QPC transmission is set to zero; this allows us to suppress the thermal fluctuations of both the edge channels and the 120 Ω measurement load, and makes the measurement insensitive to fluctuations of the amplification parameters as well as variations of the temperatures in the dilution insert.

The combination of the three-terminal geometry, the quarter wave impedance transformer and the interferometric amplification technique allows the accurate measurement of the autocorrelation of the current fluctuations emitted by the single electron emitter during extended periods of time; we demonstrate in chapter 4 a resolution smaller than 10 μK $\approx e^2 f_0/8$ in about 2 hours.

2.5 Experimental results

In this section, we present results of the experimental measurement of the autocorrelation of the current fluctuations emitted by the source. We have measured the noise power spectral density at the

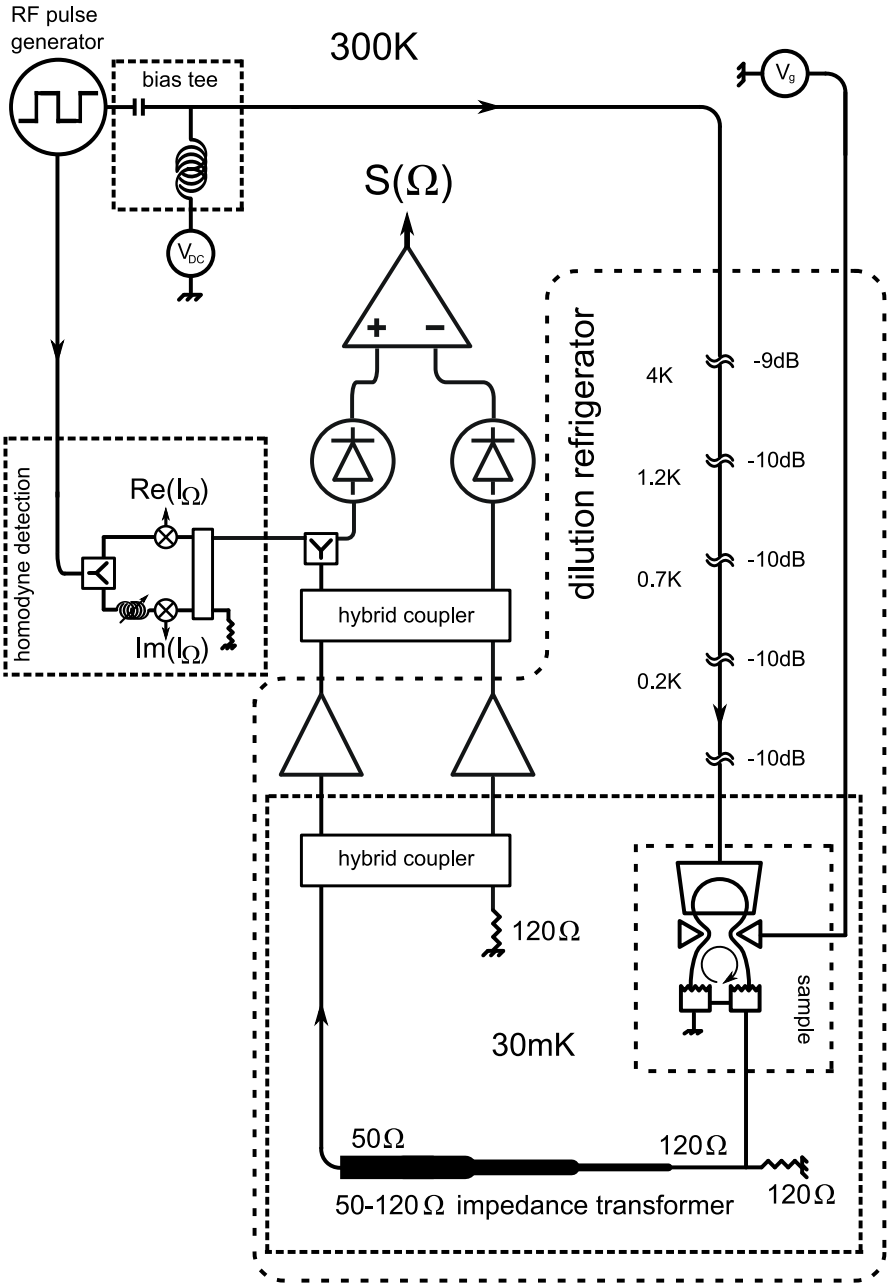

Figure 2.14: Schematic view of the setup used for high-frequency noise measurements. The derivation of the signal to a homodyne detection allows the simultaneous measurement of the average AC current and the power spectral density of the current fluctuations around 1.5 GHz.

excitation frequency $S(\Omega)$, in the charge injection regime $2eV_{exc} = \Delta$.

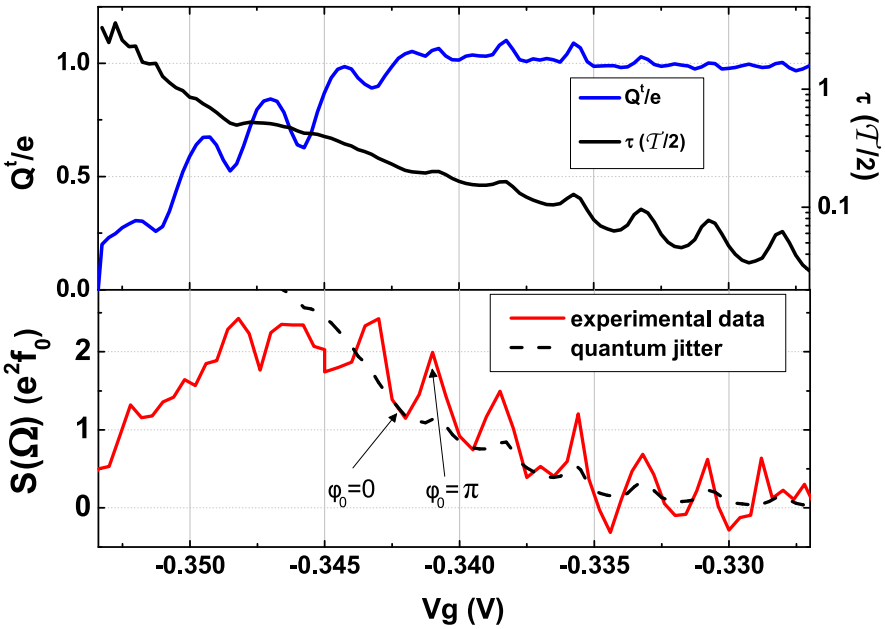

Figure 2.15: Measured noise as a function of the QPC gate voltage V_g. Upper panel: escape time and average transfered charge versus V_g, extracted from the average AC current measurements presented in chapter 1. Lower panel: noise measurements. The red line corresponds to experimental data, the black dashed line to the quantum jitter limit calculated with the values of the escape time presented in the upper panel.

2.5.1 Noise versus QPC gate voltage

We have measured the noise as a function of the QPC gate voltage V_g, plotted in Fig.2.15. The values of the noise in units of $e^2 f_0$ are deduced from the calibration of the noise measurement setup described in chapter 4. The calibration gives us the equivalent noise temperature T_S, which is then converted in the noise power spectral density $S(\Omega)$ using the formula: $S(\Omega)[e^2 f_0] = 4G_0 k_B T_S / e^2 f_0$, with $G_0 = 1/120\ \Omega$. The uncertainty on the calibration is equal to $\pm 5\%$; it is however neglected in Fig.2.15, since the error bars corresponding to the standard error on the successive measurements (see chapter 4) are larger than the uncertainty on the calibration.

As expected, $S(\Omega)$ vanishes at zero and unity transmissions, and its maximum value reaches $\sim 2e^2 f_0$. When the average transfered charge $\mathcal{Q}^t = e$, the noise has a finite value and presents oscillations corresponding to the resonant condition $\phi_0 = \pi$. The global variation of $S(\Omega)$ with V_g cannot be taken into account with an ideal QPC transmission law: in particular, neither the linear QPC transmission law (see 1.3.2.4) nor the non-linear one (see 1.4.3.2) achieve to accurately reproduce the global variation of $S(\Omega)$. However, the experimental data in the anti-resonant condition $\phi_0 = 0$ present an excellent agreement with the quantum jitter (dashed line) calculated using the measured escape time τ in Fig.2.15. In the next paragraph, we will therefore focus on the $\phi_0 = 0$ regime, which is well reproduced by the heuristic model.

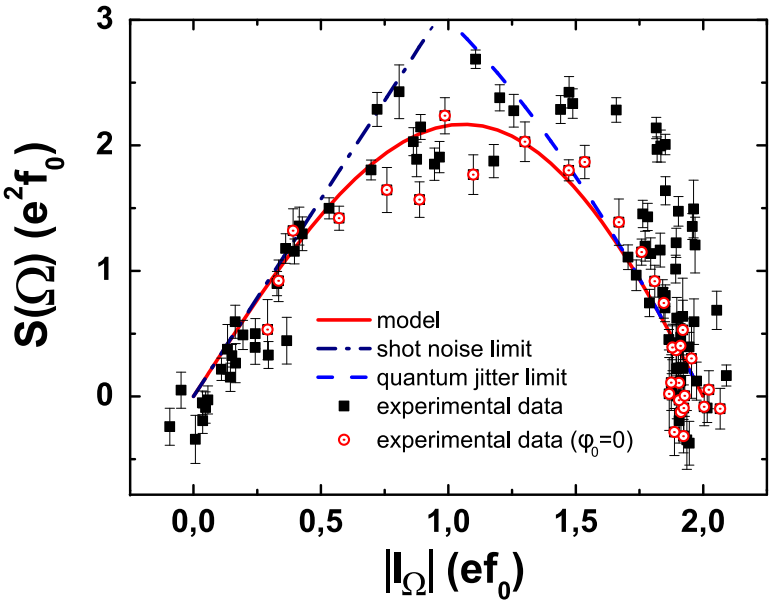

Figure 2.16: Measured noise power spectral density versus modulus of the first harmonic. The black squares are experimental data; points in the $\phi = 0$ regime are highlighted by the red circles. The red line corresponds to the theoretical formula given in Eq.2.29, and the dashed lines to the shot noise and quantum jitter limits.

2.5.2 Universal graphs

As mentioned in 2.3.2.2, the easiest way to compare our experimental data and the theoretical models without free parameters is to plot the noise as a function of the modulus of the current. The curve is shown in Fig.2.16; the red circles correspond to $\phi_0 = 0$. For high values of the current, the points in the resonant regime $\phi_0 = \pi$ systematically fall above the points in the anti-resonant regime $\phi_0 = 0$: this corresponds to the oscillations in the noise as a function of V_g presented in Fig.2.15. While the agreement between the data in the $\phi_0 = 0$ regime and the theory is good at both ends of the curves, it is less satisfactory for intermediate values of the current (between ~ 0.75 and $\sim 1.25ef_0$), where the experimental results are significantly lower than their expected values. This can be explained by the fact that for these values of the transmission, the excitation voltage does not exactly compensate the level spacing, as seen in Fig.1.16 and 1.17: $|I_\Omega|$ presents oscillations with V_g, which corresponds to a $2eV_{exc} < \Delta$ regime. The shot noise and quantum jitter regimes (dashed lines) are nonetheless well described by our results.

- **Noise versus escape time**

The simultaneous measurement of the noise and the conductance allows us to plot the noise as a function of the escape time τ: in this representation, the contribution of the quantum jitter appears clearly (see Fig.2.11), which enables an unambiguous experimental demonstration of single charge emission. We have plotted in Fig.2.17 the variation of the noise in the anti-resonant regime $\phi_0 \approx 0$, corresponding to the optimal operating conditions of the source, as a function of the escape time. The error bars on the escape time correspond to an uncertainty on the global phase tuning of $\pm 2°$, and an estimated error on the conductance measurement of $0.01ef_0$. For long escape times, the error bars become very large because both real and imaginary part of the current are essentially equal to zero.

The experimental data present an excellent agreement with the model, without any free parameter.

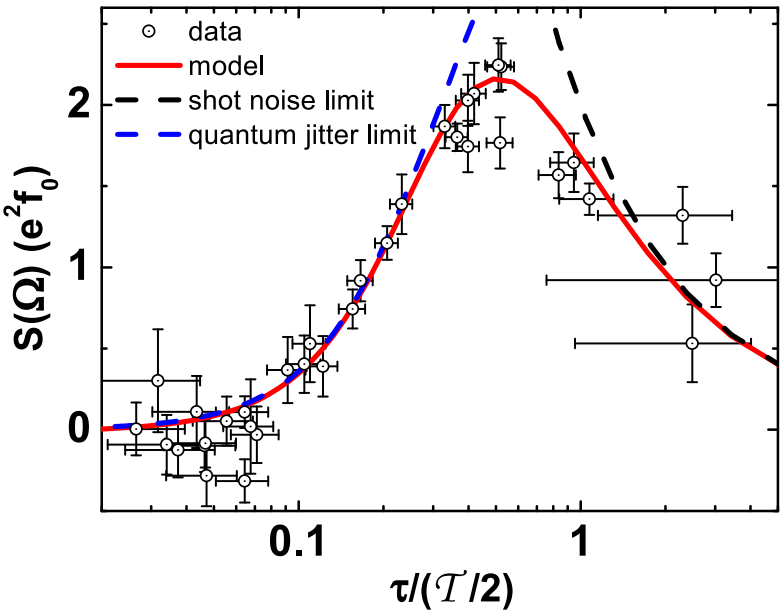

Figure 2.17: Measured noise power spectral density versus escape time, in the $\phi \approx 0$ regime (black circles). The error bars on the escape time correspond to an uncertainty of $\pm 2°$ on the global phase tuning and of $\pm 0.01 e f_0$ on the real and imaginary parts of the first harmonic. The red line corresponds to the scattering model, and the dashed lines to the shot noise and quantum jitter limits.

In particular, the quantum jitter limit is clearly demonstrated in Fig.2.17, which confirms the on-demand single electron emitter nature of our device.

2.5.3 Noise oscillations and QPC transmission law

Let us now focus on the oscillations presented by the noise as a function of the QPC gate voltage V_g. As mentioned before, these oscillations correspond to the resonant regime $\phi_0 \approx \pi$, where charges are emitted close to the Fermi energy. This regime cannot be described by the heuristic model; the scattering model shows however that the noise in this regime presents strong variations with the temperature and the shape of the excitation drive. In particular, the number of odd harmonics contained in the excitation square signal significantly changes the values of the noise at resonance.

We use an *Agilent 1134A Pulse Pattern Generator* to drive our device out of equilibrium. Square signals can be generated at frequencies up to 3.35 GHz; using a GHz spectrum analyzer, we have observed that the generated signal at 1.5 GHz presents contains three odd harmonics. In order to fit our experimental results, we have therefore calculated the noise in the scattering model with an excitation square signal containing three harmonics. We have extracted the QPC transmission law from the measurement of the escape time as a function of V_g, using Eq.1.49: $\tau = h/\Delta(1/D - 1/2)$, see Fig.2.18. The transmission presents oscillations as a function of V_g that correspond to the oscillations in the escape time.

We have combined the measured transmission and an excitation square signal containing three odd harmonics to calculate the noise as a function of V_g in the scattering model. The result is shown in Fig.2.19. As expected from the comparison between the scattering and heuristic models, the agreement between experimental and numerical data is excellent in the $\phi_0 \approx 0$ regime, particularly in the quantum jitter limit, where we have shown in the previous section that our device is indeed an on-demand single

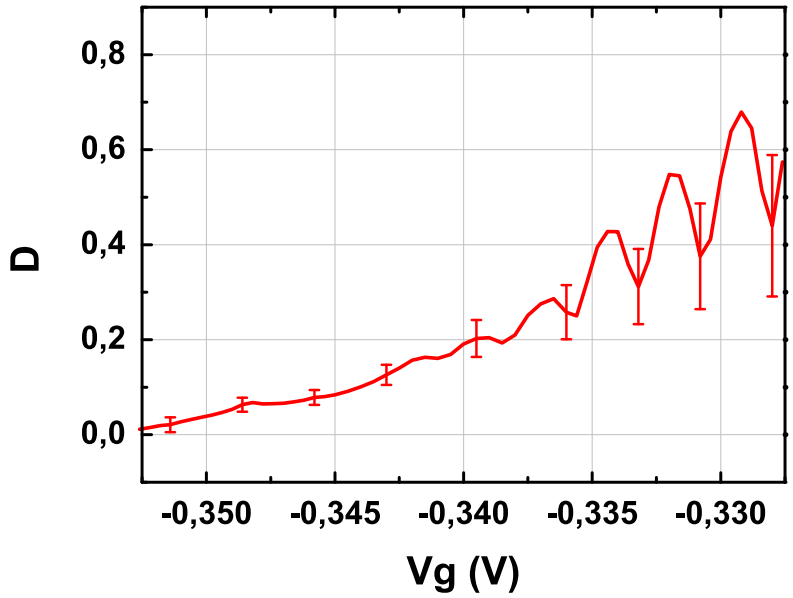

Figure 2.18: QPC transmission law, extracted from the measurements of the escape time using the formula $\tau = h/\Delta(1/D - 1/2)$. The error bars correspond to the error bars on the escape time presented in Fig.2.17.

electron emitter. In the resonant regime, the peaks in the noise are qualitatively reproduced. However, because the noise in the $\phi_0 = \pi$ regime is highly dependent on a wide range of parameters such as temperature, number of harmonics, level spacing, or excitation amplitude, it is difficult to find a quantitative agreement.

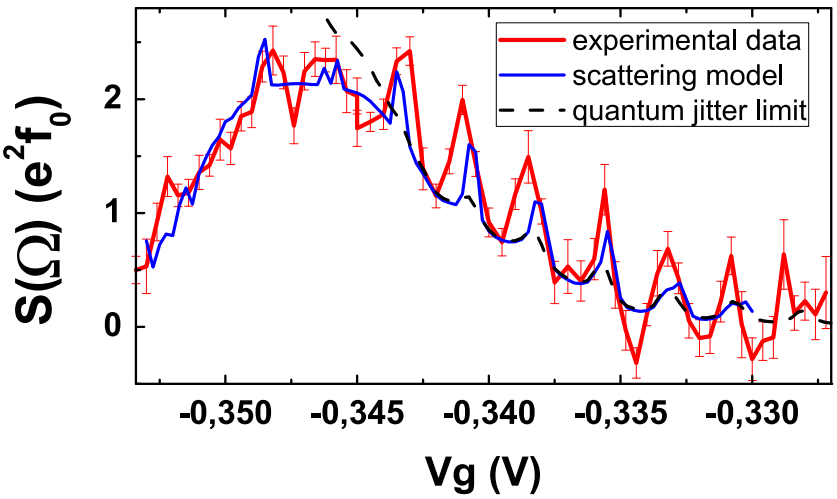

Figure 2.19: Measured noise power spectral density as a function of the QPC gate voltage V_g (red line). The blue line corresponds to the calculated noise in the scattering model, with an excitation signal containing only three odd harmonics. The dashed line corresponds to the quantum jitter limit, calculated with the measured escape time.

While the noise measured in the resonant regime is rather difficult to quantitatively reproduce with the scattering model, its origin is qualitatively understood: the finite number of harmonics con-

tained in the excitation drive creates ripples that shake the energy level in front of the Fermi energy, thus causing additional charge transfer processes. The precise nature of these processes cannot be investigated by only measuring the direct autocorrelation of the current fluctuations emitted by the source. Nonetheless, the presence of these oscillations demonstrate that the energy at which electrons are emitted is indeed controlled by the position of the level in the dot at equilibrium, and that the influence of the Fermi sea can be neglected in the optimal operating condition $\phi_0 = 0$.

Conclusion of chapter 2

In this chapter, we have studied the autocorrelation of the current fluctuations emitted by the mesoscopic capacitor driven in the charge injection regime $2eV_{exc} = \Delta$. The measurement of these high-frequency fluctuations represents a breakthrough in terms of high-frequency noise measurement techniques, and experimentally demonstrates the on-demand single charge emission. More generally, the study of the noise generated by the single electron emitter puts into light an intrinsic high-frequency noise regime, called quantum jitter, which is the signature of single charge emission. This quantum jitter depends on the uncertainty on the emission time with a simple formula given in Eq.2.27. We expect the measurement of this fundamental noise limit to be an unambiguous test of the accuracy of GHz single-charge electronic devices.

We have observed an increase of the emitted noise whenever the source is driven out of its optimal operating conditions, that is in the resonant regime $\phi_0 = \pi$. The excess noise is caused by the limited harmonic content of our excitation signal, which excites the level in the dot in front of the Fermi energy. The presence of the excess noise demonstrates that the energy of the emitted charges is well controlled.

The measurement of the direct autocorrelation of the emitted current fluctuations cannot accurately probe the generation of electron-hole pairs in the charge emission process: indeed, if an electron and a hole are generated at the exact same time, the net current at any frequency created by the pair is zero as long as one can neglect the difference between the group velocity of the electron and the hole. These electron-hole pairs can be unveiled by partitioning the emitted current using a QPC as an electronic beam splitter. In the next chapter, we will show that the correlation of the current fluctuations after partition by the QPC gives access to the number of electron-hole pairs generated by the source, as well as the energy distribution of the emitted charges.

Chapter 3

Current fluctuations in the Hanbury-Brown and Twiss geometry

3.1 Current auto and cross-correlations in the HBT geometry 83
3.1.1 Geometry 83
3.1.2 Autocorrelation 84
3.1.3 Cross-correlation 85
3.1.4 Current conservation 86
3.2 Partition of a single-charge beam: scattering model 87
3.2.1 Calculation of the partition noise 88
3.2.2 Numerical computations 92
3.2.3 Experiment proposals 99
3.3 Experimental setup 101
3.3.1 Sample geometry 102
3.3.2 Setup 103
3.4 Preliminary results 104
3.4.1 Characterization of sample *S434-8* 104
3.4.2 Noise of the single electron source 111
3.4.3 Noise in the HBT geometry 112
3.4.4 Noise measurements at -3.3 T 114

Introduction of chapter 3

The results presented in the previous chapters demonstrate that the mesoscopic capacitor indeed behaves, when driven in the $2eV_{exc} = \Delta$ regime, as a single electron emitter. Furthermore, we have shown in chapter 2 that the correlations of the current fluctuations generated by the sample are the proper tool to probe the outcome of single-charge electron quantum optics experiments. In this chapter, we present the first realization of the single-charge electronic analog of one of the most renown quantum optics experiments, that is the Hanbury-Brown and Twiss (HBT) experiment. In the quantum optics HBT experiment, a single photon is sent towards a beam splitter, and the correlations of the intensities at the two outputs of the beam splitter are measured. This experiment is now commonly performed in order to characterize single photon sources [60, 61]. The zero value of correlations at times smaller than the repetition time of the source indicates the emission of a single photon: indeed, the emission of two photons within a single operating cycle of the source would lead to a positive peak in the intensity correlations at a time corresponding to the delay between the two emissions.

Similarly to its quantum optics counterpart, the single-charge electron quantum optics HBT experiment allows to characterize single electron emitters. In particular, the HBT geometry puts into light the generation of electron/hole pairs, which, as demonstrated by the measurements of photo-assisted noise [94], are the natural excitations of a two-dimensional electron gas in presence of a high-frequency excitation. Moreover, the HBT geometry allows to probe the fundamental phenomena arising from the partition of a single electron beam by a quantum point contact.

In this chapter, we first present a theoretical description of the single-charge electron quantum optics HBT experiment based on the Floquet scattering formalism presented in the first chapter. We particularly focus on the power spectral density of the autocorrelation of the current fluctuations at one of the two outputs of the beam splitter, at both zero and high frequency. We redemonstrate the result predicted in [64]: the zero-frequency part of the power spectral density of the partition noise exactly measures the number of emitted electron-hole pairs per cycle at zero temperature. We furthermore show that the HBT geometry allows to study the energy relaxation of the emitted single charge on adjacent edge channels, similarly to what was done using biased contacts in [24, 25], as well as to measure the energy distribution of the emitted charges by using a biased contact placed at the second input of the beam splitter, leading to quantum state tomography [65].

We then present an experimental study of sample *S434-8*, leading to the first realization of the single-charge electron quantum optics HBT experiment: after describing the experimental procedure used to characterize the sample, we present measurements of the partition noise of a single charge beam. These first measurements demonstrate that our single electron emitter is spin-polarized, since it only injects charges in the outer edge channel, and that the number of excess electron/hole pairs emitted in the optimal operating conditions is negligible.

3.1 Current auto and cross-correlations in the HBT geometry

In the optics HBT experiment, one usually measures the time-resolved cross-correlation between the signals at the two outputs of the beam splitter. Single photon sources are used with typical repetition rates in the tens of MHz ($80MHz$ in [61]). Measurement setups with subnanosecond time resolution allow to accurately probe the short-times cross-correlation, and thus unambiguously demonstrate the suppression of two-particle emission events. Our single electron source however is driven at GHz frequencies; the measurement of time-resolved cross-correlation would therefore need a detection system with a bandwidth ranging from $0Hz$ to a few GHz; furthermore, in order to probe the short-time correlations for small escape times, the bandwidth of the detection system must be comparable to Δ/h, that is a few tens of GHz. Such a multi-octave microwave measurement system is however unrealistic: state-of-the art fast acquisition cards have typical bandwidths equal to 2 GHz. We therefore measure the autocorrelation of each output signals, and take advantage of the dual-outputs geometry to measure both the high-frequency and low-frequency parts of the partition noise. In a practical point of view, this allows us to reuse the high-frequency noise measurement setup developed for the measurements presented in the previous chapter.

In this section, we remind, using a scattering formalism, that current conservation in the HBT geometry implies that the autocorrelation of the current fluctuations at either one of the outputs of the beam splitter yields the same information as the cross-correlation of the two outputs, provided that the fluctuations of the current incoming on the beam splitter are known. This is however true at low frequency: at high frequency, displacement currents must be included in the current conservation. We first show that when the transmission of the QPC is set to 0.5, the autocorrelations of the two output currents fluctuations are equal. We then show that the cross-correlations are symmetric in the output current fluctuations. We finally establish a very simple equation linking the auto and cross-correlation of the output currents fluctuations to the autocorrelation of the fluctuations of the currents incoming on the QPC.

3.1.1 Geometry

The HBT geometry considered in this section is described in Fig.3.1: the device has a four-terminal (two inputs, two outputs) geometry, and is split in two by a Quantum Point Contact. We only consider the outer channel of the integer Quantum Hall Effect regime (and therefore assume that only the outer edge channel is partially transmitted through the QPC).

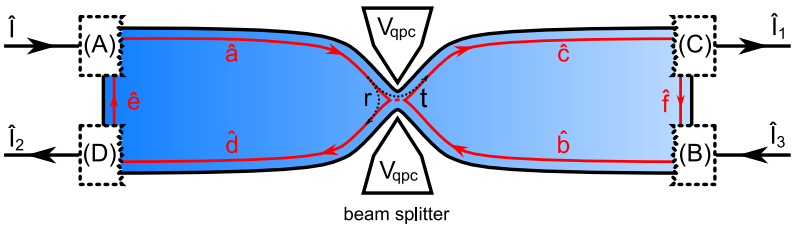

Figure 3.1: Definition of the creation/annihilation operators for the correlations in the HBT geometry.

In these conditions, we define creation/annihilation operators for each region of the device: $\hat{a}^\dagger, \hat{a}$ from contact (A) to the QPC, $\hat{b}^\dagger, \hat{b}$ from contact (B) to the QPC, $\hat{c}^\dagger, \hat{c}$ from the QPC to contact (C), $\hat{d}^\dagger, \hat{d}$ from the QPC to contact (D), $\hat{e}^\dagger, \hat{e}$ from contact (D) to contact (A), and $\hat{f}^\dagger, \hat{f}$ from contact (C) to contact (B). The input current on contact (A) (resp. (B)) is noted $\hat{I}$ (resp. $\hat{I}_3$), and the output current

flowing from contact (C) (resp (D)) noted $\hat{I}_1$ (resp. $\hat{I}_2$). The reflection and transmission amplitudes on the QPC are respectively noted $\sqrt{R}$ and $\sqrt{T}$ (with $R+T=1$), so that:

$$\begin{aligned} \hat{d} &= \sqrt{R}\hat{a} + \sqrt{T}\hat{b} \\ \hat{c} &= -\sqrt{T}\hat{a} + \sqrt{R}\hat{b} \end{aligned} \tag{3.1}$$

3.1.2 Autocorrelation

Let us first calculate the autocorrelation of the output currents $\hat{I}_1(t')$ and $\hat{I}_2(t')$, defined by (see chapter 1):

$$\begin{aligned} \hat{I}_1(t) &= \frac{e}{h}\int d\epsilon_1 d\epsilon_2 \left(\hat{c}^\dagger(\epsilon_1)\hat{c}(\epsilon_2) - \hat{f}^\dagger(\epsilon_1)\hat{f}(\epsilon_2)\right) e^{i\frac{\epsilon_1-\epsilon_2}{\hbar}t} \\ \hat{I}_2(t) &= \frac{e}{h}\int d\epsilon_1 d\epsilon_2 \left(\hat{d}^\dagger(\epsilon_1)\hat{d}(\epsilon_2) - \hat{e}^\dagger(\epsilon_1)\hat{e}(\epsilon_2)\right) e^{i\frac{\epsilon_1-\epsilon_2}{\hbar}t} \end{aligned} \tag{3.2}$$

The creation/annihilation operators are energy dependent; as in the previous chapter, we use the notation $\hat{a}_i = \hat{a}(\epsilon_i)$. Similarly to the calculation of the autocorrelation of the current fluctuations generated by the source presented in 2.2.2, we only consider the cross products of non-independent operators, that is $<\hat{c}_1^\dagger\hat{c}_4><\hat{c}_2\hat{c}_3^\dagger>$ and $<\hat{f}_1^\dagger\hat{f}_4><\hat{f}_2\hat{f}_3^\dagger>$ for the autocorrelation of the fluctuations of output current $\hat{I}_1(t)$, and $<\hat{d}_1^\dagger\hat{d}_4><\hat{d}_2\hat{d}_3^\dagger>$ and $<\hat{e}_1^\dagger\hat{e}_4><\hat{e}_2\hat{e}_3^\dagger>$ for the autocorrelation of the fluctuations of output current $\hat{I}_2(t)$. We therefore have:

$$\begin{aligned} C_{I_1I_1} = \overline{<\delta\hat{I}_1(t)\delta\hat{I}_1(t+t')>}^{t'} &= \frac{e^2}{h^2}\int d\epsilon_{1,2,3,4}\left(<\hat{c}_1^\dagger\hat{c}_4><\hat{c}_2\hat{c}_3^\dagger> + <\hat{f}_1^\dagger\hat{f}_4><\hat{f}_2\hat{f}_3^\dagger>\right) \\ &\quad\times\overline{e^{i(\epsilon_1-\epsilon_2+\epsilon_3-\epsilon_4)t/\hbar}}^{t} e^{i(\epsilon_3-\epsilon_4)t'/\hbar} \\ C_{I_2I_2} = \overline{<\delta\hat{I}_2(t)\delta\hat{I}_2(t+t')>}^{t'} &= \frac{e^2}{h^2}\int d\epsilon_{1,2,3,4}\left(<\hat{d}_1^\dagger\hat{d}_4><\hat{d}_2\hat{d}_3^\dagger> + <\hat{e}_1^\dagger\hat{e}_4><\hat{e}_2\hat{e}_3^\dagger>\right) \\ &\quad\times\overline{e^{i(\epsilon_1-\epsilon_2+\epsilon_3-\epsilon_4)t/\hbar}}^{t} e^{i(\epsilon_3-\epsilon_4)t'/\hbar} \end{aligned} \tag{3.3}$$

The term $<\hat{f}_1^\dagger\hat{f}_4><\hat{f}_2\hat{f}_3^\dagger>$ (resp. $<\hat{e}_1^\dagger\hat{e}_4><\hat{e}_2\hat{e}_3^\dagger>$) only yields the thermal fluctuations of the electrons emitted by contact (C) (resp. contact (D)). If the temperatures of the two contacts are equal, the contributions of those two terms are the same. Let us now focus on the contribution of the operators $\hat{c}^\dagger, \hat{c}$ and $\hat{d}^\dagger, \hat{d}$, and expand it in terms of the operators $\hat{a}^\dagger, \hat{a}$ and $\hat{b}^\dagger, \hat{b}$ using Eq.3.1:

$$\begin{aligned} <\hat{c}_1^\dagger\hat{c}_4><\hat{c}_2\hat{c}_3^\dagger> &= <T\hat{a}_1^\dagger\hat{a}_4 - \sqrt{RT}(\hat{a}_1^\dagger\hat{b}_4 + \hat{b}_1^\dagger\hat{a}_4) + R\hat{b}_1^\dagger\hat{b}_4> \\ &\quad\times <T\hat{a}_2\hat{a}_3^\dagger - \sqrt{RT}(\hat{a}_2\hat{b}_3^\dagger + \hat{b}_2\hat{a}_3^\dagger) + R\hat{b}_2\hat{b}_3^\dagger> \\ <\hat{d}_1^\dagger\hat{d}_4><\hat{d}_2\hat{d}_3^\dagger> &= <R\hat{a}_1^\dagger\hat{a}_4 - \sqrt{RT}(\hat{a}_1^\dagger\hat{b}_4 + \hat{b}_1^\dagger\hat{a}_4) + T\hat{b}_1^\dagger\hat{b}_4> \\ &\quad\times <R\hat{a}_2\hat{a}_3^\dagger - \sqrt{RT}(\hat{a}_2\hat{b}_3^\dagger + \hat{b}_2\hat{a}_3^\dagger) + T\hat{b}_2\hat{b}_3^\dagger> \end{aligned} \tag{3.4}$$

Since the operators $\hat{a}$ and $\hat{b}$ are assumed to be independent, the cross terms $<\hat{a}_i^\dagger\hat{b}_j>$ (and any other combination of both operators) vanish. We finally have:

$$\begin{aligned} < \hat{c}_1^\dagger \hat{c}_4 >< \hat{c}_2 \hat{c}_3^\dagger > &= T^2 < \hat{a}_1^\dagger \hat{a}_4 >< \hat{a}_2 \hat{a}_3^\dagger > + R^2 < \hat{b}_1^\dagger \hat{b}_4 >< \hat{b}_2 \hat{b}_3^\dagger > \\ &\quad + RT \left(< \hat{a}_1^\dagger \hat{a}_4 >< \hat{b}_2 \hat{b}_3^\dagger > + < \hat{b}_1^\dagger \hat{b}_4 >< \hat{a}_2 \hat{a}_3^\dagger > \right) \\ < \hat{d}_1^\dagger \hat{d}_4 >< \hat{d}_2 \hat{d}_3^\dagger > &= R^2 < \hat{a}_1^\dagger \hat{a}_4 >< \hat{a}_2 \hat{a}_3^\dagger > + T^2 < \hat{b}_1^\dagger \hat{b}_4 >< \hat{b}_2 \hat{b}_3^\dagger > \\ &\quad + RT \left(< \hat{a}_1^\dagger \hat{a}_4 >< \hat{b}_2 \hat{b}_3^\dagger > + < \hat{b}_1^\dagger \hat{b}_4 >< \hat{a}_2 \hat{a}_3^\dagger > \right) \end{aligned} \tag{3.5}$$

When the QPC is set to transmission 0.5, that is when $R = T = 0.5$, the two cross terms $< \hat{c}_1^\dagger \hat{c}_4 >< \hat{c}_2 \hat{c}_3^\dagger >$ and $< \hat{d}_1^\dagger \hat{d}_4 >< \hat{d}_2 \hat{d}_3^\dagger >$ are equal. We therefore have, if the two output contacts have the same temperature, the trivial result $C_{I_1 I_1} = C_{I_2 I_2}$: at transmission 0.5, because of the symmetry of the system, the autocorrelation of the fluctuations of the output currents are equal.

Eq.3.5 will be useful when calculating the noise of the single electron emitter in the HBT geometry.

3.1.3 Cross-correlation

Let us now calculate the cross-correlation of the fluctuations of currents $\hat{I}_1(t)$ and $\hat{I}_2(t)$, that is $C_{I_1 I_2} = \overline{< \delta\hat{I}_1(t)\delta\hat{I}_2(t+t') >}^{t'}$ and $C_{I_2 I_1} = \overline{< \delta\hat{I}_2(t)\delta\hat{I}_1(t+t') >}^{t'}$. Following Eq.3.2, the product of currents $\hat{I}_1(t)$ and $\hat{I}_2(t)$ yields products of the operators $\hat{c}_i^\dagger \hat{c}_j$ (resp. $\hat{f}_i^\dagger \hat{f}_j$) with $\hat{d}_i^\dagger \hat{d}_j$ (resp. $\hat{e}_i^\dagger \hat{e}_j$). When considering the cross-correlation of the fluctuations, the contributions of $\hat{e}_i^\dagger \hat{e}_j$ and $\hat{f}_i^\dagger \hat{f}_j$ vanish since these operators are independent. The only non-vanishing term (due to the relation between $\hat{c}^\dagger, \hat{c}$ and $\hat{d}^\dagger, \hat{d}$ given in Eq.3.1) is therefore $< \hat{c}_1^\dagger \hat{c}_2 \hat{d}_3^\dagger \hat{d}_4 >$ in the product $\hat{I}_1(t)\delta\hat{I}_2(t+t')$, and $< \hat{d}_1^\dagger \hat{d}_2 \hat{c}_3^\dagger \hat{c}_4 >$ in $\hat{I}_2(t)\delta\hat{I}_1(t+t')$. The cross-correlators of the fluctuations are therefore given (after applying Wick's theorem in order to only consider the cross terms) by:

$$\begin{aligned} C_{I_1 I_2} = \overline{< \delta\hat{I}_1(t)\delta\hat{I}_2(t+t') >}^{t} &= \frac{e^2}{h^2} \int d\epsilon_{1,2,3,4} < \hat{c}_1^\dagger \hat{d}_4 >< \hat{c}_2 \hat{d}_3^\dagger > \\ &\quad \times \overline{e^{i(\epsilon_1 - \epsilon_2 + \epsilon_3 - \epsilon_4)t/\hbar}}^{t} e^{i(\epsilon_3 - \epsilon_4)t'/\hbar} \\ C_{I_2 I_1} = \overline{< \delta\hat{I}_2(t)\delta\hat{I}_2(t+t') >}^{t'} &= \frac{e^2}{h^2} \int d\epsilon_{1,2,3,4} < \hat{d}_1^\dagger \hat{c}_4 >< \hat{d}_2 \hat{c}_3^\dagger > \\ &\quad \times \overline{e^{i(\epsilon_1 - \epsilon_2 + \epsilon_3 - \epsilon_4)t/\hbar}}^{t} e^{i(\epsilon_3 - \epsilon_4)t'/\hbar} \end{aligned} \tag{3.6}$$

We now expand these expressions in terms of the operators $\hat{a}^\dagger, \hat{a}$ and $\hat{b}^\dagger, \hat{b}$, similarly to Eq.3.4:

$$\begin{aligned} < \hat{c}_1^\dagger \hat{d}_4 >< \hat{c}_2 \hat{d}_3^\dagger > &= < -T\hat{a}_1^\dagger \hat{b}_4 - \sqrt{RT}(\hat{a}_1^\dagger \hat{a}_4 - \hat{b}_1^\dagger \hat{b}_4) + R\hat{b}_1^\dagger \hat{a}_4 > \\ &\quad \times < -T\hat{a}_2 \hat{b}_3^\dagger - \sqrt{RT}(\hat{a}_2 \hat{a}_3^\dagger - \hat{b}_2 \hat{b}_3^\dagger) + R\hat{b}_2 \hat{a}_3^\dagger > \\ < \hat{d}_1^\dagger \hat{c}_4 >< \hat{d}_2 \hat{c}_3^\dagger > &= < R\hat{a}_1^\dagger \hat{b}_4 - \sqrt{RT}(\hat{a}_1^\dagger \hat{a}_4 - \hat{b}_1^\dagger \hat{b}_4) - T\hat{b}_1^\dagger \hat{a}_4 > \\ &\quad \times < R\hat{a}_2 \hat{b}_3^\dagger - \sqrt{RT}(\hat{a}_2 \hat{a}_3^\dagger - \hat{b}_2 \hat{b}_3^\dagger) - T\hat{b}_2 \hat{a}_3^\dagger > \end{aligned} \tag{3.7}$$

Since $\hat{a}$ and $\hat{b}$ are independent, we finally obtain:

$$\begin{aligned} < \hat{c}_1^\dagger \hat{d}_4 >< \hat{c}_2 \hat{d}_3^\dagger > &= RT\left(< \hat{a}_1^\dagger \hat{a}_4 >< \hat{a}_2 \hat{a}_3^\dagger > + < \hat{b}_1^\dagger \hat{b}_4 >< \hat{b}_2 \hat{b}_3^\dagger >\right) \\ &\quad -RT\left(< \hat{a}_1^\dagger \hat{a}_4 >< \hat{b}_2 \hat{b}_3^\dagger > + < \hat{b}_1^\dagger \hat{b}_4 >< \hat{a}_2 \hat{a}_3^\dagger >\right) \\ < \hat{d}_1^\dagger \hat{c}_4 >< \hat{d}_2 \hat{c}_3^\dagger > &= RT\left(< \hat{a}_1^\dagger \hat{a}_4 >< \hat{a}_2 \hat{a}_3^\dagger > + < \hat{b}_1^\dagger \hat{b}_4 >< \hat{b}_2 \hat{b}_3^\dagger >\right) \\ &\quad -RT\left(< \hat{a}_1^\dagger \hat{a}_4 >< \hat{b}_2 \hat{b}_3^\dagger > + < \hat{b}_1^\dagger \hat{b}_4 >< \hat{a}_2 \hat{a}_3^\dagger >\right) \end{aligned} \tag{3.8}$$

The cross-correlators $C_{I_1 I_2}$ and $C_{I_2 I_1}$ are therefore equal, whatever the value of the QPC transmission. Furthermore, at transmission 0.5, a simple relation can be found between Eq.3.5 and Eq.3.8:

$$< \hat{c}_1^\dagger \hat{c}_4 >< \hat{c}_2 \hat{c}_3^\dagger > + < \hat{c}_1^\dagger \hat{d}_4 >< \hat{c}_2 \hat{d}_3^\dagger >= 2T^2\left(< \hat{a}_1^\dagger \hat{a}_4 >< \hat{a}_2 \hat{a}_3^\dagger > + < \hat{b}_1^\dagger \hat{b}_4 >< \hat{b}_2 \hat{b}_3^\dagger >\right) \tag{3.9}$$

Eq.3.9 therefore implies that the sum of the auto and cross-correlators is equal to half the sum of the autocorrelation of the incoming current fluctuations.

3.1.4 Current conservation

The result of the previous paragraph can be established with a simple consideration of current conservation: the net current flowing into the sample $\hat{I} + \hat{I}_3$ is necessarily equal to the net current leaving the sample $\hat{I}_1 + \hat{I}_2$. One has therefore:

$$\hat{I} + \hat{I}_3 = \hat{I}_1 + \hat{I}_2 \tag{3.10}$$

Let us calculate the autocorrelation of the fluctuations of the net current flowing into the sample $< \delta(\hat{I} + \hat{I}_3)\delta(\hat{I}' + \hat{I}_3') >$, with $\hat{I}' = \hat{I}(t + t')$, while assuming that $\hat{I}$ and $\hat{I}_3$ are non-correlated:

$$\begin{aligned} < \delta(\hat{I} + \hat{I}_3)\delta(\hat{I}' + \hat{I}_3') > &= < (\hat{I} + \hat{I}_3)(\hat{I}' + \hat{I}_3') > - < (\hat{I} + \hat{I}_3) >< (\hat{I}' + \hat{I}_3') > \\ &= < \hat{I}\hat{I}' + \hat{I}_3\hat{I}' + \hat{I}\hat{I}_3' + \hat{I}_3\hat{I}_3' > - < (\hat{I} + \hat{I}_3) >< (\hat{I}' + \hat{I}_3') > \\ &= < \hat{I}\hat{I}' > - < \hat{I} >< \hat{I}' > + < \hat{I}_3\hat{I}_3' > - < \hat{I}_3 >< \hat{I}_3' > \\ &= C_{II} + C_{I_3 I_3} \end{aligned} \tag{3.11}$$

One can now use Eq.3.10 to express the left term in Eq.3.11 as a function of the output currents $\hat{I}_1, \hat{I}_2$:

$$\begin{aligned} < \delta(\hat{I} + \hat{I}_3)\delta(\hat{I}' + \hat{I}_3') > &= < \delta(\hat{I}_1 + \hat{I}_2)\delta(\hat{I}_1' + \hat{I}_2') > \\ &= < (\hat{I}_1 + \hat{I}_2)(\hat{I}_1' + \hat{I}_2') > - < (\hat{I}_1 + \hat{I}_2) >< (\hat{I}_1' + \hat{I}_2') > \\ &= < \hat{I}_1\hat{I}_1' + \hat{I}_2\hat{I}_1' + \hat{I}_1\hat{I}_2' + \hat{I}_2\hat{I}_2' > - < (\hat{I}_1 + \hat{I}_2) >< (\hat{I}_1' + \hat{I}_2') > \\ &= C_{I_1 I_1} + C_{I_2 I_2} + C_{I_1 I_2} + C_{I_2 I_1} \end{aligned} \tag{3.12}$$

We therefore have:

$$C_{II} + C_{I_3I_3} = C_{I_1I_1} + C_{I_2I_2} + C_{I_1I_2} + C_{I_2I_1} \tag{3.13}$$

This last equation thus gives a direct relation between the auto and cross-correlations of the output current fluctuations, and the autocorrelation of the input current fluctuations. In particular, when the QPC is set to transmission 0.5 (see previous paragraphs), this expression becomes:

$$C_{II} + C_{I_3I_3} = 2C_{I_1I_1} + 2C_{I_1I_2} \tag{3.14}$$

As we have shown in the last paragraph, the sum of the auto and cross-correlators of the output current fluctuations is indeed equal to half the sum of the autocorrelation of the incoming current fluctuations. Furthermore, when the current $\hat{I}_3$ flowing into contact (B) is noiseless (for instance, if the contact is grounded, or biased), we have $C_{I_3I_3} = 0$, which implies:

$$C_{II} = 2C_{I_1I_1} + 2C_{I_1I_2} \tag{3.15}$$

One can therefore unequivocally deduce the cross-correlation from the autocorrelation on either output, as long as the noise of the incoming current $\hat{I}$ is known. This is the case for the single electron emitter in the HBT geometry, where the noise of the incoming current is precisely the noise of the source, described and studied in the previous chapter. We can therefore use our high frequency noise measurement setup to compare the noise at transmission 0.5 with the noise at transmission 1 of the beam splitter (provided, of course, that the source is located between contact (A) and the QPC, and the measurement setup connected to contact (C), see next section), and thus obtain all the information contained in the cross-correlation.

Finally, one can also suppose that the current $\hat{I}$ is noiseless, as it would be the case when the escape time of the single electron emitter becomes much smaller than the half-period (see previous chapter), or when no source is added, and contact (A) is simply biased. In this case, $C_{II} = 0$, and one finds:

$$C_{I_1I_1} = -C_{I_1I_2} \tag{3.16}$$

When both incoming current are noiseless, the auto and cross-correlation are thus opposite. This result was established in [95] in the case of metallic diffusive conductors, and experimentally demonstrated in [32, 96] in a two-dimensional electron gas.

3.2 Partition of a single-charge beam: scattering model

In this section, we use the scattering model presented in chapter 1 to calculate the autocorrelation of the current fluctuation at either output of the sample[3]. We then present numerical calculations of the output noise; we finally propose several experiments using our device.

[3]The zero-frequency noise in a similar HBT geometry was calculated in [97] in the case of charges generated by AC driven contacts.

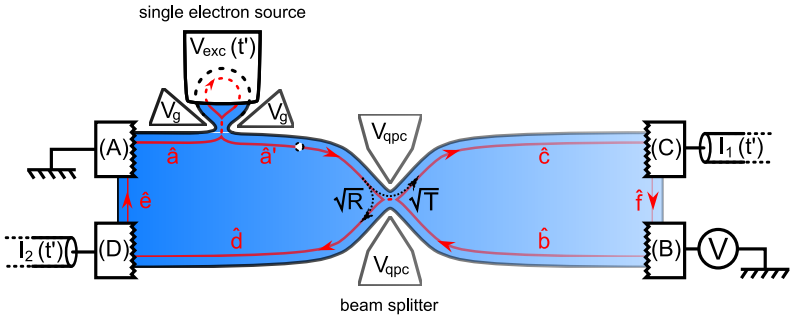

Figure 3.2: Single electron emitter in the HBT geometry.

The geometry of the sample is shown on Fig.3.2: a quantum dot used as the single electron source is inserted between contact (A) and the central QPC; we note $\hat{a}^\dagger, \hat{a}$ the creation/annihilation operators between contact (A) and the dot, and $\hat{a}'^\dagger, \hat{a}'$ the operators between the dot and the central QPC. These operators are then linked by the Floquet scattering matrix $U_m(\epsilon)$ defined in Eq.1.15:

$$\hat{a}'(\epsilon) = \sum_m U_m(\epsilon)\hat{a}(\epsilon + m\hbar\Omega) \tag{3.17}$$

A finite voltage V_{bias} can be applied to contact (B); we will show below how this can be used to measure the energy distribution of the emitted charges.

3.2.1 Calculation of the partition noise

We now calculate the partition noise of the single electron emitter in the HBT geometry, that is the autocorrelation of the fluctuations of either output currents $\hat{I}_1, \hat{I}_2$, as shown in Fig3.2. As it is demonstrated in 3.1.2, the two currents are strictly equivalent, and one only needs to replace $\sqrt{R}$ by $\sqrt{T}$ (and vice-versa) in Eq.3.5 in order to switch from the $C_{I_1I_1}$ to $C_{I_2I_2}$ (the $-$ sign in Eq.3.1 has no importance here, since both $\sqrt{R}$ and $\sqrt{T}$ are found with even powers when calculating the correlation). In this calculation, we only consider the contribution of the source (that is, terms containing $\hat{a}'^\dagger, \hat{a}'$), since any other contribution can be removed by subtracting the noise at the pinch-off (i.e. when the transmission of the source's QPC D is set to zero, see previous chapter). In these conditions, the autocorrelation of the fluctuations of the transmitted current $\hat{I}_1(t)$ are given by:

$$\begin{aligned} C_{I_1I_1}(\tau) = \overline{< \delta\hat{I}_1(t)\delta\hat{I}_1(t+t') >}^t &= \frac{e^2}{h^2}\int d\epsilon_{1,2,3,4} < \hat{c}_1^\dagger\hat{c}_4 >< \hat{c}_2\hat{c}_3^\dagger > \\ &\times \overline{e^{i(\epsilon_1-\epsilon_2+\epsilon_3-\epsilon_4)t/\hbar}}^t e^{i(\epsilon_3-\epsilon_4)t'/\hbar} \end{aligned} \tag{3.18}$$

The term $< \hat{c}_1^\dagger\hat{c}_4 >< \hat{c}_2\hat{c}_3^\dagger >$ can be replaced by its expression given in Eq.3.5. The term $< \hat{b}_1^\dagger\hat{b}_4 >< \hat{b}_2\hat{b}_3^\dagger >$, which corresponds to the partition of the current emitted by contact (B), is suppressed when taking into account the subtraction of the noise at the pinch-off of the source QPC. This yields:

$$\begin{aligned} (< \hat{c}_1^\dagger\hat{c}_4 >< \hat{c}_2\hat{c}_3^\dagger >)_{excess} &= T^2 < \hat{a'}_1^\dagger\hat{a}'_4 >< \hat{a}'_2\hat{a'}_3^\dagger > \\ &+T(1-T)\left(< \hat{a'}_1^\dagger\hat{a}'_4 >< \hat{b}_2\hat{b}_3^\dagger > + < \hat{b}_1^\dagger\hat{b}_4 >< \hat{a}'_2\hat{a'}_3^\dagger >\right) \end{aligned} \tag{3.19}$$

The term $< \hat{a'}_1^\dagger\hat{a}'_4 >< \hat{a}'_2\hat{a'}_3^\dagger >$ corresponds to the autocorrelation of the current fluctuations emitted by the source, which is calculated in 2.2.2. The Fourier transform of the correlator $C_{I_1I_1}(t')$, defined by:

$$C_{I_1I_1}(\omega) = 2\int d\tau e^{-i\omega\tau} \overline{< \delta\hat{I}_1(t)\delta\hat{I}_1(t+t') >}^t \tag{3.20}$$

is therefore equal to the sum of the noise of the single electron source partitioned by the QPC $T^2S(\omega)$ and a correlation term directly arising from the partition of the single charge electronic beam emitted by the source $T(1-T)C(\omega)$:

$$C_{I_1I_1}(\omega) = T^2S(\omega) + T(1-T)C(\omega) \tag{3.21}$$

To avoid any confusion, let us remind that the term corresponding to the partition of the current emitted by the opposite contact (B) is suppressed by subtracting the noise at the pinch-off.

The first term in Eq.3.21 has been thoroughly studied in the previous chapter; in particular, it was shown to vanish at zero frequency, so that low-frequency noise measurements would allow to only detect the contribution of the correlation term $C(\omega)$. We now calculate this term as a function of the source parameters encoded in the Floquet scattering matrix $U_m(\epsilon)$, and show that it indeed presents a finite zero-frequency part.

Following Eq.3.19, the correlation term $C(\omega)$ is given by:

$$C(\omega) = 2\frac{e^2}{h^2}\int dt' d\epsilon_{1,2,3,4} \left(< \hat{a'}_1^\dagger \hat{a'}_4 >< \hat{b}_2\hat{b}_3^\dagger > + < \hat{b}_1^\dagger\hat{b}_4 >< \hat{a'}_2\hat{a'}_3^\dagger > \right) \times \overline{e^{i(\epsilon_1-\epsilon_2+\epsilon_3-\epsilon_4)t/\hbar}}^t e^{i((\epsilon_3-\epsilon_4)/\hbar-\omega)t'} \tag{3.22}$$

$C(\omega)$ can be decomposed a sum $C(\omega) = C_e(\omega) + C_h(\omega)$. The two contributions $C_e(\omega)$ and $C_h(\omega)$, which, as we will show above, correspond respectively to the contribution of electrons and holes in the partition term $C(\omega)$, are defined by:

$$\begin{aligned}
C_e(\omega) &= 2\frac{e^2}{h^2}\int dt' d\epsilon_{1,2,3,4} < \hat{a'}_1^\dagger \hat{a'}_4 >< \hat{b}_2\hat{b}_3^\dagger > \overline{e^{i(\epsilon_1-\epsilon_2+\epsilon_3-\epsilon_4)t/\hbar}}^t e^{i((\epsilon_3-\epsilon_4)/\hbar-\omega)t'} \\
&= 2\frac{e^2}{h^2}\int dt' d\epsilon_{1,2,4} < \hat{a'}_1^\dagger \hat{a'}_4 > (1-f(\epsilon_2))\, \overline{e^{i(\epsilon_1-\epsilon_4)t/\hbar}}^t e^{i((\epsilon_2-\epsilon_4)/\hbar-\omega)t'} \\
&= 2\frac{e^2}{h}\int d\epsilon_{1,4} < \hat{a'}_1^\dagger \hat{a'}_4 > (1-f(\epsilon_4+\hbar\omega))\, \overline{e^{i(\epsilon_1-\epsilon_4)t/\hbar}}^t \\
C_h(\omega) &= 2\frac{e^2}{h^2}\int dt' d\epsilon_{1,2,3,4} < \hat{b}_1^\dagger \hat{b}_4 >< \hat{a'}_2\hat{a'}_3^\dagger > \overline{e^{i(\epsilon_1-\epsilon_2+\epsilon_3-\epsilon_4)t/\hbar}}^t e^{i((\epsilon_3-\epsilon_4)/\hbar-\omega)\tau} \\
&= 2\frac{e^2}{h^2}\int dt' d\epsilon_{1,2,3} < \hat{a'}_2\hat{a'}_3^\dagger > f(\epsilon_1)\, \overline{e^{i(\epsilon_3-\epsilon_2)t/\hbar}}^t e^{i((\epsilon_3-\epsilon_1)/\hbar-\omega)t'} \\
&= 2\frac{e^2}{h}\int d\epsilon_{2,3} < \hat{a'}_2\hat{a'}_3^\dagger > f(\epsilon_3-\hbar\omega)\, \overline{e^{i(\epsilon_3-\epsilon_2)t/\hbar}}^t
\end{aligned} \tag{3.23}$$

The development of the terms $< \hat{a'}_1^\dagger \hat{a'}_4 >$ and $< \hat{a'}_2\hat{a'}_3^\dagger >$ is similar to the one performed in the previous chapter, in Eqs.2.13-2.14. The average over time t finally yields:

$$\begin{aligned}
C_e(\omega) &= 2\frac{e^2}{h}\sum_m \int d\epsilon\, |U_m(\epsilon)|^2\, f(\epsilon+m\hbar\Omega)(1-f(\epsilon+\hbar\omega)) \\
C_h(\omega) &= 2\frac{e^2}{h}\sum_m \int d\epsilon\, |U_m(\epsilon)|^2\, (1-f(\epsilon+m\hbar\Omega))f(\epsilon-\hbar\omega)
\end{aligned} \tag{3.24}$$

The correlator $C(\omega)$ is therefore given by (with $\epsilon + m \equiv \epsilon + m\hbar\Omega$, where Ω is the drive frequency):

$$C(\omega) = 2\frac{e^2}{h}\sum_m \int d\epsilon\, |U_m(\epsilon)|^2 \left(f(\epsilon+m)(1-f(\epsilon+\hbar\omega)) + (1-f(\epsilon+m))f(\epsilon-\hbar\omega)\right) \quad (3.25)$$

We use this last equation to numerically compute the partition noise as a function of the different parameters of the sample.

3.2.1.1 Biased opposite contact

As described in the beginning of this section, the opposite contact (B) can be biased with a finite voltage V_{bias}. The partition noise of the current emitted by the contact can be removed by subtracting the noise at the pinch-off. In these conditions, the bias voltage only shifts the Fermi function corresponding to the $\hat{b}^\dagger, \hat{b}$ operators, so that $< \hat{b}^\dagger(\epsilon)\hat{b}(\epsilon') >= f(\epsilon + eV_{bias})\delta(\epsilon - \epsilon')$. We thus obtain:

$$\begin{aligned} C(\omega) = 2\frac{e^2}{h}\sum_m \int d\epsilon\, |U_m(\epsilon)|^2 \Big(&f(\epsilon+m)(1-f(\epsilon+\hbar\omega+eV_{bias})) \\ &+(1-f(\epsilon+m))f(\epsilon-\hbar\omega+eV_{bias})\Big) \end{aligned} \quad (3.26)$$

3.2.1.2 Zero-temperature, zero-frequency limit

At zero temperature, the Fermi functions in this equation can be replaced by fixed boundaries in the integrals, so that $\int d\epsilon \ldots (1-f(\epsilon)) = \int_0^{+\infty} d\epsilon \ldots$. Let us demonstrate that $C_e(\omega=0)$ ($C_h(\omega=0)$) is proportional to the total number of electrons (holes) emitted by the source N_+ (N_-) during a measurement time T_{acq}, which can be written as a function of the number of emitted electrons (holes) per period n_+ (n_-):

$$\begin{aligned} N_+ &= f_0 T_{acq} n_+ = \int_0^{+\infty} d\epsilon < \hat{a'}^\dagger(\epsilon)\hat{a'}(\epsilon) > \\ &= \int_0^{+\infty} d\epsilon \sum_{m,m'} |U_m(\epsilon)|^2 f(\epsilon+m)\delta((m-m')\hbar\Omega) \\ N_- &= f_0 T_{acq} n_- = \int_{-\infty}^{0} d\epsilon < \hat{a'}(\epsilon)\hat{a'}^\dagger(\epsilon) > \\ &= \int_{-\infty}^{0} d\epsilon \sum_{m,m'} |U_m(\epsilon)|^2 (1-f(\epsilon+m))\delta((m-m')\hbar\Omega) \end{aligned} \quad (3.27)$$

where T_{acq} is the total acquisition time, and f_0 the drive frequency. The Dirac function $\delta((m-m')\hbar\Omega)$ can be written as:

$$\delta((m-m')\hbar\Omega) = \frac{1}{h}\int_{-T_{acq}/2}^{T_{acq}/2} dt e^{i(m-m')\Omega t} = \frac{T_{acq}}{h}\delta_{m,m'} \tag{3.28}$$

When $T_{acq} \ll 2\pi/\Omega$, we obtain, at zero temperature:

$$\begin{aligned} f_0 n_+ &= \frac{1}{h}\int_0^{+\infty} d\epsilon \sum_m |U_m(\epsilon)|^2 f(\epsilon+m) \\ &= \frac{1}{h}\int_0 d\epsilon \sum_m |U_m(\epsilon)|^2 f(\epsilon+m)(1-f(\epsilon)) \\ f_0 n_- &= \frac{1}{h}\int_{-\infty}^{0} d\epsilon \sum_m |U_m(\epsilon)|^2 (1-f(\epsilon+m)) \\ &= \frac{1}{h}\int_{-\infty} d\epsilon \sum_m |U_m(\epsilon)|^2 f(\epsilon)(1-f(\epsilon+m)) \end{aligned} \tag{3.29}$$

By introducing this expression in Eq.3.25 for $\omega = 0$, one finally obtains:

$$C(\omega=0) = 2e^2 f_0 (n_+ + n_-) \tag{3.30}$$

At zero frequency and zero temperature, the correlator $C(\omega=0)$ is therefore proportional to the sum of the number of electrons emitted per period and the number of holes emitted per period. One can also write it as a function of the number of electron/hole pairs emitted per period $n_{e/h} = (n_+ + n_-)/2$. Since the autocorrelation of the current fluctuations emitted by the source vanish at zero frequency (see chapter 2), the autocorrelation of the current fluctuations after partition by the QPC $C_{I_1 I_1}(\omega=0)$ is then equal to:

$$C_{I_1 I_1}(\omega=0) = 4e^2 f_0 T(1-T) n_{e/h} \tag{3.31}$$

When the QPC transmission is set to 0.5, $C_{I_1 I_1}(\omega=0)$ (at zero temperature) is therefore a direct measurement of the number of electron/hole pairs emitted per period, in units of $e^2 f_0$. This property was first established in [64], using a Floquet scattering formalism and considering a single electronic level in the dot.

- **Biased opposite contact**

When calculating the derivative of Eq.3.26 with respect to the bias voltage applied to the opposite contact V_{bias}, one obtains, for $\omega = 0$:

$$\begin{aligned} \frac{\partial C}{\partial V_{bias}}(\omega=0) = 2\frac{e^2}{h}\sum_m \int d\epsilon\, |U_m(\epsilon)|^2 \Big(& f(\epsilon+m)(-e\frac{df}{d\epsilon}(\epsilon+eV_{bias})) \\ & -(1-f(\epsilon+m))(-e\frac{df}{d\epsilon}(\epsilon+eV_{bias}))\Big) \end{aligned} \tag{3.32}$$

At zero temperature, $(-e\frac{df}{d\epsilon}(\epsilon+eV_{bias})) = e\delta(\epsilon+eV_{bias})$. We thus obtain:

$$\begin{aligned}\frac{\partial C}{\partial V_{bias}}(\omega=0) &= 2\frac{e^2}{h}\sum_m e\,|U_m(-eV_{bias})|^2\Big(f(-eV_{bias}+m)-(1-f(-eV_{bias}+m))\Big)\\ &= 2\frac{e^2}{h}\Big(-\mathcal{N}_e(-eV_{bias})+\mathcal{N}_h(-eV_{bias})\Big)\end{aligned} \tag{3.33}$$

where $\mathcal{N}_e(-eV_{bias})$ ($\mathcal{N}_h(-eV_{bias})$) is the number of electrons (holes) per energy unit at energy $-eV_{bias}$. The derivative of $C(\omega=0)$ with respect to the bias voltage applied to the opposite contact therefore measures the energy distribution of the emitted charges.

3.2.2 Numerical computations

We now present numerical computation of the noise after partition, both at zero frequency (thus only considering the contribution of $C(\omega=0)$) and at finite frequency (thus considering both $C(\omega)$ and $S(\omega)$), for different parameters.

3.2.2.1 Zero-temperature, zero-frequency

We have plotted in Fig.3.3 the dependence of the zero-frequency part of the noise after partition by the QPC $C_{I_1I_1}(\omega=0)=T(1-T)C(\omega=0)$ as a function of the transmission of the central QPC T and the transmission of the dot's QPC D. The noise is calculated in the ideal injection conditions ($2eV_{exc}=\Delta$, $\phi_0=0$) at zero temperature. The level spacing Δ is set to 3 K, corresponding to the level spacing of sample *S434-8* studied in this chapter; the drive frequency f_0 is equal to 1.5 GHz. The variation of the noise with the central QPC transmission T is trivial, since it only contributes in the $T(1-T)$ prefactor at zero frequency. The maximum value of the curve as a function of T (for $T=0.5$) is equal to the number of emitted electron/hole pairs per cycle, which depends on the dot's QPC transmission D. For small values of D, the number of emitted electron/hole pairs vanishes because the escape time becomes much larger than the half-period of the drive. When D increases, $n_{e/h}$ becomes equal to one, thus demonstrating the emission of a single electron followed by a single hole in a cycle. Furthermore, $n_{e/h}$ is equal to unity for a wide range of values of D (typically $0.1-0.8$), indicating that a wide range of escape times is available while the single particle emission remains enforced.

When D becomes close to one, the number of emitted electron/hole pairs increases: indeed, for large transmissions, the quantization of the levels in the dot is lost, so that the source is similar to the type of source mentioned in the introduction, where the Fermi sea is modulated periodically in order to emit single charges. As demonstrated in [57], a Lorentzian-shaped pulse would allow to suppress the emission of additional electron/hole pairs.

- **Variation with the dot equilibrium potential and shape of the drive**

The results shown in chapter 2 indicate that depending on the dot equilibrium potential (that is, on ϕ_0) and the number of odd harmonics in the excitation drive, additional charge transfer processes may take place, in particular in the resonant case $\phi_0=\pi$, for a low number of harmonics.

One therefore expects the number of emitted electron/hole pairs to increase in the resonant case. We have plotted in Fig.3.4 the correlation term $T(1-T)C(\omega=0)$ for $T=0.5$, as a function of the dot's QPC transmission D and the dot equilibrium potential, for several values of the number of odd harmonics. As expected, the number of emitted electron/hole pairs increases significantly (up to a factor 3) for $\phi_0=\pi$, indicating that additional charge transfer processes indeed occur within this

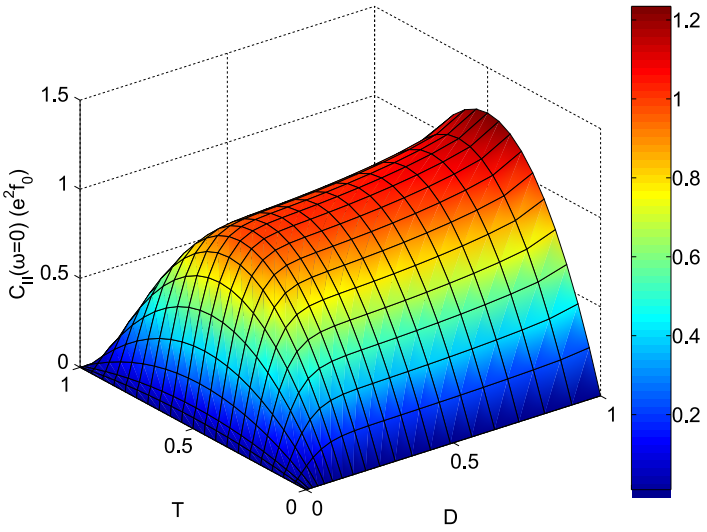

Figure 3.3: Zero-frequency part of the partition noise $C_{I_1I_1}(\omega = 0)$ as a function of the dot QPC transmission D and the central QPC transmission T, at zero temperature. For a fixed transmission D, the partition noise (in units of $e^2 f_0$) is given by $4T(1-T)n_{e/h}(D)$.

scattering formalism. Furthermore, the maximum value of additional electron/hole pairs is reached for two odd harmonics, which corresponds to an excitation signal presenting the largest ripples.

One can note that at transmission unity, the partition noise becomes independent of the dot equilibrium potential since the density of states becomes uniform.

3.2.2.2 Zero-temperature, finite frequency

When the measurement frequency ω becomes finite, one must take into account the contribution of the intrinsic noise generated by the source $S(\omega)$. Particularly, in the configuration described in Fig.3.2, when the central QPC transmission becomes close to unity, $S(\omega)$ becomes preponderant and the situation studied in chapter 2 is recovered. Since $S(\omega)$ and $C(\omega)$ are by construction independent of the transmission T, one can directly compare them, particularly their respective variation with the measurement frequency ω. This variation is plotted in Fig.3.5, for several values of the dot transmission D. For a given transmission, $S(\omega)$ and $C(\omega)$ are quite comparable, except at low frequencies, for which $S(\omega)$ vanishes. At high frequencies, $S(\omega)$ and $C(\omega)$ coincide because of the $\Delta/2$ frequency cutoff: in the anti-resonant case $\phi_0 = 0$, the system cannot emit photons at energies above $\Delta/2$. The width of the cutoff depends only on the transmission D, more precisely on the width of the energy levels of the dot $D\Delta$. When the transmission D becomes small, $S(\omega)$ and $C(\omega)$ coincide over a wide range of the measurement frequency. Indeed, for small transmissions D, $S(\omega)$ is essentially shot noise; one can then easily demonstrate, using Eq.55 in [79], that $C(\omega \neq 0) = S(\omega \neq 0)$, see appendix A.5. The frequency dependence of $S(\omega)$ and $C(\omega)$ can give access to the temporal variation of the cross-correlation $C_{I_1I_2}(t')$: indeed, as stated in Eq.3.15, $C_{I_1I_2}(t')$ can be directly deduced from the autocorrelation of the current fluctuations upstream and downstream of the QPC for $T = 0.5$: $C_{I_1I_2}(t') = C_{II}(t')/2 - C_{I_1I_1}(t')$. In the frequency domain, this reads, using Eq.3.21 with $T = 0.5$:

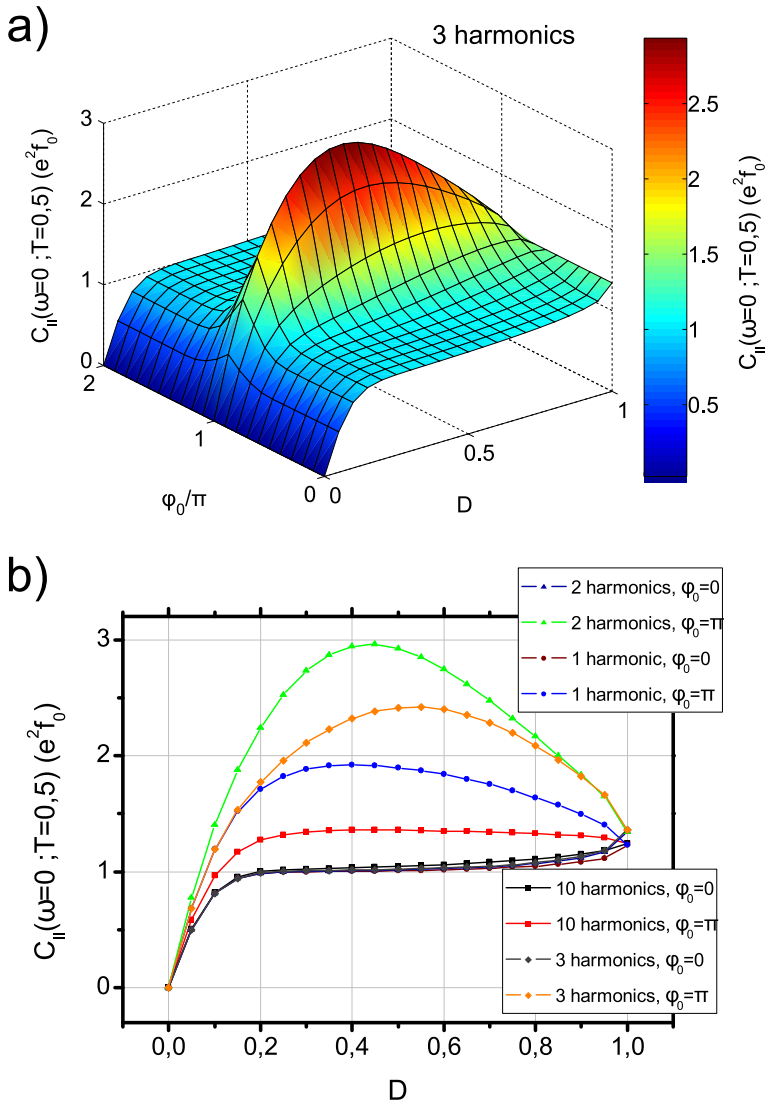

Figure 3.4: a) variation of $C_{I_1I_1}(\omega=0)$ for $T=0.5$ with the transmission D and the dot equilibrium potential, for an excitation drive containing 3 odd harmonics. In the resonant case $\phi_0=\pi$, the number of emitted electron/hole pairs per period increases significantly. **b)** variation of $C_{I_1I_1}(\omega=0)$ for $T=0.5$ with D, in both resonant ($\phi_0=\pi$) and anti-resonant ($\phi_0=0$) cases, for several shapes of the excitation drive.

$$C_{I_1I_2}(\omega) = (S(\omega) - C(\omega))/4 \tag{3.34}$$

We have plotted in Fig.3.6a the cross-correlation in the frequency domain $C_{I_1I_2}(\omega)$, calculated using the data presented in Fig.3.5, for different values of the transmission D. All data present a dip at zero frequency, corresponding to the zero-frequency cutoff of $S(\omega)$ observed in Fig.3.5. When D increases, so do the width and depth of the dip, reflecting the increasing influence of the quantum jitter in the noise. For large values of the frequency, all datasets are equal to zero because of the $\Delta/2$ high-frequency cutoff displayed by both $S(\omega)$ and $C(\omega)$.

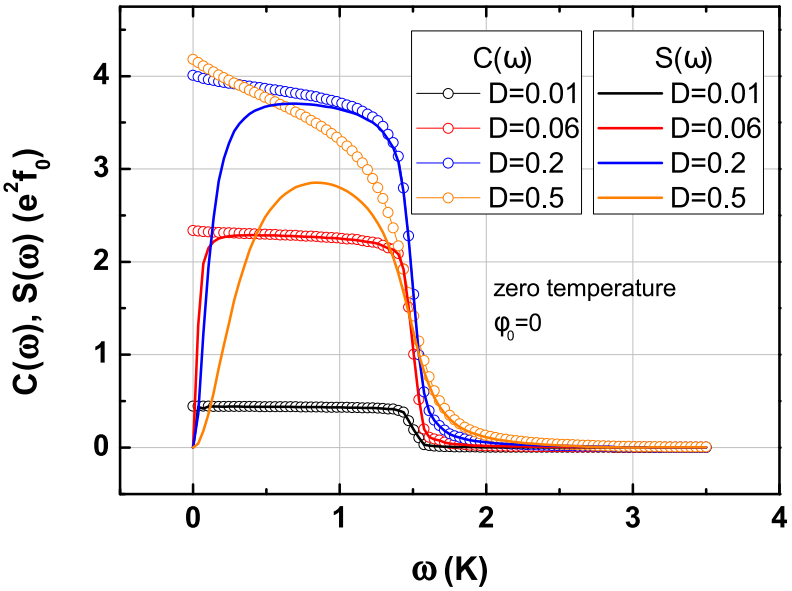

Figure 3.5: Variation of $C(\omega)$ (circles) and $S(\omega)$ (full lines) with the measurement frequency, in the $\phi_0 = 0$ case, at zero temperature. For small transmissions D, $C(\omega)$ and $S(\omega)$ coincide at finite frequency. Here, $\Delta = 3$ K, and $\Omega = 70$ mK.

The temporal variation of the cross-correlation $C_{I_1 I_2}(t')$, obtained by calculating the inverse Fourier transform of the data discussed above, is plotted in Fig.3.6b. The cross-correlation presents a negative dip at zero-time which corresponds to the expected antibunching of the charges at short times, demonstrating single particle emission. The width of the dips, given by the escape time τ, decreases with the dot QPC transmission D, reflecting the charge memory of the dot mentioned in 2.3.1: at low transmission, the escape time becomes larger than the half-period, and the source cannot emit a hole until the electron is emitted (and vice-versa). We have compared the calculated data at $D = 0.5$ with an analytic formula deduced from the heuristic model: at large enough transmission, the dot behaves as an ideal single electron source, so that the cross-correlation of the output currents $\overline{< \hat{I}_1(t)\hat{I}_2(t+t') >}^t$ is equal to zero. The cross-correlation signal is then given by the sole term $-\overline{< \hat{I}_1(t) >< \hat{I}_2(t+t') >}^t$, which, according to Eq.2.26, is equal to $-\frac{e^2 f_0}{\tau} e^{-|t'|/\tau}$. The excellent agreement between the scattering model and this heuristic formula (plotted as circles in Fig.3.6b) demonstrates once again that the scattering model effectively describes the mesoscopic capacitor as an ideal single electron emitter when using the optimal operating conditions.

- **Dependence of the noise at finite frequency on the QPC transmission T**

We have plotted in Fig.3.7 the noise after partition at the drive frequency Ω $C_{I_1 I_1}(\Omega) = T^2 S(\Omega) + T(1-T)C(\Omega)$ as a function of the QPC transmission T, for several values of the dot QPC transmission D. The shape of the curve highly depends on the transmission D, gradually changing from a monotonically increasing polynomial for small D (for which $S(\Omega)$ and $C(\Omega)$ are comparable) to an exact $T(1-T)$ curve for $D = 1$ ($S(\Omega)$ vanishes, while $C(\Omega)$ remains finite). Knowing the precise value of $S(\Omega)$ for a given transmission D allows to easily interpret the noise $C_{I_1 I_1}(\Omega)$.

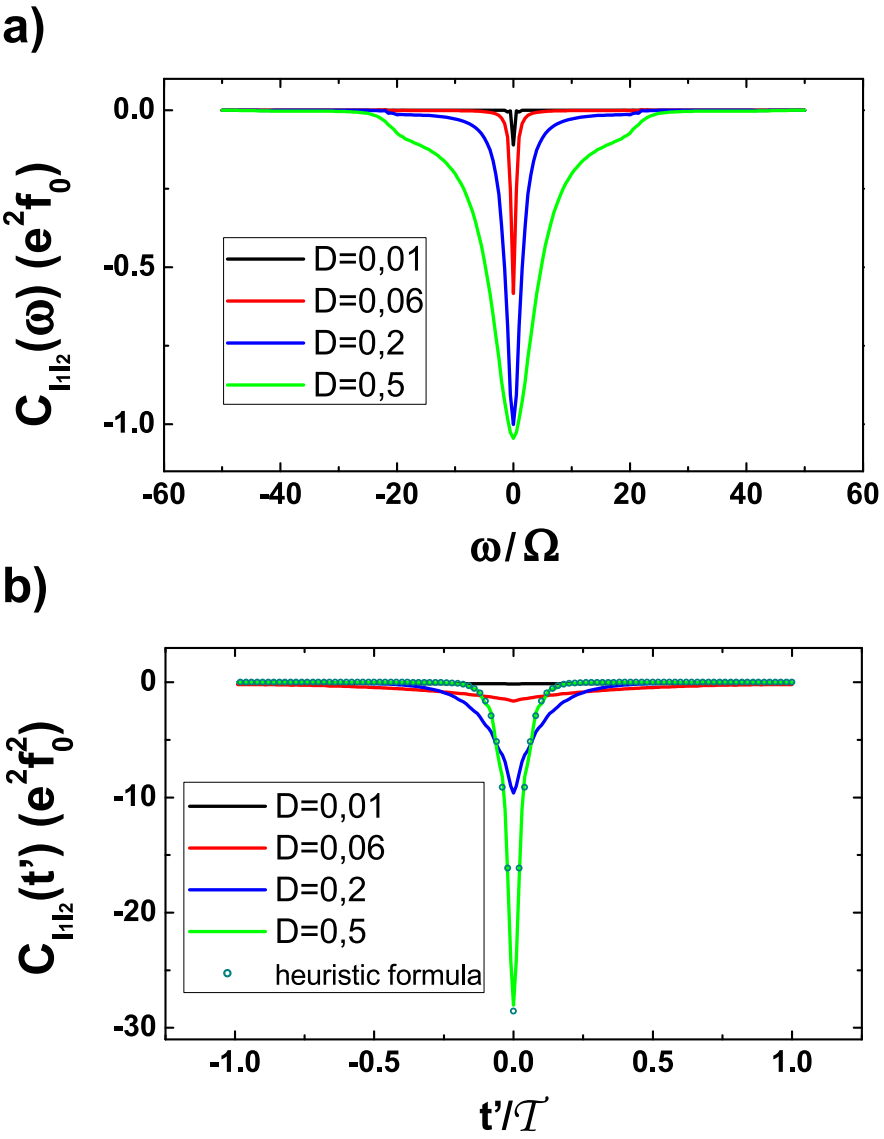

Figure 3.6: Calculation of the frequency (**a**) and time (**b**) variations of the cross-correlation, for several values of the dot QPC transmission D, at $T = 0.5$. Circles in **b)**: analytic formula $C_{I_1 I_2}(t') = -\frac{e^2 f_0}{\tau} e^{-|t'|/\tau}$, derived from the heuristic model.

3.2.2.3 Biased opposite contact

As demonstrated by Eq.3.33, the derivative of the correlation $C(\omega = 0)$ with respect to the bias voltage V_{bias} measures the energy distribution of the emitted charges. As such, it should display a strong dependence on the dot equilibrium potential, especially between the anti-resonant case $\phi_0 = 0$ and the resonant case $\phi_0 = \pi$. We have plotted in Fig.3.8 the dependence of $\frac{\partial C}{\partial V_{bias}}(\omega = 0)$ as a function of V_{bias}, in the anti-resonant and resonant cases, for several values of the dot QPC transmission D. As expected, for $\phi_0 = 0$, $\frac{\partial C}{\partial V_{bias}}(\omega = 0)$ displays a peak (dip) at $eV_{bias} = -\Delta/2$ ($eV_{bias} = +\Delta/2$), with a width proportional $D\Delta$: the single electron source indeed emits charges at an energy $\pm\Delta/2$, with an energy width $D\Delta$. In the resonant case, the energy of the emitted charges is centered on zero: the charges are mainly emitted in resonance with the Fermi energy.

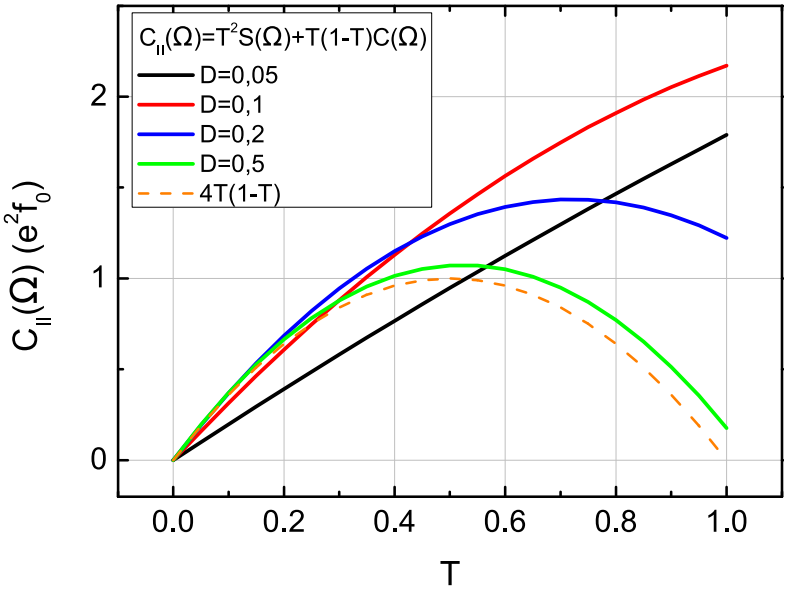

Figure 3.7: Variation of $C_{I_1I_1}(\omega = \Omega)$ with the central QPC transmission T, for several values of D. For large D, the noise becomes comparable to the $T(1-T)$ limit (dashed line).

3.2.2.4 Effect of the temperature

- **Detection of electron/hole pairs**

When one increases the temperature in the expression of the number of emitted electrons and emitted holes per period n_+ and n_- given in Eq.3.29, the Fermi functions ($(1 - f(\epsilon))$ for electrons, $f(\epsilon)$ for holes), which define the boundaries of the integrals at zero temperature, start to broaden. As a result, the value of the integrals diminishes, because the number of emitted electrons (holes) per energy unit $\mathcal{N}_e(\epsilon)$ ($\mathcal{N}_h(\epsilon)$) is integrated with a smaller weight for positive (negative) energies close to the Fermi level. At finite temperature, the autocorrelation of the current fluctuations after partition by the QPC $C_{I_1I_1}(\omega = 0)$ (for $T = 0.5$) is therefore smaller than the total number of electron/hole pairs emitted per period: the accuracy of electron/hole pairs detection is reduced by the temperature. One expects this effect to be particularly strong when charges are emitted close to the Fermi energy, that is in the $\phi_0 = \pi$ regime, or for large transmission D. We have plotted in Fig.3.9 the difference between the zero-frequency noise $C_{I_1I_1}(\omega = 0)$ in the $\phi_0 = \pi$ regime and in the $\phi_0 = 0$ regime (for $T = 0.5$), for an excitation square signal containing 1 (black), 2 (red), 3 (blue) and 10 (dark cyan) odd harmonics, at three different temperatures (0 mK (hollow symbols), 100 mK (full lines), 300 mK (full symbols)). As expected, the difference significantly diminishes when the temperature is increased: less electron/hole pairs are detected. At 300 mK, the difference becomes negative: even though more electron/hole pairs are generated when the charges are emitted close to the Fermi energy, the systems detects less of them than in the anti-resonant regime. This effect is also present at 100 mK for 10 odd harmonics. Working at low enough temperature is therefore crucial in order to precisely measure the number of pairs emitted per period, especially when one takes into account the finite sensitivity of the measurement, which yields error bars typically equal to $0.1 - 0.2e^2 f_0$.

- **Energy distribution of the emitted charges**

At finite temperature, the derivative of $C(\omega = 0)$ with respect to the bias voltage V_{bias} measures the energy distribution of the emitted charges, convoluted by the derivative of the Fermi function.

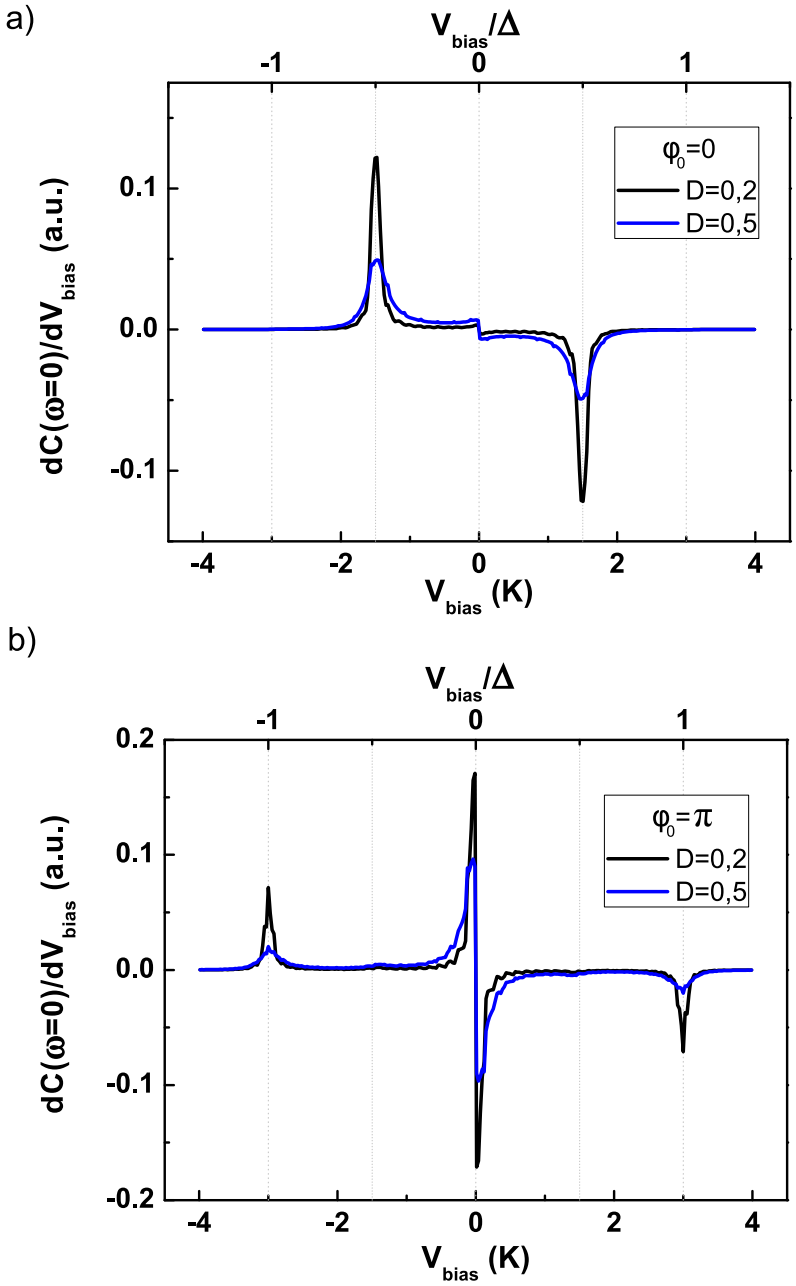

Figure 3.8: Variation of $\partial C(\omega = 0)/\partial V_{bias}$ with V_{bias}, probing the energy distribution of the emitted charges. **a)** anti-resonant case $\phi_0 = 0$: the charges are emitted at an energy $\pm\Delta/2$ above/below the Fermi level. The dot QPC transmission changes the energy width of the emitted charges. **b)** resonant case $\phi_0 = \pi$: the energy of the emitted charges is not well-defined; a large portion of it is centered around the Fermi level.

One therefore expects the peaks and dips in the energy distribution function to be smoothed by the temperature. We have plotted in Fig.3.10 the calculated derivative of $C(\omega = 0)$ with respect to V_{bias} at transmission $D = 0.2$, for three different temperatures, in the $\phi_0 = 0$ (upper panel) and $\phi_0 = \pi$ (lower panel) regimes. As for the detection of electron/hole pairs presented above, the temperature

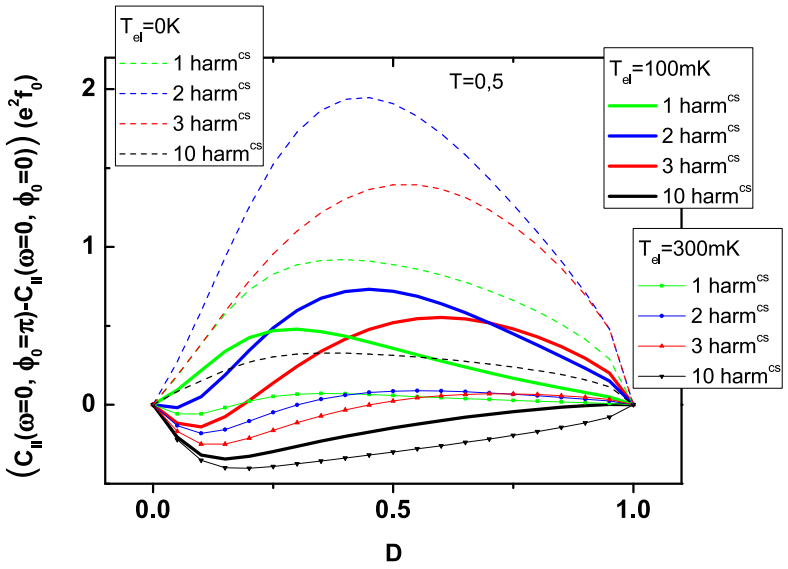

Figure 3.9: Effect of the temperature on the difference $C_{I_1I_1}(\omega = 0, \phi_0 = \pi) - C_{I_1I_1}(\omega = 0, \phi_0 = 0)$ (plotted as a function of the transmission D; $T = 0.5$). Dashed lines: zero temperature limit $T_{el} = 0$ K. Full lines: $T_{el} = 100$ mK. Thin lines with symbols: $T_{el} = 300$ mK. The colors correspond to the number of harmonics in the excitation drive: 1 (green), 2 (blue), 3 (red) and 10 (black). For any shape of the drive, the measured difference diminishes with the temperature.

significantly diminishes the accuracy of the measurement of the emitted charges energy distribution: at 100 mK, the peak corresponding to the electron emitted at energy $\Delta/2$ in the $\phi_0 = 0$ regime is reduced by $\sim 60\%$, while the variations are almost suppressed at 500 mK.

A finite temperature (within reasonable bounds, that is $\lesssim 100$ mK) is less problematic for this measurement than for the measurement of the variation of the number of emitted electron/hole pair with the dot static potential ϕ_0 described in the previous paragraph, since the detected variable is $C(\omega = 0)$, which typical levels are not affected by the temperature: only the derivative of $C(\omega = 0)$ with respect to V_{bias}) changes with the temperature (see insets in Fig.3.10: at 100 mK (red line), the variation of $C(\omega = 0)$ with V_{bias} is quite similar to the zero-temperature case (black line)).

3.2.3 Experiment proposals

Based on the numerical results presented above, one can consider several measurements using the HBT geometry:

- **Measurement of the number of emitted electron/holes pairs per period**

Provided that the electronic temperature is low enough, one can measure the zero-frequency part of the noise after partition in order to measure the number of emitted electron/hole pairs per period in several operating conditions of the source. Indeed, in the study of the noise of the source presented in the previous chapter, oscillations in the noise $S(\Omega)$ were observed as a function of the gate voltage V_g. We have shown that these oscillations correspond to an increase in the noise in the $\phi_0 = \pi$ regime, where charges are emitted close to the Fermi energy; this increase is due to the limited harmonic content of the excitation signal, which causes the highest occupied level in the dot to oscillate rapidly in front of the Fermi level. It is thus highly interesting to link the increase in $S(\Omega)$ with the variation of the number of emitted electron/hole pairs, in order to characterize the processes occurring when a

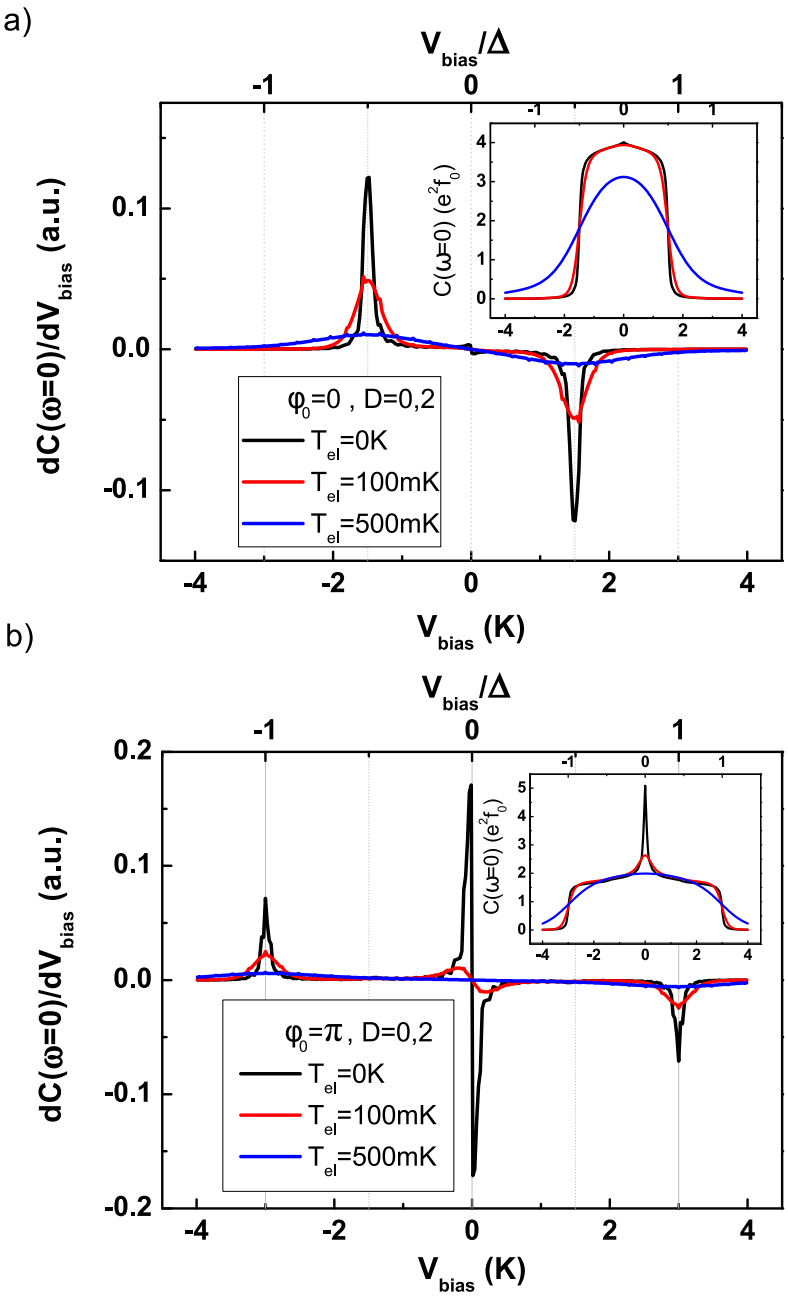

Figure 3.10: $\partial C(\omega = 0)/\partial V_{bias}$ versus V_{bias}, for increasing temperatures: 0 K (black), 100 mK (red), 500 mK (blue). **a)** anti-resonant case $\phi_0 = 0$. **b)** resonant case $\phi_0 = \pi$. Insets: variation of $C(\omega = 0)$ with V_{bias}, for the same temperatures.

charge is emitted close to the Fermi energy. One can also study the variation of the number of emitted pairs in the $\phi_0 = \pi$ regime with the excitation frequency. Indeed, one expects the number of emitted electron/hole pairs to increase when the driving frequency is lowered: it was predicted in [64] that the number of electron/hole pairs generated by placing the electronic level in the dot in resonance with the Fermi energy during a time t logarithmically diverges when t increases (*i.e.* when the driving frequency is lowered). This effect is related to the "'orthogonality catastrophe"' first predicted in [98].

- **Cross-correlation**

Following Eq.3.15, one can deduce the cross-correlation of the current fluctuations after partition from the measurement of the noise (autocorrelation) before and after partition. It would then be possible to measure the temporal variations of the cross-correlation and demonstrate, similarly to quantum optics, negative correlations at zero-time (see Fig.3.6). This representation however requires the measurement of the full spectrum of the autocorrelation. This is challenging since the measurement bandwidth of the high-frequency noise measurement setup should be increased up to several tens of GHz. Nonetheless, for transmissions below 0.2, the typical variation scale of the cross-correlation in the frequency domain is comparable with the upper cutoff frequency of the impedance transformer and the cryogenic amplifiers of our RF noise measurement setup, that is ~ 4.5 GHz $= 3f_0 = 225$ mK (see 4.1). Measuring the temporal variation of the cross-correlation for small values of the transmission is thus within reach, provided that the bandwidth of the RF measurement setup is extended to its maximum value.

- **Measurement of the emitted charges energy distribution, tomography**

The measurement of the variations of the zero-frequency partition noise with the bias voltage V_{bias} gives access to the energy distribution of the emitted charges. This opens the way to a wide range of experiments, such as the measurement of the relaxation of the emitted charges as a function of the distance between the source and the central QPC. As predicted by Charles Grenier and collaborators in [65], one can generalize this technique and apply a high-frequency voltage to the opposite contact in order to measure the off-diagonal terms of the density matrix of the emitted charge (the diagonal being the energy distribution), thus performing a full quantum tomography of the emitted charge. One can then once again study the evolution of the density matrix with the propagation length, thus characterizing the relaxation and decoherence processes occurring in Quantum Hall Effect edge channels at the single charge scale.

- **Energy relaxation between QHE edge channels**

The HBT geometry can be used to study the energy exchanges between adjacent Quantum Hall Effect edge channels: indeed, while our scattering model only considers the outer edge channels, it was recently shown [24, 25] that energy transfer processes occur between edge channels over typical length of a few micrometers. Using a central QPC, one can then measure the amount of energy transmitted from the outer channel, on which charges are emitted, to the inner channel at filling factor $\nu = 2$. Using the single electron emitter allows to study the relaxation to the inner channel at the single charge level, as a function of the energy of the emitted charge. Furthermore, measuring the zero-frequency noise reflected by the QPC at transmission 1.5 (outer channel fully transmitted to the high-frequency measurement contact, inner channel partially reflected to the low-frequency measurement contact) allows to count the number of electron/hole pairs generated in the inner channel.

3.3 Experimental setup

We now present the setup used to perform single charge experiments in the HBT geometry. The sample has two outputs, corresponding to each output of the QPC, and is connected to two noise measurement setups (high and low frequency) designed to detect noise levels of the order of $e^2 f_0$, with $f_0 = 1.5$ GHz. We first describe the geometry of the sample, then the whole setup. The noise measurement lines are described in detail in the next chapter; in particular, we have increased the bandwidth of the high-frequency noise measurement setup used to perform the experiments presented in chapter 2.

3.3.1 Sample geometry

The samples used in the experiments in the HBT geometry (batch *S434*) where made at *Laboratoire de Photonique et Nanostructures* by Yong Jin. The two-dimensional electron gas has a nominal density equal to 1.8×10^{11} cm^{-2}, and a nominal mobility equal to 2.4×10^{6} cm^2/ Vs.

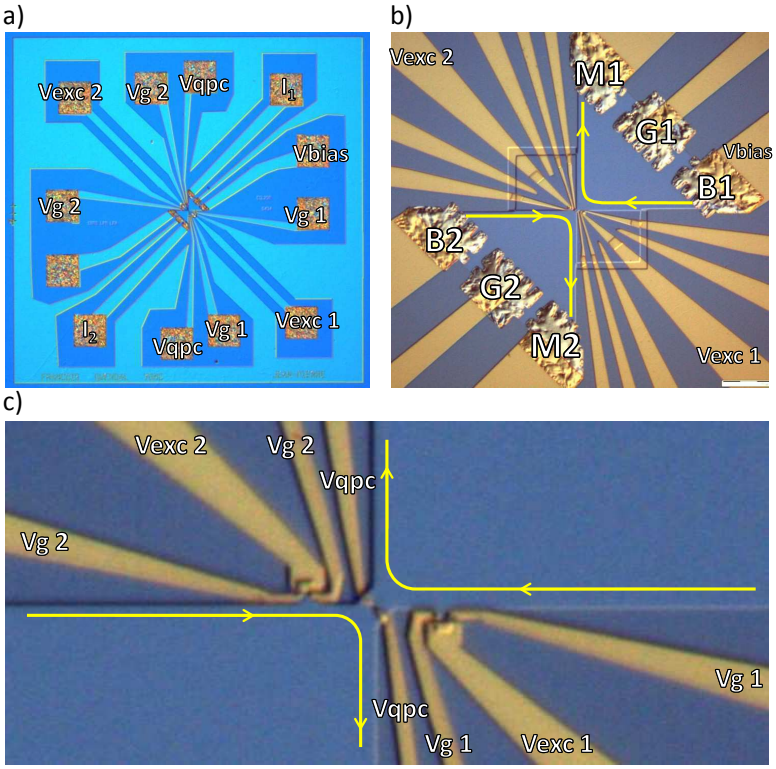

Figure 3.11: Optical view (in false colors) of the samples used in the HBT measurements. **a)**, **b)** and **c)** correspond to successive zooms. The yellow arrows illustrate the trajectories of electrons along the edge channels in the QHE regime.

We show an optical view of a typical sample from this batch in Fig.3.11: similarly to sample *S528-11*, studied in the previous chapter, most of the surface of the sample is covered by an *Au* ground plane to reduce the parasitic couplings (high frequency couplings, as well as capacitive couplings between the different QPC gates). We however have added two additional ohmic contacts (G_1, G_2), connected to the ground plane, that are placed between the measurement contact (M_1, M_2) and the bias contact (B_1, B_2) on each side of the two-dimensional electron gas. This geometry allows to keep the impedance of the sample seen by each of the two measurement lines independent of the state of the bias contacts: one can therefore either ground them, leave them floating, or connect them to a source with no influence on the measurement lines. The sample has a symmetrical geometry, thus including two quantum dots (one on each input channel of the QPC); this geometry, aimed towards Hong-Ou-Mandel electron collision experiments [12], allows us to select the source presenting the most satisfying characteristics, particularly regarding its response to the dot QPC gate voltage V_g compared to the the ideal description given in the first chapter (regularity of the level spacing, ideal QPC transmission law). The width of the quantum dot in sample *S434-8*, studied in the next section, is slightly larger than the size of sample *S528-11*: 800 nm for *S434-8*, 600 nm for sample *S528-11*. The distance between each source and the central QPC is ~ 5 μm.

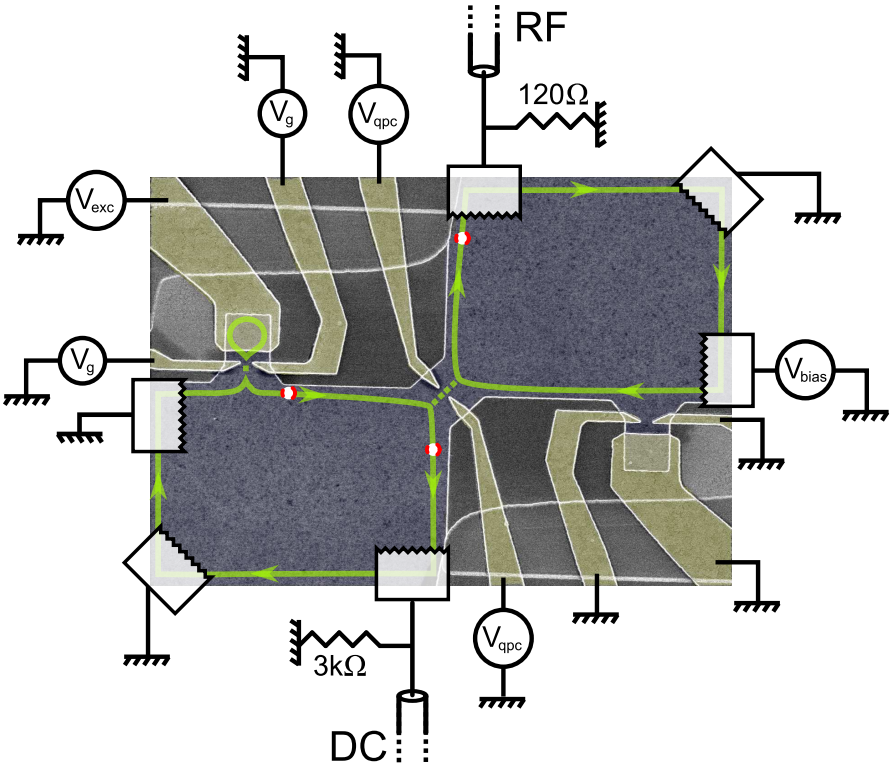

Figure 3.12: Schematic view of the configuration of the HBT experiment, based on a SEM picture of the sample (false colors). The green arrows illustrate the trajectories of electrons along the edge channels in the QHE regime, and red circles symbolize the emitted single charges. RF signals are measured in transmission on the 120Ω load, while DC signals are measured in reflection on the 3 kΩ load. The other source (bottom right) is not used.

3.3.2 Setup

The sample is mounted on the sample holder described in 4.1 (see also Fig.2.12a). We have added a second 40 GHz, 50Ω RF excitation line in order to connect the top gate of each quantum dot to one of the two lines. After selecting the quantum dot with the best characteristics, the configuration of the sample is as shown in Fig.3.12: the transmission of the central QPC T is tuned with the gate voltage V_{qpc}, while the transmission of the dot QPC D is tuned with the gate voltage V_g. The RF excitation voltage V_{exc} is generated using either the *Agilent 81134A* microwave pulse/pattern generator used in the previous chapter, or an *Anritsu MT1810A* signal generator, which presents a larger bandwidth than the *Agilent 81134A* ($\sim$ 10 odd harmonics for $f_0 = 1.5$ GHz), and shorter rise times ($35ps$). In addition to the RF excitation voltage V_{exc}, we can apply a constant gate voltage V_{DC} to the top gate of the quantum dot, similarly to the first chapter. The gates of the second quantum dot are grounded. The opposite contact can be biased with the voltage V_{bias}. The ohmic contact collecting the single charges reflected by the QPC (that is, on the same side of the QPC as the source) is shunted by a 3 kΩ load, connected to the low-frequency noise measurement setup; the ohmic contact collecting the single charges transmitted by the QPC (that is, on the other side of the QPC) is shunted by a 120Ω load, connected to the high-frequency noise measurement setup. We can therefore measure the transmission of the central QPC as a function of V_{qpc} both at high frequency (between the dot top gate and the RF measurement contact), and at low frequency (between the biased contact and the low frequency

measurement contact). The low-frequency measurements are performed at 1.2 kHz using a lock-in detection.

3.4 Preliminary results

We now present results of the experimental measurements performed with sample *S434-8*, at a base temperature of the dilution refrigerator $T_{mc} \approx 65$ mK. We first present a characterization of the sample (two-dimensional electron gas, central QPC, source and couplings between the different QPC gates); we then present measurements of the noise after partition by the central QPC at high and low frequencies.

3.4.1 Characterization of sample *S434-8*

3.4.1.1 Two-dimensional electron gas

While we had to rely, for the previous samples, on the nominal value of the electron density of each batch of samples to estimate the value of the magnetic field to apply for a given filling factor, the new geometry (particularly, the biased contact) allows to precisely study the conductance response of the two-dimensional electron gas to an applied magnetic field. We have measured the transmission

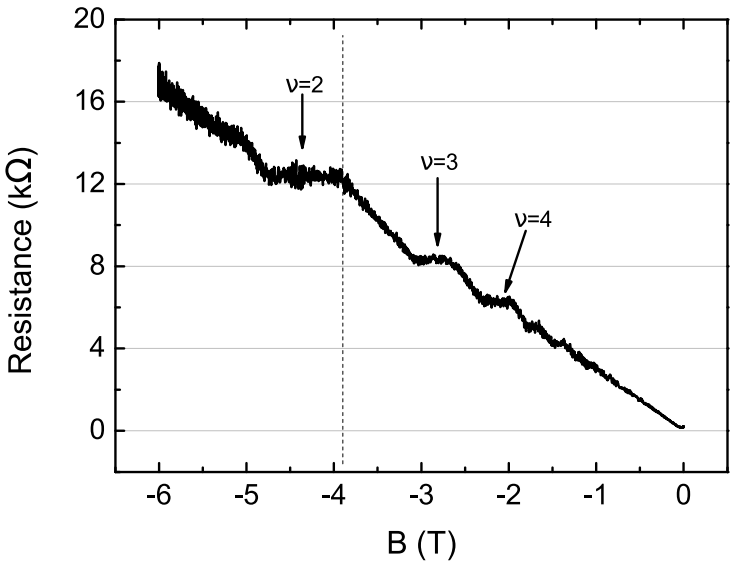

Figure 3.13: Measurement of the two-point resistance between the bias contact and the measurement contact as a function of the magnetic field. For magnetic fields larger than 1 T, the resistance presents plateaus corresponding to integer values of the filling factor. We focus our study for $B = -3.9$ T, indicated by the dashed line.

between the biased contact and the DC measurement contact, in a two-point probe configuration. The variation of the resistance between the two contacts as a function of the magnetic field B for a fully opened central QPC ($V_{qpc} = 0$) is plotted in Fig.3.13. As expected in Quantum Hall Effect systems, the resistance presents a series of plateaus at high magnetic field at integer fractions of the resistance quantum $R_K \approx 25.8$ kΩ. These plateaus correspond to integer filling factors of the QHE, where electrons propagate on edge channels without backscattering. The plateau corresponding to $\nu = 2$ ($R = R_K/2 \approx 12.9$ kΩ) appears between $B \approx -3.9$ T and $B \approx -4.7$ T. Here, the values of the

applied magnetic field are negative, which corresponds to the correct configuration where the electrons in the edge channels flow from the biased contact towards the QPC, instead of towards the grounded contact next to the biased contact (see Fig.3.12).

The low-frequency transmission of the central QPC is plotted in Fig.3.14 as a function of the magnetic field B and the QPC gate voltage V_{qpc}. We measure the voltage drop across the low-frequency measurement impedance $R_0 = 3\,\mathrm{k}\Omega$ (see Fig.3.12), connected in parallel with the impedance of the two-dimension electron gas R_K/ν. The measured voltage V_{out} is then proportional to the current I flowing from the central QPC to the low-frequency measurement contact with $V_{out} = I \times R_0 R_K/(\nu R_0 + R_K)$. The current I is itself given by the Landauer formula:

$$I = \sum_{i=1}^{\nu} \frac{T_i}{R_K} V_{bias} = \sum_{i=1}^{\nu} T_i \frac{e^2}{h} V_{bias} \tag{3.35}$$

where T_i is the transmission of the central QPC for the $i-$th channel. The measured voltage can therefore be written as a function of the bias voltage:

$$V_{out} = \frac{R_0}{\nu R_0 + R_K} \sum_{i=1}^{\nu} T_i V_{bias} \tag{3.36}$$

The height of the conductance steps therefore depends on the total number of edge channels ν, and decreases as the magnetic field is lowered. This representation allows to choose a magnetic field corresponding to an integer filling factor, for which the conductance of the central QPC presents clear quantized plateaus (in number equal to the filling factor). For consistency with other experiments aimed towards the realization of electron quantum optics experiments in two-dimensional electron gases [15, 5, 18, 19, 24, 25], we focus our study for a magnetic field $B = -3.9$ T, corresponding to a filling factor $\nu = 2$ (highlighted in red in Fig.3.14. At this filling factor, the electron phase coherence length is well known (20 μm at 20 mK, see [19]), as well as the inelastic length, characterizing the energy exchanges between the two edge channels (2.5 μm for an energy difference between the two channels equal to 115 mK, see [25]).

Lastly, Fig.3.14 shows that the irregularities in the QPC transmission law (particularly, the resonances) increase at high magnetic field; this can be clearly seen for $|B| > 3$ T (filling factors smaller than 2).

3.4.1.2 Central QPC

The study of the transmission law of the central QPC allows to check the consistency between high-frequency and low-frequency measurements: indeed, our dilution refrigerator was originally devoted to microwave-frequency measurements, which do not require the level of precaution regarding ground definition as low-frequency measurements do (especially regarding ground loops). In particular, the room-temperature amplifiers of the high-frequency measurement setup (see 4.1.1.2) can be a source of large ground loops through their power supply unit.

We have therefore measured the transmission of the central QPC as a function of its gate voltage V_{qpc} both at high ($f_0 = 1.5$ GHz, transmission between the dot top-gate and the RF measurement contact) and low (1.2 kHz, transmission between the biased contact and the DC measurement contact) frequency. For the high-frequency measurement, the dot QPC is pinched off, so that we only consider the capacitive coupling between the dot top-gate and the edge channels. The comparison between the two traces (normalized as transmission) after optimization of ground definition is shown on Fig.3.15: we have only plotted the transmission of the first channel at high frequency (black circles), since the coupling between the dot top-gate and the outer and inner edge channels are different. For the outer

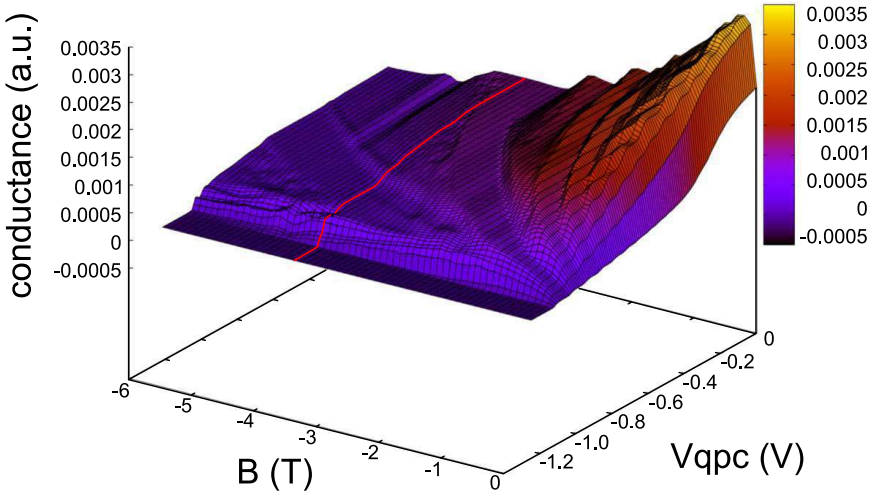

Figure 3.14: Conductance of the central QPC as a function of V_{qpc} and the magnetic field: as the magnetic filed increases, the number of plateaus corresponding to a quantized conductance in units of e^2/h decreases. The conductance at $B = -3.9$ T, corresponding to a filling factor $\nu = 2$, is emphasized in red.

channel, the agreement between high and low frequency (the latter being shown as the red line) is excellent[4], except for a small discrepancy due to a resonance around $V_{qpc} = -1$ V (see inset), where the transmission becomes energy dependent.

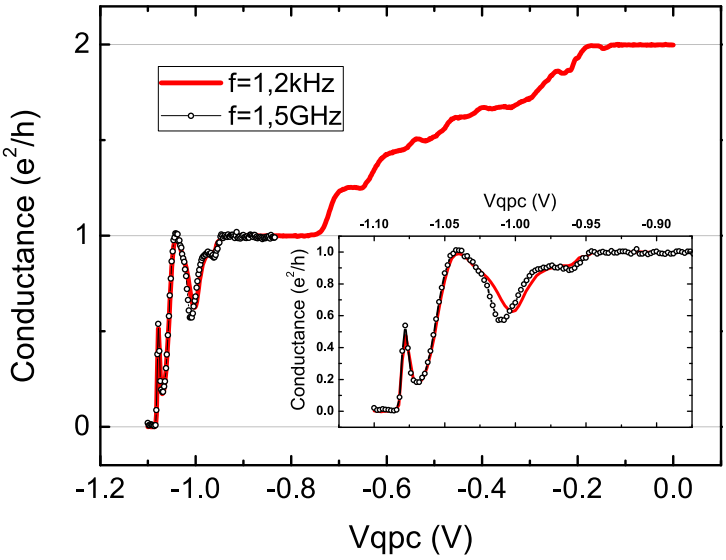

Figure 3.15: Measured transmission of the central QPC as a function of V_{qpc}, at $\nu = 2$. Red line: low-frequency measurement (1.2 kHz). Black circles: RF measurement (1.5 GHz). Inset: close-up view of the transmission of the outer channel versus V_{qpc}.

[4]This result was first observed in [99].

The results shown on Fig.3.15 allow to directly plot the measured partition noise at high and low-frequency as a function of the QPC transmission T.

3.4.1.3 Single electron source

We have characterized the single electron source of sample *S434-8* using the measurements of the first harmonic of the average AC current described in chapter 1. To perform these measurements, we have set the central QPC gate voltage V_{qpc} to zero, so as to leave the central QPC fully open (see Fig.3.15).

The temperature calibration of the source (see 1.3.2.3) yields a level spacing $\Delta \approx 3$ K, and a residual electronic temperature $T_0 \approx 70$ mK.

The variation of the modulus of the first harmonic $|I_\Omega|$ as a function of the dot QPC gate voltage V_g and the excitation amplitude V_{exc} is plotted in Fig.3.16. While the diamonds corresponding to the quantization of the first harmonic in units of $2ef_0$ (described in 1.4.3.2) are observed, the graph presents some discrepancies with the theoretical model (see for example Fig.1.17, lower panel): one can observe diamond substructures (*e.g.* for $V_g \approx -580$ mV), which appear at high excitation voltages. These substructures might be related to resonances in the QPC transmission; one can nonetheless discard them by simply choosing an operating point of the source where no such substructures are observed (*e.g.* for $V_g \approx -585$ mV indicated by the intersection of the dashed lines).

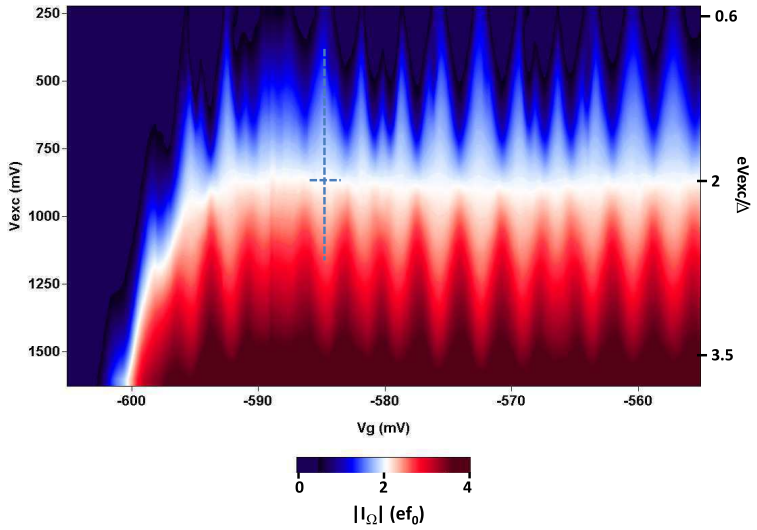

Figure 3.16: Two-dimensional plot of the first harmonic of the average AC current emitted by the single electron source versus V_g and V_{exc}, for sample *S434-8*. The intersection of the dashed lines corresponds to the optimal operating conditions of the source in the partition noise measurements.

More critical is the loss of current quantization (observed as a complete blurring of the diamonds) for $V_g = -585$ mV $\leftrightarrow -590$ mV. This is caused by a large resonance in the QPC transmission, where the transmission abruptly rises to a value close to unity (hence the loss of quantization), then decreases to a value where the quantization is recovered. This resonance is particularly troublesome because it occurs at a gate voltage range where the phase of the current undergoes its maximum variation for an ideal smooth transmission law. We have plotted in Fig.3.17a the real and imaginary part of the measured first harmonic for $2eV_{exc} = \Delta$ as a function of the QPC gate voltage V_g (full lines), as

well as the calculated current using an ideal QPC transmission law (see Eq.1.20) with the parameters $V_{g0} = -0.567$ V and $\Delta V = 7$ mV (dashed lines). In order to try to reproduce the experimental results, we have modeled the resonance with a Lorentzian curve (slightly skewed towards small negative V_g, see Fig.3.17b). The calculated current is shown in dotted lines: although they reasonably reproduce the experimental data for gate voltages above -0.59 V, it is not possible to reproduce the behavior of the experimental data for $V_g = -0.61$ V $\leftrightarrow -0.59$ V, where the imaginary part of the current is systematically larger than the real part. This behavior is not consistent with the RC-circuit description of the source presented in the first chapter.

In order to reproduce the experimental results, one would need to take into account the fact that the phase of the electron visiting the quantum dot can undergo a large variation as it comes across the localized state creating the resonance in the QPC: for instance, it was shown in [100] that the phase of electrons in an interferometer is shifted when a localized state is inserted in one of the two arms of the interferometer. In [100], a small tunable quantum dot is used as the localized state, and one can control the number of electrons in the dot; the phase shift can then be as large as π when an electron is added in the dot.

Because of this large resonance, the description of the source as an RC-circuit is not valid for gate voltages below $V_g = -0.58$ V. In particular, one cannot extract the escape time in this range of gate voltages from the measurement of the real and imaginary part of the first harmonic. Nonetheless, relevant single electron experiments can be performed for gate voltages above $V_g = -0.58$ V, corresponding to QPC transmission above ~ 0.35.

3.4.1.4 Couplings between the gates

In order to perform a typical experiment where we measure the noise as a function of the transmission of the dot QPC D while keeping the central QPC transmission T equal to 0.5, one needs to estimate the coupling between the different gates of the sample. Indeed, if the coupling between the dot QPC gates and the central QPC gate is finite, changing the dot QPC gate voltage V_g will result in a change in the central QPC transmission T. If we were to measure the noise as a function of V_g while keeping V_{qpc} constant, the result would yield a non-negligible deviation caused by changes in the transmission T. It is therefore crucial to precisely determine the coupling between the two gates, so as to compensates the changes in the transmission T when V_g is swept. We have extracted the influence of the dot QPC gate voltage V_g on the central QPC transmission from the low frequency measurements of the central QPC transmission as a function of the gate voltages V_g and V_{qpc}: we measure the transmission T as a function of the central QPC gate voltage V_{qpc} for several values of V_g. If the coupling between the two gates is zero, one expects to measure the transmission trace shown before (Fig.3.15), unaffected by the changes in V_g. For a finite coupling, the transmission traces are slightly shifted as V_g changes. We use several points in the transmission trace, including the sharp resonance at low transmission (see Fig.3.15), to determine the coupling between V_g and V_{qpc}: we find $\delta V_{qpc} = 0.02\delta V_g$. In any experiment requiring a fixed central QPC transmission T, we first set the dot to the pinch-off ($V_g = -0.635$ V), and set the transmission T to its specified value. We then open the dot QPC by changing its gate voltage V_g by the value δV_g, while automatically compensating the effect on the central QPC by changing its gate voltage V_{qpc} by the value $-0.02\delta V_g$. These automatic compensation techniques are well known in systems presenting a large number of metallic gates, such as double quantum dot structures in two-dimensional electron gases [101, 102].

We take into account the influence of the central QPC gates on the dot QPC gates by simply measuring the average AC current emitted by the source as a function of V_g, for different values of V_{qpc}. We obtain AC current traces similar to Fig.3.17, slightly shifted by the change in V_{qpc}. Measuring the same traces at a lower excitation amplitude allows to entirely determine the state of the quantum

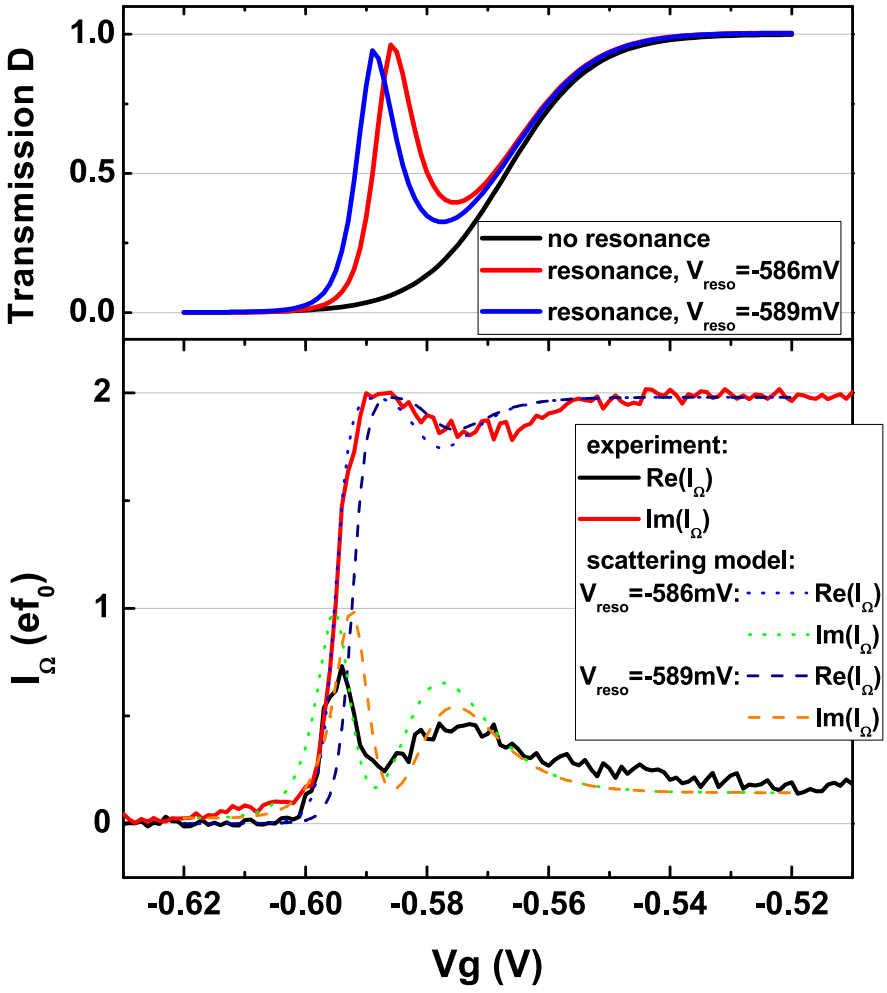

Figure 3.17: Real (black line) and imaginary (red line) parts of the first harmonic versus V_g, for $2eV_{exc} = \Delta$ (lower panel). Dashed lines: calculation of the current with the QPC transmission law presenting a resonance at $V_g = -0.586$ V (red line in the upper panel). Dotted lines: calculation of the current with the QPC transmission law presenting a resonance at $V_g = -0.589$ V (blue line in the upper panel). The black line in the upper panel corresponds to an ideal Fermi-like transmission law (parameters given in the text).

dot (transmission D, equilibrium potential ϕ_0) for any given set of gate voltages (V_g, V_{qpc}).

We finally neglect the influence of the top gate DC voltage V_{DC} on the other gates, since no influence on the dot QPC transmission was put in evidence whatsoever (see typical temperature calibration data in Fig.1.6), let alone on the central QPC. Furthermore, V_{DC} is swept on typical energy scales given by the level spacing Δ; in the experimental conditions, this corresponds to voltage scales of a few hundreds of μV, much smaller than the variation scales of both V_g and V_{qpc}.

The knowledge of the couplings allows us to isolate the contribution of the single electron emitter in various measurements involving the central QPC, such as the one shown in Fig.3.18, where we have plotted the low-frequency transmission of the central QPC (red) as a function of V_{qpc}, as well as the transmission of the average AC current emitted by the source (here, $D \approx 1$ for simplicity) by the central QPC. The majority of the source signal is measured in the outer channel, effectively demonstrating

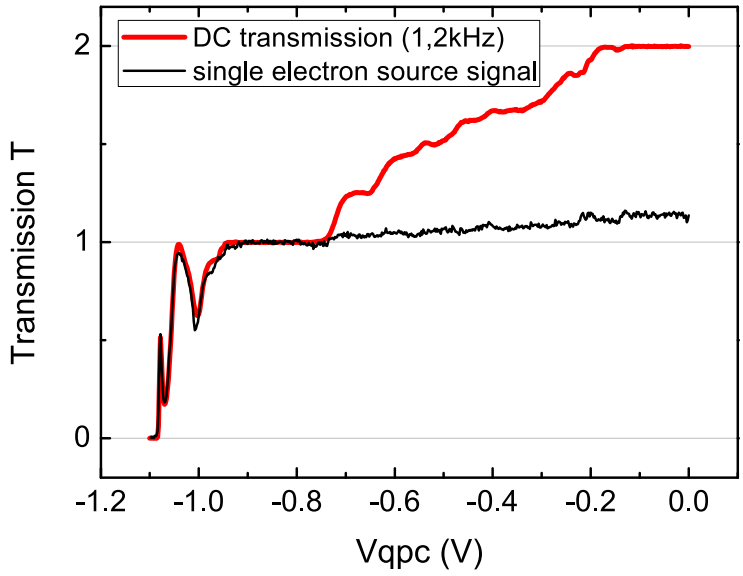

Figure 3.18: Transmission of the average AC current emitted by the source by the central QPC (black line), along with the DC transmission (red line). A finite portion of the single electron source signal is measured on the inner channel (transmission > 1 for the black line).

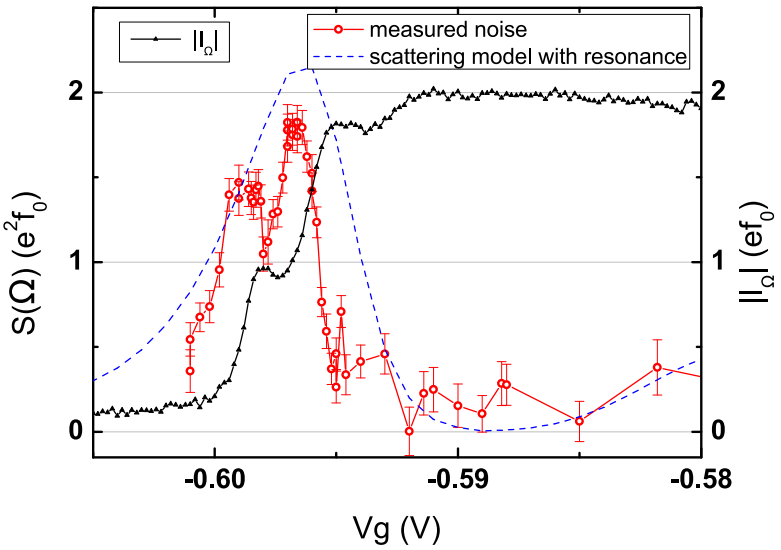

Figure 3.19: Noise of the single electron source versus V_g for sample *S434-8*. Red circles: experimental data; blue dashed line: scattering model, using the QPC transmission law with a resonance at $V_g = -0.586$ V depicted in Fig.3.17. Black line with symbols: modulus of the first harmonic of the average AC current, for $2eV_{exc} = \Delta$.

the spin selectivity of the source. This result confirms the validity of the description of the density of states in the dot in terms of electronic trajectories following the edges of the dot.

Furthermore, a small portion of the source signal is measured on the inner channel, which may either correspond to the energy relaxation of electrons emitted in the outer channel into the inner channel, or reflect a finite tunneling probability between the dot and the inner edge state.

In the next sections, we present the noise measurements performed on sample *S434-8*. We first present the measurements of the autocorrelation of current fluctuations generated, similarly to chapter 2; we then present measurements of the noise of a partitioned single electron beam, constituting the first realization of the single electron HBT experiment.

3.4.2 Noise of the single electron source

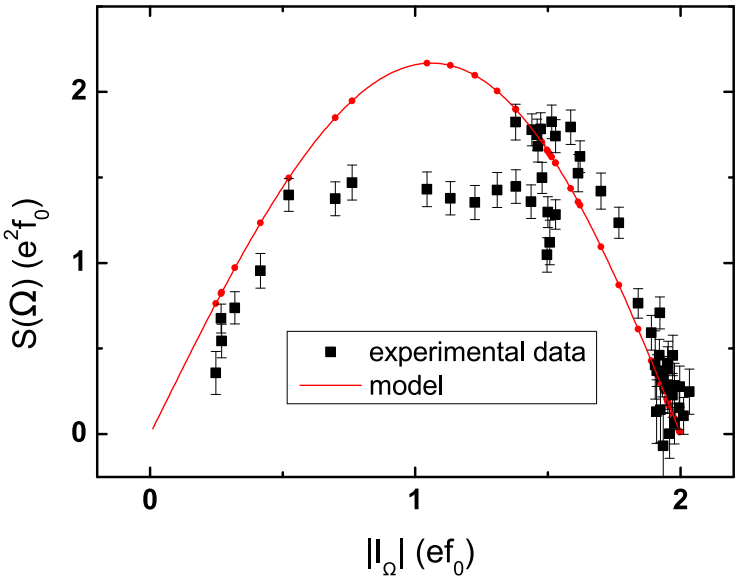

Figure 3.20: Noise of the single electron source versus modulus of the first harmonic of the current. Black squares: experimental data. Red line: model. The red dots correspond to the expected value of the measured noise, given by Eq.2.28.

We have measured the autocorrelation of the current fluctuations emitted by the source $S(\Omega)$ for $2eV_{exc} = \Delta$ as a function of the dot QPC gate voltage V_g, with the central QPC fully opened ($V_{qpc} =$ 0 V). The result is shown on Fig.3.19. The shape of the obtained curve is similar to experimental data presented in the previous chapter: the noise presents a bell-shaped variation, with its maximum value corresponding to $|I_\Omega| \approx ef_0$ (black line). However, this maximum value is slightly lower than the expected one in the scattering model (dashed line). This may be caused by the resonance in the dot QPC transmission law mentioned in the previous section. Because of the higher number of odd harmonics contained in the excitation drive compared to the previous chapter, the oscillations of the noise with the dot's equilibrium potential are less pronounced. One can nonetheless observe them for $V_g = -0.598$ V and $V_g = -0.595$ V.

The representation of the noise as a function of the modulus of the current, plotted in Fig.3.20, shows that discrepancies indeed occur at values of $|I_\Omega|$ below $\sim 1.4ef_0$, corresponding to the zone where the RC-circuit model fails to describe the mesoscopic capacitor. While the quantum jitter limit is well reproduced, the agreement between the data (black squares) and the models developed in the previous chapter (blue line and red circles) is not satisfactory; in particular, the value of the noise for $|I_\Omega| = ef_0$ is significantly lower than expected.

Even though the resonance in the dot QPC transmission invalidates the description of the source in terms of RC circuit elements at low transmissions, the data at higher transmissions are consistent with the theoretical model, particularly in the quantum jitter limit, which corresponds to the typical operating conditions of the source.

3.4.3 Noise in the HBT geometry

3.4.3.1 Zero-frequency partition noise

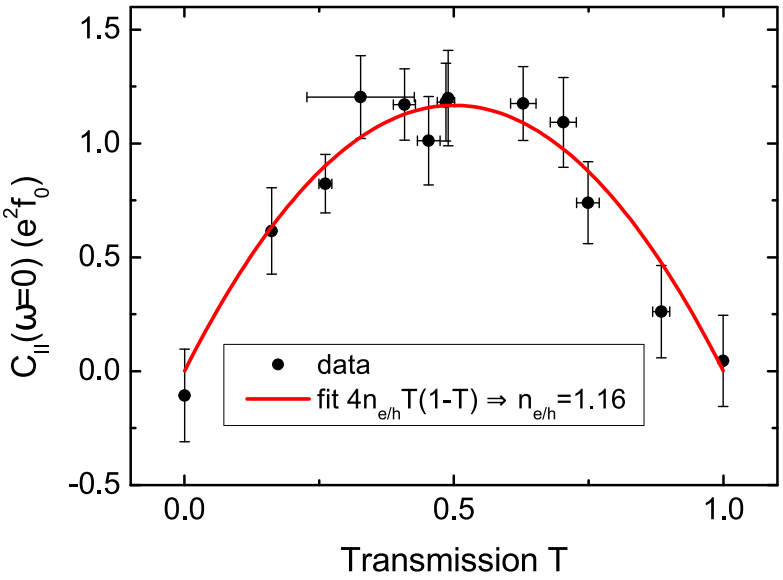

Figure 3.21: Zero-frequency part of the partition noise of the source in the HBT geometry, versus the central QPC transmission T. The zero-frequency noise for $T = 0.5$ measures the number of emitted electron/hole pairs per period $n_{e/h}$. The fit (red line) yields $n_{e/h} = 1.16 \pm 0.04$. The horizontal error bars correspond to the error on the estimation of the central QPC transmission related to the stability of the QPC transmission law.

As described in 3.2.2.1, the zero-frequency partition noise for $T = 0.5$ counts the number of emitted electron/hole pairs per period. We have measured the zero-frequency noise as a function of the central QPC gate voltage V_{qpc}. We have focused on the center of the current diamond located next to the resonance in the dot QPC transmission (intersection of the two dashed lines at $V_g \approx -0.585$ V in Fig.3.16), corresponding to the optimal operating conditions $2eV_{exc} = \Delta$ and $\phi_0 = 0$. The central QPC transmission traces shown in Fig.3.15 and Fig.3.18 allows to directly plot the noise as a function of the transmission T. The experimental data, constituting the first experimental realization of the partition of a single electron beam, is shown on Fig.3.21. We have fitted the experimental data (black dots) with the function defined in Eq.3.31, the number of emitted electron/hole pairs per period $n_{e/h}$ being taken as an adjustable parameter. The fit (red line) yields $n_{e/h} = 1.16 \pm 0.04$: this value is close to the number of emitted electron/hole pairs per cycle for a perfect single electron emitter (that is 1), thus experimentally proving that the generation of excess electron/hole pairs by the source can be neglected in the optimal operation conditions: the measured excess value is comparable with the error bars on the measurement ($\sim 0.2e^2 f_0$). Improving the low-frequency noise measurement setup (see 4.2.3) would allow the measurement of the number of emitted electron/hole pairs with more accuracy.

3.4.3.2 High frequency partition noise

We have measured the high frequency part of the noise after partition, as a function of the transmission of the central QPC T, for both outer and inner channels. We use the same operating point as for the low-frequency measurements. As described in the scattering model section, the high frequency part of

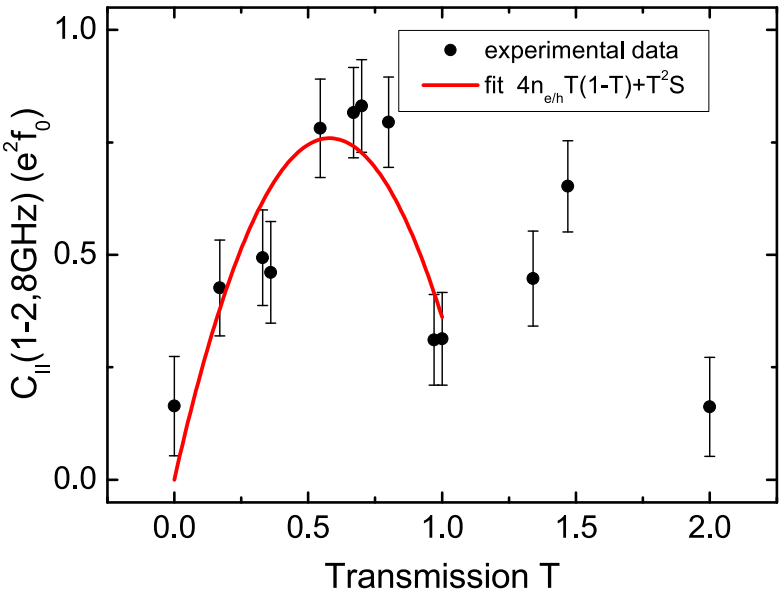

Figure 3.22: High frequency noise in the HBT geometry, measured as a function of the transmission T (black dots). Red line: adjustment with the function $4n_{e/h}T(1-T)+T^2S$. The fit yields $n_{e/h} = 0.65 \pm 0.08$ and $S = 0.37 \pm 0.09e^2f_0$.

the noise contains the contribution of the intrinsic noise of the source $S(\omega)$ with a factor T^2, and the contribution of the partition noise $C(\omega)$ with a factor $T(1-T)$. We have used the full bandwidth of the high-frequency noise measurement setup (1 GHz $\leftrightarrow$ 2.8 GHz, see 4.1.4). The result is shown in Fig.3.22: values of T above 1 correspond to the inner edge channel. In the outer channel ($T \leq 1$), the noise is bell shaped, similarly to the zero frequency part; furthermore, the noise does not vanish when the transmission T reaches unity, which corresponds to the intrinsic noise generated by the source. This curve is thus very similar to the theoretical calculation of the partition noise at finite frequency shown in Fig.3.7. However, the maximum value of the noise is significantly below the theoretical value (~ 1.3), as well as the maximum value of the zero-frequency part of the noise discussed previously (1.16). In the inner channel, the noise increases again, and reaches another local maximum for $T = 1.5$ (inner channel half-transmitted); the inner channel therefore yields a portion of the signal of the source. Because the maximum value of the high-frequency noise at $T = 0.5$ is not consistent with the number of electron/hole pairs measured at low-frequency, we believe that the high frequency part of the noise is reduced by capacitive couplings between the inner and outer channel. In order to quantitatively analyze these discrepancies, we have fitted the data for the outer channel (that is, for $T \leq 1$) with a function $4n_{e/h}T(1-T)+T^2S$, where S is the intrinsic noise of the source. The fit, shown as a red line in Fig.3.22, yields $S = 0.37 \pm 0.09e^2f_0$ and $n_{e/h} = 0.65 \pm 0.08$. The value of the number of emitted electron-hole pairs per period is not compatible with the value obtained with the low-frequency partition noise measurements (Fig.3.21). We believe that this is mainly caused by errors in the calibration of the RF noise measurement setup using the full bandwidth. Measuring the partition noise over the different available bandwidth of the RF noise measurement setup might allow to verify this hypothesis.

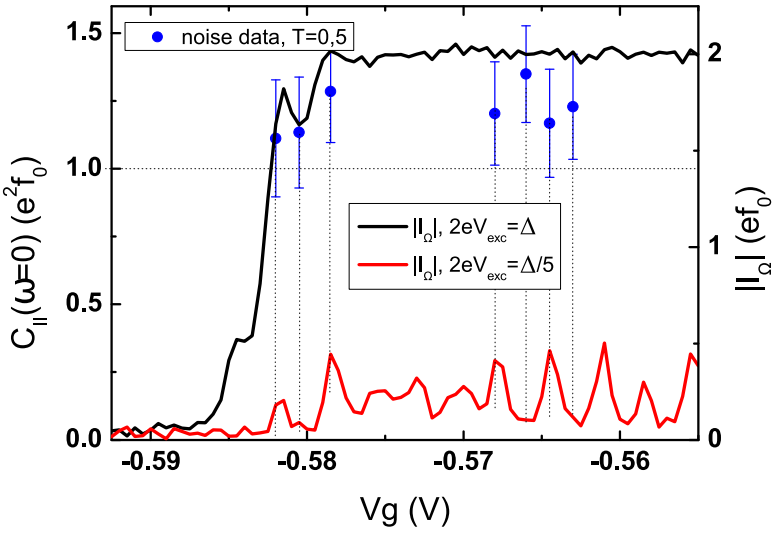

Figure 3.23: Zero-frequency noise in the HBT geometry versus V_g, measured for $T = 0.5$ (blue dots). Black line: modulus of the first harmonic, for $2eV_{exc} = \Delta$; red line: modulus of the first harmonic, for $2eV_{exc} = \Delta/5$.

3.4.3.3 Variation with the dot QPC transmission D and dot equilibrium potential

We have measured the zero-frequency noise for $T = 0.5$, for a few values of the dot QPC gate voltage V_g, so as to probe both the variation of the noise with the transmission D and the equilibrium potential ϕ_0. The result is shown in Fig.3.23; we have plotted as well the average current emitted by the source, for two values of the driving amplitude, in order to compare the noise data with the position of the energy levels in the dot. As expected, the noise shows no variation with the transmission, since all points correspond to a transmission range where the number of emitted electron/hole pairs is constant. However, there is no significant increase of the noise in the $\phi_0 = \pi$ regions ($V_g = -0.5805$ V, -0.566 V, -0.563 V).

3.4.4 Noise measurements at -3.3 T

We have performed noise measurements at $B = -3.3$ T in order to check the consistency of the results presented above. Indeed, the central QPC has a smoother transmission law for this value of the magnetic field (plotted in Fig.3.24), which may reduce the possible discrepancies caused by resonances in the central QPC.

We have measured the high frequency noise ($1 - 2.8$ GHz) as a function of the central QPC transmission T, similarly to 3.4.3.2. The obtained result, shown on Fig.3.25, is consistent with the previous results: the fit, using the same function as for $B = -3.9$ T, yields $n_{e/h} = 0.51 \pm 0.07$ and $S = 0.16 \pm 0.1 e^2 f_0$. These values, although close to the ones obtained at $B = -3.9$ T, are smaller than the latter; this remains to be investigated.

- **Measurement of the electronic temperature**

The low-frequency noise measurements as a function of the dot QPC gate voltage V_g show no variation of the noise with the dot equilibrium potential, which we suppose is caused by a high electronic temperature. We have estimated the electronic temperature for $T = 0.5$ by measuring the high frequency partition noise for $D = 1$ as a function of the excitation amplitude V_{exc}. Indeed, for $D = 1$, the noise is expected to be zero as long as eV_{exc} is smaller than the electronic temperature $k_B T_{el}$. For

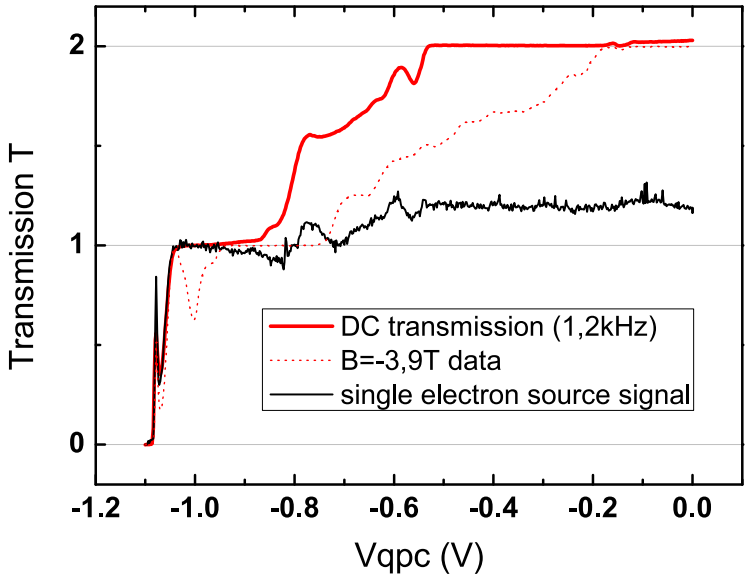

Figure 3.24: Transmission of the average AC current emitted by the source by the central QPC (black line), along with the DC transmission (red line) for $B = -3.3$ T. Dotted line: DC transmission at $B = -3.9$ T (also plotted in Fig.3.18).

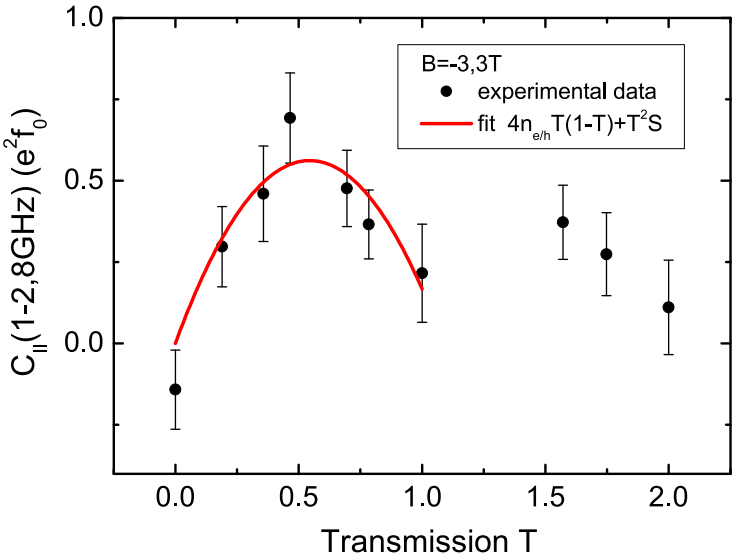

Figure 3.25: High frequency noise in the HTB geometry, measured as a function of the transmission T at $B = -3.3$ T. The fit (red line) yields $n_{e/h} = 0.51 \pm 0.07$ and $S = 0.16 \pm 0.1 e^2 f_0$.

$eV_{exc} \ll k_B T_{el}, \hbar\Omega$, one expects the noise to increase linearly. We have plotted in Fig.3.26 the measured noise (black dots) as a function of the excitation amplitude, as well as numerical computation of the noise for $T_{el} = 100$ mK, $T_{el} = 300$ mK and $T_{el} = 500$ mK (resp. black, red and blue lines). The agreement between the latter and the experimental data shows that the electronic temperature is indeed much larger than expected; the difference between this temperature and the electronic temperature measured with the calibration of the level spacing indicates that the increase in the temperature is

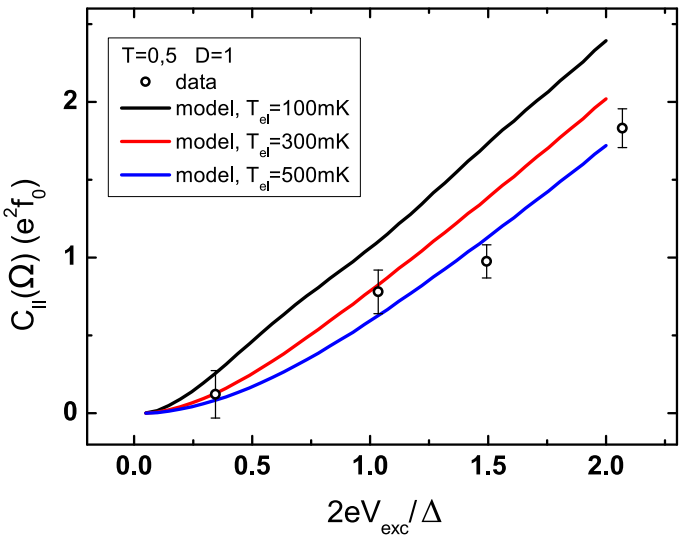

Figure 3.26: High frequency noise for $T = 0.5$ and $D = 1$, as a function of the excitation amplitude V_{exc}. Black circles: experimental data. Full lines: numerical calculations for $T_{el} = 100$ mK (black), $T_{el} = 300$ mK (black), and $T_{el} = 500$ mK (blue).

caused by the biased contact. It is therefore crucial to properly filter the wires connecting the contact.

The first measurements in the HBT geometry presented here are quite promising, since they show that in spite of the samples imperfections and the large electronic temperature, the experimental results are in reasonable agreement with the model. Particularly, the low-frequency noise measurements presented in Fig.3.21 are the first experimental realization of the probing of coherent particle transfers proposed in [64].

Conclusion of chapter 3

In this chapter, we have focused on the autocorrelation of current fluctuations after partition of the single-charge beam emitted by the single electron emitter. We have shown, using the Floquet scattering matrix model introduced in the first chapter, that the zero-frequency part of the partition noise measures the number of emitted electron/hole pairs per period, as it was first predicted in [64]. The theoretical study presented here allows us to contemplate a wide range of experiments, which would thoroughly probe the electronic transport in the QHE edge channel at the single charge scale, thus completing the many recent investigations on the subject [15, 5, 18, 19, 24, 25, 27, 26, 65].

The experimental results show that although challenging, the proposed experiments are within reach; we are currently improving the filtering of the bias lines in order to reduce the effective temperature. Improvements in the low-frequency noise measurement setup (see 4.2.3) are also considered.

Finally, the whole experimental setup presented in this chapter allows to contemplate the realization of increasingly complex single-charge electron quantum optics experiments; in particular, two particle Hong-Ou-Mandel [42] collisions of single charges [12] can be rapidly initiated, since the studied samples already comprise two single electron source in a mesoscopic collider geometry (see Fig.3.12).

Chapter 4

High-frequency and low-frequency noise measurement setups

4.1 High sensitivity ultra-low temperature RF current and noise measurement setup 121

4.1.1 Modulated double balanced amplifier 121

4.1.2 Quarter-wave impedance transformer 129

4.1.3 Operation of the setup 130

4.1.4 Modifications 132

4.2 Low frequency noise measurement setup 132

4.2.1 Description of the setup 132

4.2.2 Calibration and operation 136

4.2.3 Possible improvements 138

Introduction of chapter 4

The noise measurements presented in chapters 2 and 3 show typical noise level given by $e^2 f_0 \approx 3.8 \times 10^{-29}$ A^2/Hz at $f_0 = 1.5$ GHz. The detection of such noise levels requires highly sensitive noise measurement setup. In this chapter, we present the principle, implementation and operation of both the GHz range noise measurement setup used in the measurements presented in chapter 2, and the low-frequency (100 kHz range) measurement setup used in the measurements presented in chapter 3.

The high frequency noise measurement setup [92] combines a wideband 120 Ω to 50 Ω impedance transformer that increases the measured voltage fluctuations, and a modulated double-balanced amplifier scheme that allows the averaging of very small noise power spectral densities over extended periods of time with a high stability. We demonstrate a state of the art sensitivity of $2.3 \times 10^{-28} A^2/\text{Hz}/\sqrt{\text{Hz}}$ ($1.3 \times 10^{-29} A^2/\text{Hz}$ in 5 minutes) for noise power spectral densities in the $1.2 - 1.8$ GHz bandwidth. We also present modifications on the setup that allowed to increase the measurement bandwidth to $1 - 2.8$ GHz, used for the measurements presented in chapter 3.

The low frequency noise measurement setup relies on a rather common cross-correlation technique: the current fluctuations are converted into large voltage fluctuations using a 3 kΩ load. The signal is then split into two independent amplification chains, and the integrated power of the cross-correlation is calculated using a fast acquisition card. We demonstrate a sensitivity of $\sim 4 \times 10^{-28} A^2/\text{Hz}/\sqrt{\text{Hz}}$ (0.23×10^{-29} A^2/Hz in 5 minutes).

We have implemented the two noise measurement setups in our dilution refrigerator in order to simultaneously measure both the high-frequency and low-frequency noise.

4.1 High sensitivity ultra-low temperature RF current and noise measurement setup

The small magnitude of the emitted current fluctuations makes their measurement very challenging at microwave frequencies [87, 22, 103, 104, 88], especially since fast single charge detection suffers a mismatch problem between the high impedance ($Z \propto h/e^2 \approx 26$ kΩ) of quantum sources [105] and the low (50 Ω) impedance of microwave amplifiers. This can hardly be overcome in broadband high-frequency experiments and strongly alters the current noise power resolution (by typically five orders of magnitude), which can only be recovered by increasing the measuring time. A standard RF noise measurement method consists in integrating the noise power spectral density over a finite bandwidth using square law detectors, see Fig.4.2a. One has to take into account the noise of the first amplifier in the setup, which is usually significantly larger than the noise of the sample. The resolution is limited by the integration time, which becomes very large and may eventually exceed the timescale over which the amplification gain can vary, thus making the measurement method less reliable.

In this section, we present a highly sensitive, wideband microwave frequency noise measurement technique with a current noise resolution lying an order of magnitude below the $e^2 f_0$ threshold. We have used the implemented setup to study the current fluctuations emitted by the single electron source, see chapter 2. The coupling between the source and the amplifiers is first increased by using a broad-band 120 Ω to 50 Ω quarter-wave impedance transformer. The signal is then amplified with a phase-modulated double balanced amplifier. This setup allows a highly stable amplification on a broad bandwidth ($1.2 - 1.8$ GHz) of very low signals emitted at the base temperature of a dilution refrigerator.

In a first part, we recall the principle of the modulated double balanced amplifier, and its advantages compared to a direct amplification technique. We also describe its implementation, including a microwave homodyne detection of the average current, inside an Oxford Kelvinox 400 dilution refrigerator, as well as its calibration using Johnson noise thermometry. In a second part, we describe the impedance transformer and its realization inside a sample holder connected to the mixing chamber of the dilution refrigerator. We finally present a typical operation of the whole setup, demonstrating a stability of the measurement over more than 40 hours and a sensitivity of about 2×10^{-28} A^2/Hz/$\sqrt{\text{Hz}}$ (1.15×10^{-29} A^2/Hz in a 5 minutes integration time).

4.1.1 Modulated double balanced amplifier

We present here the amplification technique used in our setup. We first describe its principle (Fig.4.1) and discuss its expected signal-to-noise ratio. We then present the complete apparatus (Fig.4.3).

4.1.1.1 Principle of the setup

We use a modulated double balanced amplifier scheme (see Fig.4.1b) to amplify the noise of the sample. The balanced amplifier [93] is widely used in cellular phone applications as well as in astrophysics, for downconverted millimeter radiation in recent Cosmic Microwaves Background detection [106], and particle physics to detect halo axions [107]; it can be seen as the microwave analog of a Mach-Zehnder interferometer. Its key elements are the 90-degrees hybrid couplers [108], which act as the beam splitters in the interferometer. When the gains and phases acquired in both arms of the interferometer are equals, the signal in the first input IN (resp. second input ISO) of the interferometer is amplified and entirely transmitted to the second output 90° (resp. first output 0°). On the other hand, the noise of each amplifier in the inner arms is evenly distributed between the two outputs of the interferometer. As a result, when one measures the difference between the interferometer's output powers, the noise

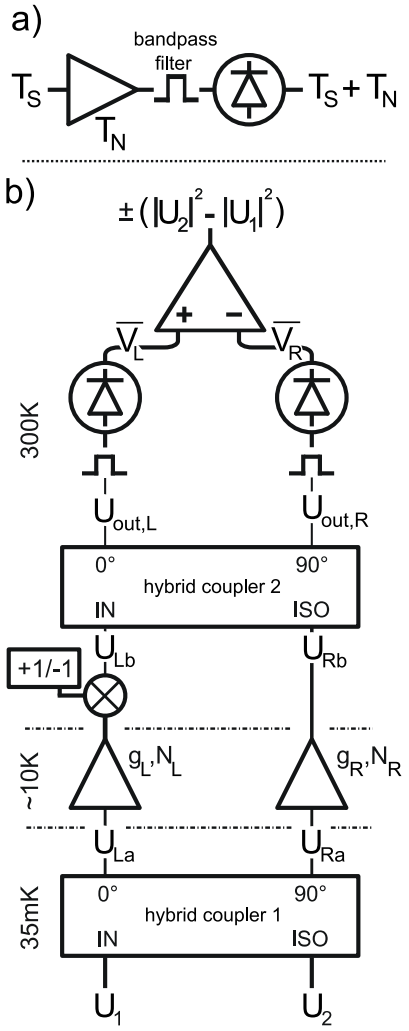

Figure 4.1: Principle of the modulated double balanced amplifier setup. The setup measures the difference between the two input noise powers, with a ± 1 factor given by the modulation.

of the amplifiers vanishes and only the difference between the two input signals remains. In addition, when a π-phase modulator is inserted in one arm inside the interferometer, one can alternatively swap the interferometer's outputs for the signal, hence alternatively change the sign of the difference between the two input signals while leaving the noise of the amplifiers unchanged. This allows to completely remove the amplifiers noise in a lock-in detection.

The 90° hybrid coupler is a four ports microwave component with a S-parameters matrix S between the complex amplitude of its two inputs (IN, ISO) and its two outputs $(0°, 90°)$ given by:

$$S = \frac{1}{\sqrt{2}} \begin{pmatrix} 1 & i \\ i & 1 \end{pmatrix} \tag{4.1}$$

Each one of the two inner arms of the interferometer includes an amplifier with a gain g_i and a noise N_i. The gain g_i includes the phase difference acquired by the signal over the arm length. The left arm also includes a π-phase modulator, which multiplies the signal by a factor ± 1 according to

the sign of the driving voltage. When the driving voltage is a low-frequency square (here, 2.7 kHz), the signal in the left arm U_{Lb} periodically switches between U_{Lb} and $-U_{Lb}$. The output signals of the interferometer, obtained after recombination of the left arm and right arm's signals on the second hybrid coupler, are filtered and applied to two square law detectors which measure the average power with an integration time of $0.1\mu s$. Finally, the measured difference between the two output powers is averaged over a long time T_0 to achieve the requested noise power resolution. Let us first consider that the ISO input signal U_2 is zero. When the IN-input monochromatic signal with a complex amplitude U_1 is split by the first hybrid coupler, Eq.4.1 gives:

$$\begin{cases} U_{La} = \frac{1}{\sqrt{2}} U_1 \\ U_{Ra} = \frac{i}{\sqrt{2}} U_1 \end{cases} \tag{4.2}$$

Here, U_{La} (resp. U_{Ra}) is the complex amplitude of the signal in the left (resp. right) inner arm of the interferometer, before amplification. After amplification, the signals become:

$$\begin{cases} U_{Lb} = \pm(\frac{1}{\sqrt{2}} g_L U_1 + N_L) \\ U_{Rb} = \frac{i}{\sqrt{2}} g_R U_1 + N_R \end{cases} \tag{4.3}$$

The ± 1 factor in U_{Lb} is given by the π-phase modulator. The signals are then recombined on the second hybrid coupler:

$$\begin{cases} U_{out,L} = \frac{1}{\sqrt{2}} \left(\frac{1}{\sqrt{2}} (\pm g_L - g_R) U_1 \pm N_L + i N_R \right) \\ U_{out,R} = \frac{1}{\sqrt{2}} \left(\frac{i}{\sqrt{2}} (\pm g_L + g_R) U_1 \pm i N_L + N_R \right) \end{cases} \tag{4.4}$$

When the interferometer is perfectly balanced, the gains and phase differences across the inner arms are equal, giving $g_L = g_R = g$. The prefactor of U_1 in $U_{out,L}$ (resp. $U_{out,R}$) is then equal to $g(\pm 1 - 1)/2 = \{0, -g\}$ (resp. $g(\pm 1 + 1)/2 = \{+g, 0\}$): the signal is entirely transmitted to only one output at a time, and periodically switched between the two outputs. The square law detectors measure the average power of the filtered signals $\overline{V_i} \propto \overline{|U_{out,i}|^2}$ over the filter bandwidth Δf:

$$\begin{cases} \overline{V_L} = \frac{\alpha_1}{2} \left(\frac{|g|^2}{2} (\pm 1 - 1)^2 \overline{|U_1|^2} + \overline{|N_L|^2} + \overline{|N_R|^2} \right) \\ \overline{V_R} = \frac{\alpha_2}{2} \left(\frac{|g|^2}{2} (\pm 1 + 1)^2 \overline{|U_1|^2} + \overline{|N_L|^2} + \overline{|N_R|^2} \right) \end{cases} \tag{4.5}$$

α_i is the power to voltage conversion factor of the quadratic detectors; it includes amplification/attenuation factors in the output arms of the setup. Eq.4.5 assumes that U_1, N_L and N_R are independent, so that all correlation terms such as $\overline{U_1^* N_L}$, $\overline{U_1^* N_R}$ or $\overline{N_L^* N_R}$ vanish. As N_L and N_R have equal contributions in both outputs, they vanish in the final subtraction $\overline{V_L} - \overline{V_R}$ if $\alpha_1 = \alpha_2 = \alpha$. This gives:

$$\overline{V_{meas}} = \mp \alpha |g|^2 \overline{|U_1|^2} \tag{4.6}$$

The measured output voltage is therefore a square signal, with a frequency $f = 2.7$ kHz and an amplitude $V_{meas} = \alpha |g|^2 \overline{|U_1|^2}$, that can be detected with conventional lock-in measurement techniques so as to make the measurement insensitive to low-frequency variations of the amplification parameters,

thus greatly enhancing the stability of the device. Since th setup is symmetric, the contribution of a signal U_2 on the second input ISO of the interferometer can easily be included:

$$\overline{V_{meas}} = \pm\alpha|g|^2\left(\overline{|U_2|^2} - \overline{|U_1|^2}\right) \tag{4.7}$$

One can generalize this formula to non-monochromatic input signals with current power spectral densities $S_{1,2}(f)$, meaning that the result has to be integrated over a finite bandwidth. We finally obtain:

$$\overline{V_{meas}} = \pm\alpha\int_0^\infty |\chi(f)g(f)|^2(S_2(f) - S_1(f))df \tag{4.8}$$

where $\chi(f)$ is the filter function of each output arm of the device, ideally given by a square window with a bandwidth Δf and equal for both arms. The setup therefore measures the difference of the power spectral densities of the two inputs. As described in the next section, we connect the first input to the sample output, and the second input to a load with a fixed temperature; interestingly, this differential setup can be used to measure the noise difference between two samples, or between two distinct ports of the same sample, leading to cross-spectrum measurements.

We shall now discuss the advantages of this setup compared to a direct amplification technique, as described in Fig.4.2a, where the noise of the sample is directly amplified, filtered and measured on a square law detector. For a direct comparison with the amplifiers noise temperature, we express the current fluctuations of the input signals S_I in terms of a noise temperature T_{S_I}:

$$Z_0 S_I = 4k_B T_{S_I} \tag{4.9}$$

where Z_0 is the load impedance (generally 50 Ω for microwave circuits), and k_B the Boltzmann constant. In each case, the sample emits a noise T_S, and is connected to the measurement load Z_0, which itself emits an equilibrium noise T_{eq}. In Fig.4.2a, the amplification adds a noise $T_N \gg T_{eq}$ (typically, $T_N \approx 7$ K and $T_{eq} \approx 30$ mK) to the signal $T_S + T_{eq}$: the measured signal is then proportional to the sum $T_S + T_N + T_{eq}$. In order to extract T_S, one usually removes $T_N + T_{eq}$ by periodically switching on and off T_S while performing a lock-in detection. In this case, the low-frequency output voltage is a square signal with an offset $T_N + T_{eq} + T_S/2$ and an amplitude $T_S/2$. If the amplifier's noise T_N is Gaussian [109], the signal-to-noise ratio is then equal to $(S/N)_{direct} = (T_S/2T_N)\sqrt{\Delta f t_{meas}}$, where Δf is the bandwidth of the filter, and t_{meas} the measurement time. This expression can be compared to the signal-to-noise ratio calculated for our setup, see Fig.4.2b: the sample and the measurement load are connected to the IN input, and a Z_0 load is connected to the ISO input. The noise temperature on the IN input is therefore equal to $T_S + T_{eq}$, while the noise on the ISO input is equal to T_{eq}. Our setup detects the difference between the two input noises, that is $\pm T_S$. The low-frequency output voltage is therefore a square signal with an amplitude T_S and no offset. The suppression of the noise offset due to the amplifiers greatly enhances the stability of the setup, since one is no more sensitive to variations of the amplifiers noise, which are usually much larger than the signal T_S. This result is illustrated by the graphs in Fig.4.2, which represent the measured lock-in voltage as a function of time for the direct amplification scheme (a) and our setup (b).

In our setup, the standard deviations of the two amplifier's noises add, while the noise offset due to the amplifiers is zero after the final subtraction. The standard deviation of the amplification noise in our setup is then $\sqrt{2}$ times the fluctuations of a single amplifier. However, since the amplitude of

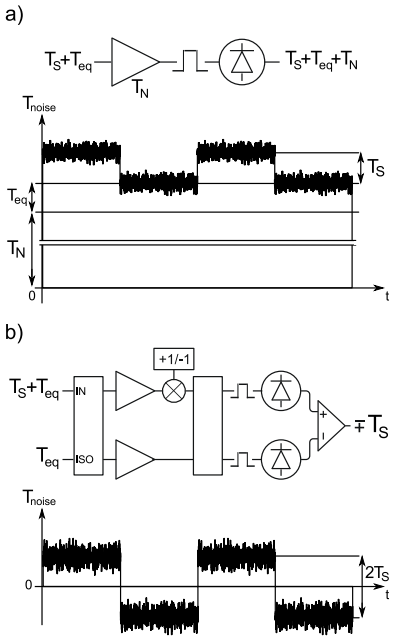

Figure 4.2: a) Direct amplification technique: the signal is amplified, filtered and applied to the square law detector, measuring the sum of the noise temperature of the signal and the measurement load $T_S + T_{eq}$ and the noise temperature of the amplifier T_N. Below is a schematic representation of the measured lock-in voltage as a function of time: the value of the lock-in voltage alternatively switches between $T_{eq} + T_N$ and $T_S + T_{eq} + T_N$. The peak-peak amplitude of the detected square voltage is equal to T_S. **b)** Our setup detects and modulates the difference between the two input noises $T_S + T_{eq}$ and T_{eq}, that is $\mp T_S$. The lock-in voltage is then centered on zero while its peak-peak amplitude is equal to $2T_S$. The standard deviation is however $\sqrt{2}$ times larger in our setup.

the measured noise is double in our setup, the signal-to-noise ratio is still larger than in the direct amplification scheme, and given by:

$$\left(\frac{S}{N}\right)_{setup} = \frac{T_S}{\sqrt{2}T_N}\sqrt{\Delta f t_{meas}} \tag{4.10}$$

For a given signal-to-noise ratio, our setup therefore allows measurements twice as fast as a direct amplification technique. However, Eq.4.10 stands for a perfectly balanced setup. Using the same calculations for a non-balanced setup, we expect the signal-to-noise ratio to be diminished by 5% for a 3 dB gain difference between the output arms, and the measurement time to be increased by 3% for a 10° phase difference between the two inner arms. Furthermore, the suppression of the noise offset due to the amplifiers greatly enhances stability, since the slow variations of T_N are automatically compensated.

The modulated double balanced amplifier technique is thus expected to increase the stability and sensitivity for high frequency noise measurements, while being relatively robust to imperfections in the setup.

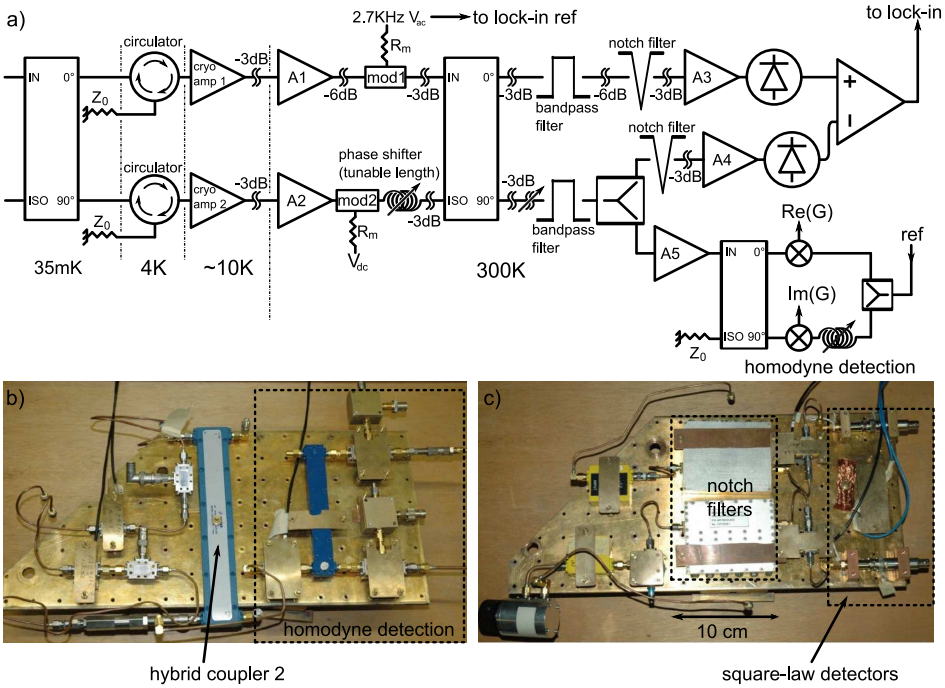

Figure 4.3: a) Schematic of the setup, as implemented in our Oxford Kelvinox 400 dilution refrigerator. **b)** and **c)** Pictures of the room-temperature parts of the setup.

4.1.1.2 Implementation

The implemented setup is shown in Fig.4.3. Two cryogenic amplifiers (*MiteQ AFS3-02000400-08-CR-4*) are used with a noise temperature of about 7 K when thermalized at 10 K in Helium vapor, and an extended bandwidth of $1-4$ GHz; these amplifiers can present a noise temperature as low as 3.5 K when thermalized in a pumped bath at 1.8 K [110]. Up to the dilution refrigerator's outputs, the setup is wired with *UT-85 SS* semirigid cryogenic microwave cables for an optimized thermalization. We also protect the sample from the back-action noise of the amplifiers using *Pamtech LTC 1384K4* cryogenic circulators whose 50 Ω loads are thermalized to the mixing chamber of the dilution fridge to reduce the background thermal noise. These optional circulators restrict the bandwidth of the whole setup to $1.2-1.8$ GHz. The lengths of the inner arms are matched using a phase shifter to tune the length of the second arm. 3 dB attenuators are regularly placed in between room temperature parts of the setup to suppress multiple reflections between the components; the 6 dB attenuator in the first inner arm is used to balance the gain difference between amplifiers $A1$ and $A2$. We insert a π-phase modulator (*Miteq BMA0104LA1MD*) in each inner arm to symmetrize the insertion losses and phase shifts (90°); however, we modulate only the signal in the first arm, feeding the first modulator with a 2.7 kHz square voltage through a 600 Ω load while the second modulator is fed with a constant current. After recombination on the second hybrid coupler, the signals are filtered in the $1.2-1.8$ GHz band. We use a 1.5 GHz excitation voltage to drive the sample out of equilibrium. The signal therefore presents a 1.5 GHz component which contains informations on the average AC current emitted by the sample, as well as a parasitic signal. We derive a portion of the signal in the second output arm using a 6 dB splitter (compensated by a 6 dB attenuator in the first output arm) and detect the in-phase and out-of-phase parts of the carrier frequency with a homodyne detection. We use a 90° hybrid coupler and multiply the 0° and 90° outputs by a 1.5 GHz local oscillator. The result of the multiplication of the 0° (resp. 90°) output yields a zero-frequency part proportional to the in-phase (resp. out-of-phase) part

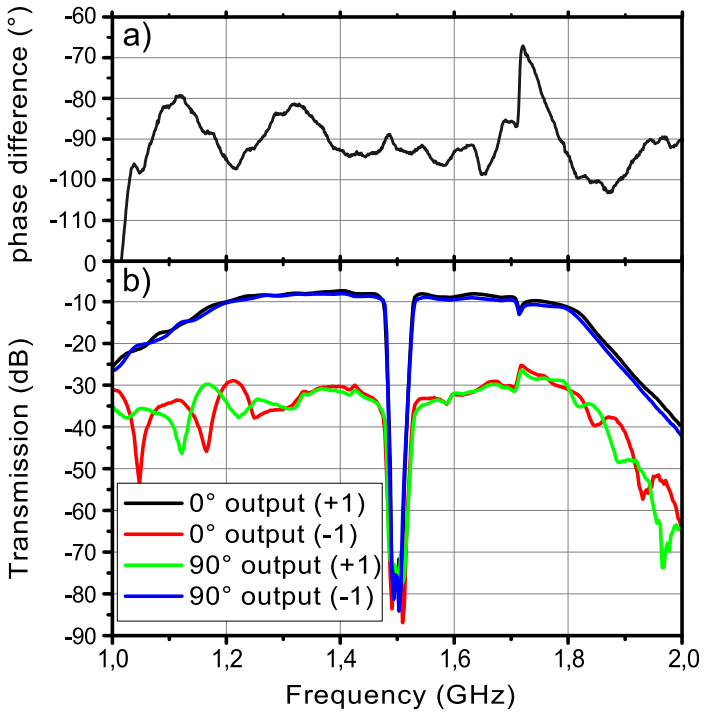

Figure 4.4: a) Phase difference between the two inner arms of the device as a function of the frequency. The signals of the two arms are measured just before the second hybrid coupler. **b)** Transmission between the input of the refrigerator and the two output arms of the setup (just before the square law detectors) for a positive (+1) and negative (−1) DC voltage on the modulator. The 1.5 GHz carrier is suppressed by more than 60 dB.

of the carrier frequency. When the modulation is turned on, the carrier frequency is switched between the two output arms; therefore, the homodyne signals are 2.7 kHz square voltages switching between zero and a value proportional to the quadrature components of the carrier frequency, and are detected with lock-in techniques. In the noise measurement part of the setup, the 1.5 GHz carrier frequency is removed (−70 dB) with *BL-Microwave* 1.5 GHz notch filters. The noises in the two output arms are subtracted with a *NF LI75-A* low frequency differential amplifier.

We have tuned the setup to optimize the phase and gain balance in the inner arms, as well as the gain balance in the output arms. The latter is done by inserting a variable attenuator, set to 0 dB, in the second output arm (the insertion loss of the attenuator compensates the gain difference in the arms). In order to characterize the gain and the phase balance, we use a vector network analyzer to measure the transmission between the first input of the setup with a 90 dB attenuation, and each one of the two inner arms just before the second hybrid coupler (Fig.4.4a), or each one of the two output arms just before the square law detectors (Fig.4.4b). The second input of the setup is connected to a 50 Ω load thermalized to the mixing chamber, and the first modulator (*mod1*) is fed with a constant (positive or negative) voltage to study both situations.

The results of the tuning are shown in Fig.4.4. The phase balance is achieved within ±5° in the 1.2 − 1.8 GHz bandwidth, which only degrades the signal-to-noise ratio by a few percents. As a result, the test signal is transmitted to only one output, with less than 1% of the power transmitted to the other output. This 20 dB difference between the two transmissions compares favorably with standard isolation values in commercial-grade microwave components. The amplification and filtering

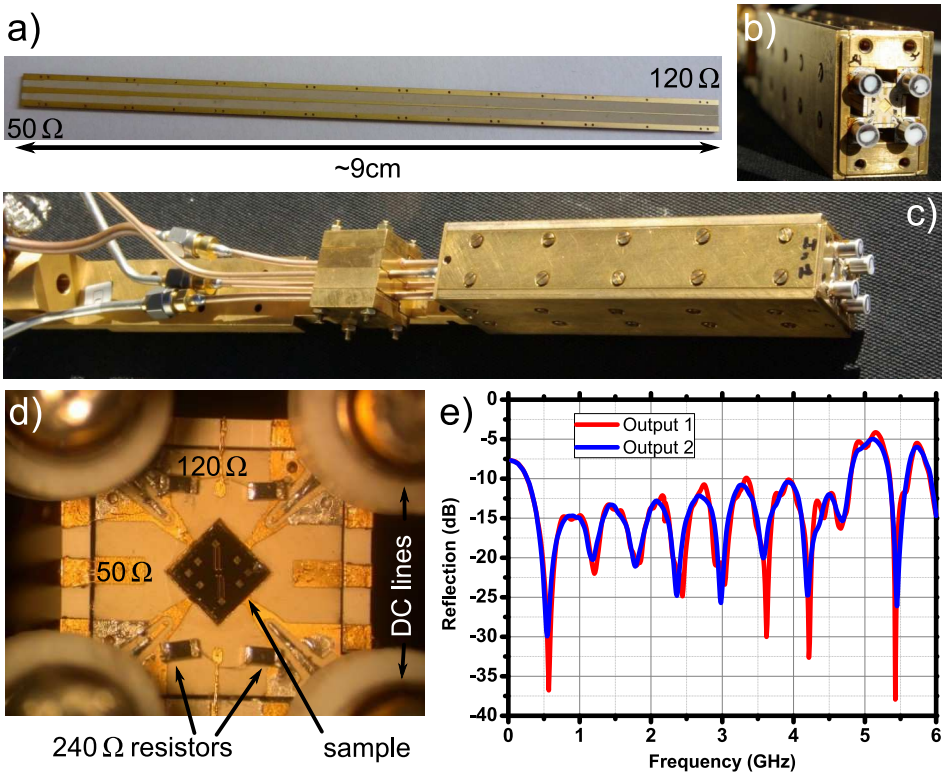

Figure 4.5: **a)** 120 Ω − 50 Ω transformer line: the coplanar waveguide is built on a $TMM10$ substrate for low-temperature performance. The width of the center conductor is 0.66 mm for the 50 Ω port, and 0.075 mm for the 120 Ω port. **b)** and **c)** Pictures of the 4-microwave ports sample holder. The 50 Ω lines and the transformer lines are encased in the four sides of the sample holder. **d)** Zoom on the center part of the sample holder; the size of the sample is 2 mm × 2 mm. e) Reflection on the 50 Ω port of the two transformer lines as a function of the frequency, measured in liquid nitrogen.

are identical (to less than 1 dB) for both outputs. The 1.7 GHz peak in the phase balance, due to the cryogenic circulators, causes a decrease of the transmission difference to ∼ 15 dB, which is still within acceptable bounds.

4.1.1.3 Calibration

We have calibrated the setup by replacing the thermalized 50 Ω load (see Fig.4.6a) connected to the second input with a variable temperature 50 Ω load, which acts as a tunable thermal noise source. The temperature of the load is measured with a calibrated RuO_2 resistance. We use a series of SMA connectors to thermically decouple the load from the mixing chamber. We obtain a calibration (Fig.4.6b) between input temperature difference ΔT and the amplitude of the measured 2.7 kHz voltage: $P_{meas}(V) = 1.37 \times 10^{-5}(\pm 5\%)\Delta T$.

4.1.2 Quarter-wave impedance transformer

For given current fluctuations, one can increase the equivalent noise temperature by increasing the load impedance Z_0 in Eq.4.9. However, since a vast majority of commercial microwave components

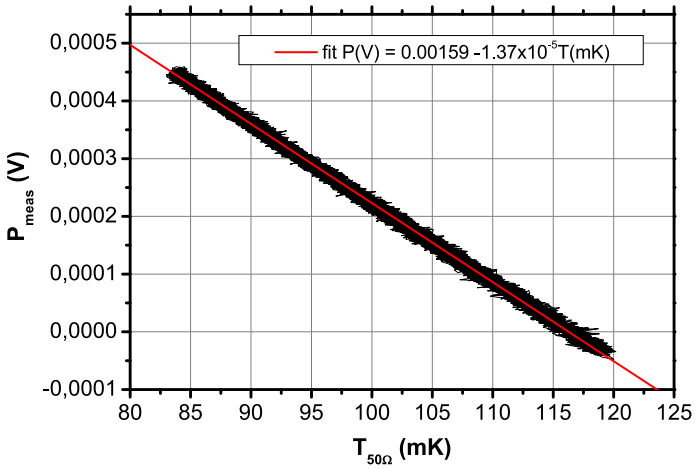

Figure 4.6: Calibration of the high-frequency noise measurement setup. The calibration yields $P_{meas}(V) = 1.37 \times 10^{-5}(\pm 5\%)\Delta T$.

are 50 Ω-adapted, one needs to transform the impedance seen by the sample from the increased Z_0 (in our case, $Z_0 = 120\ \Omega$) to 50 Ω while keeping a large bandwidth. This can be achieved by using a quarter wave impedance transformer [111, 87], which consists of a series of coplanar waveguides with gradually changing impedances. Every coplanar section has the same length, given by the quarter of the wavelength at center frequency. Depending on the series of impedances, one can either optimize the gain flatness or the total bandwidth.

We designed an 8-sections Chebychev (equal ripple) $120\ \Omega - 50\ \Omega$ transformer [5] (see Fig.4.5a), allowing a large bandwidth ($0.5 - 4.5$ GHz). The 120 Ω port is shunted by two 240 Ω $NiCr$ resistors in parallel (see Fig.4.5d) to avoid back-reflection of the noise of the measurement setup on the sample connected in parallel to the resistors, thus acting as a 120 Ω-adapted current source (we neglect the influence of the sample's impedance, of a few kΩ). We have taken into account the parasitic capacitances of the resistors (typically 0.03 pF) and the sample (~ 0.06 pF) by changing the length of each section to optimize the transmission of the device. We use a 4 microwave ports geometry for the sample holder; the two input ports are 50 Ω-adapted while each output port includes an impedance transformer. Both input and output lines are coplanar waveguides built on a TMM10 substrate, and encased in a copper sample holder (Fig.4.5b and c) thermalized to the mixing chamber of the dilution refrigerator. We have characterized the frequency response of the transformers by measuring the reflection of the 120 Ω port as a function of the frequency (see Fig.4.5e). We find a reflection of 15 dB at 77 K, which is comparable to the reflection factors in commercial microwave components. This corresponds to a power transmission through the transformer of 97%. The use of the transformer allows to increase the power spectral density of the measured signals by a factor 2.4. For a noise temperature of the amplifiers of about 7 K and a 120 Ω measurement load, Eq.4.10 gives an expected sensitivity of 2×10^{-28} $A^2/Hz/\sqrt{Hz}$.

4.1.3 Operation of the setup

We combine the effects of the quarter-wave impedance transformer and the modulated double-balanced amplifier to increase the signal of our sample, and measure it over extended periods of time with a large

[5] The impedance transformer lines were designed with a free spreadsheet applet available at `http://www.microwaves101.com/downloads/Xfmr101Rev3.xls` ; the optimization of the lines was done with AWR Microwave Office.

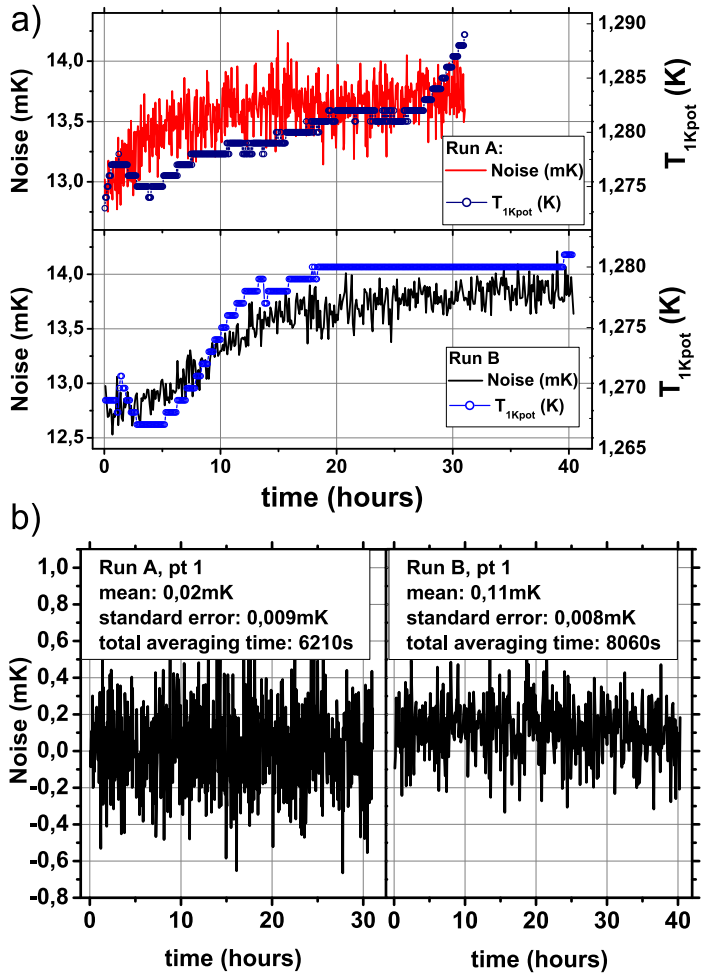

Figure 4.7: Operation of the setup: **a)** stability of the device for two non-consecutive runs: measured noise (line) and temperature of the 1K pot (circles) as a function of time. Noise data for both graphs are measured for the same reference gate voltage of the sample. The averaging time per point is 10 s for run A, and 20 s for run B. **b)** datasets obtained after subtraction of the reference for the first value of the gate voltage V_g of both runs. The dataset for run A presents a significantly larger standard deviation due to the shorter averaging time per point.

stability. In a standard noise measurement of a mesoscopic sample, one usually measures the noise $T_S(Vg)$ as a function of the device parameters, which can be tuned using one (or more) gate voltage Vg. Since the amplification parameters as well as the temperatures of the different stages of the dilution refrigerator can vary over the usual averaging times (about 1 hour per point), we perform repeated short measurements of the noise for a few (typically 5) gate voltages $Vg_{1,..,5}$ and a reference gate voltage Vg_{ref} which defines the zero of the measured noise. We thus measure the excess noise compared to a reference operating point of the sample. Since the measurement device is highly sensitive, one has to make sure that the temperature difference between the 120 Ω load connected to the sample and the load connected to the second input of the interferometer varies as slowly as possible. We connect the 120 Ω load of the second impedance transformer built on the sample holder (see Fig.4.5d) to the second input of the interferometer to keep the same thermal environment for the two loads, as well as reduce the offset due to the noise temperature difference between a 120 Ω and a 50 Ω load. We also

stabilize the temperature of the mixing chamber within less than a milliKelvin using the *femtopower* temperature regulation provided with Oxford Kelvinox refrigerators.

A typical operation of the setup is presented in Fig.4.7a: we measure the noise for each of the 5 gate voltages $T_S(Vg_{1,..,5})$ during a short time (10 s for run A, 20 s for run B). We systematically measure the noise for the reference gate voltage $T_S(Vg_{ref})$ after each gate voltage, thus creating a sequence composed of 10 short measurements ($T_S(Vg_1)$, $T_S(Vg_{ref(1)})$, $T_S(Vg_2)$, $T_S(Vg_{ref(2)})$, and so on), which we repeat a large number of times (621 for run A, 403 for run B). The total averaging time for each point is therefore at least ten times shorter than the total measurement time; a significant portion (one third for run A) of the total measurement time is spent in setting the gate voltage to its different values. We then remove the long-time variations of the signal due to slow temperature changes in the dilution refrigerator (such as the 1K pot temperature plotted in Fig.4.7a) by calculating the difference between the traces obtained for each gate voltage and their respective reference: $T_S(Vg_i) - T_S(Vg_{ref(i)})$. We finally calculate the mean value of each set of data such as the two presented in Fig.4.7b to obtain the noise, while the sensitivity of the measurement is given by the standard error. Fig.4.7b demonstrates a resolution T_{res} of less than 10 μK (*i.e.* 4.6×10^{-30} A^2/Hz) in about 2 hours; this gives a sensitivity $s = T_{res}\sqrt{t_{mes}}$ equal to 0.71 mK/$\sqrt{\text{Hz}}$, *i.e.* 3.3×10^{-28} A^2/Hz/$\sqrt{\text{Hz}}$ on a 120 Ω load. This value of the sensitivity is larger than the theoretical value; however, one has to consider the fact that the noise values are obtained after subtraction of a reference noise, hence multiplying the standard error by a factor $\sqrt{2}$. The calculated effective sensitivity of the measurement is thus $\sqrt{2}$ times larger than the sensitivity of the setup, which is then equal to 2.3×10^{-28} A^2/Hz/$\sqrt{\text{Hz}}$. This value is close to the theoretical sensitivity (see paragraph 4.1.2), demonstrating the good implementation of the device, and a large enough stability to perform measurements averaged over several hours.

We have used the setup to measure the autocorrelation of the current fluctuations emitted by the single electron source, presented in chapter 2. In particular, the noise data presented in Fig.2.15 have been obtained in about five days, each data point being measured in a total of 40 minutes using the measurement procedure described in the beginning of this section.

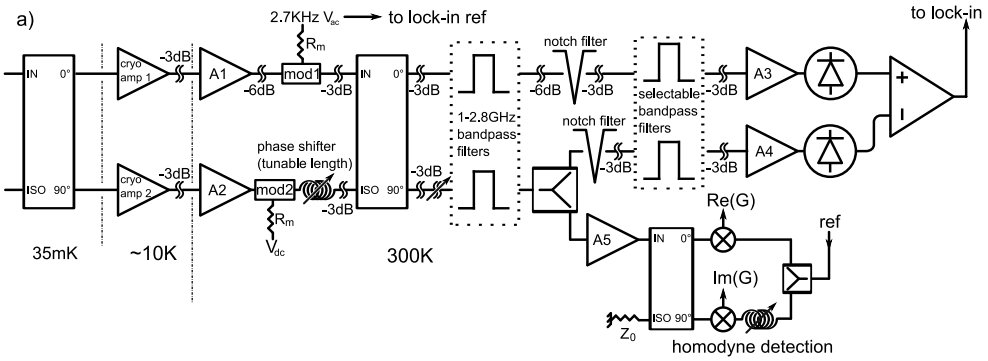

Figure 4.8: Modified high-frequency noise measurement setup. The cryogenic circulators have been removed to extend the total bandwidth to $1 - 2.8$ GHz. This bandwidth can be restricted using different bandpass filters.

4.1.4 Modifications

In order to study the temporal variation of the current fluctuations correlation in the HBT configuration as proposed in 3.2, we have modified the high frequency noise measurement setup: indeed, by measuring the value of the noise power spectral density at different frequencies, one can rebuild the current fluctuations correlation function $\overline{\langle \delta I(t)\delta I(t+\tau)\rangle}^t$. Since dividing the base bandwidth $1.2 - 1.8$ GHz

into smaller frequency intervals causes the sensitivity to diminish, we have rather increased the total bandwidth of the setup to $1-2.8$ GHz by removing the circulators and replacing some of the elements of the setup (mainly, amplifiers A3 and A4 in Fig.4.3, as well as the $1.2-1.8$ GHz filters).

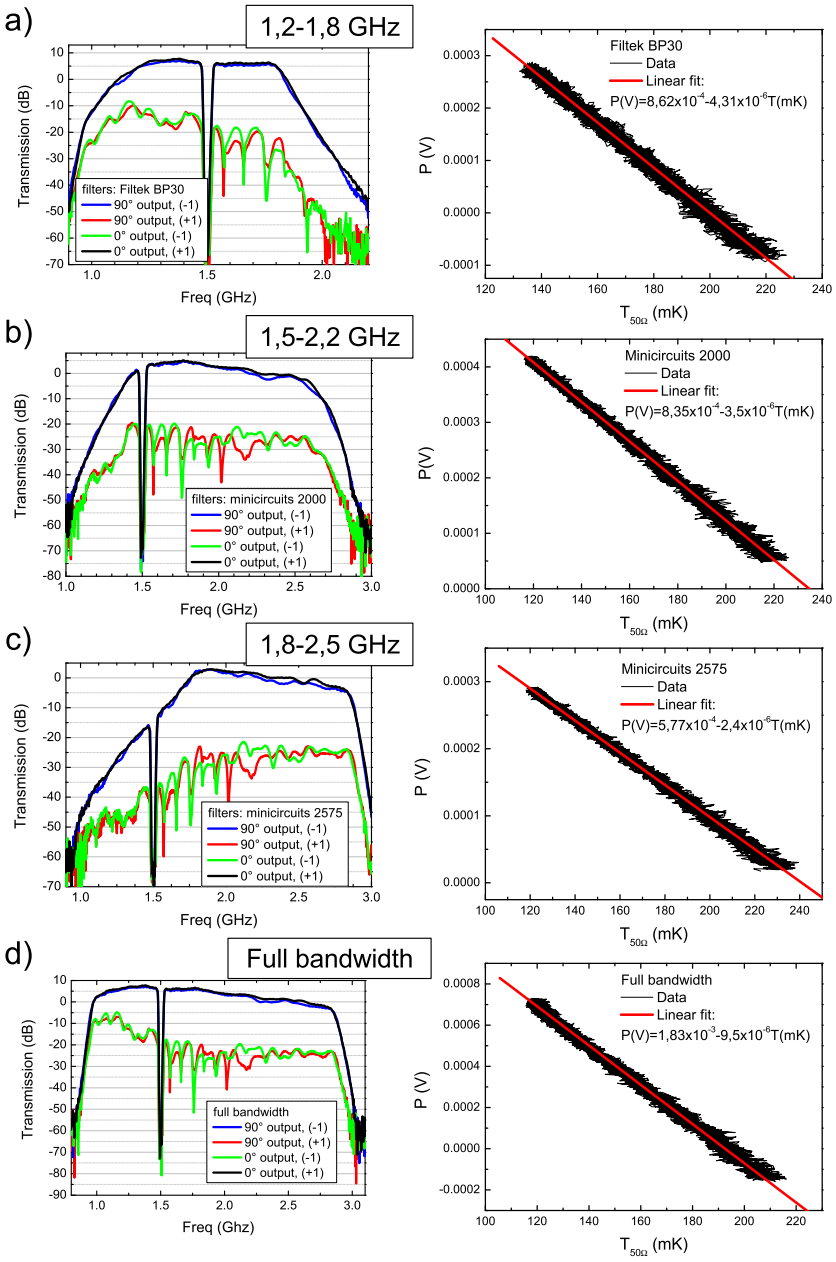

Figure 4.9: Tuning and calibration of the modified setup, for three sets of filters **(a,b,c)** and the full bandwidth **(d)**. Left panel: transmission between the input of the refrigerator and the two output arms of the setup (see Fig.4.4 for details). Right panel: calibration using a variable temperature 50 Ω load. Each calibration is performed twice to estimate the error on the conversion coefficient.

A schematic view of the modified setup is presented in Fig.4.8: after recombination on the second hybrid coupler, the signal is filtered on a larger bandwidth ($1-2.8$ GHz) using *BL-Microwave* bandpass

filters. The upper corner frequency has been set to 2.8 GHz in order to discard the second harmonic of the 1.5 GHz carrier frequency; we use the same notch-filters as in the previous version of the setup to discard the first harmonic. Another filter stage has been added right after the notch filters: in order to change the measurement frequency, we simply change the filters on this last stage. We use three sets of paired RF-filters to define the measurement bandwidths (see Fig.4.9): $1.2-1.8$ GHz, $1.5-2.2$ GHz and $1.8-2.5$ GHz. We can also remove the filters to measure the noise on the whole bandwidth of the setup ($1-2.8$ GHz).

Like the previous version, we have tuned and calibrated the setup for the four available measurement bandwidths: the result is shown on Fig.4.9. However, in order to implement the low-frequency noise measurement setup (see next section), we connect the second input of the modulated double-balanced amplifier to a 50 Ω instead of the second 120 Ω load of the sample holder, which we replace by a larger load for the low-frequency noise measurement.

The high frequency noise measurements presented in chapter 3 demonstrate the effectiveness of the modified setup. Furthermore, measuring on the full bandwidth of the setup improves the sensitivity to $\sim 1.1 \times 10^{-28}$ $A^2/Hz/\sqrt{\text{Hz}}$.

4.2 Low frequency noise measurement setup

In this section, we describe the measurement setup used in the study of low-frequency current fluctuations of a partitioned single electron beam presented in chapter 3. We first describe the measurement principle, based on cross-correlation measurements. We then describe the calibration and operation of the setup, as well as possible modifications allowing to increase the sensitivity.

4.2.1 Description of the setup

The low-frequency noise measurement setup relies on a widely used cross-correlation technique [31, 112, 113], where voltage fluctuations are detected on two independent measurement lines. The outputs of both lines are then digitized using a fast acquisition card, which finally calculates the integrated power in band of the cross-correlation of the two signals. The purpose of this technique is to render the measurement insensitive to fluctuations of the amplifiers gains, as well as the thermal noise of the wires connecting the sample to the amplifiers. Indeed, the noise offset due the amplifiers voltage noise is usually much larger than the measured signal, so that a small fluctuation of the gain causes variations in the noise offset still larger than the signal. As for the high-frequency measurement setup, it is therefore crucial to remove this noise offset; in low-frequency noise measurements, this is usually done by calculating the cross-correlation of two independent measurement lines [31, 112].

The principle of the setup is described in Fig.4.10: the current fluctuations emitted by the source (not pictured in the figure) are converted into voltage fluctuations using the measurement load R_0. The signal is then split in two measurement lines containing three amplification stages. After the last amplification stage, the signals are filtered and sent on an *Acquiris AP240* fast acquisition card (previously used in the time-domain measurements presented in 1.4.3.1). After digitization, we directly calculate the integrated power in band of the cross-correlation.

4.2.1.1 Implementation

We have replaced the 120 Ω load of the second output of the sample holder (see Fig.4.5d) by a 3 kΩ load. The measurement impedance R_0 is then given by the parallel association of the 3 kΩ load with the impedance of the edge channels of the Quantum Hall Effect (see Fig.3.12). For a filling factor $\nu = 2$, we have $R_0 \approx 2.4$ kΩ. Because this value of the measurement impedance is rather large, we

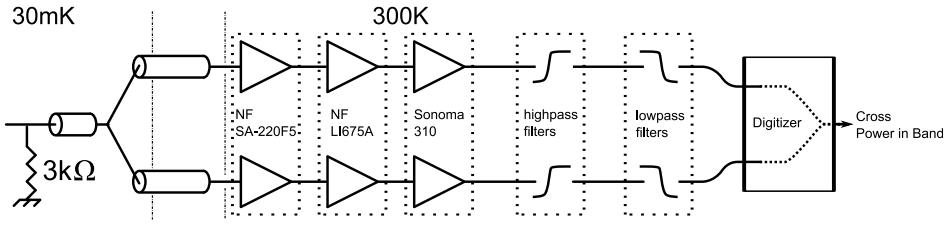

Figure 4.10: Schematic view of the low frequency noise measurement setup. The filter stages are described in Fig.4.11.

have wired the setup with $UT-85-SS$ semi-rigid cryogenic microwave coaxial cable to maximize the bandwidth. As for the high frequency measurement setup, the wires are carefully thermalized to each stage of the dilution refrigerator. The thermal load caused by the multiplication of microwave coaxial cables in the dilution refrigerator has led to an increase of the base temperature to $\sim$ 65 mK. All three amplification stages are placed at room temperature; the first stage is composed of a pair of *NF SA-220F5* amplifiers, with a voltage noise equal to 0.7 nV/$\sqrt{\text{Hz}}$. After the second and third amplifier stages (respectively, *NF LI-75A* and *Sonoma 310*), we use a pair of lab-built 6th-order highpass filters to remove the low-frequency part of the spectrum (below $\sim$ 30 kHz), which contains many parasitic signals. We then use a pair of lab-built 8th-order lowpass filters with a $\sim$ 380 kHz cutoff frequency as anti-aliasing filters. The two sets of filters are 50 Ω-adapted; their schematics and frequency response are shown in Fig.4.11.

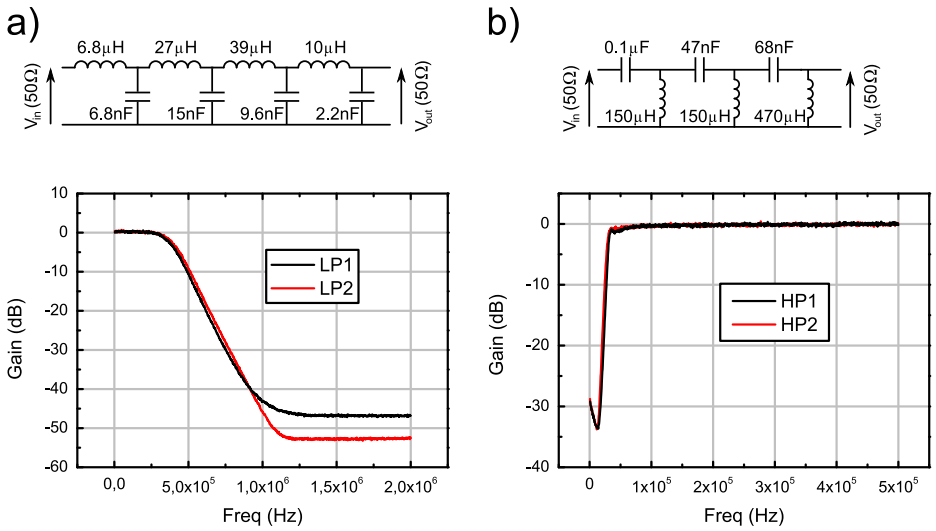

Figure 4.11: Circuit diagram and frequency response of the lab-made lowpass (LP1 and LP2, **a)** and highpass (HP1 and HP2, **b)** filters used in the low-frequency noise measurement setup. Each measurement line include one lowpass and one highpass filter (see Fig.4.10).

The two signals are then digitized (130000 samples) with a 1 MHz sampling frequency. We finally use numeric $10th$-order highpass filter with a tunable corner frequency (typically, f_c = 80 kHz) to remove any remaining low-frequency parasitic signal, and calculate the integrated power of the product of the two filtered signals. This last step increases the total measurement time by less than 8%.

4.2.1.2 Signal-to-noise ratio

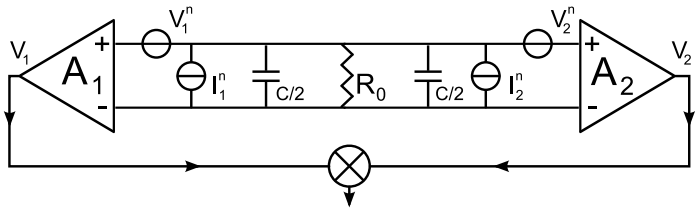

Figure 4.12: Principle of low-frequency cross-correlation measurement: the noise emitted by the sample (not depicted) is detected on the measurement load R_0 by two independent amplifiers $A1$ and $A2$, which add the input voltage noises $S_{VV}^{n_{1,2}} =< (V_{1,2}^n)^2 >$ and the current noises $S_{II}^{n_{1,2}} =< (I_{1,2}^n)^2 >$. Because the voltage noises are not correlated, their contribution to the noise offset after multiplication of the the outputs of the two lines vanish.

In order to estimate the measurement time, one must compare the noise emitted by the sample with the noise added by the first amplification stage. The principle of the comparison for the cross-correlation scheme [112] is illustrated in Fig.4.12: when connected to a measurement load R_0, a low-frequency amplifier adds both a voltage noise $S_{VV}^n =< (V^n)^2 >$ and a current noise $S_{II}^n =< (I^n)^2 >$. The addition of these noises is represented by the voltage and current generators in Fig.4.12. The current noise can be expressed as a voltage noise using the load R_0, so that the amplifier adds an effective voltage noise to the signal:

$$V_{eff}^n = V^n + R_0 I^n \tag{4.11}$$

If V^n and I^n are assumed to be independent, this yields:

$$S_{VV,eff}^n =< (V_{eff}^n)^2 >=< (V^n)^2 > +R_0^2 < (I^n)^2 >= S_{VV}^n + R_0^2 S_{II}^n \tag{4.12}$$

The optimal measurement impedance R_{opt} is obtained when the contribution of the voltage and current noise (expressed as voltage fluctuations) are equal, that is $R_{opt}^2 S_{II}^n = S_{VV}^n$.

In the cross-correlation measurement, the current noise sources of the two amplifiers are in parallel (see Fig.4.12); their contributions in the voltage noise of each measurement line therefore add, so that the voltage noise in each line is given by:

$$\begin{aligned} V_1 &= V_1^n + R_0(I_1^n + I_2^n) \\ V_2 &= V_2^n + R_0(I_1^n + I_2^n) \end{aligned} \tag{4.13}$$

For more clarity, we suppose that the two amplifiers are identical, so that $S_{VV}^{n_1} = S_{VV}^{n_2} = S_{VV}^n$ and $S_{II}^{n_1} = S_{II}^{n_2} = S_{II}^n$. The noise offset after multiplication of the outputs of the two lines is given by $< V_1 V_2 >$; since V_1^n, V_2^n, I_1^n and I_2^n are not correlated, the contribution of the voltage noises V_1^n V_2^n vanishes, so that the noise offset is equal to the sum of the contributions of the current noises $R_0^2(S_{II}^{n_1} + S_{II}^{n_2}) = 2R_0^2 S_{II}^n$. However, when considering the fluctuations of the amplifiers noise, one must still take into account the voltage noises $S_{VV}^{n_{1,2}} = S_{VV}^n$. Since the amplifiers noise is Gaussian, the output voltage fluctuations $S_{VV}^* = \sqrt{< (V_1 V_2)^2 > - < V_1 V_2 >^2}$ are given by:

$$(S_{VV}^*)^2 = (S_{VV}^n + 2R_0^2 S_{II}^n)^2 + (2R_0^2 S_{II}^n)^2 \tag{4.14}$$

Because the current noises sources are in parallel, the cross-correlation technique does not increase the signal-to-noise ratio. It however enhances the stability of the measurement, since the voltage noise offset is suppressed. In order to fully benefit from this technique, one should therefore choose a value of the measurement impedance slightly below the optimal value, in order to optimize the signal-to-noise ratio, which is calculated by the voltage fluctuation calculated above with the current noise emitted by the source (typically, $S_{ii} = e^2 f_0$), expressed as a voltage noise: $S_{VV} = R_0^2 e^2 f_0$. The signal-to-noise ratio is therefore given by:

$$\frac{S}{B} = \left(\frac{S_{VV}}{S^*_{VV}}\right)\sqrt{\Delta f t_{meas}} = \left(\frac{R_0^2 e^2 f_0}{\sqrt{(S^n_{VV} + 2R_0^2 S^n_{II})^2 + (2R_0^2 S^n_{II})^2}}\right)\sqrt{\Delta f t_{meas}} \tag{4.15}$$

where Δf is the bandwidth of the measurement lines, and t_{meas} the measurement time. We estimate Δf by considering the measurement lines as a RC-circuit, where the resistor is given by the measurement impedance R_0, and the capacitor is given by the total shunting capacitance of the wires connecting the sample to the amplifiers (see Fig.4.12). For a pair of ~ 2 meters-long *UT-85-SS* coaxial cables, the shunting capacitance C is equal to $\sim 0.4nF$. The integrated bandwidth is therefore equal to $\Delta f = 1/4R_0C$. However, we remove the low-frequency part of this bandwidth (up to 80 kHz), so that the effective bandwidth is equal to $\Delta f^* = 1/4R_0C - 80$ kHz ≈ 175 kHz for $R_0 \approx 2.4$ kΩ. The measurement time for a signal-to-noise ratio equal to 1 is therefore given by:

$$t_{meas} = \frac{(S^n_{VV} + 2R_0^2 S^n_{II})^2 + (2R_0^2 S^n_{II})^2}{(R_0^2 e^2 f_0)^2} \frac{1}{1/4R_0C - 80 \text{ kHz}} \tag{4.16}$$

With *NF SA-220F5* amplifiers ($S^n_{VV} \approx 4 \times 10^{-19} V^2/Hz$, $S^n_{II} = 4 \times 10^{-26} A^2/Hz$, so that $R_{opt} \approx 3.3$ kΩ) and $R_0 \approx 2.4$ kΩ, we have $t_{meas} \approx 110s$. This corresponds to a sensitivity equal to 3.98×10^{-28} A^2/Hz/$\sqrt{\text{Hz}}$, almost two times larger than the sensitivity of our high-frequency noise measurement setup.

4.2.2 Calibration and operation

We have calibrated the low-frequency noise measurement setup using the thermal noise of the 3 kΩ measurement impedance: provided the temperature of the measurement load R_0 is well known, one can measure the low frequency noise emitted by the load for different temperatures of the mixing chamber, and thus extract the correspondence between a temperature variation δT and a variation of the measured power in band δP. The assumption of a well-known temperature of the load is however non-trivial, since it implies that the measurement circuit is correctly thermalized to the mixing chamber. The temperature calibrations of the mesoscopic capacitor described in 1.3.2.3 (also shown in chapter 3 for sample *S434-8*) ensure that this assumption is correct for temperature larger than the effective electronic temperature (typically 70 mK). We have therefore calibrated the setup for temperatures ranging from 80 mK to ~ 500 mK. The calibration procedure is as follows: a large power ($\sim 2mW$) is applied to the heater of the mixing chamber, so as to set its temperature to ~ 500 mK. We ensure a proper thermalization of the measurement load to the mixing chamber temperature by waiting a few tens of minutes at ~ 500 mK, then turn off the heating power and let the refrigerator cool down while repeatedly measuring the low-frequency noise averaged over ~ 3 seconds. The result is shown on Fig.4.13: we have adjusted the data with a function including a noise offset (partly corresponding to

the amplifiers current noise) and a residual temperature T_0: $P(T) = P_0 + \alpha\sqrt{T_0^2 + T_{mc}^2}$. We obtain the calibration between a variation of the measured power-in-band and the equivalent noise temperature variation: $\Delta P = 5.5e - 6 \pm 10\%\Delta T$. The residual temperature is found equal to ~ 20 mK; while this value is lower than the value found in the capacitance calibration in 1.3.2.3, this measurement of the residual electronic temperature is not sensitive to gate noise, and therefore only gives the contribution to the residual temperature due to improper thermalization of the coaxial cables.

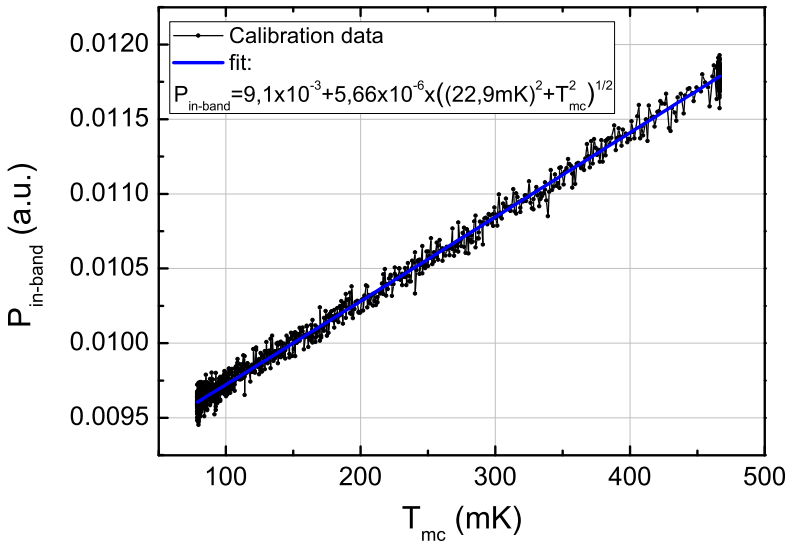

Figure 4.13: Calibration of the low-frequency measurement setup: the thermal noise of the measurement load is recorded as the mixing chamber cools down to the base temperature (averaging time: $\sim 3s$). We repeat the calibration several time to estimate the error on the conversion coefficient.

The calibration also allows us to estimate the sensitivity of the measurement setup: indeed, for an integration time equal to $\sim 3.3s$, we find a standard deviation in the measurement of the noise temperature equal to 10 mK, that is a standard deviation in the current noise power spectral density equal to $\sim 5.8e^2 f_0$. This corresponds to a measurement time for a standard deviation equal to $e^2 f_0$ $t_{meas} \approx 110s$. The sensitivity of the implemented setup is therefore equal to 4×10^{-28} A^2/Hz/$\sqrt{\text{Hz}}$, very close to the ideal sensitivity.

- **Operation**

The procedure for low-frequency noise measurements is similar to the one used for high-frequency noise measurements: we measure the noise for a given set of bias voltages during a short time (typically $10s$), then measure the noise with the QPC pinched-off while all other parameters are kept constant (especially, one has to compensate the change in the transmission of the central QPC in the HBT configuration caused by the coupling between V_g and V_{qpc}, see chapter 3). As for the high-frequency noise measurements, doing so makes the measurement insensitive to long-term variations of the environmental noise since only the contribution of the single electron emitter is measured. This sequence is repeated a large number of times (typically 700); as for high-frequency noise measurement, the stability of the dilution fridge over the whole measurement is crucial. We then subtract the two data sets in order to remove the long time variation of the background noise, and calculate the mean value and the standard error of the difference, which respectively yield the measured noise value and the error bars. Once again, because we calculate the difference between two noises, the variance increases by a factor $\sqrt{2}$, so that the effective sensitivity should become equal to 5.66×10^{-28} A^2/Hz/$\sqrt{\text{Hz}}$. In chapter 3, we

show typical low-frequency noise measurements with error bars equal to $\sim 0.2e^2 f_0$, for a total integration time per point equal to $6370s$. This corresponds to a measurement time for a unity signal-to-noise ratio $t_{meas} = 254s$: the effective sensitivity is therefore equal to 6.13×10^{-28} A^2/Hz/$\sqrt{\text{Hz}}$. This value is slightly higher than the expected effective sensitivity because the averaging time per sequence is still long enough for the background to vary; however, choosing shorter averaging times is not recommended because the total time spent changing the gate voltages might become comparable to (if not higher than) the total averaging time per point.

4.2.3 Possible improvements

The measured sensitivities (absolute as well as effective) demonstrate the proper implementation of the setup, as well as the efficiency of the measurement protocol. However, the sensitivity of our low-frequency noise measurement setup is still rather poor compared to our high-frequency noise measurement setup, let alone to state-of-the art low frequency noise measurement setups such as the one described in [114], which present sensitivities as low as 8.85×10^{-29} A^2/Hz/$\sqrt{\text{Hz}}$. While we have opted for a simple design in order to have an operational measurement setup as soon as possible, a few modifications can be made that can greatly enhance the sensitivity of the setup:

- **Resonant circuit**

The main difficulty of low-frequency noise measurements comes from microphonics caused by mechanical vibrations of the measurement cables. These vibrations induce many parasitic signals in the tens of kHz range, which can hardly be compensated by the measurement protocol. When operating at high magnetic field, these parasitic signals can become larger than the amplifiers noise even when all the wires are firmly anchored to the insert. The most straightforward way to make the measurement impervious to this effect is to simply filter out the whole frequency band where it takes place: in our case, we use a 10th-order highpass filter to remove frequencies below 80 kHz. While the measured spectra are devoid of most of the parasitic signals, we have significantly decreased the measurement bandwidth, thus increasing the measurement time by 40%. The use of a resonant circuit, however, allows to compensate the shunting capacitance of the measurement cables so as to shift the measurement bandwidth towards larger frequencies, where the parasitic signals vanish. As described in [114], the measurement impedance is shunted by an inductor (preferably thermalized to colder stage of the dilution refrigerator), thus creating a resonant parallel RLC circuit, where C is the shunting capacitance of the measurement wires. The inductance can be chosen so that the resonance frequency $f_r = 1/2\pi\sqrt{LC}$ is in the few hundreds of kHz range, while the total bandwidth is still given by $1/4R_0C$. Provided that the measured noise is white for frequencies below 1 MHz, using a resonant RLC circuit allows a measurement on the whole bandwidth with no pollution caused by 10 kHz-range parasitic signals.

While this technique is quite straightforward, it suffers from a major constraint caused by the finite resistance of the shunting inductor. Indeed, when the inductor is connected in parallel with the measurement load, its finite resistance r generates a thermal noise $S^r_{VV} = 4rk_BT_L$, where T_L is the temperature of the inductor. This voltage noise is filtered by the resonant RLC circuit, so that its contribution to the total voltage noise seen by the amplifiers is:

$$(S^r_{VV})^* = \frac{4rk_BT_L}{(1 - LC\omega^2)^2 + (\frac{L\omega}{R_0})^2} \tag{4.17}$$

For the usual values of R_0 and C, a $150\mu H$ inductor with a typical 1 Ω resistance generates a voltage noise at the resonance frequency $f_c = 650$ kHz equal to $2.6 \times 10^{-19} V^2/Hz$, that is 0.5 times the amplifiers voltage noise. Connecting the inductor at room temperature therefore increases the measurement time by a factor 2.25; it is thus necessary to implement the inductor inside the dilution

refrigerator to reduce this additional noise. In this case, one should carefully choose the inductor so that its characteristics in a cryogenic environment are well known; in particular, non-magnetic inductors are mandatory when working at large magnetic fields (see [114]).

The design and implementation of a non-magnetic inductive shunt (typically 150 μH) inserted in the low-temperature part of the measurement setup therefore would allow us to measure the noise on the full bandwidth of the setup, centered on the frequency $f_c = 650$ kHz.

- **Cryogenic amplifiers**

For a given measurement load, the bandwidth of the setup is mainly limited by the value of the shunting capacitance of the cables connecting the sample to the amplifiers. While microwave coaxial wires can be chosen to minimize the capacitance per unit length (typically 95 pF/m), the total length can hardly be diminished if the first amplification stage is placed at room temperature. Using cryogenic amplifiers thermalized at liquid helium temperature allows to reduce the length of cable by a factor ~ 2, and therefore increases the bandwidth. Furthermore, cryogenic amplifiers generally have a lower input voltage noise density than room-temperature amplifiers: for instance, the voltage noise of the cryogenic amplifiers used in [114] (*Agilent ATF-34143*) is equal to 0.4 nV/$\sqrt{\text{Hz}}$, compared to 0.7 nV/$\sqrt{\text{Hz}}$ for the *NF SA-220F5* amplifiers used in our setup. Cryogenic HEMTs with a voltage noise equal to 0.2 nV/$\sqrt{\text{Hz}}$ have also been recently developed at *Laboratoire de Photonique et Nanostructures*.

Using cryogenic amplifiers therefore allows to significantly extend the measurement bandwidth while lowering the amplifiers voltage noise, and could therefore decrease the measurement time by an order of magnitude. However, the main drawback of this technique is that cryogenic amplifiers dissipate a significant amount of heat, which might decrease the efficiency and stability of the dilution refrigerator, as well as increase liquid Helium consumption. Because of its efficiency, we are nonetheless still considering this option.

- **Removing the measurement load and using *NF LI-75A* amplifiers**

The measurement load plays a critical role in the measurement time, since a larger measurement load increases the measured signal to the power 4, but also increases the contribution of the amplifier current noise to the power 4 and diminishes the measurement bandwidth. We have plotted in Fig.4.14 the estimated measurement time for a unity signal-to-noise ratio as a function of the value of the measurement load R_0 with our current measurement setup. When the frequencies below 80 kHz are removed, the chosen measurement load ($R_0 = 2440\ \Omega$) optimizes the measurement time. When the noise is measured on the whole bandwidth (*e.g.* using the resonant circuit described above), the measurement time significantly decreases, and the value of the measurement load optimizing the measurement time is ~ 3 kΩ: as expected, this value is lower than the value of the optimal impedance $R_{opt} = 3.5$ kΩ. When the measurement load becomes higher than the optimal value, the contribution of the amplifiers current noise dominates, and the measurement time increases again.

Using amplifiers presenting a lower current noise allows to increase the measurement load, provided one can measure on the whole bandwidth: using *NF LI-75A* amplifiers, which have a higher input voltage noise density (2 nV/$\sqrt{\text{Hz}}$), but a lower current noise (0.02 pA/$\sqrt{\text{Hz}}$ instead of 0.2 pA/$\sqrt{\text{Hz}}$), in conjunction with a resonant circuit, would allow to remove the measurement load and directly measure on the impedance of the edge channels of the sample ($\sim$ 12.4 kΩ at filling factor 2) with a measurement time lower than $10s$. This scheme appears to be the most interesting in terms of improvement of the sensitivity compared to the amount of modifications. However, it is only efficient for high magnetic fields, where the impedance of the edge channels is larger than 6 kΩ, that is for filling factors lower than 4.

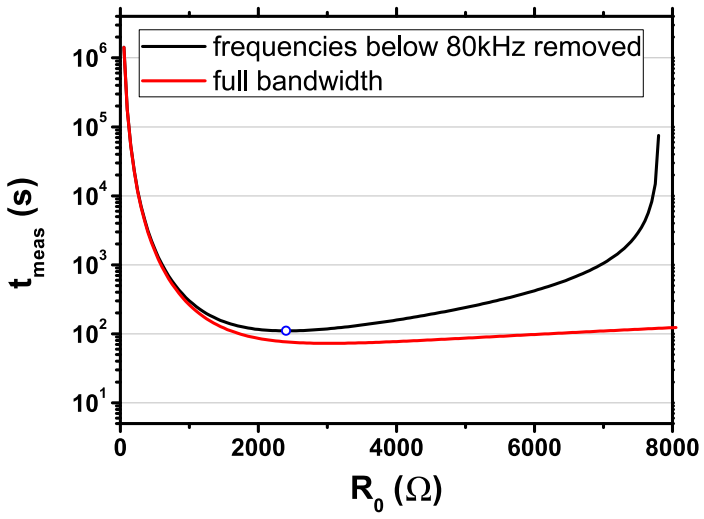

Figure 4.14: Calculated measurement time using Eq.4.16, for *NF SA-220F5* amplifiers, as a function of the measurement load R_0. Black line: the first 80 kHz of the measurement bandwidth are removed to reproduce the implemented setup. The blue circle corresponds to $R_0 = 2400\ \Omega$. Red line: the whole measurement bandwidth is used.

Conclusion of chapter 4

We have built two noise measurement setups able to measure the low-frequency (below 250 kHz) and high frequency ($1 - 2.8$ GHz) noise generated by the coherent manipulation of single electrons. Our high-frequency noise measurement setup demonstrates a state of the art sensitivity for GHz-range noise measurement, and several modification improving the sensitivity of the low-frequency noise measurement setup to state-of-the-art levels are considered. The ability to measure both low-frequency and high-frequency noise with a resolution of a fraction of $e^2 f_0$ is crucial to fully characterize the outcome of single-charge electron quantum optics experiments. Furthermore, our dual-output measurement setup, where the high-frequency noise is measured at one output, and low-frequency noise is measured at the other, might be used in further experiments where two distinct outputs are considered, such as the measurement of two-particle non-local Aharonov-Bohm effect with single charges [9], or any other experiment including a central QPC.

Conclusion

In this thesis, we have studied the noise generated by a single electron emitter, both intrinsic and after partition by a quantum point contact in a Hanbury-Brown and Twiss geometry. Similarly to quantum optics, the measurement of the fluctuations of the output currents is a relevant tool to probe the outcome of single-charge electron quantum optics experiments.

In the first chapter, we have presented a theoretical description of the mesoscopic capacitor within a Floquet scattering matrix formalism, which we have used to calculate the noise in the next chapters. We then focused both theoretically and experimentally on the average AC current emitted by the capacitor. Under a large periodic excitation drive, the current is quantized in units of $2ef_0$, where f_0 is the driving frequency, indicating that the mesoscopic capacitor can indeed be used as a single electron source. The study of the average AC current furthermore allows to characterize the parameters of the source: indeed, the value of the level spacing Δ and the residual temperature T_0 can be extracted from a temperature study of the linear regime, while the non-linear regime allows to locate the optimal operating point of the source (excitation amplitude V_{exc}, transmission D, equilibrium potential ϕ_0).

In the second chapter, we have studied the autocorrelation of the high-frequency current fluctuations emitted by the source. We have put into light the existence of an intrinsically high-frequency noise arising from the randomness in the emission times of single charges. This noise, called quantum jitter, is the signature of single charge emission: one expects to systematically measure its contribution when measuring high-frequency noise in a single-charge electron quantum optics experiment. Our experimental results demonstrate that in the optimal operating conditions of the source, the noise reduces to the quantum jitter, thus demonstrating single particle emission. We have also observed the crossover between the quantum jitter regime and the shot noise regime, where single charges are emitted randomly. In the optimal operating conditions, the agreement between the two models and the experimental data is excellent. We have measured an increase in the noise when charges are emitted close to the Fermi energy; this increase, related to the generation of additional electron/hole pairs, is well reproduced with the scattering model. The measurement of the noise emitted by the source therefore allows to put into light several regimes of noise which are well understood using the two models, thus demonstrating the validity of the description of the mesoscopic capacitor as time and energy-resolved single electron emitter.

In the third chapter, we have studied the partition of the current emitted by the single electron source by a quantum point contact, in the Hanbury-Brown and Twiss geometry. The calculation of the noise after partition within the Floquet scattering matrix formalism demonstrates the richness of the HBT geometry; in particular, the zero-frequency part of the partition noise directly counts the number of emitted electron/hole pairs per period. This property, which was first predicted in [64], allows to characterize the generation of additional electron/hole pairs when charges are emitted in resonance with the Fermi energy. It also opens the way to quantitative studies of the energy exchanges between adjacent quantum Hall effect edge channels at the single charge scale. Furthermore, the use of a biased contact at the second input of the QPC allows to measure the energy distribution of the emitted charges; the principle of this measurement can be extended to measure the diagonal terms of the density matrix (coherence) by applying RF signals to the biased contact [65], leading to the full tomography of single charges. The experimental results presented in this chapter demonstrate the feasibility of these measurements; however, they also emphasize the importance of a controlled measurement environment, particularly regarding the electronic temperature.

Finally, we have described in the fourth chapter the noise measurement setups used in the experimental studies presented in chapters 2 and 3. Indeed, both high and low-frequency noises considered in these chapters are of the order of $e^2 f_0 \approx 3.8 \times 10^{-29}$ A^2/Hz, where $f_0 = 1.5$ GHz is the drive frequency; while this value of the noise corresponds to typical resolutions in state of the art low-frequency noise measurement setups [114, 48], it is extremely challenging to reach in a high-frequency measurement. We have therefore designed and implemented a high-frequency noise measurement setup with an exceptional sensitivity of 1.3×10^{-29} A^2/Hz in a 5 minutes measurement time, based on the joint use of a quarter-wave impedance transformer which allows to increase the measurement impedance from 50 Ω to 120 Ω (thus increasing the amplitude of the voltage fluctuations), and a modulated double balanced amplifier which dramatically increases the stability of the measurement. An independent calibration of the setup allows us to compare the experimental noise data presented in the second chapter with the results yielded by the two models without any free parameter. We have also implemented a low-frequency noise measurement setup in order to perform the experiments presented in the third chapter. While the sensitivity of this setup is not as good as the sensitivity of the high-frequency noise measurement setup, one can consider several relatively simple modifications that would significantly increase its efficiency.

In conclusion, the measurements performed during my thesis are the first experimental realization of single-charge electron quantum optics experiments. We have shown that the current fluctuations yield the signature of single particle emission, as well as numerous informations on the number of emitted electron/hole pairs per period and the energy distribution of the emitted charges, thus demonstrating the fact that noise measurements are the proper tools for the realization of single-charge electron quantum optics experiments. Furthermore, we have demonstrated the effectiveness of the mesoscopic capacitor as a single electron emitter, making it a solid candidate to perform single-charge electron quantum optics experiments.

After having performed the experiments proposed in the third chapter, the implementation of single charge tomography can be considered, using the second excitation line built in our dilution refrigerator to apply RF voltages to the opposite contact. The ability to measure the energy distribution and the coherences of emitted charges opens the way to a vast quantity of experiments probing both relaxation and decoherence of single charges in QHE edge channels: one could for instance measure the density matrix after different propagation lengths by adding a gate between the source and the central QPC to change the length of the path; one can also implement the voltage probe technique used in Mach-Zehnder interferometers [19] to tune the decoherence of the emitted charges. Lastly, results presented in this thesis allow to soundly consider the use of a second synchronized single electron source to perform Hong-Ou-Mandel electronic collision experiments [12].

Appendix A

Scattering Formalism

A.1 Floquet scattering matrix

A.1.1 Sum Rules

- **Sum rule A**

Let us calculate the sum $\sum_n U^*_{n+m}(\epsilon - m\hbar\Omega)U_{n+m'}(\epsilon - m'\hbar\Omega)$, with:

$$\begin{aligned} U^*_{n+m}(\epsilon - m\hbar\Omega) &= \sum_k c_{k+n+m}c^*_k U^{0*}(\epsilon - (m+k)\hbar\Omega) \\ U_{n+m'}(\epsilon - m'\hbar\Omega) &= \sum_{k'} c^*_{k'+n+m'}c_{k'}U^0(\epsilon - (m'+k')\hbar\Omega) \end{aligned} \tag{A.1}$$

With the notation $\hbar\Omega = 1$, so that $\epsilon + m\hbar\Omega \equiv \epsilon + m$, the sum yields:

$$\begin{aligned} \sum_n U^*_{n+m}(\epsilon - m)U_{n+m'}(\epsilon - m') = \sum_{k,k'}\left(\sum_n c_{k+n+m}c^*_{k'+n+m'}\right) \\ \times c^*_k c_{k'}U^{0*}(\epsilon - m - k)U^0(\epsilon - m' - k') \end{aligned} \tag{A.2}$$

The sum rule on the c_n coefficients implies that $\sum_n c_{k+n+m}c^*_{k'+n+m'} = \delta_{k'+m',k+m}$. This yields, with $U^{0*}(\epsilon - m - k)U^0(\epsilon - m - k) = 1$:

$$\begin{aligned} \sum_n U^*_{n+m}(\epsilon - m)U_{n+m'}(\epsilon - m') &= \sum_{k,k'}\delta_{k'+m',k+m}c^*_k c_{k'}U^*_0(\epsilon - m - k)U^0(\epsilon - m' - k') \\ &= \sum_k c^*_k c_{k+m-m'} \end{aligned} \tag{A.3}$$

The sum rule on the c_n coefficients now implies:

$$\sum_n U^*_{n+m}(\epsilon - m\hbar\Omega)U_{n+m'}(\epsilon - m'\hbar\Omega) = \delta_{m,m'} \tag{A.4}$$

- **Sum rule B**

Let us demonstrate the sum rule $\Sigma = \sum_m |\sum_n U^*_n(\epsilon - n)U_{m+n}(\epsilon - n - \omega)|^2 = 1$ (with $\hbar\Omega = \hbar = 1$):

$$\begin{aligned}\Sigma &= \sum_m \left(\sum_n U_n^*(\epsilon-n)U_{m+n}(\epsilon-n-\omega)\right)\left(\sum_{n'} U_{n'}(\epsilon-n')U_{m+n'}^*(\epsilon-n'-\omega)\right)\\ &= \sum_{n,n'} U_n^*(\epsilon-n)U_{n'}(\epsilon-n')\sum_m U_{m+n}(\epsilon-n-\omega)U_{m+n'}^*(\epsilon-n'-\omega) \qquad \text{(A.5)}\\ &= \sum_n U_n^*(\epsilon-n)U_n(\epsilon-n)\end{aligned}$$

We use the first sum rule to simplify the sum over m. Let us now expand the Floquet scattering matrices in terms of c_n coefficients and equilibrium scattering matrix $U^0(\epsilon)$:

$$\Sigma = \sum_n \sum_{k,k'} c_{k+n}c_k^* c_{k'+n}^* c_{k'} U^{0*}(\epsilon-n-k)U^0(\epsilon-n-k') \qquad \text{(A.6)}$$

The successive variable substitutions $\tilde{n} = n+k$ and $\tilde{k} = k-k'$ yield:

$$\Sigma = \sum_{\tilde{n}} \sum_{\tilde{k}} c_{\tilde{n}} c_{\tilde{n}-\tilde{k}}^* \left(\sum_{k'} c_{k'+\tilde{k}}^* c_{k'}\right) U^{0*}(\epsilon-\tilde{n})U^0(\epsilon-\tilde{n}+\tilde{k}) \qquad \text{(A.7)}$$

We now use the sum rule on the c_n coefficients $\sum_{k'} c_{k'+\tilde{k}}^* c_{k'} = \delta_{\tilde{k},0}$ to demonstrate sum rule B:

$$\begin{aligned}\sum_m \left|\sum_n U_n^*(\epsilon-n)U_{m+n}(\epsilon-n-\omega)\right|^2 &= \sum_n c_n^* c_n U^{0*}(\epsilon)U^0(\epsilon)\\ &= \sum_n c_n^* c_n = 1\end{aligned} \qquad \text{(A.8)}$$

A.2 Average ac current

A.2.1 Expansion of Eq.1.32

Let us first expand the expression of $\hat{I}_b(t)$ given in Eq.1.32:

$$\hat{I}_b(t) = \frac{e}{h}\sum_{m,m',n,n'} \int d\epsilon d\epsilon' c_{n+m}c_n^* c_{n'+m'}^* c_{n'} U^{0*}(\epsilon-n)U^0(\epsilon'-n')\hat{a}^\dagger(\epsilon+m)\hat{a}(\epsilon'+m')e^{i\frac{\epsilon-\epsilon'}{\hbar}t} \qquad \text{(A.9)}$$

The variable substitutions $\tilde{\epsilon} = \epsilon - n$, $\tilde{\epsilon}' = \epsilon' - n'$, followed by $\tilde{m} = m+n$, $\tilde{m}' = m'+n'$, provide:

$$\hat{I}_b(t) = \frac{e}{h}\sum_{\tilde{m},\tilde{m}'} c_{\tilde{m}}c_{\tilde{m}'}^* \left(\sum_{n,n'} c_n^* c_{n'} e^{i(n-n')t}\right) \int d\tilde{\epsilon} d\tilde{\epsilon}' U^{0*}(\tilde{\epsilon})U^0(\tilde{\epsilon}')\hat{a}^\dagger(\tilde{\epsilon}+\tilde{m})\hat{a}(\tilde{\epsilon}'+\tilde{m}')e^{i\frac{\tilde{\epsilon}-\tilde{\epsilon}'}{\hbar}t} \qquad \text{(A.10)}$$

The sum rule on the c_n coefficients defined in Eq.1.10 implies that $\sum_{n,n'} c_n^* c_{n'} e^{i(n-n')t} = 1$. Therefore, after substituting $\{\tilde{\epsilon}, \tilde{\epsilon}', \tilde{m}, \tilde{m}'\}$ with $\{\epsilon, \epsilon', m, m'\}$ for more clarity, we obtain:

$$\hat{I}_b(t) = \frac{e}{h} \sum_{m,m'} c_m c_{m'}^* \int d\epsilon d\epsilon' U^{0*}(\epsilon) U^0(\epsilon') \hat{a}^\dagger(\epsilon + m) \hat{a}(\epsilon' + m') e^{i\frac{\epsilon - \epsilon'}{\hbar} t} \tag{A.11}$$

We can introduce the aforementioned sum rule $\sum_{m,m'} c_m^* c_{m'} e^{i(m-m')t} = 1$ in Eq.1.24 to obtain, after the substitutions $\epsilon \to \epsilon + m$ and $\epsilon' \to \epsilon' + m'$, a similar expression for $\hat{I}_c(t)$;

$$\hat{I}_c(t) = \frac{e}{h} \sum_{m,m'} c_m c_{m'}^* \int d\epsilon d\epsilon' \hat{c}^\dagger(\epsilon + m) \hat{c}(\epsilon' + m') e^{i\frac{\epsilon - \epsilon'}{\hbar} t} \tag{A.12}$$

The total current is therefore given by:

$$\hat{I}_1(t) = \frac{e}{h} \sum_{m,m'} c_m c_{m'}^* \int d\epsilon d\epsilon' \left[U^{0*}(\epsilon) U^0(\epsilon') \hat{a}^\dagger(\epsilon + m) \hat{a}(\epsilon' + m') - \hat{c}^\dagger(\epsilon + m) \hat{c}(\epsilon' + m') \right] e^{i\frac{\epsilon - \epsilon'}{\hbar} t} \tag{A.13}$$

Eq.1.34 is thus found when taking the quantum average of this last equation.

A.3 Comparison with the gauge-translation formalism

A.3.1 Average ac current

Let us compare the expression of the average ac current emitted by the mesoscopic capacitor obtained in Eq.1.32 with the expression given in Adrien Mahé's manuscript [68], calculated using a gauge translation that keeps the potential of the dot equal to zero, and modulates the potential of the contacts (Eq.1.11, p.22):

$$I_g(t) = \frac{e}{h} \sum_{n,n'} c_n^* c_{n'} \int d\epsilon \left[U^{0*}(\epsilon) U^0(\epsilon + (n' - n)\hbar\Omega) - 1 \right] f(\epsilon - n\hbar\Omega) e^{i(n-n')\Omega t} \tag{A.14}$$

After the successive variable substitutions $n' = -(k + m)$ and $n = -m$, Eq.1.32 yields:

$$I_1(t) = \frac{e}{h} \sum_{n,n'} c_{-n'}^* c_{-n} \int d\epsilon \left[U^{0*}(\epsilon) U^0(\epsilon + (n' - n)\hbar\Omega) - 1 \right] f(\epsilon - n\hbar\Omega) e^{i(n-n')\Omega t} \tag{A.15}$$

with:

$$c_{-n} = \frac{1}{T} \int_0^T dt e^{i - n\Omega t} e^{-i\frac{e}{\hbar} \int_0^t V'(\tau') d\tau'} = c_n^*[-V'] \tag{A.16}$$

This finally gives:

$$I_1(t) = \frac{e}{h} \sum_{n,n'} c_n^*[-V'] c_{n'}[-V'] \int d\epsilon \left[U^{0*}(\epsilon) U^0(\epsilon + (n' - n)\hbar\Omega) - 1 \right] f(\epsilon - n\hbar\Omega) e^{i(n-n')\Omega t} \tag{A.17}$$

This last expression is strictly equivalent to Eq.A.14, since the gauge translation changes the sign of the drive (the potential $-V'(t)$ is applied on the contacts).

A.3.2 Current fluctuations autocorrelation

We now compare the expression of the autocorrelation of the current fluctuations emitted by the source given in Eq.2.18 with its expression established in Adrien Mahé's thesis using the gauge translation (Eq.2.25, p.62):

$$S(\omega) = 2\frac{e^2}{h}\sum_m \int d\epsilon \left|\sum_n c^*_{n+m} c_n U^{0*}(\epsilon+n) U^0(\epsilon+n-\omega)\right|^2 f(\epsilon-m)(1-f(\epsilon-\omega)) \tag{A.18}$$

We first perform the variable substitution $\epsilon' \equiv \epsilon + m$ in Eq.2.18, so that the integrand becomes:

$$\Sigma = \left|\sum_n U^*_n(\epsilon'-m-n) U_{n+m}(\epsilon'-m-n-\omega)\right|^2 f(\epsilon'-m)(1-f(\epsilon'-\omega)) \tag{A.19}$$

We expand the Floquet scattering matrices $U^*_n(\epsilon'-m-n)$ and $U_{n+m}(\epsilon'-m-n-\omega)$ as a function of the c_n coefficients. We perform a variable substitution so that the sum rule on the c_n coefficients given in Eq.1.10 yields:

$$\Sigma = \left|\sum_n c^*_n c_{n-m} U^{0*}(\epsilon'-n) U^0(\epsilon'-n-\omega)\right|^2 f(\epsilon'-m)(1-f(\epsilon'-\omega)) \tag{A.20}$$

The variable substitution $n' \equiv -n$ yields:

$$\Sigma = \left|\sum_{n'} c^*_{-n'} c_{-n'-m} U^{0*}(\epsilon'+n') U^0(\epsilon'+n'-\omega)\right|^2 f(\epsilon'-m)(1-f(\epsilon'-\omega)) \tag{A.21}$$

Eq.A.16 finally yields, with the notations $n \equiv n'$ and $\epsilon \equiv \epsilon'$:

$$\Sigma = \left|\sum_n c_n[-V'] c^*_{n+m}[-V'] U^{0*}(\epsilon+n) U^0(\epsilon+n-\omega)\right|^2 f(\epsilon-m)(1-f(\epsilon-\omega)) \tag{A.22}$$

This integrand is identical to the one in Eq.A.18, with a change of the sign of the potential $V'(t)$ caused by the gauge translation.

A.4 Emission and absorption noise

We demonstrate here that the excess noise of the source (*i.e.* the remaining contribution of noise when the noise at the pinch-off is subtracted) is symmetric with the measurement: the emission and absorption noises of the single electron emitter are equal.

We first calculate $\Delta(S) = S(\omega) - S(-\omega)$, using Eq.2.18. In the expression of $S(-\omega)$, the successive variable substitutions $\epsilon' \equiv \epsilon + m + \omega$, $n' \equiv n + m$ and $m' = -m$ yield:

$$\begin{aligned}
S(-\omega) &= 2\frac{e^2}{h}\sum_m \int d\epsilon' \left|\sum_n U^*_n(\epsilon'-m-n-\omega) U_{n+m}(\epsilon'-n-m)\right|^2 f(\epsilon'-m-\omega)(1-f(\epsilon')) \\
&= 2\frac{e^2}{h}\sum_m \int d\epsilon' \left|\sum_{n'} U^*_{n'-m}(\epsilon'-n'-\omega) U_{n'}(\epsilon'-n')\right|^2 f(\epsilon'-m-\omega)(1-f(\epsilon')) \\
&= 2\frac{e^2}{h}\sum_{m'} \int d\epsilon' \left|\sum_{n'} U^*_{n'+m'}(\epsilon'-n'-\omega) U_{n'}(\epsilon'-n')\right|^2 f(\epsilon'+m'-\omega)(1-f(\epsilon'))
\end{aligned} \tag{A.23}$$

The difference $\Delta(S) = S(\omega) - S(-\omega)$ is therefore equal to:

$$\Delta(S) = 2\frac{e^2}{h}\sum_m \int d\epsilon \left|\sum_n U_n^*(\epsilon - n)U_{n+m}(\epsilon - n - \omega)\right|^2 (f(\epsilon) - f(\epsilon + m - \omega)) \tag{A.24}$$

Using the second sum rule on the Floquet scattering matrix (see A.1), the difference between absorption and emission noise at zero transmission $\Delta(S)^\circ = S(\omega, D = 0) - S(-\omega, D = 0)$ is given by:

$$\begin{aligned} \Delta(S)^\circ &= 2\frac{e^2}{h}\int d\epsilon\,(f(\epsilon) - f(\epsilon - \omega)) \\ &= 2\frac{e^2}{h}\sum_m \int d\epsilon \left|\sum_n U_n^*(\epsilon - n)U_{n+m}(\epsilon - n - \omega)\right|^2 (f(\epsilon) - f(\epsilon - \omega)) \end{aligned} \tag{A.25}$$

The difference $\Delta(S) - \Delta(S)^\circ$ is then equal to:

$$\Delta(S) - \Delta(S)^\circ = 2\frac{e^2}{h}\sum_m \int d\epsilon \left|\sum_n U_n^*(\epsilon - n)U_{n+m}(\epsilon - n - \omega)\right|^2 (f(\epsilon - \omega) - f(\epsilon + m - \omega)) \tag{A.26}$$

Similarly to A.3.2, we expand the Floquet scattering matrix as a function of the c_n coefficients and apply variable substitutions so that the sum rule on the c_n coefficients yields:

$$\Delta(S) - \Delta(S)^\circ = 2\frac{e^2}{h}\sum_m \int d\epsilon \left|\sum_n c_n c_{m+n}^* U^{0*}(\epsilon - n)U^0(\epsilon - n - \omega)\right|^2 (f(\epsilon - \omega) - f(\epsilon + m - \omega)) \tag{A.27}$$

We now assume that the c_n coefficients are real, so that $c_n c_{m+n}^* = c_n c_{m+n}$. This only corresponds to a shift in the origin of time so that the excitation drive is even in time. The successive variable substitutions $\epsilon' \equiv \epsilon + m$, $n' = n + m$ and $m' = m$ yield:

$$\begin{aligned} \Delta(S) - \Delta(S)^\circ &= 2\frac{e^2}{h}\sum_m \int d\epsilon' \left|\sum_n c_n c_{m+n} U^{0*}(\epsilon' - n - m)U^0(\epsilon' - n - m - \omega)\right|^2 \\ &\quad \times \big(f(\epsilon' - m - \omega) - f(\epsilon' - \omega)\big) \\ &= 2\frac{e^2}{h}\sum_m \int d\epsilon' \left|\sum_{n'} c_{n'-m} c_{n'} U^{0*}(\epsilon' - n')U^0(\epsilon' - n' - \omega)\right|^2 \\ &\quad \times \big(f(\epsilon' - m - \omega) - f(\epsilon' - \omega)\big) \\ &= 2\frac{e^2}{h}\sum_{m'} \int d\epsilon' \left|\sum_{n'} c_{n'+m'} c_{n'} U^{0*}(\epsilon' - n')U^0(\epsilon' - n' - \omega)\right|^2 \\ &\quad \times \big(f(\epsilon' + m' - \omega) - f(\epsilon' - \omega)\big) \end{aligned} \tag{A.28}$$

We finally obtain:

$$\begin{aligned} \Delta(S) - \Delta(S)^\circ &= 2\frac{e^2}{h}\sum_m \int d\epsilon \left|\sum_n c_{n+m} c_n U^{0*}(\epsilon - n)U^0(\epsilon - n - \omega)\right|^2 (f(\epsilon + m - \omega) - f(\epsilon - \omega)) \\ &= -\left(\Delta(S) - \Delta(S)^\circ\right) \end{aligned} \tag{A.29}$$

The difference $\Delta(S) - \Delta(S)^\circ$ is therefore equal to zero: the excess absorption and emission noises of the source are indeed equal.

A.5 Partition of a shot noise

The numerical computation of the variations of both the noise of the source $S(\omega)$ and the partition term $C(\omega)$ with the measurement frequency ω presented in 3.2.2.2 show that at low transmission of the dot QPC D, $S(\omega \neq 0)$ and $C(\omega \neq 0)$ are equal. For these values of the transmission, $S(\omega \neq 0)$ can be described as a shot noise; we rely on this property to demonstrate the result mentioned above. We use Eq.55 defined for multiterminal devices at zero temperature in [79], which expresses the correlation $S_{\alpha\beta}$ between the current fluctuations of two terminals α and β as a function of the Fermi distributions of each terminal $f_\gamma(\epsilon)$, and the scattering matrix elements $s_{\alpha\gamma}$:

$$S_{\alpha\beta} = \frac{e^2}{h} \sum_{\gamma \neq \delta} \int d\epsilon Tr[s^\dagger_{\alpha\gamma} s_{\alpha\delta} s^\dagger_{\beta\delta} s_{\beta\gamma}] \left(f_\gamma(\epsilon)(1 - f_\delta(\epsilon)) + f_\delta(\epsilon)(1 - f_\gamma(\epsilon)) \right) \tag{A.30}$$

- **Shot noise emitted by the source**

Let us first calculate the expression of the noise of the source $S(\omega \neq 0)$ in the shot-noise limit, by describing the source as a simple tunnel barrier with a low transmission $D = t^2$, as depicted in Fig.A.1.

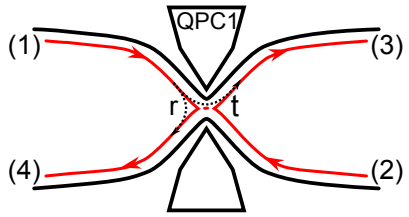

Figure A.1: Partition noise generated by a quantum point contact: terminal (1) is biased, all other terminals are grounded

Terminal (1) is biased with the voltage V_b, while all other terminals are grounded; we focus on the autocorrelation of the current fluctuations in terminal (3) S_{33}. The relevant scattering matrix elements are therefore $s_{31} = t$ and $s_{32} = r$. Eq.A.30 thus yields:

$$S_{33} = 2\frac{e^2}{h} r^2 t^2 \int d\epsilon \left(f_1(\epsilon)(1 - f_2(\epsilon)) + f_2(\epsilon)(1 - f_1(\epsilon)) \right) \tag{A.31}$$

At zero temperature,, the integral is equal to eV_b. With $r^2t^2 = D(1-D)$, we recover the well-known expression of the partition noise:

$$S_{33} = 2e \left(\frac{e^2}{h} V_b \right) D(1 - D) = 2eI \times D(1 - D) \tag{A.32}$$

Where $I = \frac{e^2}{h} V_b = G_0 V_b$ is the current in terminal (1), G_0 being the conductance of a single edge channel. When the transmission D is low, we have $S_{33} = S(\omega \neq 0) = 2eI \times D$.

- **Partition of the shot noise**

To reproduce the HBT geometry discussed in the third chapter, we now consider the configuration depicted in Fig.A.2, where the current flowing from the first QPC (terminal (3) in the previous paragraph) is partitioned by a second QPC. To suppress multiple loops between the two QPCs, an ohmic contact (5) is inserted in the lower branch between the two QPCs; we then have $s_{31} = t_1 t_2$, $s_{32} = r_2$ and $s_{42} = 0$. As in the previous paragraph, only terminal (1) is biased, and we calculate the autocorrelation of the current fluctuations in terminal (3) S_{33}. The relevant scattering matrix elements are therefore $s_{31} = t_1 t_2$, $s_{32} = r_2$ and $s_{35} = r_1 t_2$.

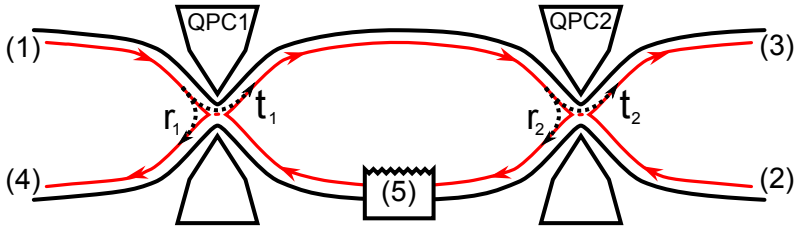

Figure A.2: Partition of a partition noise generated by a quantum point contact: terminal (1) is biased, all other terminals are grounded

In these conditions, Eq.A.30 yields:

$$\begin{aligned} S_{33} &= \frac{e^2}{h}\int d\epsilon (t_1 t_2 r_2)^2 (f_1(\epsilon)(1-f_2(\epsilon)) + f_2(\epsilon)(1-f_1(\epsilon))) \\ &+ \frac{e^2}{h}\int d\epsilon (t_1 t_2 r_1 t_2)^2 (f_1(\epsilon)(1-f_5(\epsilon)) + f_5(\epsilon)(1-f_1(\epsilon))) \\ &+ \frac{e^2}{h}\int d\epsilon (r_2 r_1 t_2)^2 (f_2(\epsilon)(1-f_5(\epsilon)) + f_5(\epsilon)(1-f_2(\epsilon))) \end{aligned} \tag{A.33}$$

Since only terminal (1) is biased, the third term in the above equation vanishes at zero temperature. We therefore have, with $t_1^2 = T_1$, $(t_2 r_2)^2 = T_2(1-T_2)$, $t_2^2 = T_2$, $(t_1 r_1)^2 = T_1(1-T_1)$:

$$S_{33} = 2e\left(\frac{e^2}{h} V_b T_1 T_2 (1-T_2) + T_1(1-T_1)T_2^2\right) = 2eI \times T_1 T_2 (1-T_2) + 2eI \times T_1(1-T_1)T_2^2 \tag{A.34}$$

As seen in the third chapter, the noise after partition by the second QPC yields a partition term multiplied by $T_2(1-T_2)$, corresponding to the partition term $C(\omega)$, and the noise upstream of the second QPC $2eI \times T_1(1-T_1)$, multiplied by the factor T_2^2, corresponding to the term $S(\omega)$. When the transmission of the first QPC T_1 becomes small, we recover a pure shot noise term for the noise upstream of the second QPC $S(\omega \neq 0) = 2eI \times T_1$, which is then equal to the partition term $C(\omega \neq 0)$.

Appendix B

Summary of the samples parameters

We present here a table summarizing the parameters of the various samples mentioned in this manuscript:

sample ID	*E3*	*S528-11*	*S434-8*
density n	$1.3 \times 10^{11} cm^{-2}$	$1.9 \times 10^{11} cm^{-2}$	$1.8 \times 10^{11} cm^{-2}$
mobility μ	$2.6 \times 10^{6} cm^{2} V^{-1} s^{-1}$	$1.3 \times 10^{6} cm^{2} V^{-1} s^{-1}$	$2.4 \times 10^{6} cm^{2} V^{-1} s^{-1}$
dimensions of the dot	$1\mu m \times 1\mu m$	$0.6\mu m \times 0.6\mu m$	$0.8\mu m \times 0.8\mu m$
level spacing Δ	$2.5 \pm 0.5K$	$4.2 \pm 0.2K$	$3 \pm 0.2K$
residual temperature T_{el}	$270 \pm 20mK$	$60 \pm 15mK$	$70 \pm 15mK$
operating frequency f_0	$32MHz$, $180MHz$, $515MHz$, $1.5GHz$	$1.5GHz$	$1.5GHz$
magnetic field B	$1.38T$	$1.79T$	$3.9T$
measurements	$I(t)$ $(32MHz)$ I_Ω $(180MHz - 1.5GHz)$	I_Ω $S(\Omega)$	I_Ω $S(\Omega)$ $C_{I_1 I_1}(\Omega)$, $C_{I_1 I_1}(0)$
references	[10, 11, 62, 70, 71]	[63, 68]	

List of figures

1 Electronic Mach-Zehnder interferometer. . . . 3
2 Quantum Hall effect. . . . 4
3 Quantum point contact. . . . 5
4 Coulomb blockade. . . . 8
5 The mesoscopic capacitor as a single electron source. . . . 9
6 Single-charge HBT measurements. . . . 13
7 Single-charge Hong-Ou-Mandel measurements. . . . 14

Realization of a Single Electron Source **15**
1.1 Modeling of a mesoscopic capacitor. . . . 17
1.2 Time-dependent scattering matrix description of the quantum dot. . . . 18
1.3 Calculated density of states in the dot for several values of the QPC transmission. . . . 21
1.4 Measurement setup for the first harmonic of the average AC current. . . . 25
1.5 Conductance as a function of the QPC gate voltage V_g. . . . 29
1.6 Calibration of the quantum capacitance of sample *S528-11*. . . . 30
1.7 Linear conductance at 1.5 GHz of sample *S528-11*, for different temperatures. . . . 31
1.8 Calculated first harmonic as a function of the excitation amplitude. . . . 34
1.9 Calculated first harmonic as a function of the excitation amplitude, for several values of the transmission. . . . 35
1.10 Calculated escape time as a function of the QPC transmission. . . . 36
1.11 AC current emitted by the source, calculated with the heuristic model. . . . 37
1.12 Escape time, calculated with the heuristic model. . . . 38
1.13 Average transfered charge per half-period, calculated with the heuristic model. . . . 39
1.14 Measured average AC current as a function of time. . . . 41
1.15 Nyquist diagram of the measured current at 1.5 GHz. . . . 42
1.16 First harmonic of the average AC current as a function of V_g, in the non-linear regime. 43
1.17 Observation of AC current quantization for sample *S528-11*. . . . 44
1.18 Two-dimensional plot of the first harmonic, as a function of V_g and V_{exc}. . . . 45
1.19 Escape time and average transfered charge as a function of V_g. . . . 46
1.20 Escape time as a function of V_{exc}. . . . 48

Current fluctuations emitted by the source **51**
2.1 Definition of the current operators. . . . 55
2.2 Scattering model: noise as a function of the transmission. . . . 59
2.3 Scattering model: noise as a function of the measurement frequency. . . . 60
2.4 Scattering model: noise as a function of the dot equilibrium potential. . . . 62
2.5 Square signals, for several number of odd harmonics 63
2.6 Scattering model: dependence on the number of harmonics. . . . 63
2.7 Heuristic model: current correlators $C_1(t')$ and $C_2(t')$. . . . 65
2.8 Heuristic model: dependence of the noise on the escape probability. . . . 67
2.9 Heuristic model: dependence of the noise on the measurement frequency. . . . 68
2.10 Calculated noise versus modulus of the current. . . . 69
2.11 Heuristic model: noise versus escape time. . . . 70

2.12 Optical and SEM pictures of sample *S528-11* . . . 71
2.13 Three-terminal geometry. . . . 72
2.14 Noise measurements: experimental setup. . . . 74
2.15 Noise versus QPC gate voltage V_g. . . . 75
2.16 Noise power spectral density versus modulus of the first harmonic. . . . 76
2.17 Measured noise versus escape time. . . . 77
2.18 QPC transmission as a function of V_g. . . . 78
2.19 Measured and calculated noise power spectral density as a function of the QPC gate voltage V_g. . . . 78

Current fluctuations in the Hanbury-Brown and Twiss geometry **81**
3.1 Definition of the creation/annihilation operators for the correlations in the HBT geometry. 83
3.2 Single electron emitter in the HBT geometry. . . . 88
3.3 Zero-frequency part of the partition noise $C_{I_1I_1}(\omega = 0)$ as a function of the dot QPC transmission D and the central QPC transmission T. . . . 93
3.4 Variation of the zero-frequency partition noise with the dot equilibrium potential and the shape of the drive. . . . 94
3.5 Variation of $C(\omega)$ and $S(\omega)$ with the measurement frequency. . . . 95
3.6 Calculation of the frequency and time variations of the cross-correlation. . . . 96
3.7 $C_{I_1I_1}(\omega = \Omega)$ versus central QPC transmission T. . . . 97
3.8 $\partial C(\omega = 0)/\partial V_{bias}$ versus V_{bias}. . . . 98
3.9 Effect of the temperature on the difference $C_{I_1I_1}(\omega = 0, \phi_0 = \pi) - C_{I_1I_1}(\omega = 0, \phi_0 = 0)$. 99
3.10 Effect of the temperature on the measurement of the energy distribution of the emitted charges. . . . 100
3.11 Optical view of the samples used in the HBT measurements. . . . 102
3.12 Configuration of the HBT experiment. . . . 103
3.13 Characterization of the two-dimensional electron gas . . . 104
3.14 Conductance of the central QPC as a function of V_{qpc} and the magnetic field. . . . 106
3.15 Transmission of the central QPC as a function of V_{qpc}, at $\nu = 2$. . . . 106
3.16 Two-dimensional plot of the first harmonic of the average AC current emitted by the single electron source versus V_g and V_{exc}, for sample *S434-8*. . . . 107
3.17 Real and imaginary parts of the first harmonic for sample *S434-8*. . . . 109
3.18 Transmission of the average AC current emitted by the source by the central QPC. . . . 110
3.19 Noise of the single electron source in sample *S434-8*. . . . 110
3.20 Noise of the single electron source versus $|I_\Omega|$. . . . 111
3.21 Zero-frequency part of the partition noise of the source in the HBT geometry, versus the central QPC transmission T. . . . 112
3.22 High frequency noise in the HBT geometry, measured as a function of the transmission T. 113
3.23 Zero-frequency noise in the HBT geometry versus V_g, for $T = 0.5$. . . . 114
3.24 Transmission of the average AC current emitted by the source by the central QPC, for $B = -3.3$ T. . . . 115
3.25 High frequency noise in the HTB geometry, measured as a function of the transmission T at $B = -3.3$ T. . . . 115
3.26 Measurement of the electronic temperature using the HBT geometry. . . . 116

High-frequency and low-frequency noise measurement setups **119**
4.1 Principle of the modulated double balanced amplifier setup . . . 122
4.2 Comparison of the signal-to-noise ratio for a direct amplification technique and for our setup. . . . 125
4.3 Schematic of the implemented RF noise measurement setup. . . . 126
4.4 Tuning of the setup. . . . 127
4.5 120 Ω to 50 Ω impedance transformer. . . . 128
4.6 Calibration of the RF noise measurement setup. . . . 129
4.7 Operation of the RF noise measurement setup. . . . 130
4.8 Modified RF noise measurement setup. . . . 131
4.9 Calibration of the modified RF noise measurement setup. . . . 133
4.10 Low frequency noise measurement setup. . . . 134
4.11 Highpass and lowpass filters. . . . 134
4.12 Principle of low-frequency cross-correlation measurement. . . . 135
4.13 Calibration of the low-frequency measurement setup. . . . 137
4.14 Measurement time as a function of the measurement load R_0. . . . 140

A.1 Partition noise generated by a quantum point contact: terminal (1) is biased, all other terminals are grounded . . . 150
A.2 Partition of a partition noise generated by a quantum point contact: terminal (1) is biased, all other terminals are grounded . . . 151

Bibliography

[1] R. Schuster, E. Buks, M. Heiblum, D. Mahalu, V. Umansky and H. Shtrikman, "Phase measurement in a quantum dot via a double-slit interference experiment", *Nature* **385**, 417–420 (1997). (Page 1.)

[2] Y. Ji, Y. Chung, D. Sprinzak, M. Heiblum, D. Mahalu and H. Shtrikman, "An Electronic Mach-Zehnder Interferometer", *Nature* **422**, 415–8 (2003). (Pages 1, 2, and 3.)

[3] A. Aharonov and Y. Sharvin, "Magnetic flux effects in disordered conductors", *Reviews of Modern Physics* **59**, 755–779 (1987). (Page 1.)

[4] E. Buks, R. Schuster, M. Heiblum, D. Mahalu and V. Umansky, "Dephasing in electron interference by a "which-path" detector", *Nature* **391**, 871–874 (1998). (Page 1.)

[5] P. Roulleau, F. Portier, P. Roche, A. Cavanna, G. Faini, U. Gennser and D. Mailly, "Direct Measurement of the Coherence Length of Edge States in the Integer Quantum Hall Regime", *Physical Review Letters* **100**, 126802 (2008). (Pages 1, 2, 4, 105, and 117.)

[6] P. Samuelsson and M. Büttiker, "Dynamic generation of orbital quasiparticle entanglement in mesoscopic conductors", *Physical Review B* **71**, 245317 (2005). (Page 1.)

[7] I. Neder, N. Ofek, Y. Chung, M. Heiblum, D. Mahalu and V. Umansky, "Interference between two indistinguishable electrons from independent sources.", *Nature* **448**, 333–337 (2007). (Pages 1 and 2.)

[8] R. Ionicioiu, G. Amaratunga and F. Udrea, "Quantum Computation with Ballistic Electrons", *International Journal of Modern Physics B* **15**, 5 (2000). (Page 1.)

[9] J. Splettstoesser, M. Moskalets and M. Büttiker, "Two-particle nonlocal Aharonov-Bohm effect from two single-particle emitters.", *Physical Review Letters* **103**, 076804 (2009). (Pages 1, 7, and 141.)

[10] G. Fève, A. Mahé, J.-M. Berroir, T. Kontos, B. Plaçais, D. C. Glattli, A. Cavanna, B. Etienne and Y. Jin, "An on-demand coherent single-electron source.", *Science* **316**, 1169–1172 (2007). (Pages 1, 10, 11, 18, and 153.)

[11] G. Fève, "Quantification du courant alternatif : la boîte quantique comme source d'électrons uniques subnanoseconde", *PhD Thesis, Université Pierre et Marie Curie* (2006). (Pages 1, 18, 19, 20, 24, 25, 26, 28, 29, 32, 40, 46, 47, and 153.)

[12] S. Ol'khovskaya, J. Splettstoesser, M. Moskalets and M. Büttiker, "Shot noise of a mesoscopic two-particle collider.", *Physical Review Letters* **101**, 166802 (2008). (Pages 2, 7, 14, 102, 117, and 144.)

[13] C. Dean, B. Piot, G. Gervais, L. Pfeiffer and K. West, "Current-induced nuclear-spin activation in a two-dimensional electron gas", *Physical Review B* **80**, 153301 (2009). (Page 2.)

[14] A. Kou, D. McClure, C. Marcus, L. Pfeiffer and K. West, "Dynamic Nuclear Polarization in the Fractional Quantum Hall Regime", *Physical Review Letters* **105**, 056804 (2010). (Page 2.)

[15] P. Roulleau, F. Portier, D. Glattli, P. Roche, A. Cavanna, G. Faini, U. Gennser and D. Mailly, "Finite bias visibility of the electronic Mach-Zehnder interferometer", *Physical Review B* **76**, 161309 (2007). (Pages 2, 105, and 117.)

[16] L. Litvin, H.-P. Tranitz, W. Wegscheider and C. Strunk, "Decoherence and single electron charging in an electronic Mach-Zehnder interferometer", *Physical Review B* **75**, 033315 (2007). (Page 2.)

[17] E. Bieri, M. Weiss, O. Göktas, M. Hauser, C. Schönenberger and S. Oberholzer, "Finite-bias visibility dependence in an electronic Mach-Zehnder interferometer", *Physical Review B* **79**, 245324 (2009). (Page 2.)

[18] P. Roulleau, F. Portier, P. Roche, A. Cavanna, G. Faini, U. Gennser and D. Mailly, "Noise Dephasing in Edge States of the Integer Quantum Hall Regime", *Physical Review Letters* **101**, 186803 (2008). (Pages 2, 105, and 117.)

[19] P. Roulleau, F. Portier, P. Roche, A. Cavanna, G. Faini, U. Gennser and D. Mailly, "Tuning Decoherence with a Voltage Probe", *Physical Review Letters* **102**, 236802 (2009). (Pages 2, 13, 105, 117, and 144.)

[20] D. Yoshioka, *The quantum Hall effect*, Springer (2002), ISBN 3540431152. (Pages 3 and 4.)

[21] M. Büttiker, "Absence of backscattering in the quantum Hall effect in multiprobe conductors", *Physical Review B* **38**, 9375–9389 (1988). (Page 4.)

[22] M. Reznikov, M. Heiblum, H. Shtrikman and D. Mahalu, "Temporal Correlation of Electrons: Suppression of Shot Noise in a Ballistic Quantum Point Contact", *Physical Review Letters* **75**, 3340–3343 (1995). (Pages 4 and 121.)

[23] L. Saminadayar, D. Glattli, Y. Jin and B. Etienne, "Observation of the e/3 Fractionally Charged Laughlin Quasiparticle", *Physical Review Letters* **79**, 2526–2529 (1997). (Pages 4, 6, and 70.)

[24] C. Altimiras, H. le Sueur, U. Gennser, A. Cavanna, D. Mailly and F. Pierre, "Non-Equilibrium Edge Channel Spectroscopy in the Integer Quantum Hall Regime", *Nature Physics* **6**, 13 (2009). (Pages 4, 82, 101, 105, and 117.)

[25] H. le Sueur, C. Altimiras, U. Gennser, A. Cavanna, D. Mailly and F. Pierre, "Energy Relaxation in the Integer Quantum Hall Regime", *Physical Review Letters* **105**, 056803 (2010). (Pages 4, 82, 101, 105, and 117.)

[26] P. Degiovanni, C. Grenier, G. Fève, C. Altimiras, H. le Sueur and F. Pierre, "Plasmon scattering approach to energy exchange and high-frequency noise in ν=2 quantum Hall edge channels", *Physical Review B* **81**, 121302 (2010). (Pages 4 and 117.)

[27] P. Degiovanni, C. Grenier and G. Fève, "Decoherence and relaxation of single-electron excitations in quantum Hall edge channels", *Physical Review B* **80**, 241307 (2009). (Pages 5 and 117.)

[28] B. van Wees, L. Kouwenhoven, H. van Houten, C. Beenakker, J. Mooij, C. Foxon and J. Harris, "Quantized conductance of magnetoelectric subbands in ballistic point contacts", *Physical Review B* **38**, 3625–3627 (1988). (Pages 5 and 6.)

[29] M. Büttiker, "Quantized transmission of a saddle-point constriction", *Physical Review B* **41**, 7906–7909 (1990). (Pages 5 and 22.)

[30] A. Szafer and A. Stone, "Theory of Quantum Conduction through a Constriction", *Physical Review Letters* **62**, 300–303 (1989). (Page 5.)

[31] A. Kumar, L. Saminadayar, D. Glattli, Y. Jin and B. Etienne, "Experimental Test of the Quantum Shot Noise Reduction Theory", *Physical Review Letters* **76**, 2778–2781 (1996). (Pages 6, 11, 61, and 132.)

[32] M. Henny, S. Oberholzer, C. Strunk, T. Heinzel, K. Ensslin, M. Holland and C. Schönenberger, "The fermionic Hanbury-Brown and Twiss experiment", *Science* **284**, 296–8 (1999). (Pages 6, 11, and 87.)

[33] W. D. Oliver, J. Kim and Y. Liu, R. C.and Yamamoto, "Hanbury Brown and Twiss-Type Experiment with Electrons", *Science* **284**, 299–301 (1999). (Pages 6 and 11.)

[34] Y. Zhang, L. DiCarlo, D. McClure, M. Yamamoto, S. Tarucha, C. Marcus, M. Hanson and A. Gossard, "Noise Correlations in a Coulomb-Blockaded Quantum Dot", *Physical Review Letters* **99**, 036603 (2007). (Page 6.)

[35] R. De-Picciotto, M. Reznikov, M. Heiblum, V. Umansky, G. Bunin and D. Mahalu, "Direct Observation of a Fractional Charge", *Nature* **389**, 3 (1997). (Page 6.)

[36] R. J. Schoelkopf, "The Radio-Frequency Single-Electron Transistor (RF-SET): A Fast and Ultrasensitive Electrometer", *Science* **280**, 1238–1242 (1998). (Page 6.)

[37] M. Devoret and R. Schoelkopf, "Amplifying quantum signals with the single-electron transistor", *Nature* **406**, 1039–46 (2000). (Page 6.)

[38] J. M. Elzerman, R. Hanson, L. H. Willems Van Beveren, B. Witkamp, L. M. K. Vandersypen and L. P. Kouwenhoven, "Single-shot read-out of an individual electron spin in a quantum dot.", *Nature* **430**, 431–5 (2004). (Page 6.)

[39] J. Chaste, L. Lechner, P. Morfin, G. Fève, T. Kontos, J.-M. Berroir, D. C. Glattli, H. Happy, P. Hakonen and B. Plaçais, "Single carbon nanotube transistor at GHz frequency.", *Nano Letters* **8**, 525–528 (2008). (Page 6.)

[40] S. E. S. Andresen, F. Wu, R. Danneau, D. Gunnarsson and P. J. Hakonen, "Highly sensitive and broadband carbon nanotube radio-frequency single-electron transistor", *Journal of Applied Physics* **104**, 033715 (2008). (Page 6.)

[41] G. Fève, P. Degiovanni and T. Jolicoeur, "Quantum detection of electronic flying qubits in the integer quantum Hall regime", *Physical Review B* **77**, 035308 (2008). (Page 6.)

[42] C. K. Hong, Z. Y. Ou and L. Mandel, "Measurement of subpicosecond time intervals between two photons by interference", *Physical Review Letters* **59**, 2044–2046 (1987). (Pages 7 and 117.)

[43] J. M. Shilton, V. I. Talyanskii, M. Pepper, D. A. Ritchie, J. E. F. Frost, C. J. B. Ford, C. G. Smith and G. A. C. Jones, "High-frequency single-electron transport in a quasi-one-dimensional GaAs channel induced by surface acoustic waves", *Journal of Physics: Condensed Matter* **8**, L531 (1996). (Page 7.)

[44] V. Talyanskii, J. Shilton, M. Pepper, C. Smith, C. Ford, E. Linfield, D. Ritchie and G. Jones, "Single-electron transport in a one-dimensional channel by high-frequency surface acoustic waves", *Physical Review B* **56**, 15180–15184 (1997). (Page 7.)

[45] J. Cunningham, V. Talyanskii, J. Shilton, M. Pepper, M. Simmons and D. Ritchie, "Single-electron acoustic charge transport by two counterpropagating surface acoustic wave beams", *Physical Review B* **60**, 4850–4855 (1999). (Page 7.)

[46] A. Robinson and V. Talyanskii, "Shot Noise in the Current of a Surface Acoustic-Wave-Driven Single-Electron Pump", *Physical Review Letters* **95**, 247202 (2005). (Page 7.)

[47] M. D. Blumenthal, B. Kaestner, L. Li, S. Giblin, T. J. B. M. Janssen, M. Pepper, D. Anderson, G. Jones and D. A. Ritchie, "Gigahertz quantized charge pumping", *Nature Physics* **3**, 343–347 (2007). (Page 7.)

[48] N. Maire, F. Hohls, B. Kaestner, K. Pierz, H. W. Schumacher and R. J. Haug, "Noise measurement of a quantized charge pump", *Applied Physics Letters* **92**, 082112 (2008). (Pages 7, 70, and 144.)

[49] F. Battista and P. Samuelsson, "Proposal for non-local electron-hole turnstile in the Quantum Hall regime", *ArXiv:1006.0136* (2010). (Page 7.)

[50] S. P. Giblin, S. J. Wright, J. D. Fletcher, M. Kataoka, M. Pepper, T. J. B. M. Janssen, D. A. Ritchie, C. A. Nicoll, D. Anderson and G. A. C. Jones, "An accurate high-speed single-electron quantum dot pump", *New Journal of Physics* **12**, 073013 (2010). (Page 7.)

[51] D. Averin, A. Korotkov and K. Likharev, "Theory of single-electron charging of quantum wells and dots", *Physical Review B* **44**, 6199–6211 (1991). (Page 9.)

[52] P. McEuen, E. Foxman, U. Meirav, M. Kastner, Y. Meir, N. Wingreen and S. Wind, "Transport spectroscopy of a Coulomb island in the quantum Hall regime", *Physical Review Letters* **66**, 1926–1929 (1991). (Page 9.)

[53] H. Pothier, P. Lafarge, C. Urbina, D. Esteve and M. Devoret, "Single-Electron Pump Based on Charging Effects", *EPL (Europhysics Letters)* **17**, 249 (1992). (Page 9.)

[54] M. W. Keller, J. M. Martinis, N. M. Zimmerman and A. H. Steinbach, "Accuracy of electron counting using a 7-junction electron pump", *Applied Physics Letters* **69**, 1804 (1996). (Page 9.)

[55] M. Büttiker, H. Thomas and A. Prêtre, "Mesoscopic capacitors", *Physics Letters A* **180**, 364–369 (1993). (Pages 10 and 26.)

[56] L. S. Levitov, H. W. Lee and G. B. Lesovik, "Electron Counting Statistics and Coherent States of Electric Current", *Journal of Mathematical Physics* **37**, 43 (1996). (Page 10.)

[57] J. Keeling, I. Klich and L. Levitov, "Minimal Excitation States of Electrons in One-Dimensional Wires", *Physical Review Letters* **97**, 116403 (2006). (Pages 10 and 92.)

[58] T. Martin and R. Landauer, "Wave-packet approach to noise in multichannel mesoscopic systems", *Physical Review B* **45**, 1742–1755 (1992). (Page 10.)

[59] R. Glauber, "The Quantum Theory of Optical Coherence", *Physical Review* **130**, 2529–2539 (1963). (Page 10.)

[60] P. Michler, A. Kiraz, C. Becher, W. V. Schoenfeld, P. M. Petroff, L. Zhang, E. Hu and A. Imamoglu, "A quantum dot single-photon turnstile device.", *Science* **290**, 2282–5 (2000). (Pages 11, 52, and 82.)

[61] Z. Yuan, B. E. Kardynal, R. M. Stevenson, A. J. Shields, C. J. Lobo, K. Cooper, N. S. Beattie, D. A. Ritchie and M. Pepper, "Electrically driven single-photon source.", *Science* **295**, 102–5 (2002). (Pages 11, 52, 82, and 83.)

[62] J. Gabelli, G. Fève, J.-M. Berroir, B. Plaçais, A. Cavanna, B. Etienne, Y. Jin and D. C. Glattli, "Violation of Kirchhoff's laws for a coherent RC circuit.", *Science* **313**, 499–502 (2006). (Pages 11, 32, and 153.)

[63] A. Mahé, F. D. Parmentier, E. Bocquillon, J.-M. Berroir, D. C. Glattli, T. Kontos, B. Plaçais, G. Fève, A. Cavanna and Y. Jin, "Current correlations of an on-demand electron source as an evidence of single particle emission", *ArXiv:1004.1985, accepted for publication in Phys.Rev. B Rapid Communications* (2010). (Pages 12, 37, and 153.)

[64] J. Keeling, A. Shytov and L. Levitov, "Coherent Particle Transfer in an On-Demand Single-Electron Source", *Physical Review Letters* **101**, 196404 (2008). (Pages 12, 82, 91, 100, 116, 117, and 143.)

[65] C. Grenier, R. Hervé, E. Bocquillon, F. D. Parmentier, B. Plaçais, J.-M. Berroir, G. Fève and P. Degiovanni, "Single electron quantum tomography in quantum Hall edge channels", *ArXiv:1010.2166* (2010). (Pages 13, 82, 101, 117, and 143.)

[66] M. Moskalets and M. Büttiker, "Floquet scattering theory of quantum pumps", *Physical Review B* **343**, 205320 (2002). (Page 17.)

[67] S. Hwang, D. Tsui and M. Shayegan, "Experimental evidence for finite-width edge channels in integer and fractional quantum Hall effects", *Physical Review B* **48**, 8161–8165 (1993). (Page 17.)

[68] A. Mahé, "Bruit de charge d'une source d'électrons uniques subnanoseconde", *PhD Thesis, Université Pierre et Marie Curie* (2009). (Pages 18, 19, 20, 24, 26, 37, 40, 43, 57, 147, and 153.)

[69] M. Büttiker, H. Thomas and A. Prêtre, "Current partition in multiprobe conductors in the presence of slowly oscillating external potentials", *Zeitschrift für Physik B Condensed Matter* **94**, 133–137 (1994). (Page 21.)

[70] J. Gabelli, "Mise en évidence de la cohérence quantique des conducteurs en régime dynamique", *PhD Thesis, Université Pierre et Marie Curie* (2006). (Pages 24, 25, 26, 28, 29, 32, and 153.)

[71] A. Mahé, F. D. Parmentier, G. Fève, J.-M. Berroir, T. Kontos, A. Cavanna, B. Etienne, Y. Jin, D. C. Glattli and B. Plaçais, "Subnanosecond Single Electron Source in the Time-Domain", *Journal of Low Temperature Physics* **153**, 339–349 (2008). (Pages 26, 40, and 153.)

[72] C. Mora and K. Le Hur, "Universal resistances of the quantum resistance-capacitance circuit", *Nature Physics* **6**, 697–701 (2010). (Pages 28 and 46.)

[73] M. Büttiker and S. E. Nigg, "Role of coherence in resistance quantization", *The European Physical Journal Special Topics* **172**, 9 (2008). (Page 36.)

[74] R. Landauer, "Electrical resistance of disordered one-dimensional lattices", *Philosophical Magazine* **21**, 863–867 (1970). (Page 36.)

[75] S. E. Nigg, R. López and M. Büttiker, "Mesoscopic charge relaxation.", *Physical Review Letters* **97**, 206804 (2006). (Page 46.)

[76] J. Splettstoesser, M. Governale, J. König and M. Büttiker, "Charge and spin dynamics in interacting quantum dots", *Physical Review B* **81**, 165318 (2010). (Page 46.)

[77] G.-L. Ingold and Y. V. Nazarov, 21–107 *Charge Tunneling Rates in Ultrasmall Junctions*, Plenum Press, New York (1992). (Page 47.)

[78] M. Assmann, F. Veit, M. Bayer, M. van Der Poel and J. M. Hvam, "Higher-order photon bunching in a semiconductor microcavity.", *Science* **325**, 297–300 (2009). (Page 52.)

[79] Y. M. Blanter and M. Büttiker, "Shot Noise in Mesoscopic Conductors", *Physics Reports* **336**, 1–166 (1999). (Pages 54, 93, and 150.)

[80] M. Moskalets and M. Büttiker, "Time-resolved noise of adiabatic quantum pumps", *Physical Review B* **75**, 035315 (2007). (Page 54.)

[81] H. Park and K.-H. Ahn, "Admittance and Noise in an Electrically Driven Nanostructure: Interplay between Quantum Coherence and Statistics", *Physical Review Letters* **101**, 116804 (2008). (Pages 54 and 58.)

[82] A. A. Clerk, S. M. Girvin, F. Marquardt and R. J. Schoelkopf, "Introduction to quantum noise, measurement, and amplification", *Reviews of Modern Physics* **82**, 1155–1208 (2010). (Pages 54 and 55.)

[83] R. Deblock, E. Onac, L. Gurevich and L. P. Kouwenhoven, "Detection of quantum noise from an electrically driven two-level system.", *Science* **301**, 203–6 (2003). (Page 55.)

[84] P.-M. Billangeon, F. Pierre, H. Bouchiat and R. Deblock, "Emission and Absorption Asymmetry in the Quantum Noise of a Josephson Junction", *Physical Review Letters* **96**, 136804 (2006). (Page 55.)

[85] Q. Le Masne, H. Pothier, N. O. Birge, C. Urbina and D. Esteve, "Asymmetric Noise Probed with a Josephson Junction", *Physical Review Letters* **102**, 067002 (2009). (Page 55.)

[86] G. B. Lesovik and R. Loosen, "On the detection of finite-frequency current fluctuations", *Journal of Experimental and Theoretical Physics Letters* **65**, 295–299 (1997). (Page 58.)

[87] E. Zakka-Bajjani, J. Ségala, F. Portier, P. Roche, D. Glattli, A. Cavanna and Y. Jin, "Experimental Test of the High-Frequency Quantum Shot Noise Theory in a Quantum Point Contact", *Physical Review Letters* **99**, 236803 (2007). (Pages 61, 121, and 129.)

[88] R. Danneau, F. Wu, M. Craciun, S. Russo, M. Tomi, J. Salmilehto, A. Morpurgo and P. Hakonen, "Shot Noise in Ballistic Graphene", *Physical Review Letters* **100**, 196802 (2008). (Pages 61 and 121.)

[89] M. Albert, C. Flindt and M. Büttiker, "Accuracy of the quantum capacitor as a single-electron source", *Physical Review B* **82**, 041407 (2010). (Page 66.)

[90] H. Birk, M. de Jong and C. Schönenberger, "Shot-Noise Suppression in the Single-Electron Tunneling Regime", *Physical Review Letters* **75**, 1610–1613 (1995). (Page 70.)

[91] A. Bid, N. Ofek, M. Heiblum, V. Umansky and D. Mahalu, "Shot Noise and Charge at the 2/3 Composite Fractional Quantum Hall State", *Physical Review Letters* **103**, 236802 (2009). (Pages 70 and 73.)

[92] F. D. Parmentier, A. Mahé, A. Denis, J.-M. Berroir, D. C. Glattli, B. Plaçais and G. Fève, "A high sensitivity ultralow temperature RF conductance and noise measurement setup.", *Review of Scientific Instruments* **82**, 013904 (2011). (Pages 73 and 120.)

[93] R. Engelbrecht and K. Kurokawa, "A wide-band low noise L-band balanced transistor amplifier", *Proceedings of the IEEE* **53**, 237–247 (1965). (Pages 73 and 121.)

[94] L.-H. Reydellet, P. Roche, D. Glattli, B. Etienne and Y. Jin, "Quantum Partition Noise of Photon-Created Electron-Hole Pairs", *Physical Review Letters* **90**, 176803 (2003). (Page 82.)

[95] C. Beenakker and M. Büttiker, "Suppression of shot noise in metallic diffusive conductors", *Physical Review B* **46**, 1889–1892 (1992). (Page 87.)

[96] S. Oberholzer, E. Bieri, C. Schönenberger, M. Giovannini and J. Faist, "Positive Cross Correlations in a Normal-Conducting Fermionic Beam Splitter", *Physical Review Letters* **96**, 046804 (2006). (Page 87.)

[97] V. Rychkov, M. Polianski and M. Büttiker, "Photon-assisted electron-hole shot noise in multiterminal conductors", *Physical Review B* **72**, 155326 (2005). (Page 87.)

[98] P. Anderson, "Infrared Catastrophe in Fermi Gases with Local Scattering Potentials", *Physical Review Letters* **18**, 1049–1051 (1967). (Page 100.)

[99] J. Gabelli, G. Fève, T. Kontos, J.-M. Berroir, B. Placais, D. C. Glattli, B. Etienne, Y. Jin and M. Büttiker, "Relaxation time of a chiral quantum R-L circuit.", *Physical Review Letters* **98**, 166806 (2007). (Page 106.)

[100] M. Avinun-Kalish, M. Heiblum, O. Zarchin, D. Mahalu and V. Umansky, "Crossover from 'mesoscopic' to 'universal' phase for electron transmission in quantum dots.", *Nature* **436**, 529–533 (2005). (Page 108.)

[101] K. C. Nowack, F. H. L. Koppens, Y. V. Nazarov and L. M. K. Vandersypen, "Coherent control of a single electron spin with electric fields.", *Science* **318**, 1430–3 (2007). (Page 108.)

[102] G. Shinkai, T. Hayashi, T. Ota and T. Fujisawa, "Correlated Coherent Oscillations in Coupled Semiconductor Charge Qubits", *Physical Review Letters* **103**, 056802 (2009). (Page 108.)

[103] R. Schoelkopf, P. Burke, A. Kozhevnikov, D. Prober and M. Rooks, "Frequency Dependence of Shot Noise in a Diffusive Mesoscopic Conductor", *Physical Review Letters* **78**, 3370–3373 (1997). (Page 121.)

[104] J. Gabelli, L.-H. Reydellet, G. Fève, J.-M. Berroir, B. Plaçais, P. Roche and D. Glattli, "Hanbury Brown-Twiss Correlations to Probe the Population Statistics of GHz Photons Emitted by Conductors", *Physical Review Letters* **93**, 056801 (2004). (Page 121.)

[105] F. Wu, L. Roschier, T. Tsuneta, M. Paalanen, T. Wang and P. Hakonen, "Setup for shot noise measurements in carbon nanotubes", *AIP Conference Proceedings* **850**, 1482–1483 (2006). (Page 121.)

[106] M. Gervasi, G. Boella, F. Cavaliere, G. Grossetti, A. Passerini, G. Sironi, A. Tartari and M. Zannoni, "Dual output polarimeter devoted to the study of the Cosmic Microwave Background", *Proceedings of SPIE: Polarimetry in Astronomy* **4843**, 336–347 (2003). (Page 121.)

[107] S. Asztalos, E. Daw, H. Peng, L. Rosenberg, C. Hagmann, D. Kinion, W. Stoeffl, K. van Bibber, P. Sikivie, N. Sullivan, D. Tanner, F. Nezrick, M. Turner, D. Moltz, J. Powell, M.-O. André, J. Clarke, M. Mück and R. Bradley, "Large-scale microwave cavity search for dark-matter axions", *Physical Review D* **64**, 092003 (2001). (Page 121.)

[108] R. Simons, *Coplanar waveguide circuits, components, and systems*, John Wiley and Sons (2001), ISBN 0471161217. (Page 121.)

[109] J. S. Bendat and A. G. Piersol, *Random Data: Analysis and Measurement Procedures*, John Wiley and Sons (2010), ISBN 0470248777. (Page 124.)

[110] A. Chincarini, G. Gemme, M. Iannuzzi, R. Parodi and R. Vaccarone, "Gain and noise analysis of HEMT amplifiers from room temperature to superfluid He", *Classical and Quantum Gravity* **23**, S293–S298 (2006). (Page 126.)

[111] D. M. Pozar, *Microwave engineering*, John Wiley and Sons (2005), ISBN 0471448788. (Page 129.)

[112] D. C. Glattli, "Quantum shot noise of conductors and general noise measurement methods", *The European Physical Journal Special Topics* **172**, 163–179 (2009). (Pages 132 and 135.)

[113] T. Delattre, C. Feuillet-Palma, L. G. Herrmann, P. Morfin, J.-M. Berroir, G. Fève, B. Plaçais, D. C. Glattli, M. S. Choi, C. Mora and T. Kontos, "Noisy Kondo impurities", *Nature Physics* **5**, 208–212 (2009). (Page 132.)

[114] L. DiCarlo, Y. Zhang, D. T. McClure, C. M. Marcus, L. N. Pfeiffer and K. W. West, "System for measuring auto- and cross correlation of current noise at low temperatures", *Review of Scientific Instruments* **77**, 073906 (2006). (Pages 138, 139, and 144.)